# Variational principles in nonlinear mechanics using convex optimization and automated numerical tools

Jeremy Bleyer

# Mémoire d'Habilitation à Diriger des Recherches

# Variational principles in nonlinear mechanics using convex optimization and automated numerical tools

Jérémy Bleyer

Ecole nationale des ponts et chaussées
Chercheur au Laboratoire Navier
Ingénieur des Ponts, des Eaux et des Forêts
Professeur chargé de cours à l'Ecole Polytechnique

Soutenue le 22 Novembre 2024 devant le jury composé de:

| | | |
|---|---|---|
| Laura de Lorenzis | Rapporteure | ETH Zürich |
| Vincent Acary | Rapporteur | INRIA Grenoble |
| Peter Noe Poulsen | Rapporteur | Technical University of Denmark (DTU) |
| Grégoire Allaire | Examinateur | École Polytechnique |
| Djimedo Kondo | Examinateur | Sorbonne Université |
| Nicolas Moës | Examinateur | Université catholique de Louvain |

*À Marion, William & Hugo*
*À Marguerite & Maria*

# Contents

# Chapter 1

# Curriculum vitae


## Jérémy Bleyer

Born on July 15th 1988 in Mulhouse, France
Researcher at Laboratoire Navier
École des Ponts, Université Gustave Eiffel, CNRS, Marne-la-vallée, France

☎ +33 (0)1 64 15 37 43
✉ jeremy.bleyer@enpc.fr
https://bleyerj.github.io
IdHAL: jeremy-bleyer, ORCID: 0000-0001-8212-9921


### Curriculum

| | |
|---|---|
| **Jan 2017 – now** | Researcher at Laboratoire Navier, ENPC, Univ Gustave Eiffel, CNRS, UMR 8205 |
| **Jan 2016 – Dec 2016** | Postdoctoral researcher at Ecole Polytechnique Fédérale de Lausanne, Switzerland |
| **Sep 2012 – Dec 2015** | PhD from Université Paris-Est, *Numerical methods for the yield design of civil engineering structures*, supervised by Patrick de Buhan at Laboratoire Navier |
| **Sep 2010 – now** | Engineer of *Corps des Ponts, des Eaux et des Forêts* |

### Teaching

| | |
|---|---|
| **Sep 2020 – now** | Part-time Associate Professor at École Polytechnique, Mechanical Engineering Department |
| **Sep 2017 – now** | Assistant Professor at École des Ponts ParisTech, Civil Engineering Department |
| **Sep 2011 – Sep 2017** | Teaching Assistant École des Ponts ParisTech |

### Education

| | |
|---|---|
| **Sep 2010 – Sep 2012** | École des Ponts ParisTech, Engineering degree, Civil Engineering Department |
| **Sep 2010 – Sep 2011** | Master of Science, Mechanics of Materials and Structures (ENPC, Université Paris-Est) with highest honors |
| **Sep 2007 – Sep 2010** | École Polytechnique, Engineering degree, Mechanical Engineering Department |

### Honors and awards

| | |
|---|---|
| **2023 Jean Mandel Prize** | |
| **2016 PhD award** | Delivered by Université Paris-Est |
| **2016 PhD award** | Delivered by École des Ponts ParisTech |
| **2010 Medal L.E. Rivot** | Delivered by the French Academy of Sciences: "*particular interest for scientific research and quality of work in the domain of mechanical and computational sciences*" |

## Scientific supervision

### PhD students

2023-now **Alice Gribonval**, *Modeling of 3D-printed concrete structures*, advisor Karam Sab, industrial collaboration with XtreeE

2023-now **Giulia d'Orio**, *Reinforced concrete behavior for modeling and safety of nuclear civil engineering structures*, advisor Arthur Lebée, industrial collaboration with EDF R& D

2023-now **Gaspard Blondet**, *Advanced modeling of cross-laminated timber panel behavior*, advisor Arthur Lebée, fellowship of ENS Paris-Saclay and ENPC

2021-now **Sabine Boulvard**, *Failure design of reinforced concrete beams subject to shear and torsional loadings in fire conditions*, advisor Karam Sab, industrial collaboration with CSTB

2021-now **Zakaria Chafia**, *Multi-scale modelling strategies for predicting the failure behaviour of cementitious materials*, advisor Julien Yvonnet (Université Gustave Eiffel), funded by LabeX MMCD

2020-2023 **Goustan Bacquaert**, *Behaviour of geomaterials for the modeling and safety analysis of geotechnical structures*, advisor Djimédo Kondo (Sorbonne Université), CIFRE funding in collaboration with Électricité de France

2018-2021 **Leyla Mourad**, *Topology optimization of structural load-bearing capacity through limit analysis*, advisor Karam Sab, joint thesis with University Saint-Joseph, Lebanon

2018-2021 **Paul Bouteiller**, *Failure modeling of composites laminates in a layerwise plate model*, advisor Karam Sab, industrial collaboration with Dassault Aviation

2017-2021 **Lucille Salha**, *Mesh adaptation and hybridization for efficient stress prediction in a layerwise plate model*, advisor Karam Sab, joint thesis with University Saint-Joseph, Lebanon

2017-2020 **Chadi El Boustani**, *Innovative optimization-based numerical methods for modeling the nonlinear behavior of steel structures*, advisor Karam Sab, CIFRE funding in collaboration with Strains

2015-2018 **Karol Cascavita**, *Hybrid discretization methods for Signorini contact and Bingham flow problems*, advisors Alexandre Ern and Xavier Chateau, funded by LabeX MMCD

2015-2018 **Hugues Vincent**, *Development of a yield design model until failure for 3D reinforced concrete structures*, advisor Patrick de Buhan, CIFRE funding in collaboration with Strains

**Main advisor** (80%) for H. Vincent, C. El Boustani, L. Salha, P. Bouteiller, L. Mourad.
**Co-advisor** (50%) for S. Boulvard and Z. Chafia.
**Participation** (20%) for G. Bacquaert and K. Cascavita.

### Postdoctoral fellows

2023 **Mohammad Mainroodi**, *Physics-informed neural networks for the analysis of nonlinear structures*, joint supervision with S. Brisard

2021 **Jean-Michel Scherer**, *Multiphase-field modeling of anisotropic brittle fracture in additively-manufactured polycrystals*, joint supervision with Stella Brach (LMS-X), funded by the *Coup de Pouce* grant from Fédération Francilienne de Mécanique

### Master students

2023 **Alice Gribonval**, *Modeling of 3D-printed concrete structures*, master thesis ENPC, joint supervision with XtreeE company

2022 **Andrey Latyshev**, *Finite-element implementation of standard and softening plasticity using convex programming*, engineering thesis ENPC, joint supervision with Corrado Maurini (Sorbonne Université)

2022 **Maximin Duvillard**, *Robust optimization of structures in presence of uncertainties*, engineering thesis ENPC

2021 **Zakaria Chafia**, *Multilayer micromechanical model of failure in a matrix/inclusion composite*, master thesis ENPC

2020 **Pimprenelle Parmentier**, *Robust optimization for handling uncertainties in structural analysis*, master thesis ENPC, joint supervision with Vincent Leclère (CERMICS, ENPC)

2019 **Antoine Martin**, *Buckling behaviour of CLT panels under concentrated load*, master thesis ENPC, joint supervision with Arthur Lebée (Navier, ENPC)

2019 **Eki Agouzal**, *Simulation of yield stress fluid flows with free surfaces*, 6 months internship from ENPC, joint supervision with Xavier Chateau (Navier, ENPC)

2018 **Joël Keumo Tematio**, *Buckling modeling of a cylindrical steel grid using an homogenization approach*, master thesis Ecole Polytechnique, joint supervision with Maged Sidhom (IFPEN)

2018 **Mehdi Assad**, *Implementation of the Bending-Gradient on FEniCS*, research internship of Ecole Polytechnique, joint supervision with Arthur Lebée (Navier, ENPC)

### Visiting students

2023 **Hana Herndon**, Georgia Institute of Technology, *Quantifying the uncertainty in a steel bridge with corrosion-induced damage*

2017 **Thomas Westergaard Jensen**, Technical University of Denmark, *Finite-element limit analysis of bridge structures*

## Invitations

2023 **Workshop** CSMA Juniors
*Hands-on session: Introduction to FEniCSx*

2022 **Workshop** Homogenization and optimization of polymers, Ecole Polytechnique
*Conic programming approach for the simulation and optimization of nonlinear membranes*

2020 **Workshop** Design challenges of 3D printing in the construction industry
*Topology optimization for designing structures with optimal load-bearing capacity*

2020 **Workshop** ENPC-University of Tokyo
*An overview of computational limit analysis for civil engineering applications*

2019 **Workshop** RAM3 - Recent Advances in Mechanics and Mathematics of Materials
*An overview of computational limit analysis for civil engineering applications*

2015 **Visit (6 weeks)** to University of Newcastle, Australia, with K. Krabbenhoft and A. Lyamin

**Invited seminars** at CEA, EDF, LMS (Ecole Polytechnique), GeM (Centrale Nantes), University of Luxembourg

## Reviewing activities

I have been reviewing for the following journals (14 papers in average): Applied Mathematical Modelling, Composites Part B: Engineering, Composites Structures, Comptes Rendus - Mécanique, Computational Materials Science, Computer Methods in Applied Mechanics and Engineering, Engineering Fracture Mechanics, Engineering Structures, European Journal of Mechanics - A/Solids, International Journal for Numerical Methods in Engineering, International Journal for Numerical and Analytical Methods in Geomechanics, International Journal of Computational Methods, International Journal of Fracture, International Journal of Solids and Structures, Journal of the Mechanics and Physics of Solids, Marine Georesources & Geotechnology, Meccanica, Mechanics of Materials.

I have also been reviewing for the SIGGRAPH conference.

2024 grant proposal for the *ERC*

2024 grant proposal for the *The Israel Science Foundation*

2022 grant proposal for the *Fonds zur Förderung der wissenschaftlichen Forschung* (Austrian Science Fund)

2018 book proposal for ICE Publishing

## Grants

2023 **ANR PRC ANOHONA** *Advanced nonlinear homogenization for structural analysis*, Member

2022 **Digital Europe** (7M€) *Digital Twins for Complex Infrastructures and Urban ecosystems*, European consortium, WP leader

2021 **Labex MMCD**, PhD thesis funding for Zakaria Chafia, with J. Yvonnet (MSME)
*Multi-scale modelling strategies for predicting the failure behaviour of cementitious materials*

2021 **Coup de Pouce F2M** (40 k€), with S. Brach (LMS) *Multiphase-field modeling of anisotropic brittle fracture in additively-manufactured polycrystals*

**Denied**

2022 ANR JCJC (PI) OROMIS *Robust optimization for uncertainty quantification in structural design*

2020 Nuclear Valley DAS4 *Digitization for Optimization of Nuclear Design and Construction*

2017 FEDER Ile de France *Yield design of construction wood assemblies*

## Industrial contracts

**CSTB**, support for Sabine Boulvard PhD thesis

**Turbostream Ltd**, scientific consulting mission

**Électricité de France**, support for Goustan Bacquaert PhD thesis

**Setec tpi**, support for Leyla Mourad PhD thesis

**Dassault Aviation**, support for Paul Bouteiller PhD thesis

**Strains**, support for Chadi El Boustani and Hugues Vincent PhD theses + scientific consulting mission

## Involvement in the scientific community

### PhD thesis committees

#### International

2023 **Sindhu Nagaraja**, ETH Zürich
*Phase-field modeling of brittle fracture: anisotropy and efficient discretization*
Jury: Corrado Maurini, Jérémy Bleyer, Laura de Lorenzis, Aldo Steinfeld

2017 **Morten A. Herfelt**, Technical University of Denmark
*Numerical limit analysis of precast concrete structures*
Jury: Henrik Stang, Jérémy Bleyer, Bent Steen Andreasen, Peter Noe Poulsen, Linh Cao Hoang, Jesper Frøbert Jensen

**France**

2024 **Nikhil Mohanan**, Ecole Polytechnique - IPP
*On the intergranular response during laser scanning of additively manufactured stainless steel: a thermomechanical simulation study*
Jury: Laurent Delannay, Vincent Taupin, Anna Ask, Eric Charkaluk, Martin Diehl, Maurine Montagnat, Javier Segurado, Manas Upadhyay, Jérémy Bleyer, Nicolò Grilli, Thomas Helfer

2023 **Xinyuan Zhai**, ENSTA ParisTech - IPP
*Crack propagation in elastic media with anisotropic fracture toughness : experiments and phase-field modeling* Jury: Corrado Maurini, Benoit Roman, Jeremy Bleyer, Fabien Szmytka, Véronique Lazarus, Stella Brach, Thomas Corre, Andrés A. León Baldelli

2023 **Goustan Bacquaert**, Sorbonne Université
*Behavior of geomaterials for modeling and safety of geotechnical structures* Jury: Pierre Besuelle, Laurent Stainier, Samuel Forest, Laura de Lorenzis, Jean-Jacques Marigo, François Voldoire, Jeremy Bleyer, Djimédo Kondo, Corrado Maurini, Vinicius Alves-Fernandes, Simon Raude

2023 **David Siedel**, Mines Paris - PSL
*A robust numerical approach for the description of brittle fracture and viscoplastic behavior of fuel rods*
Jury: Riccardo Rossi, Sylvain Drapier, Vanessa Lleras, Djimédo Kondo, Jérémy Bleyer, Jacques Besson, Thomas Helfer, Olivier Fandeur, Samuel Forest, Nicolas Pignet

2022 **Salim Chaibi**, ISAE Toulouse
*Prediction of low-velocity/low-energy impact damages in the latest generation of carbon-epoxy laminated composites*
Jury: Emmanuelle Abisset, Peter Davies, Rodrigue Desmorat, Zoheir Aboura, Jérémy Bleyer, Carlos G. Dávila, Johann Rannou, Christophe Bouvet.

2022 **Paul Bouteiller**, ENPC
*Simulation of laminate composite failure using stress-based layerwise plate models*
Jury: Véronique Lazarus, Federica Daghia, Corrado Maurini, Johann Rannou, Christophe Bouvet, Fabrice Congourdeau, Jérémy Bleyer, Karam Sab.

2021 **Leyla Mourad**, ENPC-Université Saint-Joseph (Beyrouth)
*Strength-based topology optimization of structures using limit analysis* Jury: Fabrice Gatuingt, Boris Desmorat,Grégoire Allaire, Jérémy Bleyer, Romain Mesnil, Joanna Nseir, Karam Sab, Wassim Raphael.

2021 **Lucille Salha**, ENPC-Université Saint-Joseph (Beyrouth)
*Mesh adaptation and hybridization for efficient stress prediction in a layerwise plate model*
Jury: Toni Sayah, Olivier Polit, Steven Marguet, Jérémy Bleyer, Joanna Bodgi, Karam Sab

2020 **Chadi El Boustani**, ENPC *Innovative optimization-based numerical methods for modeling the non-linear behavior of steel structures* Jury: Habibou Maitournam, Nicolas Moës, Mohammed Hjiaj, Mickaël Abbas, Laurence Davaine, Jérémy Bleyer, Xavier Cespedes, Karam Sab

2019 **Mohammad El Hajj Diab**, IFSTTAR *Analysis of structural robustness : characterization of accidental/exceptional events and of their impacts on infrastructures* Jury: Stéphane Grange,

Alan O'Connor, Mohammed Hjiaj, Jérémy Bleyer, Robby Caspeele, Jean-François Demonceau, Cédric Desprez, André Orcesi

2018 **Karol Cascavita**, ENPC
*Hybrid discretization methods for Signorini contact and Bingham flow problems*
Jury: Raphaèle Herbin, Pierre Saramito, Patrick Hild, Miguel Angel Fernandez Varela, Erik Burman, Jérémy Bleyer, Xavier Chateau, Alexandre Ern.

2018 **Hugues Vincent**, ENPC
*Development of a yield design model for 3D reinforced concrete structures*
Jury: Aurelio Muttoni, Samir Maghous, Géry de Saxcé, Jérémy Bleyer, Patrick de Buhan.

2018 **Mingguan Yang**, ENPC
*Stability of reinforced concrete walls under fire conditions by a yield design approach*
Jury: Jean-Marc Franssen, François Buyle-Bodin, Mohammed Hjiaj, Jérémy Bleyer, Duc Toan Pham, Patrick de Buhan.

### Participation to councils or committees

**Elected member** of Laboratoire Navier council

**Member** of the Civil Engineering Department council at ENPC

**Member** of a hiring committee for a *Maître de conférences* position at Sorbonne Université/Polytech Sorbonne (2021)

### Organization of scientific events

**Core member** of the MEALOR Summer school[1]

**Core member** of the GdR MePhy *Mécanique et Physique des Systèmes Complexes*[2]

**Co-animator** (formerly with Sébastien Brisard) of a working group on Computational tools in Laboratoire Navier

**Co-animator** of the seminar of the *Architectural Materials and Structures* research team at Laboratoire Navier

**Co-organizer** (with Jack Hale and Garth Wells) of the mini-symposium *Developments in automatic code-generation software for computational mechanics* at WCCM-ECCOMAS 2020, Paris (online)

## Others

### Open science activities

I am strongly involved in the FEniCS users community. I provide regular help on the users forum and I maintain a set of commented demos called *Numerical tours of Computational Mechanics using FEniCSx* oriented towards solid and structural mechanics applications: https://bleyerj.github.io/comet-fenicsx/

[1] https://mealor2.sciencesconf.org/
[2] https://mephysociety.wordpress.com/

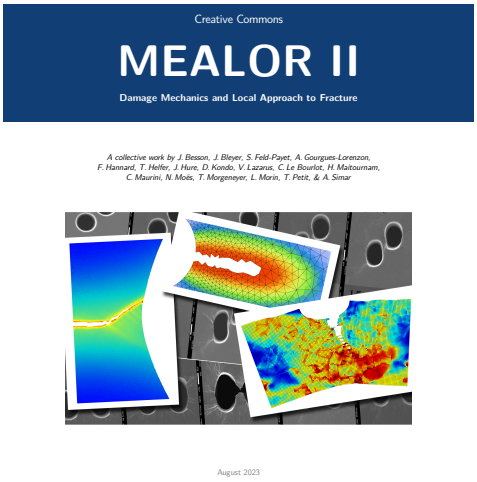


Figure 1.1: MEALOR II : Damage Mechanics and Local Approach to Fracture

Formerly, using the legacy FEniCS package at: https://comet-fenics.readthedocs.io/

I am the developer of the open-source `fenics_optim` package:

Repository: https://gitlab.enpc.fr/navier-fenics/fenics-optim

Documentation: https://fenics-optim.readthedocs.io

I am also involved in the development of the `MFrontGenericInterfaceSupport` open-source project lead by Thomas Helfer (CEA):
https://thelfer.github.io/mgis/web/index.html

For the MEALOR II Summer School, we wrote a book (Fig. 1.1) discussing the physics and mechanics of brittle and ductile fracture under monotonic loading, covering theoretical, numerical, and experimental aspects as well as the latest applications and research developments of the local approach to fracture. This collective work is in open-access and released with CC-BY-SA license.

### Outreach

- Interview *La construction, un chantier d'avenir pour la mécanique*, 25 mai 2022. CNRS le Journal, Mécanique : dans l'atelier du futur
- Article revue Transitions: Bleyer J., Arquier M., Fliscounakis A., Développement d'outils de calculs innovants dans l'ingénierie de génie civil. Transitions. Les nouvelles Annales des Ponts et Chaussées, 2022, Bâtiments et construction en transition, 2, pp.54-59
- EELISA Innovation Talks/Matinale des Ponts: Digital Twins, March 28$^{th}$ 2023

# Chapter 2

# Introduction

The purpose of this chapter is to provide a brief summary of my academic and teaching experiences. I will start by outlining my master's, PhD, and postdoctoral research projects. Then, I will summarize my current research work at the Laboratoire Navier. Since I have a strong passion for teaching, I will also describe my past and current teaching activities. Finally, I will discuss the objectives and structure of this manuscript.

## Contents

## 2.1 An overview of my academic history

### 2.1.1 Master research projects

My academic journey began in 2010 when I completed my studies at École Polytechnique and started working as an intern at *Setec Tpi*, a French engineering firm specializing in civil engineering, building engineering, and nuclear engineering, among others. I was part of the development team of their in-house finite-element solver, called *Pythagore*, under the supervision of Xavier Cespedes and Mathieu Arquier. My research internship focused on implementing elasto-plastic shell elements in Pythagore, which was a challenging task for a student who had just learned mechanics and had no prior knowledge of shell structures.

I deeply cherished this internship as I learned a great deal about shell theory, finite-elements, and plasticity. It also gave me the opportunity to apply these tools to real projects in civil engineering and construction. I am grateful to the development team for this experience. This internship sparked my interest in numerical methods, civil engineering applications, research, and teaching, which ultimately led to my PhD thesis topic. I am also proud to have continued this scientific collaboration through the years, including supervising industrial PhD theses initiated by the team members who later founded the engineering firm *Strains*.

In 2011, I completed my master's thesis at École des Ponts under the supervision of Alain Ehrlacher. My research focused on using complex potentials to solve planar elastic problems through (semi)-analytical resolution. I was fascinated by the application of mathematical concepts such as complex analysis to practical problems, particularly in fracture mechanics. However, I realized that I preferred hands-on implementation of numerical methods over lengthy calculations using the Cauchy principal values and the residue theorem.

### 2.1.2 PhD thesis at laboratoire Navier

My PhD thesis was inspired by discussions between Xavier Cespedes, Mathieu Arquier, and my future advisor Patrick de Buhan regarding the development of numerical methods based on the concepts of limit analysis theory for civil engineering applications. Limit analysis, or yield design theory, as formalized by Salençon (2013), allows for the direct computation of the ultimate load that a structure can sustain without solving for its complete nonlinear behavior on a given loading path. The variational approaches based on stress (resp. virtual displacement) fields can provide a lower (resp. upper) bound estimate of the structure limit load by combining equilibrium equations with strength conditions. However, its numerical implementation is challenging as it involves solving convex optimization problems that are highly non-smooth and of large scale. At that time, the Pythagore team's attempts to use general-purpose optimization methods had failed to produce reliable results in a reasonable amount of time. I was offered the opportunity to work on the topic of *Numerical methods for the yield design of civil engineering structures*, which I gladly accepted. After conducting a literature survey, I discovered that the most promising methods for solving these problems were based on a formulation as conic programming and dedicated interior-point algorithms. To this day, these numerical techniques form the basis of many of my works and will be thoroughly discussed in this manuscript.

Regarding mechanical aspects, the main challenges on which I focused were the following:

- the development of dedicated finite-element (FE) discretization techniques, either with respect to stresses, or with respect to virtual displacements. A notable specificity of limit analysis is that inter-element discontinuities can be considered, contrary to most classical FE discretizations. In particular, I proposed various implementations for thin

(Bleyer and de Buhan, 2013b) and thick (Bleyer and de Buhan, 2014c; Bleyer et al., 2015b) plates as well as shell structures (Bleyer and de Buhan, 2016; Bleyer, 2021), thereby showing that the classical problem of shear locking can be easily avoided using such discontinuous formulations.

- The formulation of complex strength criteria via the conic programming framework. Notably, I worked on a multi-scale approach of yield design in order to account for the strength properties of heterogeneous materials (e.g. multilayered plates or shells, composite beams, reinforced soils, etc.). In particular, I relied on the concepts of homogenization theory (Bleyer and de Buhan, 2014b,a, 2016) combined with judicious approximation procedures of the resulting homogenized yield surface (Bleyer and de Buhan, 2013d,a).

- The application of these concepts on civil engineering examples such as the fire resistance of high-rise reinforced concrete panels or on a periodic curved canopy for the Austerlitz railway station.

In addition to my PhD work, I collaborated with Mathilde Maillard, who was also pursuing her PhD at Laboratoire Navier, on a side project. Her PhD was studying the coating of yield stress or visco-plastic, fluids for which the existing numerical methods were difficult to use. After reviewing the constitutive models of visco-plastic fluids, I proposed using interior-point solvers, which outperformed the commonly used Augmented Lagrangian algorithms (Bleyer et al., 2015c; Bleyer, 2018a).

During my PhD, I was also invited by Kristian Krabbenhoft and Andrei Lyamin from the University of Newcastle, Australia to work on limit analysis of shells. This opportunity also allowed me to initiate a collaboration with Xue Zhang, who was researching the simulation of submarine landslides using the Particle Finite Element Method. I found that viscoplastic models are useful in describing the rheological behavior of sediments.

### 2.1.3 Postdoctoral researcher at Ecole Polytechnique Fédérale de Lausanne

In 2016, Jean-François Molinari offered me the opportunity to work as a postdoctoral researcher at the École Polytechnique Fédérale de Lausanne (EPFL) where I was introduced to a unique research culture and enjoyed a positive work and living environment. During my PhD, I mainly focused on the plasticity of structures under quasi-static conditions. However, at EPFL, I embarked on a new project exploring fast dynamic fracture of brittle materials. My objectives were twofold: to gain experience in using phase-field approaches for modeling brittle fracture dynamics, and to evaluate the ability of these numerical methods to accurately simulate complex physical phenomena like macro- and microbranching instabilities and crack velocity limitations, which arise in dynamic fracture. These aspects will be discussed in more detail in Chapter 8, Section 8.2.

## 2.2 Summary of my research activities at Laboratoire Navier

In 2017, I joined Laboratoire Navier as a permanent researcher in the *Architectured Materials and Structures* team. Since then, my research has focused on developing advanced mechanical models as well as innovative simulation tools to study the failure of materials and structures. I strive to cover a wide spectrum of disciplines, ranging from applied mathematics (convex analysis and optimization in particular), theoretical mechanics (homogenization, generalized

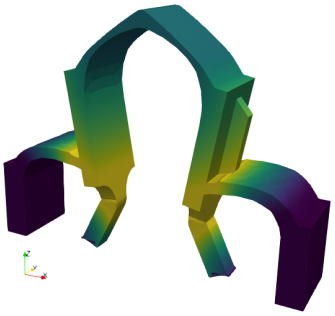

(a) Abbey made of masonry

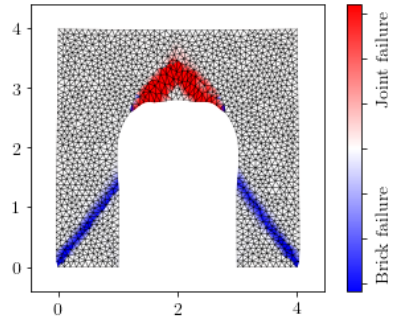


(b) Collapse of an arch including brick failure (in blue) as well as joint failure (in red)

Figure 2.1: Numerical yield design collapse mechanisms for masonry structures

media, variational principles) and computational mechanics (finite element method, nonlinear solvers). While some of my works may be quite fundamental, I also aim to implement them in various engineering applications, primarily in civil engineering, often in partnership with industry. My methodologies are chosen with a focus on two important societal concerns: sustainable construction and risk management.

In the following sections, I have organized my research activities into four main categories. Note that most illustrations concern research topics which will not be presented in the main part of the manuscript.

### 2.2.1 Limit/yield design analysis for civil engineering

After my PhD studies, I continued to advance both theoretical and numerical methods for implementing limit analysis on various mechanical models. A major shift from my PhD work was to abandon my custom Matlab implementations, as these were tedious to maintain and lacked extensibility. Instead, I focused on creating a highly generic computational framework using the open-source FEniCS library to handle the finite-element discretization and `Mosek` conic programming solver for optimization. With FEniCS' high-level syntax, I aimed to develop a *domain-specific language* that would allow for easy formulation of convex optimization problems, which could then be discretized and solved efficiently. This work was released as a Python package named *fenics_optim* (Bleyer, 2020b). Its versatility has been demonstrated through various applications in computational fluid and solid mechanics, optimal transport, and image processing (Bleyer, 2020a). Most recently, we also utilized this framework to automate the formulation of limit analysis problems for various mechanical models (Bleyer and Hassen, 2021). This framework will be described in further detail in Chapter 5.

The developments of such limit analysis tools have also been applied to civil engineering problems in the context of industrial collaborations. In particular, the industrial PhD thesis of Hugues Vincent with the civil engineering firm *Strains* has been focused on numerical limit analysis of massive 3D reinforced-concrete (RC) structures (Vincent et al., 2018, 2020) (e.g. bridge pier cap, footings, etc.) and masonry structures (e.g. vaults, abbey), see Fig. 2.1. The results of these studies were integrated into Strains' numerical suite of design tools, providing advanced and more efficient solutions for the analysis of such structures, see Section 5.5.2 for more details. The second PhD thesis in collaboration with Strains was that of Chadi El Boustani which focused on the analysis of complex 3D steel joints, as discussed

in Section 5.5.1. The work covered both limit analysis and elastoplastic analysis through the development of a specialized interior-point solver (El Boustani et al., 2020a,b). The solver was also adapted for large deformations (El Boustani et al., 2020c). The results were promising, enabling fully nonlinear analyses of complex steel structures despite the non-convex nature of the optimization problem.

In addition to my research in the field of civil engineering, I have also collaborated with the Centre Scientifique et Technique du Bâtiment (CSTB) on projects related to fire safety. One such collaboration was Mingguan Yang during his PhD thesis, where we analyzed the failure of high-rise RC panels, considering both geometrical nonlinearities caused by thermal strain and reduced strength capacities of steel and concrete at high temperatures. Currently, I am supervising with Duc Toan Pham the thesis of Sabine Boulvard, who is investigating the failure of RC beams under shear and torsional loadings in fire conditions.

### 2.2.2 Automated numerical tools

My research activities require an important part of numerical development. I strive to make them as open as possible for enhancing collaboration, transparency and reproducibility of published results. Moreover, I decided to focus my developments on the FEniCS FE platform which enables to make them as generic as possible for easier extensibility and prototyping. As a result, I became very involved in the user community.

For instance, I have never really contributed to the software development but I wanted instead to improve the set of FEniCS tutorials by targeting specifically users from the solid mechanics and structures community. Indeed, many tutorials in the official documentation deal with applied mathematics or fluid mechanics problems. I therefore started publishing a series of Numerical Tours of Computational Mechanics using FEniCS[1] (Bleyer, 2018c). These tutorials allow students or researchers with a mechanics background to learn how to use FEniCS through examples they are familiar with. These works also allowed me to approach the modeling of problems that appear less natural to formulate in FEniCS than it seems (beam, plate and shell models in particular). The success of this project within the international FEniCS community has led to the establishment of multiple collaborative relationships.

The most notable is my collaboration with Thomas Helfer (CEA Cadarache) with whom I started developing a generic interface between FEniCS and the MFront code generator for material behavior (Helfer et al., 2021). This interface bridged a crucial gap in the capabilities of FEniCS by enabling easy integration of complex nonlinear material constitutive laws into different variational formulations. The interface was integrated into the open-source MFront Generic Interface Support project (Helfer et al., 2020). This collaboration has not only advanced the functionality of FEniCS, but also expanded MFront to handle generalized behaviors, such as multiphysics problems and generalized continua.

Additionally, I have collaborated with colleagues in diverse fields to bring my numerical expertise to their projects. I worked with Manas Upadhyay from LMS, École Polytechnique on advanced numerical models for simulating the impact of laser-heating in metallic additive manufacturing and dislocation transport in metallic materials. In particular, we developed a time-explicit Runge-Kutta discontinuous Galerkin solver for the transport equation of the dislocation density tensor (Fig. 2.2) (Upadhyay and Bleyer, 2022). Second, I also got introduced to biomechanics by Hervé Turlier and Hudson Borja da Rocha from Collège de France to work

[1] https://comet-fenics.readthedocs.io. Up-to-date version now available at https://bleyerj.github.io/comet-fenicsx/.

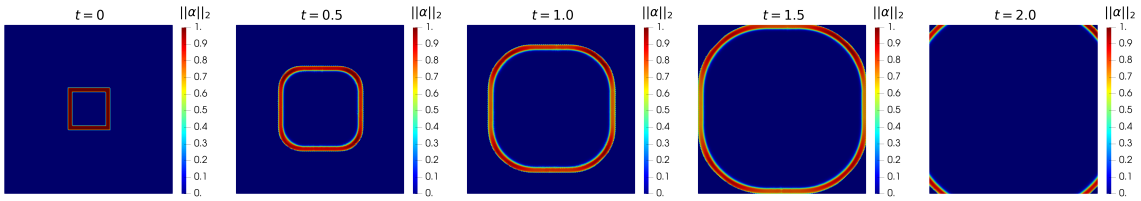


Figure 2.2: Expansion of a polygonal dislocation loop. Snapshots of the magnitude of the dislocation density tensor $\boldsymbol{\alpha}$ at $t = 0$, 0.5, 1, 1.5 and 2 sec.

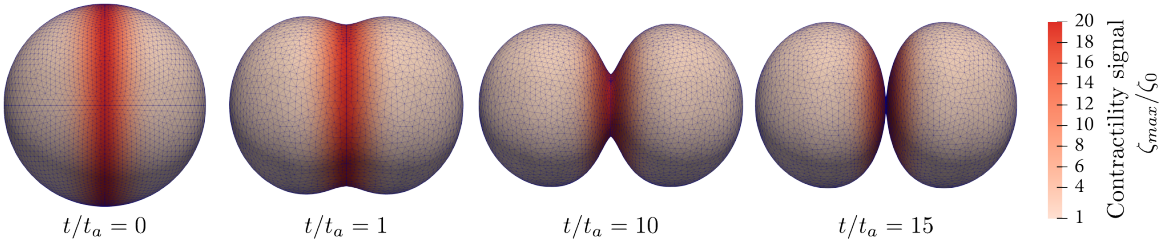


Figure 2.3: FEniCS simulation of cytokinesis (cell contractile activity in red)

on the formulation and implementation in FEniCS of a viscous shell theory of the cellular cortex (da Rocha et al., 2022) that incorporates active terms to account for shape changes like cell division (Fig. 2.3). Finally, I have also been invited by the *CSMA junior* association to host a hands-on session on FEniCS in March 2023 during its annual workshop.

### 2.2.3 Going beyond classical yield design/limit analysis theory

The classical framework of yield design and limit analysis theory described in Section 2.2.1 assumes given geometry, loading conditions, and material strength properties, and computes the ultimate load using optimization solvers. In 2020, I started exploring two different extensions to this classical framework.

The first extension was initiated with the PhD of Leyla Mourad, where our goal was to find a structure with minimal volume and maximum load-bearing capacity. We extended the limit analysis formulations towards topology optimization. Previously, there was no general framework that bridged these two domains, with the topology optimization community mostly focusing on elastic or simple nonlinear behaviors. We formulated a generic optimization problem, similar to limit analysis, but with the addition of a pseudo-density field representing the distribution of material as an optimization variable. This allowed us to easily consider various strength criteria, including materials that can only sustain compression stress states, such as rocks or masonry. We later extended the formulation to optimize over two distinct materials, to account for reinforcements. A typical application of this work is the optimization of massive reinforced-concrete structures, allowing us to simplify the generation of strut-and-tie models and optimize the use of steel reinforcement in concrete structures, in collaboration with the civil engineering firm Setec Tpi. These works will be presented in more details in Chapter 6.

The second extension of the classical framework of yield design and limit analysis theory aims to include uncertainty. The potential sources of uncertainty, such as material properties, loading conditions, and geometry imperfections, can significantly impact the ultimate load of a structure. Moreover, engineers are interested in a safe (or pessimistic) estimate of the

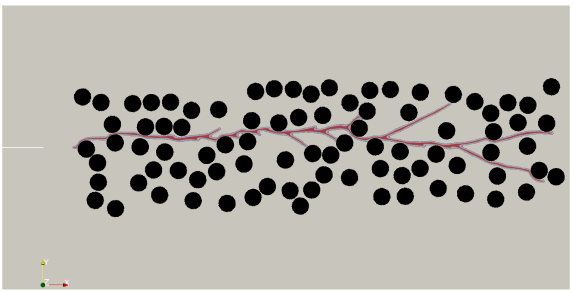

Figure 2.4: Crack (in red) branching interaction with tough inclusions (black)

structural capacity rather than its mean value. There exist different ways of reaching this goal such as reliability methods (FORM/SORM) which aim at estimating the probability of failure of a system or a structure. However, such methods may suffer from a lack of accuracy or from a sensitivity to the probability distribution of random input parameters which is not always available. Instead, I decided to investigate another methodology based on the theory of robust optimization which fits well within the convex programming framework of computational limit analysis. Indeed, robust optimization theory does not require knowledge of probability distributions and instead focuses on finding a solution that is robust or feasible for any possible realization of the uncertain parameters. This makes it well-suited for cases where information about randomness might be imperfect. The latter is indeed simply represented by a so-called *uncertainty set*. However, it does not provide any probabilistic assessment of structural reliability but only a safe estimate of the worst-case value. In some cases, the robust optimization counterparts of uncertain optimization problems can be reformulated as deterministic optimization problems, generally of much larger size, which can be solved with the same numerical tools as discussed before. In collaboration with Vincent Leclère (CERMICS, École des Ponts), we started to propose a completely original formulation of limit analysis in presence of uncertainty using these robust optimization concepts (Bleyer and Leclère, 2022) which will be presented in Chapter 7.

### 2.2.4 Fracture models of heterogeneous materials

The last part of my research activities is centered around the prediction and simulation of brittle fracture in various materials. As mentioned before, this topic has been initiated during my postdoctoral fellowship at EPFL regarding dynamic fracture in brittle materials. Brittle fracture is notoriously difficult to simulate since smeared representations of the crack using damage fields are mathematically ill-posed and produce mesh-dependent results due to strain and damage localization in a narrow band of elements. Some kind of regularization procedure is therefore required in order to obtain mesh-independent results. Since my post-doc I focused mostly on phase-field, or equivalently, damage gradient models which will be mentioned in Section 8.2.

One of my main research topic in this field is related to the interaction of a crack with heterogeneities (Fig. 2.4) or its propagation in anisotropic composite materials. Currently, the PhD thesis of Zakaria Chafia (funded by Labex MMCD) which I co-supervise with Julien Yvonnet (Univ Gustave Eiffel) aims at proposing upscaling procedures to account for the failure behaviour of cementitious materials at the macroscopic level. Currently, it is

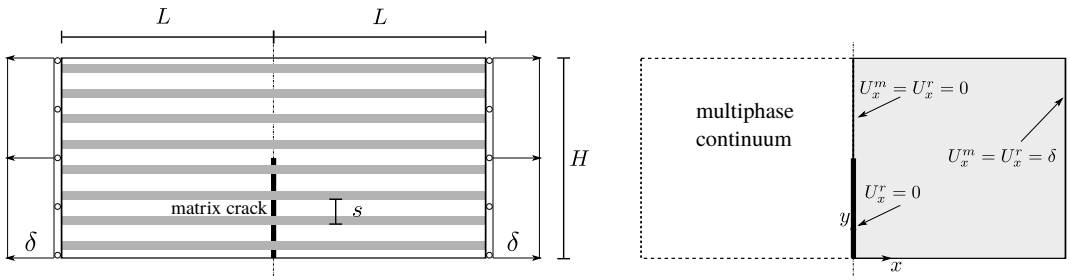


(a) Classical heterogeneous model (left) and generalized multiphase model (right)

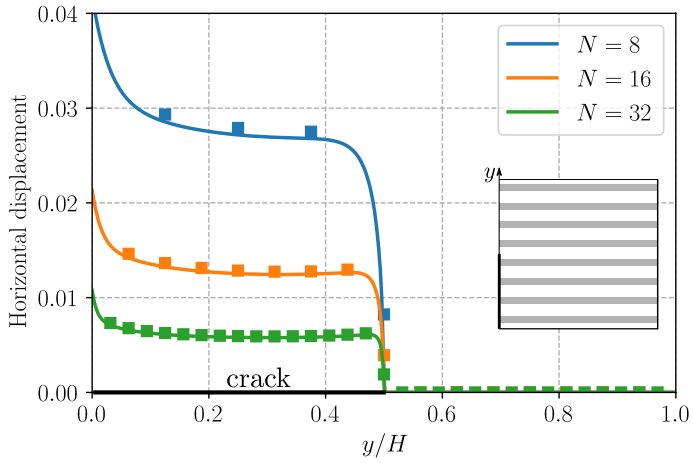


(b) Crack-opening displacement as a function of the total number of fibers $N$

Figure 2.5: Modeling of a matrix crack bridged by intact fibers using a *multiphase* generalized continuum

very difficult to properly account for the influence of the microstructure on the macroscopic failure behaviour of a structure. A direct simulation would indeed require tremendous computational effort to resolve these fine length scales. It is however known that fracture is very difficult to homogenize due to localization phenomena which can occur at various scales. To do so, we are currently trying to benefit from the formulation of regularized brittle fracture as a damage gradient model and derive the corresponding effective damage model.

On a closely related topic, I also try to develop new mechanical models which can properly account for the fracture of fiber-reinforced materials or multilayered plates. In both cases, past works at Laboratoire Navier have investigated generalized continuum models, so-called *multiphase* or *multiparticle* models, which consist in multiple phases (e.g. the matrix and the reinforcement for a fibrous material or each layer in a laminated plate), each possessing its own kinematics, and which can interact with each other. Concerning fibrous materials, I have proposed a homogenization procedure which can identify the generalized continuum mechanical parameters from the resolution of a unit cell auxiliary problem (Bleyer, 2018b). This allows for the extension of such models to nonlinear behaviors, such as cracking of the matrix phase that is partially bridged by intact fibers (Fig. 2.5). By using a phase-field model for the matrix phase and a debonding damage model of the fiber/matrix interface, it becomes possible to simulate complex crack behavior where both mechanisms compete with each other (Fig. 2.6).

In Paul Bouteiller's PhD thesis, which was funded by Dassault Aviation, we studied similar models for multilayered composite plates. A significant amount of theoretical work

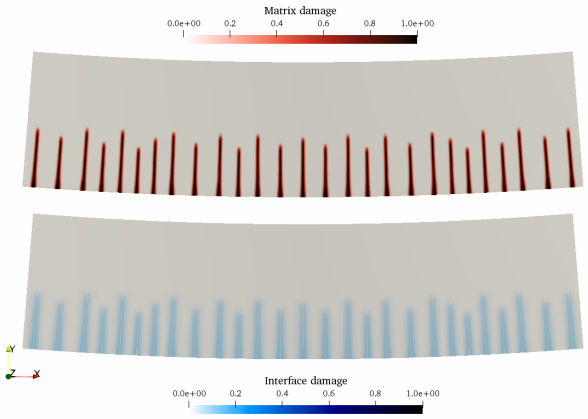


Figure 2.6: Multi-cracking of the matrix phase and partial debonding of the matrix/fiber inclusion with a mutiphase model

was required to efficiently formulate the model for dynamic and nonlinear behaviors. We simulated the impact of a laminated plate with mode I and mode II debonding of the ply interfaces, as well as the anisotropic brittle fracture of the plies. Part of this work will be presented in Chapter 8, Section 8.2.

## 2.3 Teaching activities

Teaching has always been a true vocation for me. I had the opportunity to work as a teaching assistant with Patrick de Buhan in 2011, prior to starting my PhD. I was impressed by his teaching style and enthusiasm. I find it fulfilling and satisfying to share my knowledge and skills with others and assist them in reaching their potential. In the following section, I will provide a brief overview of my teaching experience with a focus on my most recent responsibilities.

### 2.3.1 since 2017, *Eléments finis pour le génie civil* - ENPC

I am currently teaching a course on the Finite Element Method (*Éléments finis pour le génie civil*) at École des Ponts ParisTech, with a total of 32 hours. I proposed to launch this course on finite-elements because there was a lack of theoretical introduction to this topic in the civil engineering curriculum at ENPC. I believed it was important for students to have an understanding of the underlying concepts behind commercial finite-element solvers, which are often used without a full understanding. In this class, I aim to foster a critical perspective in interpreting numerical results. The course is attended by two different student groups: 3$^{rd}$-year engineering students of ENPC (≈30 students) + students of Mastère Spécialisé - Génie Civil Européen (15-20 students). In addition to the lectures, I also supervise the first group of students in the application part. For this purpose, I have created a pedagogical finite-element Python package, called `wombat`[2], which uses an Object-Oriented Programming structure and helps students understand the fundamentals of finite-element formulation (Fig. 2.7). The class revolves around the following topics:

[2]We follow a Python-based tradition of naming `Python` modules or `Python`-based software from exotic animals: `pandas`, `Spyder`, `Anaconda`, etc. The wombat is a peaceful marsupial found in Australia.

- solve small strain linear elastic structures for 2D truss, beam and solid elements (linear and quadratic triangles)
- modal analysis
- transient analysis (Newmark schemes)
- linear buckling analysis
- material non-linearities (cable elements, elastoplastic bars, etc.)

The class finishes with numerical projects in which students are proposed to implement a new finite-element based on the developments presented during the class. Such projects are also a good occasion for them to approach slightly more advanced concepts of structural mechanics. Typical project topics are:

- quadrangular elements and shear locking issues
- Timoshenko beam elements (shear locking, sandwich beams)
- axisymmetric solid elements
- cylindrical shell elements
- planar grid elements (bending/torsion coupling and analogy with plate models)
- cross-section mechanical characteristics (axial, bending and shear stiffnesses), reduction of properties in fire conditions

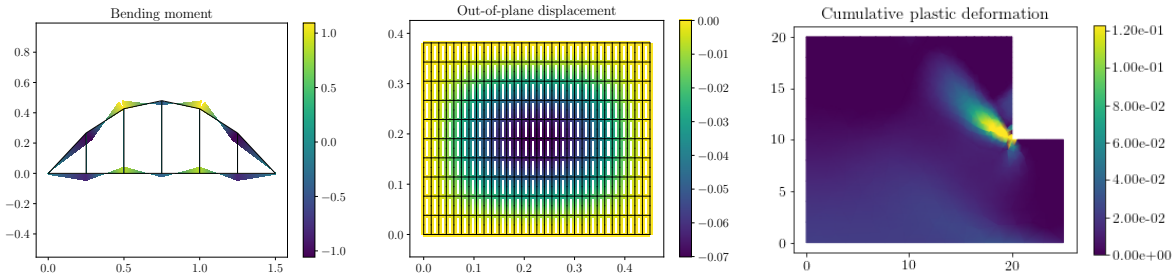


(a) Bending moment distribution in a simple bow-string bridge model

(b) Out-of-plane deflection of a planar grid of beams

(c) Equivalent plastic strain for a vertical slope stability problem

Figure 2.7: Some finite-element computations using the `wombat` module

The `wombat` module is also used in other classes at ENPC (*Dynamique des structures*, *Dynamique avancée des structures*) and at Sorbonne Université.

### 2.3.2 since 2020, *Damage mechanics*, Master 2 level - SU/ENPC

Since 2020, I am co-responsible for a class on *Damage mechanics* at the Master 2 level (≈ 80 students), jointly accredited by Sorbonne Université and Ecole des Ponts ParisTech. This course aims at:

- providing the theoretical foundation of damage mechanics for quasi-brittle materials, in particular regarding the formulation of macroscopic constitutive behaviours coupling elasticity and damage;

- studying the problematic of initiation and evolution of damage in a numerical setting in order to investigate the ill-posedness of local damage models;
- proposing an outlook towards regularization methods though gradient damage models.

I share this responsibility with Kim Pham (ENSTA), formerly with Djimédo Kondo (SU), who delivers the first 9 hours on the theoretical basis through the thermodynamical framework of irreversible processes. In the next 9 hours, I introduce the students to the numerical aspects of an isotropic local damage model in the FEniCS environment. The students are then exposed to classical issues such as mesh-dependency in order to illustrate the ill-posed character of such models. I then give an introduction to regularizing formulations using damage gradient (phase-field) approaches. Finally, we study the corresponding numerical implementation and how this strategy succeeds, or not, in regularizing the problem of crack propagation in brittle materials.

### 2.3.3 since 2020, at École Polytechnique

Since 2020, I am *Professeur chargé de cours d'exercice incomplet* at École Polytechnique in the Departement of Mechanics. Currently, I am teaching for the *Mécanique des milieux déformables* course supervised by Basile Audoly (40h, 40 students) and the *Solid Mechanics* course supervised by Oscar Lopez-Pamies, and now Patrick Le Tallec (40h, 40 students).

Before that, I have also been mentoring experimental project in civil engineering with Gilles Forêt (Navier, ENPC) between 2018 and 2020.

### 2.3.4 Past teaching activities

In the past, I have also been a teaching assistant for different courses at ENPC:

- 2014–2015 and 2017–2019 : *Solid Mechanics* supervised by L. Dormieux, 1$^{st}$ year engineering degree at ENPC, 85h/year.
- 2011–2015 and 2017–2019 : *Plasticity and Yield design* supervised by P. de Buhan, 2$^{nd}$ year engineering degree at ENPC, Civil Engineering Department, 40h/year.
- 2012–2015 : *Homogenization in yield design* supervised by P. de Buhan, master 2 level, ENPC, 20h/year.
- 2012, 2014, 2015 : *Refresher course in Solid Mechanics*, supervised by P. de Buhan, 2$^{nd}$ year engineering degree at ENPC, Civil Engineering Department, 20h/year.
- 2011 : *Mechanics of materials and structures at finite strains* supervised by P. de Buhan, master 2 level, ENPC, 20h/year.

During my postdoctoral leave in 2016, I was also a teaching assistant for the *Continuum Mechanics* course at EPFL (3$^{rd}$ year Bachelor), supervised by Jean-François Molinari (30h/year).

## 2.4 Organization of the manuscript

### 2.4.1 Foreword

When starting writing this *Habilitation*, I tried to find what could be the common denominator to my research activities. As you will see next, there were many candidates at

first: limit analysis theory which dates back to my PhD thesis? nonlinear mechanics more generally? modern numerical tools? After some reflection, it appeared to me that there was a more profound concept which is central in all branches of physics and which is really at the core of my research work: *variational principles*.

Variational principles can be generally characterized by the fact that they formulate laws of physics (equilibrium state or dynamic evolution of a system) as the result of an optimization problem. As such, they reveal a fundamental structure of a given physical phenomenon through the optimization of a given scalar quantity (the objective function to be optimized) over a space of admissible states. The founding idea related to the notion of variational principle is due to Pierre de Fermat who proposed his famous "*Least Time Principle*" in geometrical optics. Their development then benefited in particular from the formalization of *variational calculus* by Euler and Lagrange. Maupertuis was then the first to propose a variational principle in mechanics called the "*Least Action Principle*" from which the equations of motion can be recovered through the corresponding Euler-Lagrange equations. This global point of view is, in my opinion, mathematically beautiful but also extremely powerful and fertile. Unfortunately, it is often less considered compared to a local formulation of the physical evolution laws which results from it. In this work, I would like to give to variational principles in mechanics the attention they deserve.

Obviously, variational principles are closely linked to the discipline of mathematical optimization. One of the most important distinction in optimization is between convex and non-convex problems. Convex optimization, and therefore, convex variational problems, benefit from a rich set of results and properties studied by convex analysis. In particular, duality in convex optimization is for me a particularly fertile way of understanding a problem, both from its primal and dual form. I will make extensive use of such a deep and elegant concept in the following works.

If variational principles may appear as an old topic at first sight, convex optimization is a relatively young branch of mathematics which experienced tremendous developments, especially regarding numerical solvers, in the last decades and which is supported by various applications in different fields of engineering and, more recently, in machine learning. In particular, recent algorithms are now very efficient in solving non-differentiable, or *non-smooth*, problems involving millions of optimization variables. In this work, I will therefore mostly focus on non-smooth convex variational problems but will also discuss some applications in the non-convex world. It is to be noted that this domain was pioneered by the works of Jean-Jacques Moreau who introduced founding ideas and notions, both in mechanics and mathematics.

### 2.4.2 Outline

Chapter 3 provides a brief introduction to the fundamental concepts of convex analysis and convex optimization, with a focus on readers who are unfamiliar with these topics. An overview of the available algorithms is presented with a particular emphasis on interior-point methods which are the main tools used in this work. The chapter then concludes by briefly discussing the available solvers and modeling languages.

Chapter 4 focuses on the variational principles of solid and structure mechanics, including elasticity, unilateral behaviors, and viscoplastic fluids. The chapter then focuses on the incremental variational principle for dissipative materials. An original contribution is the derivation of the corresponding dual problem. Their use is then illustrated in the context of elasto-plastic hardening behaviors. Using concepts of convex analysis, their asymptotic behavior at large loadings is also discussed.

Chapter 5 presents my research on limit analysis theory. The chapter first introduces a

generic framework for limit analysis problems, which is easily formulated using the FEniCS-based package `fenics_optim`. The versatility of the numerical tools is demonstrated through various academic problems, including plate, shell, and generalized continuum models. The chapter also reviews some applications of limit analysis in civil engineering, such as the analysis of 3D steel or reinforced concrete structures.

Chapter 6 extends the concepts and numerical tools to shape optimization in structural mechanics. The chapter proposes a convex optimization approach to topology optimization formulations and extends it to generic constitutive models. The approach is applied to a limit analysis setting, resulting in a topology optimization formulation that maximizes the overall load-bearing capacity. The chapter discusses the choice of strength criteria and considers multi-material optimization, focusing on uniaxial reinforcements. The chapter concludes by presenting the application of similar concepts to form-finding of optimal shell or vault structures.

Chapter 7 explores different modeling strategies to account for uncertainties in non-linear mechanics problems. The chapter proposes two optimization approaches: a robust optimization formulation of limit analysis problems that finds the worst-case limit load, and a risk-averse optimization approach that derives the best and worst-case estimates of the mechanical response of dissipative media using the Conditional Value-at-Risk (CVaR) measure.

Chapter 8 discusses the use of gradient-based variational approaches for the regularization of softening behaviors. It first presents some results on phase-field or damage-gradient regularization of brittle fracture, focusing on dynamic and anisotropic fracture. Second, a novel regularization strategy for softening plasticity is discussed. In both cases, the underlying variational problems are no longer convex but benefit, in their numerical resolution, to their link to related convex problems.

Chapter 9 draws general conclusions regarding the presented works and discusses some ideas for future research.

| Convex analysis | |
|---|---|
| $f^*(\boldsymbol{y})$ | Convex conjugate function of $f(\boldsymbol{x})$ |
| $f^\circ(\boldsymbol{y})$ | Polar function of $f(\boldsymbol{x})$ |
| $\text{persp}_f(t, \boldsymbol{x})$ | Perspective of $f(\boldsymbol{x})$ |
| $f_\infty(\boldsymbol{x})$ | Recession function of $f(\boldsymbol{x})$ |
| $\text{dom}\, f$ | Effective domain of $f(\boldsymbol{x})$ |
| $\text{epi}\, f$ | Epigraph of $f(\boldsymbol{x})$ |
| $\delta_G(\boldsymbol{x})$ | Indicator of a set $G$ |
| $\pi_G$ | Support function of a set $G$ |
| $g_G(\boldsymbol{x})$ | Gauge function of a set $G$ |
| $\text{conv}\{A; B\}$ | Convex hull of two sets $A$ and $B$ |

| Probabilities | |
|---|---|
| $\mathbb{P}[X]$ | Probability of $X$ |
| $\mathbb{E}[X]$ | Expected value of $X$ |
| $\text{var}[X]$ | Variance of $X$ |
| $\text{std}[X]$ | Standard deviation of $X$ |
| $\mathcal{R}[X]$ | Risk-measure of $X$ |
| $\text{VaR}_\beta(X)$ | Value-at-Risk of $X$ at confidence level $\beta$ |
| $\text{CVaR}_\beta(X)$ | Conditional Value-at-Risk of $X$ at confidence level $\beta$ |

Table 2.1: Table of notations

# Chapter 3

# Convex optimization

This chapter aims at giving a very short introduction to basic concepts in convex analysis (Section 3.1) and convex optimization (Section 3.2) which will be extensively used in the following chapters. The exposition is deliberately simple and targets readers not familiar with these concepts. A more thorough exposition can be found in classical textbooks such as (Rockafellar, 1970) or (Boyd and Vandenberghe, 2004). In Section 3.3, a general overview of available algorithms is provided with a specific emphasis on interior-point methods. Finally, existing solvers and modeling languages are also briefly discussed.

## Contents

## 3.1 A short introduction to convex analysis

### 3.1.1 Convex sets and functions

In the following, we will work in the standard Euclidean space $\mathbb{R}^n$ with inner product $\boldsymbol{x}^{\mathrm{T}}\boldsymbol{y}$ for simplicity but all of these notions can be extended to general Hilbert spaces. All convex functions considered in this work will be valued in the extended real line $\overline{\mathbb{R}} = \mathbb{R} \cup \{\pm\infty\}$.

**Definition 1** (Convex sets)**.** A set $G \subset \mathbb{R}^n$ is said to be *convex* if and only if

$$\forall(\boldsymbol{x}, \boldsymbol{y}) \in G \times G \text{ and } \lambda \in [0;1], \quad (1-\lambda)\boldsymbol{x} + \lambda\boldsymbol{y} \in G \tag{3.1}$$

Typical examples include linear spaces $\{\mathbf{A}\boldsymbol{x} = \mathbf{b}\}$ or half-spaces $\{\mathbf{A}\boldsymbol{x} \leq \mathbf{b}\}$, balls of the $L_p$-norm $\{\|\boldsymbol{x}\|_p \leq 1\}$ with $p \geq 1$, intersections of convex sets, etc.

**Definition 2** (Convex functions)**.** A function $f : \mathbb{R}^n \mapsto \overline{\mathbb{R}}$ is said to be *convex* if and only if

$$\forall(\boldsymbol{x}, \boldsymbol{y}) \in \mathbb{R}^n \times \mathbb{R}^n \text{ and } \lambda \in [0;1], \quad f\left((1-\lambda)\boldsymbol{x} + \lambda\boldsymbol{y}\right) \leq (1-\lambda)f(\boldsymbol{x}) + \lambda f(\boldsymbol{y}) \tag{3.2}$$

Typical examples include affine functions, $L_p$-norms with $p \geq 1$, supremum of convex functions, largest eigenvalue of a symmetric matrix, etc.

**Definition 3** (Domain, epigraph and indicator function)**.** The *effective domain* dom $f$ is the set of points such that $f(\boldsymbol{x}) < +\infty$.
The *epigraph* epi $f$ is defined as:

$$\text{epi}\, f = \{(\boldsymbol{x}, t) \in \mathbb{R}^n \times \mathbb{R} \text{ s.t. } f(\boldsymbol{x}) \leq t\} \tag{3.3}$$

Both dom $f$ and epi $f$ are convex sets when $f$ is convex.

The *indicator* function $\delta_G(\boldsymbol{x})$ of a convex set $G$ is convex and defined as:

$$\delta_G(x) = \begin{cases} 0 & \text{if } \boldsymbol{x} \in G \\ +\infty & \text{otherwise} \end{cases} \tag{3.4}$$

Note that some authors use the term *characteristic function* rather than indicator function. The difference is generally due to the use of 1 (resp. 0) rather than 0 (resp. $+\infty$) to the denote membership (resp. non-membership). Again, we use Rockafellar's terminology in this work.

Unless otherwise stated, all convex functions $f(\boldsymbol{x})$ will be assumed to be:

- *proper*: they never take value $-\infty$ and are never identically equal to $+\infty$ i.e. its domain dom $f$ is non-empty
- *lower-semicontinuous* (lsc): roughly speaking, values of $f$ around a point $\boldsymbol{x}$ are all greater than or equal to $f(\boldsymbol{x})$. More precisely, for any $\boldsymbol{x} \in$ dom $f$:

$$f(\boldsymbol{x}) \leq \liminf_{\boldsymbol{x}_h \to \boldsymbol{x}} f(\boldsymbol{x}_h) \tag{3.5}$$

**Definition 4** (Positively homogeneous functions)**.** A function is said to be *positively homogeneous of degree* $p$ if:

$$f(\lambda\boldsymbol{x}) = \lambda^p f(\boldsymbol{x}) \quad \forall\lambda > 0 \tag{3.6}$$

Note that the term *positively homogeneous*, without specifying the degree, generally implies the important case of degree $p = 1$. In this case, the epigraph is a convex cone.

### 3.1.2 Convex cones

**Definition 5** (Convex cones)**.** A set $K$ is a *convex cone* if:

$$\forall (\boldsymbol{x}, \boldsymbol{y}) \in K \times K \text{ and } \alpha, \beta \geq 0, \quad \alpha \boldsymbol{x} + \beta \boldsymbol{y} \in K \tag{3.7}$$

Typical examples include $L_p$-norm cones $\{(\boldsymbol{x}, t)$ such that $\|x\|_p \leq t\}$ with $p \geq 1$, the set of positive semi-definite matrices, the set of positive convex functions, etc.

**Definition 6** (Dual and polar cones)**.** For a convex cone $K$:

- the *dual cone* $K^*$ is defined as:

$$K^* = \{\boldsymbol{y} \in \mathbb{R}^n \text{ such that } \boldsymbol{y}^{\mathrm{T}} \boldsymbol{x} \geq 0 \quad \forall \boldsymbol{x} \in K\} \tag{3.8}$$

- the *polar cone* $K^\circ$ is defined as:

$$K^\circ = \{\boldsymbol{y} \in \mathbb{R}^n \text{ such that } \boldsymbol{y}^{\mathrm{T}} \boldsymbol{x} \leq 0 \quad \forall \boldsymbol{x} \in K\} \tag{3.9}$$

We thus have $K^* = -K^\circ$.

Finally, such cones can be used to state *Moreau's orthogonal decomposition* with respect to cone $K$ as follows:

$$\forall \boldsymbol{x} \in \mathbb{R}^n, \ \exists \boldsymbol{x}^+ \in K \text{ and } \boldsymbol{x}^- \in K^\circ \text{ such that } \boldsymbol{x} = \boldsymbol{x}^+ + \boldsymbol{x}^- \text{ and } (\boldsymbol{x}^+)^{\mathrm{T}} \boldsymbol{x}^- = 0 \tag{3.10}$$

Moreover, $\boldsymbol{x}^+$ (resp. $\boldsymbol{x}^-$) are in fact obtained as the orthogonal projections of $\boldsymbol{x}$ onto $K$ (resp. $K^\circ$).

### 3.1.3 Subdifferential and optimality conditions

The subdifferential defines a generalized notion of derivatives (or gradients) for non-smooth functions. If $f$ is non-differentiable at $x$, it possesses many tangent directions.

**Definition 7** (Subgradient and subdifferential)**.** A *subgradient* is any direction $g$ which characterizes such tangents. It is defined as:

$$\boldsymbol{g} \in \mathbb{R}^n \text{ is a subgradient} \quad \Leftrightarrow f(\boldsymbol{x}) + (\boldsymbol{y} - \boldsymbol{x})^{\mathrm{T}} \boldsymbol{g} \leq f(\boldsymbol{y}) \quad \forall \boldsymbol{y} \tag{3.11}$$

The set of all subgradients of $f$ at $\boldsymbol{x}$ defines the *subdifferential* $\partial f(x)$.

It is a non-empty convex set. In the case where $f$ is differentiable at $\boldsymbol{x}$, the subdifferential contains only the gradient of $f$:

$$\partial f(\boldsymbol{x}) = \{\nabla f(\boldsymbol{x})\} \tag{3.12}$$

If $f = g_1 + g_2$ is the sum of two convex functions, then:

$$\partial f(\boldsymbol{x}) = \partial g_1(\boldsymbol{x}) \oplus \partial g_2(\boldsymbol{x}) \tag{3.13}$$

where $A \oplus B = \{c \text{ s.t. } c = a + b \text{ where } a \in A, b \in B\}$ denotes the Minkowski sum between two sets $A$ and $B$.

From (3.11), we see that the subdifferential gives an optimality condition for the minimization of $f(\boldsymbol{x})$:

$$\boldsymbol{x}^* = \arg\min_{\boldsymbol{x}} f(\boldsymbol{x}) \quad \Leftrightarrow \quad 0 \in \partial f(\boldsymbol{x}^*) \tag{3.14}$$

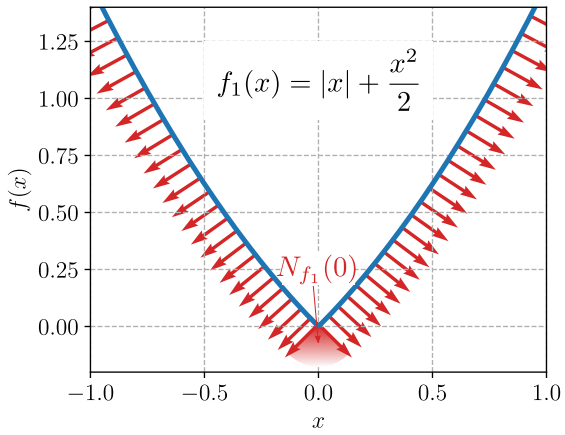


(a) The graph of $f_1(x)$ and its normal gradients.

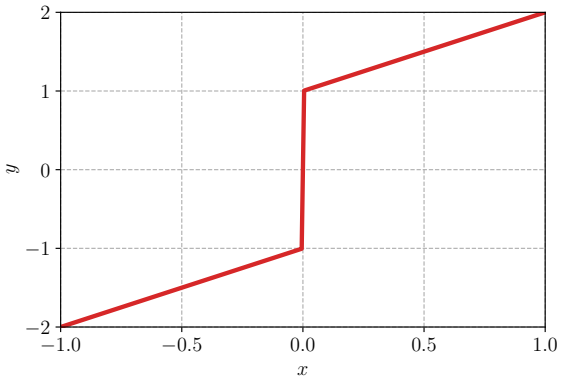


(b) The subdifferential $y \in \partial f_1(x)$

Figure 3.1: The function $f_1(x)$ (3.16) and its subdifferential

which generalizes the fact that for a smooth function the minimum is attained at a critical point such that $\nabla f(\boldsymbol{x}^*) = 0$.

From (3.11), we also see that a subgradient $\boldsymbol{g}$ is such that $(\boldsymbol{g}, -1)$ defines an hyperplane supporting the function epigraph. In the smooth case, $\boldsymbol{g} = \nabla f$ is such that $(\nabla f, -1)$ defines a normal vector to the function graph. Therefore, we define the *normal cone* to $f$ as the cone generated by the subdifferential:

$$N_f(\boldsymbol{x}) = \{(t\boldsymbol{g}, -t) \in \mathbb{R}^n \times \mathbb{R} \quad \forall \boldsymbol{g} \in \partial f(\boldsymbol{x}),\ t \geq 0\} \tag{3.15}$$

As an example for $\gamma \geq 0$, the function:

$$f_\gamma(x) = |x| + \gamma \frac{x^2}{2} \tag{3.16}$$

is convex on $\mathbb{R}$ but non-smooth at $x = 0$ (Fig. 3.1a). Its subdifferential (Fig. 3.1) is:

$$\partial f_\gamma(x) = \begin{cases} \{-1 + \gamma x\} & \text{if } x < 0 \\ \{1 + \gamma x\} & \text{if } x > 0 \\ [-1; 1] & \text{if } x = 0 \end{cases} \tag{3.17}$$

### 3.1.4 Conjugate functions

A key notion in convex analysis is the Legendre-Fenchel transform which enables to define the notion of conjugate functions.

**Definition 8** (Convex conjugate function)**.** The *convex conjugate* $f^*(\boldsymbol{y})$ of a function $f(\boldsymbol{x})$ as follows:

$$f^*(\boldsymbol{y}) = \sup_{\boldsymbol{x} \in \mathbb{R}^n} \{\boldsymbol{x}^{\mathrm{T}}\boldsymbol{y} - f(\boldsymbol{x})\} \tag{3.18}$$

Note that we use here the term *conjugate* as used by Rockafellar (1970) for instance, rather than the term *polar* which is sometimes also used. The reason for this is that we will make use of another definition of the *polar* function, denoted by $f^\circ$ in Chapter 7.

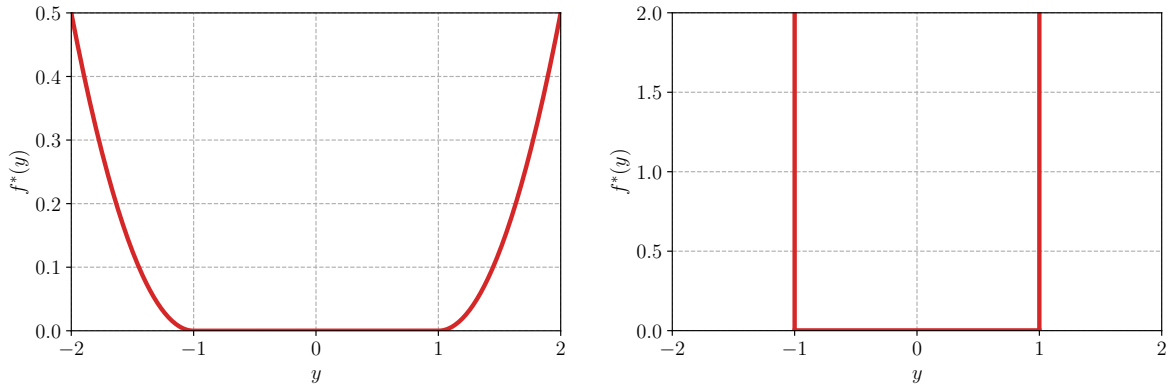


(a) $f_1^*(y)$ (b) $f_0^*(y)$

Figure 3.2: The conjugate of function $f_\gamma(x)$ for $\gamma = 1$ and $\gamma = 0$.

The Fenchel-Moreau theorem states that $f = f^{**}$ if $f$ is convex proper lsc. The Young-Fenchel inequality states that:

$$f(\boldsymbol{x}) + f^*(\boldsymbol{y}) \geq \boldsymbol{x}^{\mathrm{T}}\boldsymbol{y} \quad \forall \boldsymbol{x}, \boldsymbol{y} \tag{3.19}$$

Furthermore, equality in the Young-Fenchel inequality is attained if and only if:

$$f(\boldsymbol{x}) + f^*(\boldsymbol{y}) = \boldsymbol{x}^{\mathrm{T}}\boldsymbol{y} \;\Leftrightarrow\; \boldsymbol{y} \in \partial f(\boldsymbol{x}) \;\Leftrightarrow\; \boldsymbol{x} \in \partial f^*(\boldsymbol{y}) \tag{3.20}$$

which means that $\boldsymbol{x} \in \partial f^*(\boldsymbol{y})$ realizes the supremum in (3.18). As we will see at length in this work, such concepts are at the core of the development of constitutive laws for standard generalized materials, see Section 4.5.1.

**Definition 9** (Support functions)**.** The support function $\pi_G$ of a convex set is the conjugate to its indicator $\delta_G$:

$$\pi_G(\boldsymbol{y}) = (\delta_G)^*(\boldsymbol{y}) = \sup_{\boldsymbol{x} \in G} \boldsymbol{x}^{\mathrm{T}}\boldsymbol{y} \tag{3.21}$$

In particular, it defines the equation of the tangent hyperplane to $G$ with normal vector $y$.

Conversely, the conjugate function of a positively homogeneous function is the indicator of a convex set.

Returning to example (3.16), the conjugate function is given by:

$$f_\gamma^*(y) = \begin{cases} \dfrac{(y+1)^2}{2\gamma} & \text{if } y \leq -1 \\ 0 & \text{if } |y| \leq 1 \\ \dfrac{(y-1)^2}{2\gamma} & \text{if } y \geq 1 \end{cases} \tag{3.22}$$

The corresponding graphs have been represented on Fig. 3.2 for the two cases $\gamma = 1$ and $\gamma = 0$. Note that in the latter case, the previous expressions turn out to be $f_0^* = \delta_{[-1;1]}$, the indicator of the segment $[-1;1]$. Indeed, in the case $\gamma = 0$, $f_0(x) = |x|$ is a homogeneous function and its conjugate is therefore the indicator of a convex set.

Other examples of conjugate functions may include:

- strictly convex quadratic functions:

$$f(\boldsymbol{x}) = \frac{1}{2}\boldsymbol{x}^{\mathrm{T}}\mathbf{Q}\boldsymbol{x} \text{ with } \mathbf{Q} = \mathbf{Q}^{\mathrm{T}} \succ 0, \quad f^*(\boldsymbol{y}) = \frac{1}{2}\boldsymbol{y}^{\mathrm{T}}\mathbf{Q}^{-1}\boldsymbol{y} \tag{3.23}$$

- $L_p$-norms with $p \geq 1$:

$$f(\boldsymbol{x}) = \alpha\|\boldsymbol{x}\|_p \text{ with } \alpha > 0, \quad f^*(\boldsymbol{y}) = \delta_G(\boldsymbol{y}) \text{ where } G = \{\boldsymbol{y} \text{ s.t. } \|\boldsymbol{y}\|_q \leq \alpha\} \tag{3.24}$$

  where $\|\cdot\|_q$ is the dual norm of $\|\cdot\|_p$ with $q$ such that $\frac{1}{p} + \frac{1}{q} = 1$.

- the sum of two functions $f(\boldsymbol{x}) + g(\boldsymbol{x})$:

$$(f+g)^*(\boldsymbol{y}) = (f^* \square g^*)(\boldsymbol{y}) = \begin{array}{ll} \inf\limits_{\boldsymbol{y}_1, \boldsymbol{y}_2} & f^*(\boldsymbol{y}_1) + g^*(\boldsymbol{y}_2) \\ \text{s.t.} & \boldsymbol{y} = \boldsymbol{y}_1 + \boldsymbol{y}_2 \end{array} \tag{3.25}$$

  where $f \square g$ denotes the *infimal convolution* between two functions $f$ and $g$.

## 3.2 Convex optimization

### 3.2.1 Convex and conic optimization problems

Convex optimization problems (or *convex programs*) can take different equivalent forms, one of them being:

$$\begin{array}{ll} \min\limits_{\boldsymbol{x} \in \mathbb{R}^n} & f(\boldsymbol{x}) \\ \text{s.t.} & g_i(\boldsymbol{x}) \leq 0 \quad \forall i = 1, \ldots, m \end{array} \tag{3.26}$$

where $f$ and $g_i$ are assumed to be convex functions. $f$ describes the *objective function* of the optimization whereas the $g_i$ encode constraints. The latter may be formalized into a global constraint $\boldsymbol{x} \in G$ where $G$ is the convex set of admissible constraints. Obviously, the main interest in studying convex optimization problem over non-convex ones is that local minima are also global minima and that very efficient algorithms exist to solve them.

However, even in the convex case, there exist different algorithms depending on the size of the problem and, more importantly, on its *structure*. In fact, trying to solve (3.26) using general-purpose non-linear programming solvers will generally fail for large problems. For this reason, research works in the mathematical programming community are usually focused on specific classes of problems to develop efficient dedicated methods. For instance, unconstrained problems with smooth objectives can be solved efficiently using descent algorithms whereas non-smooth or smooth + non-smooth objectives[1] will require different strategies such as proximal algorithms or interior-point methods.

#### Conic programming

One of the most fruitful change of perspective in the last decades is related to the study of *conic programming*.

[1] such as $f_\gamma$ for instance

**Definition 10** (Conic programs)**.** A *conic program* can be defined as a minimization problem of a linear function over a conic section such as:

$$\begin{aligned} \min_{\boldsymbol{x}\in\mathbb{R}^n} \quad & \mathbf{c}^{\mathrm{T}}\boldsymbol{x} \\ \text{s.t.} \quad & \mathbf{A}\boldsymbol{x} = \mathbf{b} \\ & \boldsymbol{x} \in K \end{aligned} \tag{3.27}$$

where $\mathbf{A} \in \mathbb{R}^{m\times n}, \mathbf{b} \in \mathbb{R}^m, \mathbf{c} \in \mathbb{R}^n$ are given data describing a linear subspace and a linear function and where $K$ is a convex cone.

A key result is that any convex program can be written in the form of a conic program such as (3.27), see for instance Nesterov and Nemirovsky (1992). For example, for any convex objective function $f(\boldsymbol{x})$, we can introduce an additional scalar variable $t$ and use the epigraph form to replace $\min f(\boldsymbol{x})$ with:

$$\begin{aligned} \min_{\boldsymbol{x}\in\mathbb{R}^n, t\in\mathbb{R}} \quad & t \\ \text{s.t.} \quad & f(\boldsymbol{x}) \leq t \end{aligned} \tag{3.28}$$

As a result, objective functions can be converted, without loss of generality, to linear functions to be optimized over a convex set. Then, any convex set can be converted to a convex cone using its conical hull.

Consequently, the structure of the original problem is in fact encoded into the cone $K$. We therefore see that different classes of problems can be represented, depending on the *structure* of $K$.

### Linear Programming

The most famous class of problems is that of *Linear Programming* (LP) which is obtained when $\boldsymbol{x} \in K$ turns out to be $\boldsymbol{x} \geq 0$, the corresponding cone being here the positive orthant $K = \mathbb{R}^n_+$. Linear Programming applications cover almost all the spectrum of engineering (energy, finance, transportation, structural engineering, etc.).

### Second-Order Cone Programming

A further generalization of LP is obtained when considering $K$ to contain second-order cones such as:

$$\mathcal{Q}_d = \{(\boldsymbol{x}, t) \in \mathbb{R}^{d-1} \times \mathbb{R} \text{ s.t. } \|\boldsymbol{x}\|_2 \leq t\} \tag{3.29}$$

The resulting class of problems is called *Second-Order Cone Programming* (SOCP). It enables for instance to model quadratic programming problems (the objective and constraints are convex quadratic functions), see also Lobo et al. (1998) for many applications.

### Semi-Definite Programming

A further generalization of SOCP, and thus LP, is obtained when considering positive semi-definite (PSD) matrices as optimization variables. The affine constraints $\mathbf{A}\boldsymbol{x} = \mathbf{b}$ may therefore represent linear matrix equalities whereas linear matrix inequalities are modeled using the cone of PSD matrices of dimension $d \times d$ which is denoted as $\mathcal{S}^+_d$. Such a generalization is called *Semi-Definite Programming* (SDP) and is also used in many practical applications. For instance, it is often used to relax combinatorial non-convex optimization problems into convex problems which can be solved efficiently. Note that for $d = 2$, SDP constraints can be equivalently formulated as SOCP constraints.

**Power Cone and Exponential Programming**

As we will discuss in the next section, the growth of this subfield of mathematical optimization is mainly due to the development of very efficient algorithms which have been initially developed for LP then extended to SOCP and SDP problems. Indeed, the above mentioned cones, namely positive orthants, second-order and PSD cones, are self-dual (i.e. $K = K^*$), which has been a corner-stone for the development of such algorithms. More recently, a similar strategy also proved successful for other classes of cones which are not self-dual such as:

- power cones $\mathcal{P}_d^\alpha$ parameterized by $\alpha$ s.t. $0 < \alpha < 1$ and $d \geq 3$:

$$\mathcal{P}_d^\alpha = \{\boldsymbol{z} = (z_0, z_1, \bar{\boldsymbol{z}}) \in \mathbb{R} \times \mathbb{R} \times \mathbb{R}^{d-2} \text{ and } z_0^\alpha z_1^{1-\alpha} \geq \|\bar{\boldsymbol{z}}\|_2, \;\; z_0, z_1 \geq 0\} \tag{3.30}$$

- exponential cones:

$$\mathcal{K}_{\text{exp}} = \{\boldsymbol{z} \in \mathbb{R}^3 \text{ s.t. } \boldsymbol{z} = (z_0, z_1, z_2) \text{ and } z_0 \geq z_1 \exp(z_2/z_1), \;\; z_0, z_1 \geq 0\} \tag{3.31}$$

The set of all such cones which can be tackled by efficient algorithms has been termed by Juditsky and Nemirovski (2021) as the *magic family*. Although a very large class of problems can already be modeled in the framework of SDP, the recent extension to power and exponential cones paves the way for new applications of such techniques to other objective functions or constraints. For instance, minimizing a norm other than $p = 1, 2$ or $\infty$ was not possible before introducing power cones, similarly exponential-based functions such as logistic regression problem were unavailable until recently.

Although conic programs should represent any convex program, strictly speaking, we will from now on abusively consider as conic programs programs which can be represented using cones from the magic family. Despite limiting ourselves to this family of cones, it turns out that it already covers a very wide range of convex optimization functions appearing in practice.

### 3.2.2 Conic duality

As mentioned before, duality is a very powerful concept in mathematical optimization. In the case of conic programs of the form (3.27), we can form the following Lagrangian:

$$\mathcal{L}(\boldsymbol{x}, \boldsymbol{y}, \boldsymbol{s}) = \mathbf{c}^{\mathrm{T}}\boldsymbol{x} - \boldsymbol{y}^{\mathrm{T}}(\mathbf{A}\boldsymbol{x} - \mathbf{b}) - \boldsymbol{s}^{\mathrm{T}}\boldsymbol{x} \tag{3.32}$$

where $\boldsymbol{y} \in \mathbb{R}^m$ is the Lagrange multiplier associated with the linear constraint $\mathbf{A}\boldsymbol{x} = \mathbf{b}$. $\boldsymbol{s} \in \mathbb{R}^n$ is the dual conic variables associated with the conic constraint $\boldsymbol{x} \in K$. In particular, $\boldsymbol{s}$ is restricted to lie into the corresponding dual cone i.e. $\boldsymbol{s} \in K^*$. The corresponding min/max problem therefore reads:

$$\max_{\boldsymbol{y} \in \mathbb{R}^m, \boldsymbol{s} \in K^*} \min_{\boldsymbol{x} \in \mathbb{R}^n} \mathbf{c}^{\mathrm{T}}\boldsymbol{x} - \boldsymbol{y}^{\mathrm{T}}(\mathbf{A}\boldsymbol{x} - \mathbf{b}) - \boldsymbol{s}^{\mathrm{T}}\boldsymbol{x} \tag{3.33}$$

so that when eliminating $\boldsymbol{x}$ one has:

$$\mathbf{c} - \mathbf{A}^{\mathrm{T}}\boldsymbol{y} - \boldsymbol{s} = 0 \tag{3.34}$$

which finally gives the dual problem:

$$\begin{aligned} \max_{\boldsymbol{y} \in \mathbb{R}^m, \boldsymbol{s} \in \mathbb{R}^n} \quad & \mathbf{b}^{\mathrm{T}}\boldsymbol{y} \\ \text{s.t.} \quad & \mathbf{A}^{\mathrm{T}}\boldsymbol{y} + \boldsymbol{s} = \mathbf{c} \\ & \boldsymbol{s} \in K^* \end{aligned} \tag{3.35}$$

which results in the same optimal value as (3.27) under appropriate constraint qualification.

As a result, we obtain the following optimality conditions for the pair of problems (3.27)-(3.35):

$$\mathbf{A}\boldsymbol{x} = \mathbf{b} \tag{3.36a}$$
$$\mathbf{A}^{\mathrm{T}}\boldsymbol{y} + \boldsymbol{s} = \mathbf{c} \tag{3.36b}$$
$$\boldsymbol{x} \in K \tag{3.36c}$$
$$\boldsymbol{s} \in K^* \tag{3.36d}$$
$$\boldsymbol{x}^{\mathrm{T}}\boldsymbol{s} = 0 \tag{3.36e}$$

where the last condition (3.36e) is the *complementary slackness condition*.

**Remark 1.** Note also that we can write problem (3.27) as $\min \mathbf{c}^{\mathrm{T}}\boldsymbol{x} + \delta_{G\cap K}(\boldsymbol{x})$ where $G = \{\boldsymbol{x} \text{ s.t. } \mathbf{A}\boldsymbol{x} = \mathbf{b}\}$ is the affine subspace. Then the optimality conditions can be written using subdifferentials as:

$$0 \in \{\mathbf{c}\} \oplus N_{G\cap K}(\boldsymbol{x}) \oplus N_K(\boldsymbol{x}) = \{\mathbf{c}\} \oplus N_G(\boldsymbol{x}) \oplus N_K(\boldsymbol{x}) \tag{3.37}$$

where the normal cone $N_G(\boldsymbol{x}) = \{\boldsymbol{z} \in \mathbb{R}^n \text{ s.t. } \boldsymbol{z} = \mathbf{A}^{\mathrm{T}}\boldsymbol{y}\}$ and $N_K(\boldsymbol{x}) = -K^* \cap \{\boldsymbol{x}\}^{\perp}$. We indeed recover (3.34) along with the complementary slackness condition (3.36e).

## 3.3 Algorithms and solvers

As mentioned before, the choice of an appropriate algorithm for solving an optimization problem is a decisive step which has to be taken under the light of the problem specific structure. Without giving an exhaustive list of all available algorithms, let us just mention the important classes of algorithms for various types of convex problems, with a deeper focus on those used in this work. More details can for instance be found in (Boyd and Vandenberghe, 2004) or (Nocedal and Wright, 1999). Note also that convex optimization algorithms can also be used for local optimization of non-convex functionals. However, we do not discuss global optimization strategies for non-convex functions such as stochastic gradients which are extremely popular in machine learning or metaheuristic techniques.

### 3.3.1 Unconstrained optimization

The simplest optimization algorithm for smooth unconstrained problems are descent methods: $x_{k+1} = x_k - \lambda \nabla f(x_k)$. For instance, the gradient descent method is a *first-order method* as it does not require to invert a linear system to find the optimal descent direction. It relies instead on first-order derivatives only. Newton's method is its most natural extension, being a *second-order method* which requires solving a linear system involving the objective function Hessian matrix $\nabla\nabla f(x_k)$. Due to its simplicity, the gradient descent converges only linearly and cannot be applied to non-smooth functions.

Newton's method is an extremely attractive and widely used method due to its quadratic convergence near the optimal point. Computational cost due to the Hessian system inversion can be overcome using approximation techniques such as quasi-Newton methods (Broyden, BFGS, Levenberg–Marquardt...). Finally, globalization strategies such as line-search or trust-region methods can be used to increase the radius of convergence of the method around the optimal point.

### 3.3.2 Constrained optimization

Solving constrained optimization problems is much more difficult than unconstrained ones. A first set of algorithms rely on eliminating the constraints and solving an equivalent unconstrained optimization problem.

Penalty methods are a simple way of adding the cost of violating the constraints in the objective function. The penalty parameter will set the trade-off cost of this violation compared to the initial objective function. Penalty methods are therefore *exterior-point methods* since iterates can fall outside the initial feasible region due to the relaxed constraints. Obviously an important practical difficulty is the selection of the penalty hyperparameter and the associated problem ill-conditioning when it becomes to large. Note that, as of now, penalty methods are widely used in deep-learning strategies to enforce physical constraints in an approximate way.

Augmented Lagrangian methods combine the idea of using Lagrange multipliers (it is a *primal-dual* method) with the penalty method and alleviate the need for using a large enough parameter.

Following the same idea of removing the constraints, active-set methods identify, in an iterative fashion, the set of active and inactive constraints in order to solve unconstrained problems until final identification of the active set of constraints. Successive linear programming or sequential quadratic programming can be interpreted as active set methods and consist in replacing the objective and the constraints by a linear or quadratic approximation around the current iterate. Unfortunately, such techniques rely on some smoothness assumption of the objective or constraints.

Barrier methods can be seen as a counter-part of penalty methods in which constraints are replaced by a barrier function i.e. a function which diverges as the point approaches the feasible region boundary. These methods are therefore *interior-point methods* since each iterate remains feasible. In particular, this requires the initial point to be feasible which is not always easy to find without any knowledge of the underlying problem. Although not being extremely efficient since they suffer from similar drawbacks as penalty methods, barrier methods found new interests due to their connection with the much more efficient *primal-dual interior point methods*.

### 3.3.3 Non-smooth problems

#### Smoothing

As we have seen, many methods are dedicated to smooth problems. Reformulation and smoothing methods are a first class of methods which consist in using a specific regularization technique to eliminate non-smoothness, thus reformulating the problem as a smooth optimization program. These techniques suffer from a similar drawback as penalty methods, namely the choice of the regularization parameter, the ill-conditioning when approaching the original behaviour and, even more importantly, a change in the underlying physical model when applied to mechanical problems. For instance, biviscous regularization is a widely used technique to replace intrinsic viscoplastic models of yield-stress fluids by a surrogate non-linear viscous behaviour. Unfortunately, abandoning the original non-smooth behaviour results in a loss on the existence of real solid (rigid) regions in viscoplastic flows, return to rest in finite time, etc.

#### Semi-smooth Newton methods

Unlike traditional Newton methods that require the objective function to be twice continuously differentiable, semi-smooth Newton methods extend their applicability to functions that may not have smooth derivatives but exhibit some degree of regularity, such as piecewise linear or piecewise smooth functions. These methods leverage generalized derivatives, like the Clarke subdifferential or the B-subdifferential, to iteratively approximate and solve the optimization problem.

#### Proximal point methods

Proximal algorithms (Parikh et al., 2014) can be seen as a generalization of descent methods to problems involving non-smooth or composite (smooth + non-smooth) objective functions. These algorithms iteratively minimize the objective function by solving a sequence of simpler subproblems that involve the *proximal operator*:

$$\text{prox}_{\lambda f}(\boldsymbol{x}) = \arg\min_{\boldsymbol{y}} f(\boldsymbol{y}) + \frac{1}{2\lambda}\|\boldsymbol{x} - \boldsymbol{y}\|_2^2 \tag{3.38}$$

which essentially performs a regularized minimization that balances proximity to a given point and reduction of the objective function value. Proximal algorithms, such as the Alternating Direction Method of Multipliers (ADMM) (Glowinski and Le Tallec, 1989), are known for their robustness and efficiency, especially in large-scale and high-dimensional problems. ADMM can be seen as a variant of Augmented Lagrangian approaches with partial updates. Such techniques have recently gained some attention in the context of conic optimization and have been implemented in open-source solvers such as `SCS` (O'Donoghue et al., 2016), `COSMO` (Garstka et al., 2021), `CDCS` (Zheng et al., 2017), etc. Unfortunately, such first-order methods converge quite slowly and can be used in practice only at the expense of a reduced accuracy in the computed solution. They are nowadays quite popular in the image and signal processing community which are mostly motivated by obtaining a sufficient decrease of some loss function (e.g. noise level) rather than computing accurately the solution to the underlying optimization problem.

### 3.3.4 Conic programming problems

#### Linear Programming

As mentioned before, Linear Programming is an extremely important class of non-smooth optimization problems which appears in a wide range of applications, often when complex problems under constraints have been linearized.

It was first efficiently solved using the *simplex method* developed by Dantzig et al. (1955). The simplex method relies on finding the minimum of the objective function by exploring the vertices of the polytope defined by the constraints in the opposite direction of the gradient. The starting point for the simplex method must be a vertex. Thereafter, every iteration moves to an adjacent vertex, decreasing the objective as it goes, until an optimal vertex is found. Simplex methods are a well established technology for LP however their extension to non-linear constraints is not straightforward. Another drawback is the exponential theoretical complexity of the algorithm which makes it impractical for some large-scale LP problems.

#### Interior-point methods

A ground-breaking advance in the resolution of large-scale LP has been achieved with the development of *interior-point methods* (IPM) by Karmarkar (1984) which exhibited polynomial

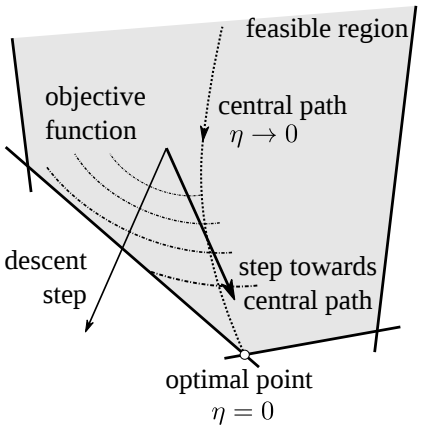


Figure 3.3: General idea of an interior-point algorithm following the *central path*

worst-case complexity. One decade later, *primal-dual methods* appeared as an even better version of IPM by simultaneously solving for primal as well as dual (Lagrange multipliers) variables.

Another ground-breaking development is due to the introduction of the *self-concordant barrier functions* by Nesterov and Nemirovskii (1994) which enabled to extend IPM to a much wider family of convex optimization problems than LP such as SOCP and SDP (Nesterov and Todd, 1997, 1998). The advent of interior-point methods is often considered as a revolution in optimization theory which now views linear and non-linear programming in a unified perspective. Since then, other important algorithmic developments allowed IPM to exhibit very good practical performances, especially regarding robustness of convergence (Mehrotra, 1992; Alizadeh and Goldfarb, 2003; Andersen et al., 2003; Boyd and Vandenberghe, 2004), see for instance (Wright, 2005) for a global overview.

**General overview of primal-dual IPM for conic programming**

To fix ideas, let us very briefly describe the main ingredients of primal-dual IPM for conic programs such as (3.27). First, the extension of IPM from LP to general conic programs relies on self-dual cones[2] such as the second-order cone $\mathcal{Q}_d$ or the cone of PSD matrices $\mathcal{S}_d^+$. We therefore assume that $K$ is a product of self-dual cones and is also self-dual: $K = K^*$.

The main idea of IPM consists in finding a solution to the optimality conditions (3.36) by following the neighborhood of a curve called the *central path* corresponding to solutions $\boldsymbol{z}(\eta) = (\boldsymbol{x}(\eta), \boldsymbol{y}(\eta), \boldsymbol{s}(\eta))$ to the following perturbed optimality conditions:

$$\boldsymbol{r}_\eta(\boldsymbol{z}) = \begin{bmatrix} \mathbf{A}^{\mathrm{T}}\boldsymbol{y} + \boldsymbol{s} - \mathbf{c} \\ \mathbf{A}\boldsymbol{x} - \mathbf{b} \\ \boldsymbol{x} \circ \boldsymbol{s} - \eta e \end{bmatrix} = 0, \text{ and } \boldsymbol{x}, \boldsymbol{s} \in \operatorname{int} K \times \operatorname{int} K \tag{3.39}$$

where $\boldsymbol{x} \circ \boldsymbol{s} \in \mathbb{R}^n$ involves a product $\circ$ of the Jordan algebra associated with symmetric cones, see (Alizadeh and Goldfarb, 2003) for more details. In particular, for $\boldsymbol{x}, \boldsymbol{s} \in K \times K$, the original complementary condition $\boldsymbol{x}^{\mathrm{T}}\boldsymbol{s} = 0$ is equivalent to $\boldsymbol{x} \circ \boldsymbol{s} = 0$. The main difference with the original system therefore comes from the perturbation of the complementary condition which is now replaced with $\boldsymbol{x} \circ \boldsymbol{s} = \eta \boldsymbol{e}$ where $\boldsymbol{e}$ is the unit vector associated with the Jordan product and $\eta \geq 0$ is the so-called *barrier parameter*. Clearly, for $\eta = 0$, $\boldsymbol{z}(0)$ is a primal-dual solution

[2]Note again that IPM has recently been extended also to non self-dual cones such as the power and exponential cone.

to the original system. The central path has the property of consisting of points which are well-centered i.e. which lie far from the feasible boundary except when $\eta \to 0$. Indeed, when using descent steps for constrained optimization problems, step sizes are usually very small because descent steps rapidly hit the boundary of the feasible region. The use of the central path will instead allow for large descent steps to be taken when following a minimizing path far from the feasible region boundary.

The IPM will therefore consists in repeatedly solving the perturbed system (3.39) for a decreasing sequence of $\eta$. Given a current value $\eta^{(k)}$ at iteration $k$, a Newton descent step is obtained by solving:

$$\mathbf{J}^{(k)}\Delta z = -\boldsymbol{r}^{(k)}(\boldsymbol{z}^{(k)}) \text{ where } \mathbf{J}^{(k)} = \begin{bmatrix} 0 & \mathbf{A}^{\mathrm{T}} & \mathbf{I}_n \\ \mathbf{A} & 0 & 0 \\ \mathbf{S}^{(k)} & 0 & \mathbf{X}^{(k)} \end{bmatrix} \tag{3.40}$$

where $\mathbf{I}_n$ is the identity matrix and $\mathbf{X}^{(k)}$, $\mathbf{S}^{(k)}$ are matrices resulting from the linearization of $\boldsymbol{x} \circ \boldsymbol{s}$ around $\boldsymbol{x}^{(k)}, \boldsymbol{s}^{(k)}$.

From the computed descent direction $\Delta z$ the next iterate $\boldsymbol{z}^{(k+1)}$ is obtained by a line-search on the maximum allowable step length $\alpha \in [0; 1]$ i.e. $\boldsymbol{z}^{(k+1)} = \boldsymbol{z}^{(k)} + \alpha\Delta z$ so that $\boldsymbol{x}^{(k+1)}$, $\boldsymbol{s}^{(k+1)} \in \operatorname{int} K \times \operatorname{int} K$. The barrier parameter is then reduced before the next step is taken.

There exist different ways, often based on heuristics, to decrease the value of the barrier parameter. In general, let us simply say that they depend on the distance of the current iterate from the central path. Broadly speaking, if the iterate is close to the central path (i.e. $\alpha$ is close to 1) an aggressive step can be taken and the barrier parameter can be strongly reduced. Conversely, if the iterate is close to the boundary, a centering step in which the barrier parameter does not reduce much is taken to "recenter" the iterate near the central path. There are obviously additional improvements which are really essential to achieve good performance in practice such as Nesterov-Todd scaling, Mehrotra predictor-corrector schemes, etc. We refer to (Andersen et al., 2003; Bleyer, 2018a) for more details.

### 3.3.5 Solvers and modeling languages

There exist many available solvers dedicated to LP, SOCP and/or SDP including commercial solvers such as CPLEX (CPLEX, 2018), Gurobi (Gurobi Optimization, LLC, 2023), COPT (Ge et al., 2022), Mosek (MOSEK ApS, 2019b) or open-source solvers such as ECOS (Domahidi et al., 2013), SCS (O'Donoghue et al., 2016), Clarabel (Goulard and Chen, 2023) or SDPT3 (Toh et al., 1999) just to name a few. Regarding the latter, they exhibit different level of performances depending on the wanted application. For instance, ECOS has been designed for embedded systems and is therefore well-suited for small-scale systems whereas SCS is based on a first-order operator-splitting method which can be very efficient for large-scale systems but for a moderate accuracy.

All of the previous solvers have been designed to solve conic programs expressed in a given *canonical form* such as (3.27) or (3.35) or another equivalent form[3]. A specific convex optimization problem must therefore be first transformed into one of such canonical forms before calling a numerical solver. For instance, if we want to solve the following Lasso regression problem:

$$\begin{aligned} \min_{\boldsymbol{x}} \quad & \frac{1}{2}\|\mathbf{C}\boldsymbol{x} - \mathbf{d}\|_2^2 \\ \text{s.t.} \quad & \|\boldsymbol{x}\|_1 \leq 1 \end{aligned} \tag{3.41}$$

[3] with the notable exception of Clarabel which can natively tackle a quadratic objective.

we would first need to introduce additional optimization variables such as:

$$\begin{aligned} \min_{\boldsymbol{x},\boldsymbol{y},t} \quad & t \\ \text{s.t.} \quad & \mathbf{C}\boldsymbol{x} - \boldsymbol{y} = \mathbf{d} \\ & \|\boldsymbol{x}\|_1 \leq 1 \\ & \frac{1}{2}\|\boldsymbol{y}\|^2 \leq t \end{aligned} \tag{3.42}$$

to obtain a linear function and a linear subspace condition. The last constraints should then be further re-expressed, with potentially additional optimization variables, as constraints involving cones from the magic family. Obviously, we see that such a reformulation process can quickly become cumbersome and time-consuming if one is interested in studying different types of models.

Fortunately, this step can be automated using *domain-specific languages* (DSL). A DSL is computer language which is specialized for a specific task. In the present case, we are interested in a domain-specific *modeling* language which consists in a set of rules and composable objects to express the structure of a given convex optimization problem. Examples of such DSL for convex optimization include `CVX` in Matlab (Grant and Boyd, 2014) and `CVXPY` in Python (Diamond and Boyd, 2016) but also `JuMP` in Julia (Dunning et al., 2017). The power of such DSL is that they can combine standard Matlab/Python or Julia code with specialized objects or functions used to define and solve a convex optimization problem by calling various solvers. In particular, they express composable convex expressions in the form of a graph and perform automatically the transformation of such a representation into the canonical representation, which may be different depending on the solver. In this work, we will often work with `CVXPY` to define small-scale convex optimization problems. For instance, the Lasso problem (3.41) can be defined as simply as:

```
import cvxpy as cp
import numpy as np

# generate random data
m, n = 200, 10
C = np.random.rand(m, n)
d = np.random.rand(m)

# define problem
x = cp.Variable(n)
objective = 0.5*cp.norm2(C*x-d)**2
constraints = [cp.norm1(x) <= 1]
problem = cp.Problem(cp.Minimize(objective), constraints)
problem.solve(solver=cp.MOSEK)
```

where we required `CVXPY` to use the `Mosek` solver.

# Chapter 4

# Convex variational principles in mechanics

This chapter provides a comprehensive overview of the variational principles underlying the formulation of various mechanical behaviors of solids and structures. Rather than an exhaustive historical presentation, our aim is to showcase their practical use in a range of applications, including elasticity, unilateral behaviors, and viscoplastic fluids. In particular, we motivate their use for a given context and provide insights into the corresponding numerical optimization problems. We focus on time-discrete variational formulations for standard dissipative materials, and explore both the well-known primal formulation and the less frequently considered dual formulation. The chapter also includes a discussion of the use of these formulations in an elasto-plastic setting and an analysis of their asymptotic behavior for large load conditions.

## Contents

## 4.1 Elasticity

### 4.1.1 Elastostatics

**Primal variational principle**

The most widely known variational principle describing small strain linear elasticity problems is the principle of *minimum potential energy*. This principle states that the solution $\boldsymbol{u}$ realizes the minimum of the potential energy $E_{\text{pot}}(\boldsymbol{u})$, i.e. the elastic energy minus the work of external forces, among all admissible displacements:

$$\min_{\boldsymbol{u}\in\mathcal{U}_{\text{ad}}} E_{\text{pot}}(\boldsymbol{u}) = \min_{\boldsymbol{u}\in\mathcal{U}_{\text{ad}}} \int_\Omega \psi(\boldsymbol{\varepsilon})\,\mathrm{d}\Omega - \int_\Omega \boldsymbol{f}\cdot\boldsymbol{u}\,\mathrm{d}\Omega - \int_{\partial\Omega_{\text{N}}} \boldsymbol{T}\cdot\boldsymbol{u}\,\mathrm{d}S \tag{4.1}$$

where $\boldsymbol{\varepsilon} = \frac{1}{2}(\nabla\boldsymbol{u} + \nabla^{\text{T}}\boldsymbol{u}) = \nabla^s\boldsymbol{u}$ is the infinitesimal strain, $\psi(\boldsymbol{\varepsilon}) = \frac{1}{2}\boldsymbol{\varepsilon} : \mathbb{C} : \boldsymbol{\varepsilon}$ with $\mathbb{C}$ the elastic stiffness and $\boldsymbol{f}$ (resp. $\boldsymbol{T}$) are prescribed body (resp. traction) forces in the domain (resp. on the Neumann boundary $\partial\Omega_{\text{N}}$). Finally, $\mathcal{U}_{\text{ad}}$ denotes the set of *kinematically admissible* displacement characterized by regularity conditions and imposed Dirichlet boundary conditions $\boldsymbol{u}_{\text{D}}$:

$$\mathcal{U}_{\text{ad}} = \left\{\boldsymbol{u} \in H^1(\Omega) \text{ and s.t. } \boldsymbol{u} = \boldsymbol{u}_{\text{D}} \text{ on } \partial\Omega_{\text{D}}\right\} \tag{4.2}$$

The first-order optimality condition reads in this case:

$$\forall \boldsymbol{v} \in \mathcal{U}_0, \quad \delta E_{\text{pot}}(\boldsymbol{u};\boldsymbol{v}) = \int_\Omega \nabla^s\boldsymbol{u} : \mathbb{C} : \nabla^s\boldsymbol{v}\,\mathrm{d}\Omega - \int_\Omega \boldsymbol{f}\cdot\boldsymbol{v}\,\mathrm{d}\Omega - \int_{\partial\Omega_{\text{N}}} \boldsymbol{T}\cdot\boldsymbol{v}\,\mathrm{d}S = 0 \tag{4.3}$$

where $\delta E_{\text{pot}}(\boldsymbol{u};\boldsymbol{v})$ denotes the first variation at $\boldsymbol{u}$ in direction $\boldsymbol{v}$ and $\mathcal{U}_0$ is the space of admissible displacements with homogeneous boundary condition (i.e. $\mathcal{U}_{\text{ad}}$ with $\boldsymbol{u}_{\text{D}} = 0$). The variational equality (4.3) corresponds to the *virtual work principle* complemented with the elastic constitutive law $\boldsymbol{\sigma} = \mathbb{C} : \boldsymbol{\varepsilon}$. Finally, owing to the strict convexity of $E_{\text{pot}}(\boldsymbol{u})$, the first-order condition is sufficient to characterize the minimum which is also unique.

When restricting to a finite-dimensional subspace $\mathcal{U}_h \subset \mathcal{U}_{\text{ad}}$ such as the one obtained after a classical finite-element discretization, the minimum potential energy principle becomes:

$$\min_{\bar{\boldsymbol{u}}\in\mathbb{R}^n} \frac{1}{2}\bar{\boldsymbol{u}}^{\text{T}}\mathbf{K}\bar{\boldsymbol{u}} - \mathbf{F}^{\text{T}}\bar{\boldsymbol{u}} \tag{4.4}$$

where $\bar{\boldsymbol{u}}$ denotes the global vector of degrees of freedom, $\mathbf{K}$ is the global stiffness matrix and $\mathbf{F}$ the global vector of equivalent nodal forces. We clearly obtain a simple unconstrained quadratic optimization problem with optimality conditions:

$$\mathbf{K}\bar{\boldsymbol{u}} - \mathbf{F} = 0 \tag{4.5}$$

**Dual variational problem**

If the previous *primal* variational problem is widely known and lies at the basis of the finite-element method, the corresponding *dual* variational problem is less used, at least from the numerical perspective. Upon standard derivation, the dual problem is formulated in terms of admissible stresses and states that the optimal stress field realizes the minimum of the *complementary energy* $E_{\text{comp}}(\boldsymbol{\sigma})$:

$$\min_{\boldsymbol{\sigma}\in\mathcal{S}_{\text{ad}}} E_{\text{comp}}(\boldsymbol{\sigma}) = \min_{\boldsymbol{\sigma}\in\mathcal{S}_{\text{ad}}} \int_\Omega \psi^*(\boldsymbol{\sigma})\,\mathrm{d}\Omega - \int_{\partial\Omega_{\text{D}}} (\boldsymbol{\sigma}\boldsymbol{n})\cdot\boldsymbol{u}_{\text{D}}\,\mathrm{d}S \tag{4.6}$$

where $\psi^*(\boldsymbol{\sigma}) = \frac{1}{2}\boldsymbol{\sigma} : \mathbb{C}^{-1} : \boldsymbol{\sigma}$, $\boldsymbol{n}$ is the unit exterior normal and $\mathcal{S}_{\text{ad}}$ denotes the set of *statically admissible* stress fields defined as:

$$\mathcal{S}_{\text{ad}} = \left\{ \boldsymbol{\sigma} \in H(\text{div}; \Omega) \text{ s.t. } \left| \begin{array}{l} \text{div}\, \boldsymbol{\sigma} + \boldsymbol{f} = 0 \text{ in } \Omega \\ \boldsymbol{\sigma}\boldsymbol{n} = \boldsymbol{T} \text{ on } \partial\Omega_{\text{N}} \end{array} \right. \right\} \tag{4.7}$$

where $H(\text{div}; \Omega)$ is the space of symmetric stress tensors which are $L^2(\Omega)$ and such that $\text{div}\, \boldsymbol{\sigma} \in L^2(\Omega)$. Note that this enforces in particular that $\boldsymbol{\sigma}\boldsymbol{n}$ must be continuous inside the domain.

Let us also point out that both problems are dual to each other in the sense that they provide the same solution and that at the optimum[1]:

$$E_{\text{pot}}(\boldsymbol{u}) = -E_{\text{comp}}(\boldsymbol{u}) \tag{4.8}$$

**Remark 2.** Note that we should also mention mixed variational principles such as the Hellinger-Reissner principle which is nothing else than the corresponding max/min saddle point problem obtained from the Lagrangian associated with (4.1) and (4.6):

$$\max_{\boldsymbol{\sigma} \in \mathcal{S}_{\text{ad}}} \min_{\boldsymbol{u} \in \mathcal{U}_{\text{ad}}} \int_\Omega \boldsymbol{\sigma} : \boldsymbol{\varepsilon} - \frac{1}{2}\boldsymbol{\sigma} : \mathbb{C}^{-1} : \boldsymbol{\sigma}\, \text{d}\Omega - \int_\Omega \boldsymbol{f} \cdot \boldsymbol{u}\, \text{d}\Omega - \int_{\partial\Omega_{\text{N}}} \boldsymbol{T} \cdot \boldsymbol{u} \tag{4.9}$$

Similarly, the three-field Hu-Washizu principle corresponds to the same Lagrangian where the compatibility equation $\boldsymbol{\varepsilon} = \nabla^s \boldsymbol{u}$ has been included as an explicit constraint and included in the Lagrangian.

One of the main reason explaining the prevalence of the primal approach over the dual one in a discrete setting is due to the fact that it is extremely difficult to devise conforming approximations of $\mathcal{S}_{\text{ad}}$. For brevity, we will not review the literature concerning stress-based finite-elements and related approaches and refer the reader to (de Almeida and Maunder, 2017) for a good introduction on this topic. Instead, let us just formalize what would be obtained when considering a fully discontinuous piecewise-polynomial interpolation of the stress inside each finite-elements. To fix ideas, let us consider the stress field to be linear inside each element but with a discontinous interpolation with respect to adjacent elements and that there is no imposed traction. Strong equilibrium can then be enforced for piecewise-constant body forces inside each element. Strong traction continuity conditions can also be enforced by imposing that $[\![\boldsymbol{\sigma}(\boldsymbol{x}_j)]\!]\boldsymbol{n} = 0$ across a given finite-element facet of normal $\boldsymbol{n}$ with vertices $\boldsymbol{x}_j$. Eventually, one obtains a quadratic optimization problem with affine equality constraints:

$$\begin{array}{ll} \min\limits_{\bar{\boldsymbol{\sigma}}} & \frac{1}{2}\bar{\boldsymbol{\sigma}}\mathbf{S}\bar{\boldsymbol{\sigma}} - \bar{\boldsymbol{u}}_{\text{D}}^{\text{T}}\bar{\boldsymbol{\sigma}} \\ \text{s.t.} & \mathbf{H}\bar{\boldsymbol{\sigma}} + \mathbf{F} = 0 \\ & \mathbf{B}\bar{\boldsymbol{\sigma}} = 0 \end{array} \tag{4.10}$$

where $\mathbf{S}$ is a global compliance matrix, $\mathbf{H}$ is a global equilibrium matrix collecting each element internal equilibrium condition and $\mathbf{B}$ is a global equilibrium matrix collecting inter-element jump conditions and free traction boundary conditions.

We therefore see from (4.10) that optimality conditions result in the following linear system involving Lagrange multipliers $\bar{\boldsymbol{u}}$ corresponding to the first constraint and $\bar{\boldsymbol{v}}$ corresponding

[1] The true dual in the optimization vocable would rather be $\max -E_{\text{comp}} = -\min E_{\text{comp}}$ so that both problems yield the same objective value at the optimum.

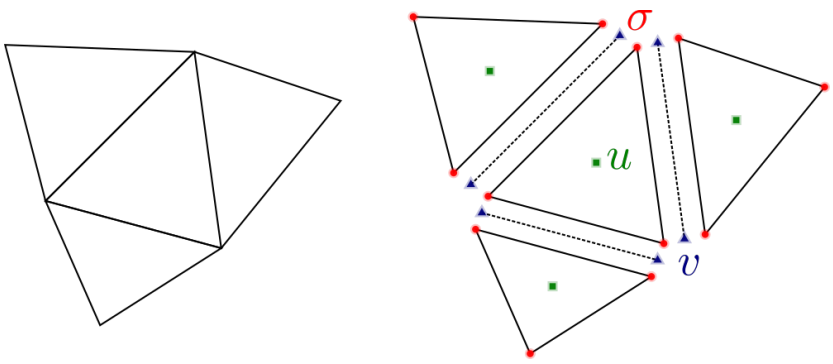


Figure 4.1: Left: geometrical 2D mesh. Right: FE discretization of the mixed approach: piecewise linear stresses $\boldsymbol{\sigma}$, piecewise-constant cell-displacement $\boldsymbol{u}$ and piecewise-linear facet-displacement $\boldsymbol{v}$.

to the second constraint:

$$\max_{\bar{\boldsymbol{u}},\bar{\boldsymbol{v}}} \min_{\bar{\boldsymbol{\sigma}}} \frac{1}{2}\bar{\boldsymbol{\sigma}}\mathbf{S}\bar{\boldsymbol{\sigma}} - \bar{\boldsymbol{u}}_{\mathrm{D}}^{\mathrm{T}}\bar{\boldsymbol{\sigma}} - \bar{\boldsymbol{u}}^{\mathrm{T}}(\mathbf{H}\bar{\boldsymbol{\sigma}} + \mathbf{F}) - \bar{\boldsymbol{v}}^{\mathrm{T}}\mathbf{B}\boldsymbol{\sigma} \tag{4.11}$$

$$\Rightarrow \begin{bmatrix} \mathbf{S} & -\mathbf{H}^{\mathrm{T}} & -\mathbf{B}^{\mathrm{T}} \\ -\mathbf{H} & 0 & 0 \\ -\mathbf{B} & 0 & 0 \end{bmatrix} \begin{Bmatrix} \bar{\boldsymbol{\sigma}} \\ \bar{\boldsymbol{u}} \\ \bar{\boldsymbol{v}} \end{Bmatrix} = \begin{Bmatrix} \bar{\boldsymbol{u}}_{\mathrm{D}} \\ \mathbf{F} \end{Bmatrix} \tag{4.12}$$

From a mechanical stand point, $\boldsymbol{u}$ and $\boldsymbol{v}$ can both be interpreted as displacements, the former being defined in cells only whereas the latter is defined on facets only. Moreover, since $\boldsymbol{\sigma}$ is linear, local equilibrium can be enforced using piecewise-constant $\boldsymbol{u}$ whereas traction continuity is enforced with piecewise-linear $\boldsymbol{v}$, see Fig. 4.1.

In the finite-element literature, such approaches looking simultaneously for stress and displacement fields is generally termed as a *mixed approach*. More precisely, mixed approaches generally refer to conforming discretizations of the $H(\mathrm{div})$ space. However, up to now, no simple mixed FE is available for the general 3D elasticity problem. When relaxing the traction continuity condition and enforcing it in the discrete formulation as presented above is a process called *hybridization*. This allows for the use of simpler FE space at the expense of an additional Lagrange multiplier to solve for. However, it turns out the matrices $\mathbf{S}$ and $\mathbf{H}$ enjoy a block-structure associated with FE cells, it is therefore possible to perform static condensation of the stress $\boldsymbol{\sigma}$ and cell-displacement $\boldsymbol{u}$ variables at the cell level. The resulting system being formulated only on the facet-Lagrange multiplier $\boldsymbol{v}$, see (Arnold and Brezzi, 1985; Cockburn et al., 2009; Gong et al., 2019).

**Use in up-scaling approaches**

In our point of view, *up-scaling* techniques refer to methods that reduce the complexity of modeling a heterogeneous material at a microscopic scale while preserving the key properties that affect its behavior at the macroscopic scale. The goal is to achieve a computationally efficient representation of the material's behavior without sacrificing too much accuracy. Up-scaling can be achieved in various ways such as *homogenization* where the microscopic details are averaged out by using an effective homogeneous model of the material. In this case, the original 3D continuum is replaced with an other 3D continuum model (possibly a generalized one such strain-gradient, micromorphic models, etc.). Up-scaling can also refer to dimensional reduction of a 3D continuum at the microscopic scale towards a 1D beam or 2D plate/shell model at the macroscopic level.

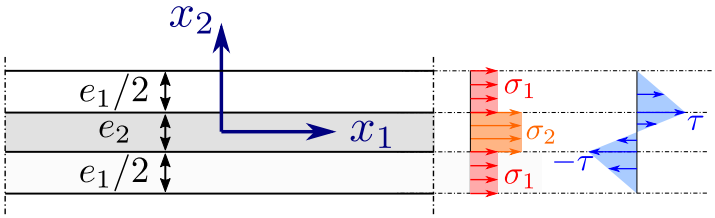


Figure 4.2: Geometry of the bi-material and shear-lag stress distribution assumptions

In all cases, primal and dual variational principles are often used in such a context to derive variationally consistent macroscopic effective models from approximations of kinematic or static quantities at the microscopic scale. Primal (resp. dual) variational principles can provide upper (resp. lower) bounds on effective properties such as Voigt (resp. Reuss) or Hashin-Shtrikman bounds in homogenization. As regards the derivation of plate models for instance, the use of an approximation on the 3D displacement field in the primal approach (4.1) results in a "stiff" model where strain compatibility is verified exactly but local equilibrium is verified in a weak sense only. Conversely, the use of an approximation on the 3D stress field in the dual approach (4.6) results in a "compliant" model where local equilibrium is verified exactly and strain compatibility is verified in a weak sense only. Obviously, the relevance of using one approach over another highly depends on the considered application. Note that when using mixed variational principles where both displacement and stresses are simultaneously approximated, the bounding character of the resulting model is lost in general.

As an illustration, let us consider a very simple up-scaling case considering the bi-material of Fig. 4.2 in plane-stress state in the $(x_1, x_2)$-plane. The bilayer consists of one central core of thickness $e_2$ surrounded by two symmetric skins of thickness $e_1/2$. Each material (skins and core) is isotropic elastic with Young modulus $E_i$ and shear modulus $\mu_i$ for $i = 1, 2$. We consider a rectangular region $\Omega = \omega \times [-e/2; e/2]$ where $e = e_1 + e_2$. We are interested in a generalized 1D model along $x_1$ which is capable of describing the behaviour of both layers and, in particular, the shear transfer mechanism occurring at the interface. Note that this model is a proxy for the 3D multiphase continuum model and the more advanced multilayered plate models discussed in Section 2.2.4. Such a simple model is called the *shear lag* model in the corresponding literature. Here, we provide a simple variational construction based on the dual stress-based principle.

Let us indeed assume the following form for the local 2D stress-field $\boldsymbol{\sigma}(x_1, x_2)$ (see again Fig. 4.2-right):

$$\sigma_{11}(x_1, x_2) = \begin{cases} \sigma_1(x_1) & \text{for } |x_2| > e_2/2 \\ \sigma_2(x_1) & \text{for } |x_2| < e_2/2 \end{cases} \tag{4.13a}$$

$$\sigma_{12}(x_1, x_2) = \begin{cases} \dfrac{2\tau x_2}{e_2} & \text{for } |x_2| < e_2/2 \\ (\pm e - 2x_2)\dfrac{\tau}{e_1} & \text{for } \pm x_2 \geq e_2/2 \end{cases} \tag{4.13b}$$

$$\sigma_{22}(x_1, x_2) = 0 \tag{4.13c}$$

where $\sigma_i(x_1)$ and $\tau(x_1)$ are unknown fields which will form the generalized stresses of the shear-lag model. Clearly, $\sigma_i$ can be interpreted as the partial stress in layer $i$ while $\tau(x_1)$ is

the interfacial shear stress. We assume stress-free conditions on top and bottom surfaces and potential Dirichlet conditions on the boundary $\partial\omega \times [-e/2; e/2]$

Injecting assumptions (4.13) into (4.6) yields for the elastic stress energy:

$$\int_\Omega \frac{1}{2}\boldsymbol{\sigma} : \mathbb{C}^{-1} : \boldsymbol{\sigma}\, \mathrm{d}\Omega = \int_\omega \sum_{i=1}^{2} \left( \frac{e_i}{2E_i}\sigma_i^2 + \frac{e_i}{6\mu_i}\tau^2 \right) \mathrm{d}\omega \tag{4.14}$$

whereas the work of imposed displacements reduces to:

$$\int_{\partial\Omega_\mathrm{D}} (\boldsymbol{\sigma}\boldsymbol{n}) \cdot \boldsymbol{u}_\mathrm{D}\, \mathrm{d}S = \int_{\partial\omega} \sum_{i=1}^{2} e_i \sigma_i u_{i,\mathrm{D}}\, \mathrm{d}S \tag{4.15}$$

where $u_{i,\mathrm{D}}$ denotes the averaged horizontal imposed displacement $\boldsymbol{u}_\mathrm{D}$ over the layer $i$. Finally, the set of admissible stresses $\mathcal{S}_\mathrm{ad}$ now reduces to the following set of admissible generalized stresses $\boldsymbol{\Sigma} = (\sigma_1, \sigma_2, \tau)$:

$$\mathcal{S}_\mathrm{ad} = \left\{ (\sigma_1, \sigma_2, \tau) \text{ s.t. } \left| \begin{array}{l} \sigma_1'(x_1) - \dfrac{2\tau(x_1)}{e_1} = 0 \\ \sigma_2'(x_1) + \dfrac{2\tau(x_1)}{e_2} = 0 \end{array} \right. \right\} \tag{4.16}$$

We therefore have the following corresponding minimum complementary energy principle describing the 1D shear lag model:

$$\begin{array}{rl} \displaystyle\min_{\sigma_1,\sigma_2,\tau} & \displaystyle\int_\omega \left( \frac{e_1}{2E_1}\sigma_1^2 + \frac{e_2}{2E_2}\sigma_2^2 + \frac{1}{\kappa}\tau^2 - e_1\sigma_1 u_{1,\mathrm{D}} - e_2\sigma_2 u_{2,\mathrm{D}} \right) \mathrm{d}\omega \\ \text{s.t.} & e_1\sigma_1'(x_1) - 2\tau(x_1) = 0 \\ & e_2\sigma_2'(x_1) + 2\tau(x_1) = 0 \end{array} \tag{4.17}$$

where $\kappa = \dfrac{6}{\dfrac{e_1}{\mu_1} + \dfrac{e_2}{\mu_2}}$ is a shear interaction stiffness between both layers.

Introducing $u_1$ (resp. $u_2$) as the two Lagrange multipliers associated with both constraints, we see that the optimality conditions read as:

$$\frac{\sigma_1(x_1)}{E_1} = u_1'(x_1) \tag{4.18a}$$

$$\frac{\sigma_2(x_1)}{E_2} = u_2'(x_1) \tag{4.18b}$$

$$\frac{\tau(x_1)}{\kappa} = u_1(x_1) - u_2(x_1) \tag{4.18c}$$

$$u_i(x_1) = u_{i,D}(x_1) \quad i = 1, 2 \text{ on } \partial\omega \tag{4.18d}$$

As expected, we obtain the corresponding generalized Dirichlet boundary conditions as well as the generalized constitutive equations of the model, expressed in "compliance" form. For this simple model, they relate each partial stress $\sigma_i$ to the corresponding uniaxial strain $\epsilon_i = u_i'$ via the layer Young modulus and, more interestingly, the interfacial shear stress $\tau$ to the relative displacement between both layers $u_1 - u_2$ via the shear interaction stiffness $\kappa$. The latter depends on the thickness of both layers and will be at the origin of size effects in the response of the shear lag model. Finally, the Lagrange multipliers $u_i$ are interpreted here as *the* generalized displacement of phase $i$. To be more precise, the optimality conditions of the initial variational problem show that such generalized displacements $u_i(x_1)$ can be interpreted as the average of the horizontal microscopic displacement field $\boldsymbol{u}(x_1, x_2) \cdot \boldsymbol{e}_1$ over layer $i$. We see here that dual-based variational principles allow for a strong enforcement of equilibrium equations but, in return, allow for a weak control only of microscopic kinematics.

### 4.1.2 Elastodynamics

#### Primal variational principle

It is widely known that the evolution equations of dynamic mechanical systems can be described by Hamilton's stationary action variational principle which defines the *action* from the potential and kinetic energy of the system, see (Bedford, 1985) for instance. In the context of elastodynamics, the action can be defined as:

$$\mathcal{A}_{\mathrm{p}}[\boldsymbol{u}] = \int_{t_0}^{t_1} \int_{\Omega} \left( \frac{1}{2} \rho \|\dot{\boldsymbol{u}}\|^2 - \frac{1}{2} \boldsymbol{\varepsilon} : \mathbb{C} : \boldsymbol{\varepsilon} \right) \mathrm{d}\Omega \, \mathrm{d}t \tag{4.19}$$

where $t_0$ and $t_1$ are two specified times with given state $\boldsymbol{u}(t_0) = \boldsymbol{u}_0$ and $\boldsymbol{u}(t_1) = \boldsymbol{u}_1$. In the above, we omit external loads for simplicity. Hamilton's principle then states that the true trajectory $\boldsymbol{u}(t)$ on $[t_0; t_1]$ is a stationary point of the action $\mathcal{A}$. The corresponding optimality conditions, the *Euler-Lagrange equations*, then provide the corresponding differential equations characterizing the solution.

Note that classical time integration methods typically approach the solution of differential equations by discretizing the equations directly in time. On the other hand, *variational time integrators* are are a specialized class of time discretization techniques that instead discretize the time-continuous variational principle, yielding a time-discrete variational counterpart. This approach leads to several advantages, such as preserving important physical quantities such as convservation of energy and momentum as well as underlying symmetries, resulting in increased stability and accuracy compared to traditional methods.

#### Dual variational principle

A much more confidential principle in elastodynamics is the corresponding dual principle to Hamilton's principle which relies on stress fields. A first version has been proposed by Toupin (1952) using the stress impulse $\boldsymbol{\mathcal{T}}(t) = \boldsymbol{\mathcal{T}}(t_0) + \int_{t_0}^{t} \boldsymbol{\sigma}(s) \mathrm{d}s$. The corresponding complementary elastodynamic principle (Fraeijs de Veubeke, 1971; Tabarrok, 1984) states that the following functional is stationary at the solution:

$$\mathcal{A}_{\mathrm{d}}[\boldsymbol{\mathcal{T}}] = \int_{t_0}^{t_1} \int_{\Omega} \left( \frac{1}{2} \dot{\boldsymbol{\mathcal{T}}} : \mathbb{C}^{-1} : \dot{\boldsymbol{\mathcal{T}}} - \frac{1}{2\rho} \| \operatorname{div} \boldsymbol{\mathcal{T}} \|^2 \right) \mathrm{d}\Omega \, \mathrm{d}t \tag{4.20}$$

for all $\boldsymbol{\mathcal{T}}$ such that $\dot{\boldsymbol{\mathcal{T}}} \boldsymbol{n} = 0$ on $\partial\Omega_{\mathrm{N}}$. Note again that we do not consider imposed Dirichlet boundary conditions for simplicity.

An equivalent two-field principle can be obtained by introducing the momentum density $\boldsymbol{p}$ as an independent unknown, i.e. $\boldsymbol{p} = \operatorname{div} \boldsymbol{\mathcal{T}}$. The complementary elastodynamic principle is therefore equivalent to the following functional stationarity:

$$\mathcal{A}_{\mathrm{d}}[\boldsymbol{\sigma}, \boldsymbol{p}] = \int_{t_0}^{t_1} \int_{\Omega} \left( \frac{1}{2} \boldsymbol{\sigma} : \mathbb{C}^{-1} : \boldsymbol{\sigma} - \frac{1}{2\rho} \|\boldsymbol{p}\|^2 \right) \mathrm{d}\Omega \, \mathrm{d}t \tag{4.21a}$$

for all $\boldsymbol{\sigma}, \boldsymbol{p}$ such that:

$$\operatorname{div} \boldsymbol{\sigma} = \dot{\boldsymbol{p}} \text{ on } \Omega \tag{4.21b}$$

$$\boldsymbol{\sigma} \boldsymbol{n} = 0 \text{ on } \partial\Omega_{\mathrm{N}} \tag{4.21c}$$

**Remark 3.** As (4.21a), Hamilton's principle can also be formulated as a two field-principle involving the displacement $\boldsymbol{u}$ and the velocity $\boldsymbol{v}$ under the constraint $\boldsymbol{v} = \dot{\boldsymbol{u}}$. Inspection of both objective function provide a nice duality between the stress and displacement involved in the elastic energy and between the momentum and velocity in the kinetic energy. Note that Hamiltonian mechanics consist in performing a partial Legendre transform from the velocity $\boldsymbol{v}$ to the momentum $\boldsymbol{p}$.

Interestingly, we have used such a principle when dealing in (Bouteiller et al., 2022) with layerwise plate models which are formulated from the 3D dual elastic principle, in the same spirit as the shear lag model. However, their extension to dynamic scenarios was initially not straightforward. While models derived from a primal variational principle can easily be extended to dynamics by using the same Ansatz for both the microscopic displacement and velocity fields, this is not the case for stress-based models. In this case, generalized degrees of freedom are obtained through duality with the generalized equilibrium equations. When transitioning to a dynamic setting, the challenge is to compute the generalized inertias from the local density distribution of the underlying material. In some cases, generalized dofs may have a clear physical interpretation, making it simple to define the generalized inertias, but this is not always the case. To address this, a systematic procedure is required to obtain a consistent elastodynamic version of stress-based models.

This procedure relies on the dual principle (4.21a) in which an Ansatz for the microscopic momentum $\boldsymbol{p}$ is considered, rather than the microscopic velocity. This Ansatz must be consistent with the corresponding Ansatz for the stress field which impacts the corresponding microscopic dynamic equation. Going back to the shear lag model for the sake of illustration, the latter is given by:

$$\dot{p}(x_1, x_2) = \begin{cases} \sigma_1'(x_1) - \dfrac{2\tau(x_1)}{e_1} & \text{for } |x_2| > e_2/2 \\ \sigma_2'(x_1) + \dfrac{2\tau(x_1)}{e_2} & \text{for } |x_2| < e_2/2 \end{cases} \tag{4.22}$$

where $p = \boldsymbol{p} \cdot \boldsymbol{e}_1$ is the longitudinal momentum density. A consistent use of the variational principle (4.21a) therefore requires to choose a scalar piecewise-constant momentum with respect to $x_2$:

$$p(x_1, x_2) = \begin{cases} p_1(x_1) & \text{for } |x_2| > e_2/2 \\ p_2(x_1) & \text{for } |x_2| < e_2/2 \end{cases} \tag{4.23}$$

yielding the following generalized dynamic equations for $x_1 \in \omega$:

$$e_1 \dot{p}_1(x_1) = e_1 \sigma_1'(x_1) - 2\tau(x_1) \tag{4.24a}$$
$$e_2 \dot{p}_2(x_1) = e_2 \sigma_2'(x_1) + 2\tau(x_1) \tag{4.24b}$$

Assuming that the material density in both layers is described by a generic function $\rho(x_2)$, the kinetic energy term in (4.21a) specializes to:

$$\int_{t_0}^{t_1} \int_\Omega \frac{1}{2\rho} \|\boldsymbol{p}\|^2 \, \mathrm{d}\Omega \, \mathrm{d}t = \int_{t_0}^{t_1} \int_\omega \frac{1}{2} \left( e_1 \left\langle \frac{1}{\rho} \right\rangle_1 p_1^2 + e_2 \left\langle \frac{1}{\rho} \right\rangle_2 p_2^2 \right) \mathrm{d}\omega \, \mathrm{d}t \tag{4.25}$$

where $\langle \star \rangle_i$ denotes the average of $\star$ over layer $i$.

Introducing the same Lagrange multipliers $u_1$ (resp. $u_2$) as in Section 4.1.1) (now associated with the dynamic equations (4.24)), the optimality conditions of (4.21a) now read:

$$\frac{\sigma_1(x_1)}{E_1} = u_1'(x_1) \tag{4.26a}$$

$$\frac{\sigma_2(x_1)}{E_2} = u_2'(x_1) \tag{4.26b}$$

$$\frac{\tau(x_1)}{\kappa} = u_1(x_1) - u_2(x_1) \tag{4.26c}$$

$$\left\langle \frac{1}{\rho} \right\rangle_1 p_1 = \dot{u}_1 \tag{4.26d}$$

$$\left\langle \frac{1}{\rho} \right\rangle_2 p_2 = \dot{u}_2 \tag{4.26e}$$

As a result, we can remark that this approach yields $m_i = 1/\left\langle 1/\rho \right\rangle_i$ as the generalized inertia associated with the motion of layer $i$. On the contrary, if we had assumed that layer $i$ was animated by a uniform translation motion of velocity $\dot{u}_i$, we would have naturally used $m_i = \left\langle \rho \right\rangle_i$ as the corresponding inertia.

In the general case, see (Bouteiller et al., 2022), the above procedure yields the generalized momentum/velocity constitutive relation: $\dot{\boldsymbol{U}} = \boldsymbol{D}\boldsymbol{P}$ where $\dot{\boldsymbol{U}}$ is the generalized velocity vector, $\boldsymbol{P}$ the generalized momentum vector. Inverting this relation as $\boldsymbol{P} = \boldsymbol{D}^{-1}\dot{\boldsymbol{U}}$, $\boldsymbol{D}^{-1}$ can be interpreted as the generalized mass matrix of the considered model.

## 4.2 Contact conditions

The previous primal and dual variational principle of linear elastostatics and elastodynamics can also be extended to situations involving contact conditions.

### 4.2.1 Elastic and unilateral support conditions

Let us first start with the case where elastic support conditions are considered. Consider a portion $\partial\Omega_C$ of the boundary on which the domain $\Omega$ is connected to a linear density of springs with initial length $g_0(\boldsymbol{x})$ and aligned along the unit direction $\boldsymbol{N}$. In the deformed configuration, the new length in this direction is $g_N(\boldsymbol{x}) = g_0(\boldsymbol{x}) + \boldsymbol{u}(\boldsymbol{x}) \cdot \boldsymbol{N}$. Assuming that the density of spring stiffness is $K_N$, the equilibrium of such a system is characterized by the variational principle (4.1) where the potential energy is complemented with the springs contribution to the elastic energy:

$$E_{\text{el, springs}}(\boldsymbol{u}) = \int_{\partial\Omega_C} \frac{1}{2} K_N (g_N(\boldsymbol{x}) - g_0(\boldsymbol{x}))^2 \, \mathrm{d}S = \int_{\partial\Omega_C} \frac{1}{2} K_N (\boldsymbol{u}(\boldsymbol{x}) \cdot \boldsymbol{N})^2 \, \mathrm{d}S \tag{4.27}$$

Obviously, this can be further generalized to tangential spring stiffnesses or nonlinear elasticity provided that the latter is derived from a convex potential $\psi_c(g_N, \boldsymbol{g}_T)$ with respect to the *gap* measure of normal component $g_N$ and tangential component $\boldsymbol{g}_T$.

*Unilateral contact* against a fixed obstacle can then be formalized as a specialized case of nonlinear spring elasticity in which:

$$\psi_c(g_N, \boldsymbol{g}_T) = \begin{cases} 0 & \text{if } g_N \geq 0 \\ +\infty & \text{otherwise} \end{cases} \tag{4.28}$$

The corresponding primal variational principle therefore reads:

$$\begin{aligned} \min_{\boldsymbol{u}} \quad & \int_\Omega \frac{1}{2}\boldsymbol{\varepsilon} : \mathbb{C} : \boldsymbol{\varepsilon}\, \mathrm{d}\Omega - \int_\Omega \boldsymbol{f}\cdot\boldsymbol{u}\, \mathrm{d}\Omega - \int_{\partial\Omega_\mathrm{N}} \boldsymbol{T}\cdot\boldsymbol{u}\, \mathrm{d}S \\ \text{s.t.} \quad & \boldsymbol{u} = \boldsymbol{u}_\mathrm{D} \text{ on } \partial\Omega_\mathrm{D} \\ & \boldsymbol{u}\cdot\boldsymbol{N} \geq -g_0 \text{ on } \partial\Omega_\mathrm{C} \end{aligned} \tag{4.29}$$

which turns out to be quadratic optimization problem with linear equality and inequality constraints.

One can show that the dual variational principle will involve:

$$\psi_\mathrm{c}^*(\sigma_N, \boldsymbol{\sigma}_T) = \begin{cases} 0 & \text{if } \sigma_N \leq 0 \text{ and } \boldsymbol{\sigma}_T = 0 \\ +\infty & \text{otherwise} \end{cases} \tag{4.30}$$

where $\sigma_N = \boldsymbol{N}\cdot(\boldsymbol{\sigma}\boldsymbol{N})$ is the normal traction and $\boldsymbol{\sigma}_T = \boldsymbol{\sigma}\boldsymbol{N} - \sigma_N\boldsymbol{N}$ is the tangential traction. In particular, as $\psi_\mathrm{c}$ is the indicator of the unilateral cone $\mathbb{R}^+ \times \mathbb{R}^2$, $\psi_\mathrm{c}^*$ is the indicator of the dual cone $\mathbb{R}^- \times \{0\}$.

### 4.2.2 Including frictional contact

Including frictional contact in the previous formulation poses however tremendous additional complexity due to the fact that Coulomb's friction law does not satisfy the normality rule (or maximum dissipation principle). Indeed, the corresponding stress criterion is described by the Coulomb friction cone:

$$\mathcal{K}_\mu = \{(\sigma_N, \boldsymbol{\sigma}_T) \in \mathbb{R}^3 \text{ s.t. } \mu\sigma_N + \|\boldsymbol{\sigma}_T\| \leq 0\} \tag{4.31}$$

The corresponding dual variables being the normal and slip velocities $(\dot{g}_N, \dot{\boldsymbol{g}}_T) = (\dot{u}_N, \dot{\boldsymbol{u}}_T)$, an *associative* friction law would require the latter to belong to the corresponding dual cone:

$$\mathcal{K}_\mu^* = \{(\dot{u}_N, \dot{\boldsymbol{u}}_T) \in \mathbb{R}^3 \text{ s.t. } \dot{u}_N \leq \mu\|\dot{\boldsymbol{u}}_T\|\} \tag{4.32}$$

along with the complementarity condition:

$$\sigma_N\dot{u}_N + \boldsymbol{\sigma}_T\cdot\dot{\boldsymbol{u}}_T = 0 \tag{4.33}$$

In particular, we see that, in the case of a frictional sliding contact with a non zero velocity, an associative friction law would predict a non-zero normal velocity such that $\dot{u}_N = \mu\|\dot{\boldsymbol{u}}_T\|$, that is a dilation proportional to the friction coefficient.

However, as regards real materials, dilation of frictional contact is considered to be zero. One therefore needs to abandon the use of an associated rule and turn instead to a non-associated rule stating that, if frictional sliding occurs, then $\dot{u}_N = 0$ and $\|\dot{\boldsymbol{u}}_T\| > 0$. It turns out that Coulomb friction can still be formulated using second-order cones by introducing a modified velocity $\dot{\tilde{\boldsymbol{u}}} = (\dot{u}_N + \mu\|\dot{\boldsymbol{u}}_T\|, \dot{\boldsymbol{u}}_T)$.

Then, the Coulomb law is equivalent to saying that $(\sigma_N, \boldsymbol{\sigma}_T) \in \mathcal{K}_\mu$ and $\dot{\tilde{\boldsymbol{u}}} \in \mathcal{K}_\mu^*$ along with the complementarity condition. In this case, one indeed recovers a purely sliding behaviour with $\dot{u}_N = 0$. However, there is no longer a potential associated with the above formulation, meaning that a problem including friction can no longer be formulated as a convex optimization problem. Instead, one ends up with a so-called *non-monotone second-order complementarity* problem which is inherently more difficult to solve than a convex SOCP problem. For more details on the numerous available strategies to deal with such 3D contact problems, we refer the reader to the extensive review by Acary et al. (2018). Let us just mention that some strategies might involve convexifying the problem by still retaining an associative optimization formulation or by using a fixed-point algorithm solving a sequence of SOCP problems.

## 4.3 Asymmetric behaviours

All of the previous primal and dual variational principles of linear elastostatics and elastodynamics can also be extended without any difficulty to more general settings, in particular when replacing the quadratic strain energy $\frac{1}{2}\boldsymbol{\varepsilon} : \mathbb{C} : \boldsymbol{\varepsilon}$ with a generic convex strain energy potential $\psi(\boldsymbol{\varepsilon})$ in (4.1). Similarly, the dual principle (4.6) can be extended by accounting for the corresponding conjugate stress energy potential $\psi^*(\boldsymbol{\sigma})$.

### 4.3.1 No-tension materials

One typical example consists of elastic materials which cannot sustain any tensile state due to their brittle behaviour in tension e.g. rocks, masonry, etc. Rather than modeling explicitly such a brittle behaviour, a simplified analysis of such materials relies on a constitutive model where zero stiffness is assumed for tensile states, leading to the so-called *no-tension material* behaviour. Note that the latter is non-dissipative and can be seen as an extension of the unilateral contact law to a 3D behaviour. The no-tension material model can be formulated using the following complementary elastic energy:

$$\psi^*(\boldsymbol{\sigma}) = \begin{cases} \frac{1}{2}\boldsymbol{\sigma} : \mathbb{C}^{-1} : \boldsymbol{\sigma} & \text{if } \boldsymbol{\sigma} \in \mathcal{K}_- \\ +\infty & \text{otherwise} \end{cases} \tag{4.34}$$

where $\mathcal{K}_-$ is a cone corresponding to "negative" stress states. There may exist different definitions of what "negative" means but authors generally rely on the cone of negative semi-definite stress states $\mathcal{K}_- = -\mathbb{S}^+$. In this case, "negative" means that all principal stresses are compressive only.

The corresponding stress-strain relation is then derived from the above potential as follows:

$$\boldsymbol{\varepsilon} \in \partial\psi^*(\boldsymbol{\sigma}) = \partial\psi^*_{\text{el}}(\boldsymbol{\sigma}) \oplus \partial\delta_{\mathcal{K}_-}(\boldsymbol{\sigma}) \tag{4.35}$$

$$= \{\mathbb{C}^{-1} : \boldsymbol{\sigma}\} \oplus \mathcal{K}_-^\circ \tag{4.36}$$

so that:

$$\boldsymbol{\varepsilon} = \boldsymbol{\varepsilon}_{\text{el}} + \boldsymbol{\varepsilon}_{\text{c}} \tag{4.37a}$$

$$\boldsymbol{\sigma} = \mathbb{C}\boldsymbol{\varepsilon}_{\text{el}} \tag{4.37b}$$

$$\boldsymbol{\varepsilon}_{\text{c}} \succcurlyeq 0, \quad \boldsymbol{\sigma} \preccurlyeq 0, \quad \boldsymbol{\sigma} : \boldsymbol{\varepsilon}_{\text{c}} = 0 \tag{4.37c}$$

which also corresponds to the primal strain energy potential:

$$\psi(\boldsymbol{\varepsilon}) = \inf_{\boldsymbol{\varepsilon}_{\text{el}}} \frac{1}{2}\boldsymbol{\varepsilon}_{\text{el}} : \mathbb{C} : \boldsymbol{\varepsilon}_{\text{el}} \quad \text{s.t.} \quad \boldsymbol{\varepsilon} \succcurlyeq \boldsymbol{\varepsilon}_{\text{el}} \tag{4.38}$$

which involves the *elastic* strain as an internal state variable which has to be optimized for.

As a result, the corresponding discrete problem yields a quadratic optimization problem with SDP constraints in 3D (SOCP in 2D). Again, this problem is highly non-smooth due to the abrupt change in behaviour between tension and compression.

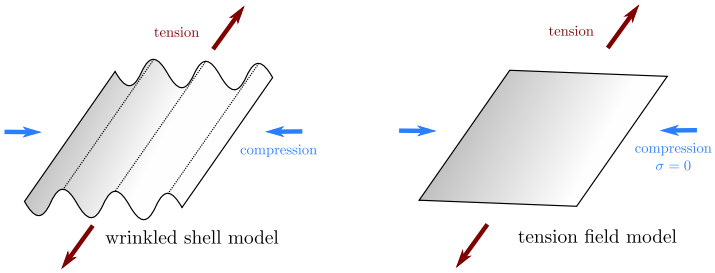


Figure 4.3: Left: wrinkled membrane model. Right: tension field membrane model.

### 4.3.2 Membranes

#### Non-convex variational principle

On a close topic, we consider the deformation of a thin hyperelastic membrane. In the finite-strain setting, the hyperelastic potential of a 3D material can be expressed as a function of some nonlinear strain measure such as the Cauchy-Green strain tensor $\boldsymbol{C} = \boldsymbol{F}^{\mathrm{T}}\boldsymbol{F}$ where $\boldsymbol{F} = \boldsymbol{I} + \nabla\boldsymbol{u}$ is the deformation gradient. The free energy hyperelastic potential is then $\psi(\boldsymbol{C})$ and the displacement field can be obtained as the solution to the following minimum principle:

$$\begin{aligned} \inf_{\boldsymbol{u},\boldsymbol{C}} \quad & \int_\Omega \psi(\boldsymbol{C})\,\mathrm{d}\Omega - \int_\Omega \boldsymbol{f}\cdot\boldsymbol{u}\,\mathrm{d}\Omega - \int_{\partial\Omega_{\mathrm{N}}} \boldsymbol{T}\cdot\boldsymbol{u}\,\mathrm{d}S \\ \text{s.t.} \quad & \boldsymbol{C} = \boldsymbol{I} + \nabla\boldsymbol{u} + \nabla\boldsymbol{u}^{\mathrm{T}} + \nabla\boldsymbol{u}^{\mathrm{T}}\nabla\boldsymbol{u} \\ & \boldsymbol{u} = 0 \text{ on } \partial\Omega_{\mathrm{D}} \end{aligned} \tag{4.39}$$

In the general case, such a problem is not convex which makes the analysis of hyperelastic materials rather complex. In particular, some equilibrium positions can be unstable and lead to buckling phenomena.

#### Tension field elastic membrane

As regards thin hyperelastic membranes, local buckling (or wrinkling) will occur at very low load levels in compressed regions, see Fig. 4.3. In the limit of infinitely thin membranes, compressed stress states cannot be supported at all. Tension field theory (Wagner, 1929; Reissner, 1938) has been proposed in order to simplify the analysis of thin membranes.

In the finite-deformation case, the tension-field theory has been first formalized by Pipkin (1994) by introducing a relaxed strain energy functional. More precisely, introducing the following convex relaxation of $\psi$:

$$\begin{aligned} \psi_{\mathrm{memb}}(\boldsymbol{C}) = \inf_{\boldsymbol{C}_{\mathrm{el}}} \quad & \psi(\boldsymbol{C}_{\mathrm{el}}) \\ \text{s.t.} \quad & \boldsymbol{C}_{\mathrm{el}} \succcurlyeq \boldsymbol{C} \end{aligned} \tag{4.40}$$

the tension field variational principle is obtained when replacing $\psi$ with $\psi_{\mathrm{memb}}$ in (4.39):

$$\begin{aligned} \inf_{\boldsymbol{u},\boldsymbol{C}_{\mathrm{el}}} \quad & \int_\Omega \psi(\boldsymbol{C}_{\mathrm{el}})\,\mathrm{d}\Omega - \int_\Omega \boldsymbol{f}\cdot\boldsymbol{u}\,\mathrm{d}\Omega - \int_{\partial\Omega_{\mathrm{N}}} \boldsymbol{T}\cdot\boldsymbol{u}\,\mathrm{d}S \\ \text{s.t.} \quad & \boldsymbol{C}_{\mathrm{el}} \succcurlyeq \boldsymbol{I} + \nabla\boldsymbol{u} + \nabla\boldsymbol{u}^{\mathrm{T}} + \nabla\boldsymbol{u}^{\mathrm{T}}\nabla\boldsymbol{u} \\ & \boldsymbol{u} = 0 \text{ on } \partial\Omega_{\mathrm{D}} \end{aligned} \tag{4.41}$$

The above relaxed potential then provides a tension-field constitutive equation in terms of the second Piola-Kirchhoff stress $\boldsymbol{S}$ as follows:

$$\boldsymbol{S} = 2\frac{\partial \psi}{\partial \boldsymbol{C}}(\boldsymbol{C}_{\text{el}}) \tag{4.42a}$$

$$\boldsymbol{C} = \boldsymbol{C}_{\text{el}} + \boldsymbol{C}_{\text{w}} \tag{4.42b}$$

$$\boldsymbol{C}_{\text{w}} \preccurlyeq 0, \quad \boldsymbol{S} \succcurlyeq 0, \quad \boldsymbol{S} : \boldsymbol{C}_{\text{w}} = 0 \tag{4.42c}$$

where $\boldsymbol{C}_{\text{w}}$ can be seen as an inelastic *wrinkling* strain accounting for the occurrence of wrinkles in compressed regions. As a consequence, the resulting stress is always tensile. Clearly, in the small-strain setting, the above formulation corresponds exactly to the case of a linear *no-compression material* as discussed in Section 4.3.1 for a linear no-tension material.

### Conic reformulation

Finally, Pipkin (1994) showed that when $\psi$ is a convex function of $\boldsymbol{C}$, $\psi_{\text{memb}}$ turns out to be a convex function of $\boldsymbol{F}$ or, equivalently, of the displacement gradient $\boldsymbol{G} = \nabla \boldsymbol{u}$. Indeed, if $\psi(\boldsymbol{C}_{\text{el}})$ is convex, the relaxed minimum principle (4.41) is a convex program due to the following conic reformulation of the SDP constraint (see also Kanno (2011)):

$$\boldsymbol{C}_{\text{el}} \succcurlyeq \boldsymbol{C} = \boldsymbol{I} + \boldsymbol{G} + \boldsymbol{G}^{\text{T}} + \boldsymbol{G}^{\text{T}}\boldsymbol{G} \tag{4.43}$$

Let us first recall the *Schur complement lemma* for a PSD block-matrix:

**Lemma 1.** *Let $\boldsymbol{Z}$ be a symmetric block-matrix*

$$\boldsymbol{Z} = \begin{bmatrix} \boldsymbol{U} & \boldsymbol{V} \\ \boldsymbol{V}^T & \boldsymbol{W} \end{bmatrix} \tag{4.44}$$

*in which $\boldsymbol{W} \succ 0$. Then $\boldsymbol{Z} \succcurlyeq 0$ if and only if $\boldsymbol{U} - \boldsymbol{V}\boldsymbol{W}^{-1}\boldsymbol{V}^T \succcurlyeq 0$.*

Let us then consider the following symmetric matrix:

$$\boldsymbol{Z} = \begin{bmatrix} \boldsymbol{C}_{\text{el}} & \boldsymbol{I} + \boldsymbol{G}^{\text{T}} \\ \boldsymbol{I} + \boldsymbol{G} & \boldsymbol{I} \end{bmatrix} \succcurlyeq 0 \tag{4.45}$$

we have $\boldsymbol{W} = \boldsymbol{I} \succ 0$ and $\boldsymbol{U} - \boldsymbol{V}\boldsymbol{W}^{-1}\boldsymbol{V}^{\text{T}} = \boldsymbol{C}_{\text{el}} - (\boldsymbol{I}+\boldsymbol{G}^{\text{T}})(\boldsymbol{I}+\boldsymbol{G}) = \boldsymbol{C}_{\text{el}} - \boldsymbol{I} - \boldsymbol{G} - \boldsymbol{G}^{\text{T}} - \boldsymbol{G}^{\text{T}}\boldsymbol{G} = \boldsymbol{C}_{\text{el}} - \boldsymbol{C}$. As a result, using the Schur complement lemma, $\boldsymbol{Z} \succcurlyeq 0$ if and only if $\boldsymbol{C}_{\text{el}} \succcurlyeq \boldsymbol{C}$.

In conclusion, if $\psi(\boldsymbol{C})$ admits a convex conic representation in terms of $\boldsymbol{C}$, problem (4.41) is a convex conic program. In Kanno (2011), only Saint-Venant-Kirchhoff materials were considered for which $\psi(\boldsymbol{C})$ is a quadratic function. In Bleyer (2022), we provided a conic formulation for more realistic hyperelastic models including an incompressible Ogden or neo-Hookean material.

### Annular square membrane deformation

By way of illustration, we consider a square annular membrane initially located in the $(Ox_1x_2)$ plane, embedded in $\mathbb{R}^3$. Its outer boundary of size $W_{\text{out}} = 50$ mm is fixed whereas the inner boundary, of size $W_{\text{in}} = 17.5$ mm, is subjected to an in-plane torsion of angle 90° and to an out-of-plane vertical displacement of amplitude $tW_{\text{out}}/2$ for $t = 0$ to $t = 1$. The variational problem (4.41) is discretized using linear triangular finite-elements and solved with Mosek interior point solver, see Chapter 5 for more details on the numerical toolchain.

(a) $t = 0.2$ (b) $t = 0.5$ (c) $t = 1$

Figure 4.4: Annular square deformed membrane at various loading steps. Blue regions denote wrinkled regions. Black arrows indicate principal stresses amplitude and orientation.

Fig. 4.4 reports different snapshots of the deformation and wrinkled state of the membrane. We can observe that initially a large inner region is in a wrinkled state due to compression induced by the torsion. At larger load steps, the wrinkled region extent tends to diminish due to the important tension exerted by the vertical displacement. In the last stage, the shape of the wrinkled regions is quite complex due to the combination of excessive shearing and elongation. The obtained wrinkled regions are quite similar to those obtained in de Rooij and Abdalla (2015) with a slightly different material model. Finally, let us remark that it was not necessary to subdivide the final loading into smaller load steps. Interior-point methods are known to be remarkably robust and quite insensitive to a good or bad initial guess of the solution. The final solution, as well as even more extremely deformed configurations for $t > 1$, could be obtained in only 20 iterations.

## 4.4 Plasticity-like behaviours

Numerical resolution of elastoplastic computations are commonly approached via an elastic predictor/plastic corrector approach embedded in a global Newton-Raphson procedure. *Return-mapping schemes* (Simo and Hughes, 2006) refer to the resolution of plasticity evolution equations at the local (material point level). Such a procedure can be shown to be equivalent to solving an inner local minimization problem with respect to plastic strain increments. Some recent works have proposed to rely on conic solvers for solving this local problem (Bruno et al., 2020). Obviously, global convergence of the Newton procedure is not guaranteed and one typically needs a good initial guess to achieve efficiency and robustness. Other approaches may include semi-smooth Newton methods (Christensen, 2002; Sander and Jaap, 2020), general interior-point methods (Krabbenhoft et al., 2007), sequential quadratic programming, (Bilotta et al., 2012), accelerated proximal gradient methods (Kanno, 2016), etc.

In this section, we discuss variational principles for problems involving a plastic-like behaviour. Let us first mention that variational principles for plasticity have first been given by Hill (1948) on the basis of the maximum dissipation principle and Maier (1968) was the first to propose primal and dual principles formulated as quadratic convex optimization programs.

### 4.4.1 Deformation theory of plasticity

Mathematical analysis of plasticity problems is often simplified by considering the so-called *deformation theory* of plasticity. Instead of considering the original history-dependent formulation of plasticity involving total strain and plastic strain rates, the deformation theory of plasticity can be seen as a nonlinear elasticity formulation involving a relation between total stress and total strains, ignoring history effects. For instance, for linear elasticity and perfect plasticity, a variational formulation can be obtained from:

$$\begin{array}{ll} \inf\limits_{\boldsymbol{u},\boldsymbol{\varepsilon}^{\mathrm{P}}} & \displaystyle\int_{\Omega} \psi(\boldsymbol{\varepsilon},\boldsymbol{\varepsilon}^{\mathrm{P}})\,\mathrm{d}\Omega - W_{\mathrm{ext}}(\boldsymbol{u}) \\ \text{s.t.} & \boldsymbol{\varepsilon} = \nabla^{s}\boldsymbol{u} \\ & \boldsymbol{u} = 0 \text{ on } \partial\Omega_{\mathrm{D}} \end{array} \tag{4.46}$$

where $W_{\mathrm{ext}}$ is the work of external loads and with the following non-linear potential:

$$\psi(\boldsymbol{\varepsilon},\boldsymbol{\varepsilon}^{\mathrm{P}}) = \frac{1}{2}(\boldsymbol{\varepsilon}-\boldsymbol{\varepsilon}^{\mathrm{P}}) : \mathbb{C} : (\boldsymbol{\varepsilon}-\boldsymbol{\varepsilon}^{\mathrm{P}}) + \pi_G(\boldsymbol{\varepsilon}^{\mathrm{P}}) \tag{4.47}$$

where $\pi_G$ is the support function of the elastic domain. For instance, for von Mises plasticity, the elastic domain is:

$$G = \left\{ \boldsymbol{\sigma} \text{ s.t. } \sqrt{\frac{3}{2}} \| \operatorname{dev}(\boldsymbol{\sigma}) \|_2 \leq \sigma_0 \right\} \tag{4.48}$$

and the support function is given by:

$$\pi_G(\boldsymbol{\varepsilon}^{\mathrm{P}}) = \begin{cases} \sqrt{\frac{2}{3}}\sigma_0 \| \boldsymbol{\varepsilon}^{\mathrm{P}} \|_2 & \text{if } \operatorname{tr} \boldsymbol{\varepsilon}^{\mathrm{P}} = 0 \\ +\infty & \text{otherwise} \end{cases} \tag{4.49}$$

The structural response is therefore no longer history-dependent. Such a theory provides useful results only in situations of proportional loadings and where no local elastic unloading occurs. A better variational treatment of elastoplasticity will be given later in Section 4.5. Finally, the dual variational problems involves the following conjugate potential:

$$\psi^*(\boldsymbol{\sigma}) = \frac{1}{2}\boldsymbol{\sigma} : \mathbb{C}^{-1} : \boldsymbol{\sigma} + \delta_G(\boldsymbol{\sigma}) \tag{4.50}$$

**Remark 4.** The formulation of no-tension materials discussed in Section 4.3.1 is equivalent to a deformation plasticity formulation with an elastic domain $G$ corresponding to pure compression stress states $\mathcal{K}_-$.

### 4.4.2 Limit analysis

Variational problems involving perfect plasticity behaviours generally possess a solution only if the loading level is sufficiently low. Indeed, above a certain *limit load*, no stable equilibrium complying with plastic yield conditions can be found. The computation of such a limit load is the purpose of *limit analysis* theory which can be formulated by adapting both variational problems.

Considering the primal formulation (4.46), a limit analysis formulation can be obtained by assuming a rigid elastic behaviour, enforcing $\boldsymbol{\varepsilon} = \boldsymbol{\varepsilon}^{\mathrm{P}}$. The resulting objective function involves only $\pi_G$ and the work of external loads. It is homogeneous of degree 1 so that

optimal solutions are determined up to a positive multiplicative constant. To fix such a constant, one generally considers the following normalized problem:

$$\begin{aligned} \lambda^+ = \min_{\boldsymbol{u}} \quad & \int_\Omega \pi_G(\boldsymbol{\varepsilon})\,\mathrm{d}\Omega \\ \text{s.t.} \quad & \boldsymbol{\varepsilon} = \nabla^s \boldsymbol{u} \\ & \boldsymbol{u} = 0 \text{ on } \partial\Omega_\mathrm{D} \\ & W_\mathrm{ext}(\boldsymbol{u}) = 1 \end{aligned} \tag{4.51}$$

which is the *kinematic (upper-bound)* formulation of limit analysis. Standard convex duality then shows that the dual reads:

$$\begin{aligned} \lambda^+ = \max_{\lambda,\boldsymbol{\sigma}} \quad & \lambda \\ \text{s.t.} \quad & \operatorname{div} \boldsymbol{\sigma} + \lambda \boldsymbol{f} = 0 \text{ in } \Omega \\ & \boldsymbol{\sigma}\boldsymbol{n} = \lambda \boldsymbol{T} \text{ on } \partial\Omega_\mathrm{N} \\ & \boldsymbol{\sigma} \in G \text{ in } \Omega \end{aligned} \tag{4.52}$$

where the load factor $\lambda$ appears as an additional scalar optimization variable. Problem (4.52) corresponds to the *static (lower-bound)* formulation of limit analysis. It amounts to finding the maximum load factor such that there exists a stress field $\boldsymbol{\sigma}$ in equilibrium with the scaled loading $(\lambda \boldsymbol{f}, \lambda \boldsymbol{T})$ and complying with the yield condition $\boldsymbol{\sigma} \in G$. Importantly, both problems (4.51) and (4.52) yield the same optimal value $\lambda^+$ corresponding to the structure limit load. The theorems of limit analysis state that the structure is safe if $\lambda < \lambda^+$ and will collapse if $\lambda > \lambda^+$. In this case, the optimal "displacement" $\boldsymbol{u}$ in (4.51) provides the corresponding plastic collapse mechanism.

Clearly, one main difference between all of the previous problems and those of limit analysis is that there is no quadratic (or strictly convex) objective function in the latter. The objective is homogeneous of degree 1 which makes its numerical resolution using Newton-like procedure extremely challenging. In fact, there is no notion of any constitutive relation anymore which reduces only to the fact that $\boldsymbol{\sigma}$ and $\boldsymbol{\varepsilon}$ must belong to convex sets and normal cones:

$$\boldsymbol{\sigma} \in \partial \pi_G(\boldsymbol{\varepsilon}) = G \quad \text{and} \quad \boldsymbol{\varepsilon} \in \partial \delta_G(\boldsymbol{\sigma}) = N_G(\boldsymbol{\sigma}) \tag{4.53}$$

This observation is one of the main reasons for which IPM solvers have been successfully used to solve numerical limit analysis problems. A more detailed presentation of limit analysis problems, their numerical resolution and applications is given in Chapter 5.

**Remark 5.** A very closely related theory to limit analysis is that of *shakedown analysis*. Shakedown analysis deals with cyclic loadings and consists in finding the maximum load level for which there exists an *elastic shakedown state*, i.e. an asymptotic elastic steady-state state. Above such a level, structures may undergo an asymptotic steady-state plastic cycle (*palstic shakedown*) or unbounded plastic evolution (*ratcheting*). Both cases can be detrimental to structural safety and it is therefore important to compute the structure elastic shakedown limit. Koiter and Melan theorems respectively correspond to the shakedown extension of the kinematic and static limit analysis theorems.

### 4.4.3 Viscoplastic fluids

If elastoplasticity can be seen as a mathematical middle ground between elasticity (quadratic potential) and limit analysis (homogeneous potential), another kind of middle ground is provided by *viscoplastic* or *yield stress* fluids. Indeed, such fluids behave like a standard Newtonian

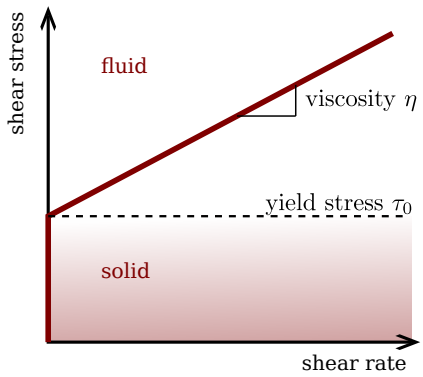


Figure 4.5: Rheological behaviour of a Bingham fluid

fluid only if the local stress reaches a critical threshold, the fluid *yield stress* $\tau_0$. If the stress is below $\tau_0$, the fluid behaves like a rigid solid. Such fluids occur in many industrial applications such as civil engineering (fresh concrete), petroleum or cosmetics (crude oil, toothpaste, foams, mayonnaise), natural hazards (lava, muds), etc. One of the most simple model to describe such fluids is the *Bingham* model which assumes a linear Newtonian behaviour, characterized by a viscosity $\eta$, above the yield stress, see Fig. 4.5. For recent reviews on yield stress fluids, we refer to Balmforth et al. (2014); Coussot (2016).

It can be shown that the solution velocity field $\boldsymbol{v}$ in steady-state conditions is given by the solution to:

$$\begin{aligned} \min_{\boldsymbol{v}} \quad & \int_\Omega \left( \eta \boldsymbol{d} : \boldsymbol{d} + \tau_0 \sqrt{2\boldsymbol{d} : \boldsymbol{d}} \right) \mathrm{d}\Omega \\ \text{s.t.} \quad & \boldsymbol{d} = \nabla^s \boldsymbol{v} \\ & \operatorname{div} \boldsymbol{v} = 0 \\ & \boldsymbol{v} = \boldsymbol{v}_\mathrm{D} \text{ on } \partial\Omega_\mathrm{D} \end{aligned} \tag{4.54}$$

where $\boldsymbol{d}$ is the strain rate tensor and $\boldsymbol{v}_\mathrm{D}$ denotes imposed velocities on the Dirichlet boundary. The objective function:

$$\phi(\boldsymbol{d}) = \eta \boldsymbol{d} : \boldsymbol{d} + \tau_0 \sqrt{2\boldsymbol{d} : \boldsymbol{d}} \tag{4.55}$$

indeed contains a quadratic viscous contribution and a homogeneous yield-stress contribution. Its subgradient provides the corresponding stress-strain rate relationship:

$$\boldsymbol{\sigma} \in \partial\phi(\boldsymbol{d}) = \{2\eta \boldsymbol{d}\} + G \tag{4.56}$$

where $G$ is the convex domain such that $\tau_0 \sqrt{2\boldsymbol{d} : \boldsymbol{d}}$ is its support function. We therefore see that:

$$\boldsymbol{\sigma} = 2\eta \boldsymbol{d} + \boldsymbol{\lambda} \tag{4.57}$$

where $\boldsymbol{\lambda}$ is an overstress verifying $\boldsymbol{\lambda} \in G$ and $\boldsymbol{d} \in N_G(\boldsymbol{\lambda})$. More precisely, we have:

$$G = \left\{ \boldsymbol{\lambda} \text{ s.t. } \sqrt{\frac{1}{2}\boldsymbol{\lambda} : \boldsymbol{\lambda}} \leq \tau_0 \right\} \tag{4.58a}$$

$$\sqrt{\frac{1}{2}\boldsymbol{\lambda} : \boldsymbol{\lambda}} < \tau_0 \Rightarrow \boldsymbol{d} = 0 \tag{4.58b}$$

$$\boldsymbol{d} \neq 0 \Rightarrow \boldsymbol{\lambda} = \sqrt{2}\tau_0 \frac{\boldsymbol{d}}{\|\boldsymbol{d}\|_2} \tag{4.58c}$$

Introducing a typical velocity $V$ and a typical length-scale $L$ for the problem, we can see that the above variational principle is characterized by a single non-dimensional number, the so-called *Bingham number* $\texttt{Bi} = \dfrac{\tau_0 L}{\eta V}$. This number measures the relative influence of yield stress compared to viscosity. For $\texttt{Bi} \gg 1$, the fluid behaves very much like a collapse mechanism in limit analysis. Conversely, $\texttt{Bi} \ll 1$, the fluid is close to being a classical Newtonian fluid since yield stress is very low so that flow occurs almost instantaneously. As hinted before, viscoplastic variational problems are another way of combining a quadratic behaviour (viscous term) with a homogeneous term (yield stress term). In this case, $\phi$ is the sum of both kinds of terms whereas the potential of elastoplastic behaviours is formed from the *inf-convolution* of similar terms.

Regarding their numerical simulation, viscoplastic fluids are very challenging because of the distinction between flowing and non flowing regimes. This non-smoothness in the expression of the constitutive relation necessitates to resort to more advanced techniques than those traditionally used for Newtonian fluids for instance. Regularized models have first been proposed to replace the non-smooth viscoplastic constitutive law by a smooth purely viscous model (Bercovier and Engelman, 1980; Papanastasiou, 1987). Augmented Lagrangian (AL) approaches have then emerged as an interesting alternative to the use of regularized models to solve viscoplastic fluid flows, it is now one of the most popular method to solve such problems (Fortin and Glowinski, 1982; Glowinski and Le Tallec, 1989; Saramito and Roquet, 2001; Dean et al., 2007; Glowinski and Wachs, 2011). However, it suffers from a slow convergence rate so that three-dimensional simulations are still extremely expensive. Recently, it has been pointed out that such AL schemes can be accelerated quite easily, yielding a faster convergence rate (Treskatis et al., 2016). For a review on the simulation of viscoplastic fluids and various extensions, we refer to Saramito and Wachs (2017) and references herein. In Bleyer et al. (2015c); Bleyer (2018a), we proposed to solve the corresponding variational problem using conic programming and IP solvers and demonstrated their computational advantages over AL algorithms.

As an illustration, we consider the classical lid-driven cavity problem where $\boldsymbol{v} = V\boldsymbol{e}_x$ is imposed on the top boundary with $\boldsymbol{v} = 0$ on the remaining boundary of square cavity. The solution is obtained from a custom IP solver written in FEniCS (see Bleyer (2017) for more details) using a quadratic discretization of the velocity field on triangular elements. Iso-stress contour lines and unyielded regions (in gray) are reported in Fig. 4.6. In particular, the location of such regions for different Bingham numbers is consistent with results from the literature, see for instance Syrakos et al. (2013); Treskatis et al. (2016).

## 4.5 Standard dissipative materials

We have seen that variational problems naturally describe the non-dissipative materials characterized by a free-energy potential $\psi(\boldsymbol{\varepsilon})$. The treatment of dissipative materials is more involved since we need to account both for energy and dissipation terms depending on *internal state variables*. Building upon the works of Ziegler (1963) and Moreau (1970) who introduced the notion of a pseudo-potential of dissipation, Halphen and Nguyen (1975) formalized such concepts more generally with the introduction of *Generalized Standard Materials* (GSM). Such a setting enables in particular to easily construct constitutive laws which automatically satisfy the principles of thermodynamics.

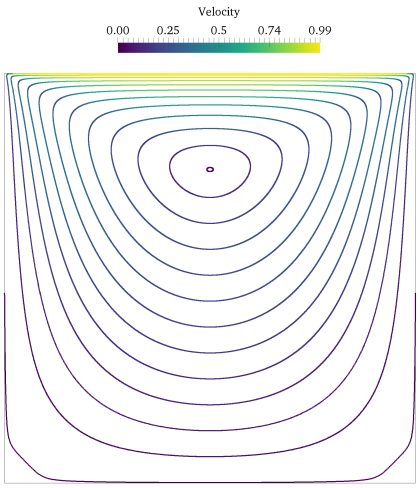


(a) `Bi` = 0

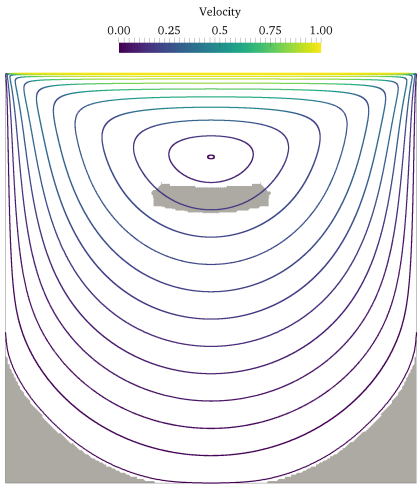


(b) `Bi` = 1

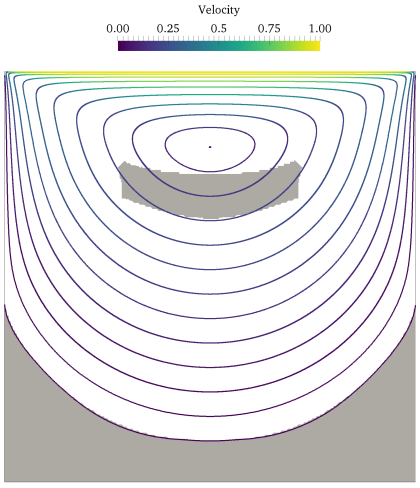


(c) `Bi` = 2

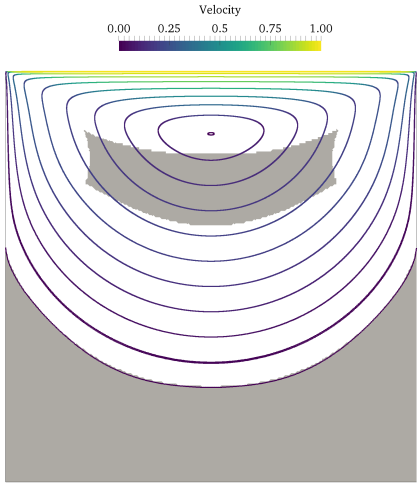


(d) `Bi` = 5

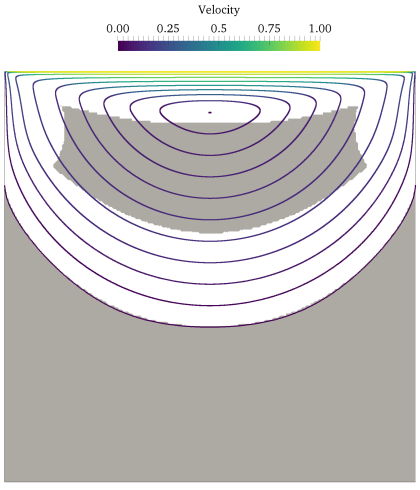


(e) `Bi` = 20

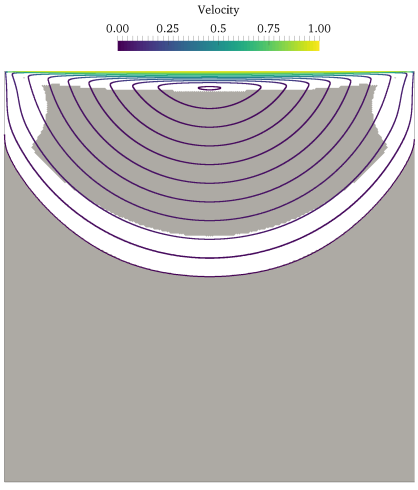


(f) `Bi` = 200

Figure 4.6: Velocity streamlines and unyielded elements (in gray) for the lid-driven cavity problem ($h = L/200$) with varying Bingham numbers. The bottom unyielded region is fixed whereas the central one rotates due to the surrounding moving fluid.

### 4.5.1 Generalized Standard Materials

Let us consider a material described by the total strain $\boldsymbol{\varepsilon}$ and a set of internal state variables $\boldsymbol{\alpha}$. The GSM framework postulates the existence of:

- a free energy density $\psi(\boldsymbol{\varepsilon}, \boldsymbol{\alpha})$
- a dissipation pseudo-potential $\phi(\dot{\boldsymbol{\varepsilon}}, \dot{\boldsymbol{\alpha}}; \boldsymbol{\alpha})$

In particular, the latter is assumed to be a *positive convex function* of the state variable rates $(\dot{\boldsymbol{\varepsilon}}, \dot{\boldsymbol{\alpha}})$. The semi column followed by $\boldsymbol{\alpha}$ means that it may also depend on the state itself.

In duality to internal state variables, there exist associated thermodynamic forces. The constitutive equations relating forces to state variables are obtained from the corresponding potentials:

$$\boldsymbol{\sigma} = \boldsymbol{\sigma}^{\mathrm{nd}} + \boldsymbol{\sigma}^{\mathrm{d}} \tag{4.59a}$$

$$0 = \boldsymbol{Y}^{\mathrm{nd}} + \boldsymbol{Y}^{\mathrm{d}} \tag{4.59b}$$

$$(\boldsymbol{\sigma}^{\mathrm{nd}}, \boldsymbol{Y}^{\mathrm{nd}}) \in \partial_{(\boldsymbol{\varepsilon},\boldsymbol{\alpha})}\psi(\boldsymbol{\varepsilon}, \boldsymbol{\alpha}) \tag{4.59c}$$

$$(\boldsymbol{\sigma}^{\mathrm{d}}, \boldsymbol{Y}^{\mathrm{d}}) \in \partial_{(\dot{\boldsymbol{\varepsilon}},\dot{\boldsymbol{\alpha}})}\phi(\dot{\boldsymbol{\varepsilon}}, \dot{\boldsymbol{\alpha}}; \boldsymbol{\alpha}) \tag{4.59d}$$

where the subscript $\star^{\mathrm{nd}}$ (resp. $\star^{\mathrm{d}}$) refers to a *non-dissipative* (resp. *dissipative*) quantity. Note that, in most cases, the free energy is a smooth function so that the subgradient often reduces to a classical differentiation whereas the pseudo-potential is often non-smooth in many applications. Moreover, the Young-Fenchel property (3.20) also provides the inverse constitutive relations using the corresponding conjugate potentials:

$$(\boldsymbol{\varepsilon}, \boldsymbol{\alpha}) \in \partial_{(\boldsymbol{\sigma}^{\mathrm{nd}},\boldsymbol{Y}^{\mathrm{nd}})}\psi^*(\boldsymbol{\sigma}^{\mathrm{nd}}, \boldsymbol{Y}^{\mathrm{nd}}) \tag{4.60a}$$

$$(\dot{\boldsymbol{\varepsilon}}, \dot{\boldsymbol{\alpha}}) \in \partial_{(\boldsymbol{\sigma}^{\mathrm{d}},\boldsymbol{Y}^{\mathrm{d}})}\phi^*(\boldsymbol{\sigma}^{\mathrm{d}}, \boldsymbol{Y}^{\mathrm{d}}; \boldsymbol{\alpha}) \tag{4.60b}$$

Finally, if equations (4.59) describe the constitutive relations for a generic GSM materials, we must mention two important specific cases. The first one is the case where the total strain $\boldsymbol{\varepsilon}$ is not considered as a dissipative variable e.g. (visco)elasticity, elasto(visco)plasticity, damage, etc. Then, $\boldsymbol{\sigma}^{\mathrm{d}} = 0$ and $\boldsymbol{\sigma} = \boldsymbol{\sigma}^{\mathrm{nd}}$. The second important case is that of *rate-independent* behaviours such as elastoplasticity, as opposed to elastoviscoplasticity for instance. Rate-independent cases are associated with a homogeneous dissipation pseudo-potential. This specific situation results in (4.59d) being an inclusion in a convex set and (4.60b) being an inclusion in the corresponding normal cone.

### 4.5.2 Primal incremental variational principle

In practice, solving the evolution of a GSM material is achieved using a time discretization scheme. Dividing the total interval into finite time intervals $[t_n; t_{n+1}]$, an approximate solution $(\boldsymbol{u}_{n+1}, \boldsymbol{\alpha}_{n+1})$ is computed based on the knowledge of the solution at the previous time step $(\boldsymbol{u}_n, \boldsymbol{\alpha}_n)$. There may exist different strategies for choosing a time discretization scheme. The most common strategy is to discretize in time the evolution equations (4.59), using a fully implicit Euler scheme or a $\theta$-scheme. The nonlinear resolution of the constitutive equations is then embedded into a global Newton-Raphson method solving for the system equilibrium. In some instances, the resulting time-discrete system may loose some structural properties of the original evolution equation, leading for instance to non-symmetric tangent operators.

Another approach relies on the formulation of an incremental variational principle over $[t_n, t_{n+1}]$ with increments of strains and internal state variables (Ortiz and Stainier, 1999; Miehe, 2002; Mielke, 2005; Maso et al., 2006).

**Definition 11** (Primal incremental variational problem)**.** The solution $(\boldsymbol{u}_{n+1}, \boldsymbol{\alpha}_{n+1})$ is computed from the resolution of the following incremental variational problem:

$$(\boldsymbol{u}_{n+1}, \boldsymbol{\alpha}_{n+1}) = \underset{\boldsymbol{u}\in\mathcal{U}_{\text{ad}},\boldsymbol{\alpha}}{\arg\min} \int_\Omega \left( \psi(\boldsymbol{\varepsilon}, \boldsymbol{\alpha}) + \Delta t \phi \left( \frac{\Delta \boldsymbol{\varepsilon}}{\Delta t}, \frac{\Delta \boldsymbol{\alpha}}{\Delta t}; \boldsymbol{\alpha}_{n+\theta} \right) \right) \mathrm{d}\Omega - W_{\text{ext},n+1}(\boldsymbol{u}) \tag{4.61}$$

The incremental variational problem (4.61) therefore amounts to solving for displacement and internal state variables increments by minimizing a potential which is parameterized by the previous state. We see that, even with convex $\psi$ and $\phi$, the resulting problem is not necessarily convex, owing to the dependence of the pseudo-dissipation potential to the state which has been evaluated at time $t_{n+\theta} = t_n + \theta\Delta t$ with $\theta \in [0;1]$. Choosing $\theta = 0$ for this term leads to a semi-implicit scheme which restores the original convexity. In the following, we will assume for simplicity that the dissipation potential does not depend on the state, unless otherwise stated. As a result, the incremental problem can also be formally written in a more compact form as:

$$\boldsymbol{u}_{n+1} = \underset{\boldsymbol{u}\in\mathcal{U}_{\text{ad}}}{\arg\min}\, J(\boldsymbol{\varepsilon}; \boldsymbol{\varepsilon}_n, \boldsymbol{\alpha}_n) - W_{\text{ext},n+1}(\boldsymbol{u}) \tag{4.62}$$

$$\text{where } J(\boldsymbol{\varepsilon}; \boldsymbol{\varepsilon}_n, \boldsymbol{\alpha}_n) = \int_\Omega j(\boldsymbol{\varepsilon}; \boldsymbol{\varepsilon}_n, \boldsymbol{\alpha}_n)\, \mathrm{d}\Omega \tag{4.63}$$

$$j(\boldsymbol{\varepsilon}; \boldsymbol{\varepsilon}_n, \boldsymbol{\alpha}_n) = \min_{\boldsymbol{\alpha}} \psi(\boldsymbol{\varepsilon}, \boldsymbol{\alpha}) + \Delta t \phi \left( \frac{\boldsymbol{\varepsilon} - \boldsymbol{\varepsilon}_n}{\Delta t}, \frac{\boldsymbol{\alpha} - \boldsymbol{\alpha}_n}{\Delta t} \right) \tag{4.64}$$

where $J$ can be seen as an incremental global potential and $j$ is the associated volume density. The latter is obtained through an implicit minimization over the state variables $\boldsymbol{\alpha}$ as a function of the observable state variable $\boldsymbol{\varepsilon}$. Both of them are parameterized by the values $(\boldsymbol{\varepsilon}_n, \boldsymbol{\alpha}_n)$ of the state variables at the previous time step. The final variational problem is therefore very similar to a non-linear elastic principle such as (4.1) except that the potential changes at each increment. The optimality condition:

$$\boldsymbol{\sigma} \in \partial j(\boldsymbol{\varepsilon}; \boldsymbol{\varepsilon}_n, \boldsymbol{\alpha}_n) \tag{4.65}$$

represents the final stress/strain relation where internal state variables are implicitly solved for in the partial minimization. Akin to variational time integrators, using such variational formulations of constitutive relation updates (Ortiz and Stainier, 1999; Heuzé and Stainier, 2022) enables to preserve properties of the underlying variational structure, such as symmetries of the tangent operator for instance.

**Remark 6.** The discrete evolution $[0;T]$ involves a sequential resolution of problems (4.61) since each problem relies on the previous solution. There have been attempts to solve for the whole evolution curve on a given time interval $[0;T]$ in a single computation. For instance, Mielke and Ortiz (2008) proposed a single variational principle based on a weighted sum of each incremental contribution. The corresponding Pareto weights are exponentially decaying in time in order to preferentially solve the first, then the second incremental problem and so on. Unfortunately, such a construction yields an extremely poorly conditioned optimization problem which cannot be solved numerically in an efficient manner. The Brezis-Ekeland-Nayrolle principle has also been applied to the case of standard plasticity (Buliga and de Saxcé, 2017; Cao et al., 2020), resulting in a two-field variational problem involving the stress and the displacement. The latter is however not *jointly convex* with respect to both stress and displacement which makes its numerical resolution for large scale problems more difficult.

### 4.5.3 Dual incremental variational principle

To our knowledge, we did not find in the literature any derivation of the dual problem to (4.61) in the general case. The latter involves stresses and thermodynamic forces rather than strain and internal variables as primary unknowns. Considering $\boldsymbol{u}_{\mathrm{D}} = 0$ for simplicity, it reads:

**Definition 12** (Dual incremental variational problem)**.** The solution $(\boldsymbol{\sigma}_{n+1}, \boldsymbol{Y}_{n+1})$ is computed from the resolution of the following incremental variational problem:

$$
\begin{aligned}
(\boldsymbol{\sigma}_{n+1}, \boldsymbol{Y}_{n+1}) = \underset{\boldsymbol{\sigma},\boldsymbol{Y},\boldsymbol{\sigma}^{\mathrm{nd}},\boldsymbol{\sigma}^{\mathrm{d}},\boldsymbol{Y}^{\mathrm{nd}},\boldsymbol{Y}^{\mathrm{d}}}{\arg\min} \quad & \int_\Omega \left( \psi^*(\boldsymbol{\sigma}^{\mathrm{nd}}, \boldsymbol{Y}^{\mathrm{nd}}) + \Delta t \phi^*(\boldsymbol{\sigma}^{\mathrm{d}}, \boldsymbol{Y}^{\mathrm{d}}) + \boldsymbol{\sigma}^{\mathrm{d}} : \boldsymbol{\varepsilon}_n + \boldsymbol{Y}^{\mathrm{d}} \boldsymbol{\alpha}_n \right) \mathrm{d}\Omega \\
\text{s.t.} \quad & \operatorname{div} \boldsymbol{\sigma} + \boldsymbol{f}_{n+1} = 0 \quad \text{in } \Omega \\
& \boldsymbol{\sigma}\boldsymbol{n} = \boldsymbol{T}_{n+1} \quad \text{on } \partial\Omega_{\mathrm{N}} \\
& \boldsymbol{\sigma} = \boldsymbol{\sigma}^{\mathrm{nd}} + \boldsymbol{\sigma}^{\mathrm{d}} \\
& 0 = \boldsymbol{Y}^{\mathrm{nd}} + \boldsymbol{Y}^{\mathrm{d}}
\end{aligned}
\tag{4.66}
$$

In the case where $\boldsymbol{\varepsilon}$ is not considered to be a dissipative variable, it reduces to:

$$
\begin{aligned}
(\boldsymbol{\sigma}_{n+1}, \boldsymbol{Y}_{n+1}) = \underset{\boldsymbol{\sigma},\boldsymbol{Y}}{\arg\min} \quad & \int_\Omega \left( \psi^*(\boldsymbol{\sigma}, -\boldsymbol{Y}) + \Delta t \phi^*(\boldsymbol{Y}) + \boldsymbol{Y} \boldsymbol{\alpha}_n \right) \mathrm{d}\Omega \\
\text{s.t.} \quad & \operatorname{div} \boldsymbol{\sigma} + \boldsymbol{f}_{n+1} = 0 \quad \text{in } \Omega \\
& \boldsymbol{\sigma}\boldsymbol{n} = \boldsymbol{T}_{n+1} \quad \text{on } \partial\Omega_{\mathrm{N}}
\end{aligned}
\tag{4.67}
$$

where we introduced $\boldsymbol{Y} = \boldsymbol{Y}^{\mathrm{d}} = -\boldsymbol{Y}^{\mathrm{nd}}$. This expression is consistent with the one derived by De Angelis and Cancellara (2017) in the viscoplastic case.

**Remark 7.** In the case of rate-independent materials, $\phi$ is a homogeneous function so that (4.61) simplifies as:

$$
(\boldsymbol{u}_{n+1}, \boldsymbol{\alpha}_{n+1}) = \underset{\boldsymbol{u} \in \mathcal{U}_{\mathrm{ad}}, \boldsymbol{\alpha}}{\arg\min} \int_\Omega \left( \psi(\boldsymbol{\varepsilon}, \boldsymbol{\alpha}) + \phi\left(\boldsymbol{\alpha} - \boldsymbol{\alpha}_n\right) \right) \mathrm{d}\Omega - W_{\mathrm{ext},n+1}(\boldsymbol{u}) \tag{4.68}
$$

This results in $\phi^*$ being the indicator of some convex set $G$ and (4.67) reduces to:

$$
\begin{aligned}
(\boldsymbol{\sigma}_{n+1}, \boldsymbol{Y}_{n+1}) = \underset{\boldsymbol{\sigma},\boldsymbol{Y}}{\arg\min} \quad & \int_\Omega \left( \psi^*(\boldsymbol{\sigma}, -\boldsymbol{Y}) + \boldsymbol{Y} \boldsymbol{\alpha}_n \right) \mathrm{d}\Omega \\
\text{s.t.} \quad & \operatorname{div} \boldsymbol{\sigma} + \boldsymbol{f}_{n+1} = 0 \quad \text{in } \Omega \\
& \boldsymbol{\sigma}\boldsymbol{n} = \boldsymbol{T}_{n+1} \quad \text{on } \partial\Omega_{\mathrm{N}} \\
& \boldsymbol{Y} \in G \quad \text{in } \Omega
\end{aligned}
\tag{4.69}
$$

## 4.6 Application to elasto-plastic problems

### 4.6.1 Illustration on von Mises plasticity with isotropic hardening

As an illustration of the previous principles, let us consider here the specific case of an elastoplastic material with isotropic non-linear hardening. The state variables are the plastic strain $\boldsymbol{\varepsilon}^{\mathrm{p}}$ and the cumulated equivalent plastic strain $p$. The Helmholtz free energy is composed of an elastic term and a hardening term:

$$
\psi(\boldsymbol{\varepsilon}, \boldsymbol{\varepsilon}^{\mathrm{p}}, p) = \psi_{\mathrm{el}}(\boldsymbol{\varepsilon} - \boldsymbol{\varepsilon}^{\mathrm{p}}) + \psi_{\mathrm{h}}(p) \tag{4.70}
$$

We consider a von Mises yield criterion of uniaxial strength $\sigma_0$ such that the dissipation potential is given by:

$$\phi(\dot{\boldsymbol{\varepsilon}}^{\mathrm{p}}, \dot{p}) = \begin{cases} \sigma_0 \sqrt{\frac{2}{3}} \| \dot{\boldsymbol{\varepsilon}}^{\mathrm{p}} \| & \text{if } \operatorname{tr}(\dot{\boldsymbol{\varepsilon}}^{\mathrm{p}}) = 0 \\ +\infty & \text{otherwise} \end{cases} \tag{4.71}$$

In addition, we should also define the link between the cumulated plastic strain and the plastic strain tensor: $\sqrt{\frac{2}{3}} \| \dot{\boldsymbol{\varepsilon}}^{\mathrm{p}} \| = \dot{p}$. However, this constraint cannot be enforced as such in the definition of $\phi$ since it is not a convex constraint. Nevertheless, we can use the epigraph form of $\sigma_0 \sqrt{\frac{2}{3}} \| \dot{\boldsymbol{\varepsilon}}^{\mathrm{p}} \|$ to naturally introduce the link with $\dot{p}$ while preserving convexity as follows:

$$\phi(\dot{\boldsymbol{\varepsilon}}^{\mathrm{p}}, \dot{p}) = \begin{cases} \sigma_0 \dot{p} & \text{if } \operatorname{tr}(\dot{\boldsymbol{\varepsilon}}^{\mathrm{p}}) = 0 \,;\, \sqrt{\frac{2}{3}} \| \dot{\boldsymbol{\varepsilon}}^{\mathrm{p}} \| \leq \dot{p} \\ +\infty & \text{otherwise} \end{cases} \tag{4.72}$$

Let us denote by $\boldsymbol{Y}_{\boldsymbol{\varepsilon}^{\mathrm{p}}}$ and $Y_p$ the corresponding thermodynamic forces. The dual pseudo-potential is given by:

$$\phi^*(\boldsymbol{Y}_{\boldsymbol{\varepsilon}^{\mathrm{p}}}, Y_p) = \begin{cases} 0 & \text{if } \sqrt{\frac{3}{2}} \| \operatorname{dev}(\boldsymbol{Y}_{\boldsymbol{\varepsilon}^{\mathrm{p}}}) \| + Y_p \leq \sigma_0 \\ +\infty & \text{otherwise} \end{cases} . \tag{4.73}$$

The dual Gibbs free energy is given by:

$$\psi^*(\boldsymbol{\sigma}, -\boldsymbol{Y}_{\boldsymbol{\varepsilon}^{\mathrm{p}}}, -Y_p) = \begin{cases} \psi^*_{\mathrm{el}}(\boldsymbol{\sigma}) + \psi^*_h(-Y_p) & \text{if } \boldsymbol{\sigma} = \boldsymbol{Y}_{\boldsymbol{\varepsilon}^{\mathrm{p}}} \\ +\infty & \text{otherwise} \end{cases} \tag{4.74}$$

Later, we will use $R = -Y_p \in \psi_{\mathrm{h}}(p)$ to denote the hardening force.

The primal variational principle (4.68) writes:

$$\begin{aligned} (\boldsymbol{u}_{n+1}, \boldsymbol{\varepsilon}^{\mathrm{p}}_{n+1}, p_{n+1}) = \underset{\boldsymbol{u} \in \mathcal{U}_{\mathrm{ad}}, \boldsymbol{\varepsilon}^{\mathrm{p}}, p}{\arg\min} \quad & \int_\Omega \left( \frac{1}{2} (\boldsymbol{\varepsilon} - \boldsymbol{\varepsilon}^{\mathrm{p}}) : \mathbb{C} : (\boldsymbol{\varepsilon} - \boldsymbol{\varepsilon}^{\mathrm{p}}) + \psi_{\mathrm{h}}(p) + \sigma_0 (p - p_n) \right) \mathrm{d}\Omega - W_{\mathrm{ext},n+1}(\boldsymbol{u}) \\ \text{s.t.} \quad & \operatorname{tr}(\boldsymbol{\varepsilon}^{\mathrm{p}}) = 0 \quad \text{in } \Omega \\ & \sqrt{\tfrac{2}{3}} \| \boldsymbol{\varepsilon}^{\mathrm{p}} - \boldsymbol{\varepsilon}^{\mathrm{p}}_n \| \leq p - p_n \quad \text{in } \Omega \end{aligned} \tag{4.75}$$

The dual variational principle (4.69) writes:

$$\begin{aligned} \boldsymbol{\sigma}_{n+1}, R_{n+1} = \underset{\boldsymbol{\sigma}, R}{\arg\min} \quad & \int_\Omega \left( \frac{1}{2} \boldsymbol{\sigma} : \mathbb{C}^{-1} : \boldsymbol{\sigma} + \psi^*_{\mathrm{h}}(R) - \boldsymbol{\sigma} : (\boldsymbol{\varepsilon}_n - \boldsymbol{\varepsilon}^{\mathrm{p}}_n) - R p_n \right) \mathrm{d}\Omega \\ \text{s.t.} \quad & \operatorname{div} \boldsymbol{\sigma} + \boldsymbol{f}_{n+1} = 0 \quad \text{in } \Omega \\ & \boldsymbol{\sigma} \boldsymbol{n} = \boldsymbol{T}_{n+1} \quad \text{on } \partial\Omega_{\mathrm{N}} \\ & \sqrt{\tfrac{3}{2}} \| \operatorname{dev}(\boldsymbol{\sigma}) \| \leq \sigma_0 + R \quad \text{in } \Omega \end{aligned} \tag{4.76}$$

Note that since $\boldsymbol{\sigma}_n, R_n$ and $\boldsymbol{\sigma}_{n+1}, R_{n+1}$ both satisfy the plastic yield criterion, it will also be satisfied for any linear time interpolation between $\boldsymbol{\sigma}_n, R_n$ and $\boldsymbol{\sigma}_{n+1}, R_{n+1}$ between times $t_n$ and $t_{n+1}$ owing to the convexity of the yield surface.

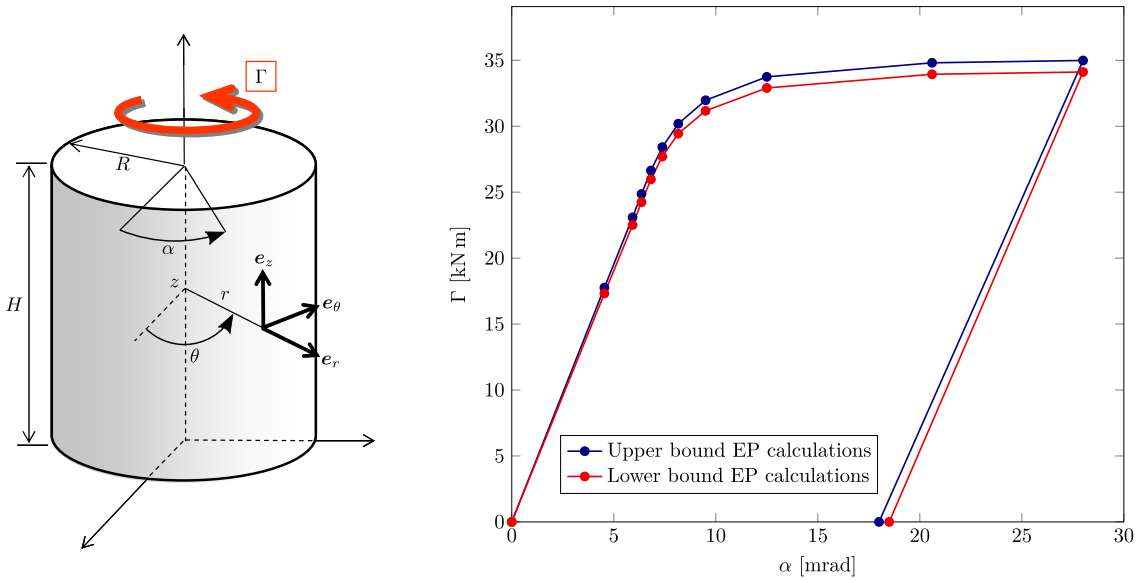


(a) Problem setting

(b) Torsion moment/rotation angle elastoplastic curve

Figure 4.7: Primal/dual FE computations for the torsion of an elastoplastic cylinder, taken from (El Boustani, 2020)

### 4.6.2 Primal-dual FE discretizations

Note that both problems (4.75) and (4.76) are SOC constrained convex optimization problems. In the linear hardening case, the objective will be quadratic. Similarly to the elastic case in (4.8), both optimal values are opposite for the true elastoplastic solution. When restricting both minimum problems to finite-dimensional subspace obtained from a displacement or stress-based finite-element discretization for instance, both objective functions will differ. With carefully selected spatial discretization, a displacement-based discretization (upper bound scheme) will yield a stiffer response in the elastic regime and a larger limit load in at plastic collapse. Conversely, an equilibrium stress-based discretization (lower bound scheme) will yield a softer response and a smaller plastic collapse limit load. This is illustrated in Fig. 4.7 which corresponds to the torsion moment/rotation angle curve of a 3D cylinder using both kinds of FE discretization schemes. The primal-dual gap between both discretizations can be used as an error indicator with respect to the true solution and can be used in an adpative mesh refinement procedure for instance, see (El Boustani et al., 2020b).

### 4.6.3 Large load steps computations

We consider a 2D rectangular domain fixed on both lateral extremities and subjected to a uniform downwards vertical body force $\boldsymbol{f} = -f\boldsymbol{e}_y$ in a plane strain setting. We use a Voce-type exponential hardening law:

$$\psi_{\mathrm{h}}(p) = (\sigma_u - \sigma_0)\left(p + \frac{1}{\omega}\exp(-\omega p)\right) \tag{4.77a}$$

$$R(p) = \frac{\partial \psi_{\mathrm{h}}}{\partial p} = (\sigma_u - \sigma_0)(1 - \exp(-\omega p)) \tag{4.77b}$$

where $\sigma_0$ (resp. $\sigma_u$) is the initial (resp. ultimate) yield strength and $\omega$ a saturation parameter. We set $E = 210\,\mathrm{GPa}$, $\nu = 0.3$, $\sigma_0 = 450\,\mathrm{MPa}$, $\sigma_u = 700\,\mathrm{MPa}$ and $\omega = 50$. Fig. 4.8 shows the

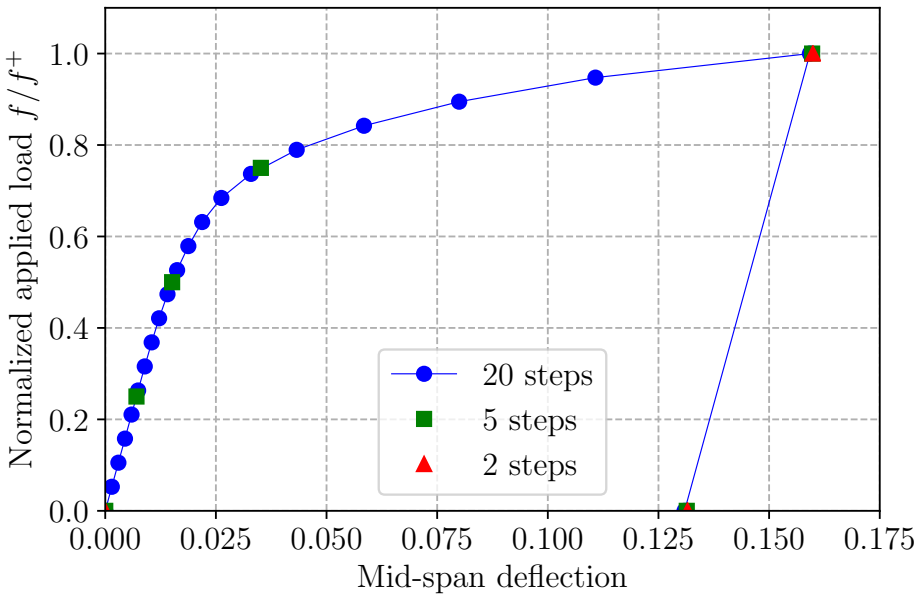


Figure 4.8: Load-deflection evolution depending on the total number of load increments (only one used in the unloading phase).

load-displacement curve using different numbers of load steps. Interestingly, the computed displacement at the ultimate state near collapse ($f = f^+$) is already very accurate using a single load step, see also (Krabbenhoft et al., 2007; El Boustani et al., 2020b). Each resolution with Mosek v.9.0 took between 2.5 and 3.5 seconds (10 to 18 IP iterations) depending on the loading step (fully plastic steps near $f = f^+$ took a larger number of iterations than initial elastic steps). Even when refining the mesh size, we found that the number of required iterations remained very similar. This indicates that the IP solver exhibits a very robust behaviour in terms of number of iterations with respect to the problem size. Similarly, solver robustness does not seem to be affected by the load step amplitude since the number of IP iterations remains very similar.

Although not being fully competitive against standard Newton methods in multi-step plasticity for this specific von Mises plasticity behaviour, the conic programming approach becomes interesting when much larger load steps are considered. It becomes even more interesting when dealing with non-smooth yield surfaces such as Tresca, Mohr-Coulomb, Rankine, etc. for which projection onto the yield surface might be troublesome in standard return mapping procedures. For such yield surfaces, non-smoothness is naturally included in the underlying conic formulation (Bisbos and Pardalos, 2007) and readily tackled by the corresponding solvers.

### 4.6.4 Extension to finite-strain elastoplasticity

In El Boustani et al. (2020c), we extended the use of interior-point algorithms to conic programs involving either smooth but non-convex or non-smooth but convex objectives or constraints. A typical application for such kind of problems is finite-strain elastoplasticity. We addressed such problems using the logarithmic strain framework proposed in Miehe et al. (2002) which has been shown to be well suited for describing finite-strain metal plasticity. In

this framework, the chosen total strain measure is the Hencky logarithmic strain:

$$\boldsymbol{E} = \frac{1}{2}\log(\boldsymbol{F}^T\boldsymbol{F}) \tag{4.78}$$

where $\boldsymbol{F} = \boldsymbol{I} + \nabla\boldsymbol{u}$ is the deformation gradient.

An attractive feature of using logarithmic strain measures is that classical small strain constitutive relations can be naturally extended to a finite-strain setting. In particular, the total (Hencky) strain can be split additively into an elastic and plastic contributions:

$$\boldsymbol{E} = \boldsymbol{E}^{\mathrm{el}} + \boldsymbol{E}^{\mathrm{p}} \tag{4.79}$$

Small-strain constitutive relations are then formulated in terms of $\boldsymbol{E}^{\mathrm{el}}$ and $\boldsymbol{E}^{\mathrm{p}}$.

A variational principle close to (4.39) and (4.68) describes the incremental evolution of such a system as follows:

$$\begin{aligned}(\boldsymbol{u}_{n+1}, \boldsymbol{E}^{\mathrm{p}}_{n+1}, p_{n+1}) = \underset{\boldsymbol{u}\in\mathcal{U}_{\mathrm{ad}}, \boldsymbol{E}^{\mathrm{p}}, p}{\arg\min} \quad & \int_\Omega \left(\psi(\boldsymbol{E} - \boldsymbol{E}^{\mathrm{p}}) + \psi_{\mathrm{h}}(p) + \phi\left(\boldsymbol{E}^{\mathrm{p}} - \boldsymbol{E}^{\mathrm{p}}_n, p - p_n\right)\right) \mathrm{d}\Omega - W_{\mathrm{ext},n+1}(\boldsymbol{u}) \\ \text{s.t.} \quad & \boldsymbol{E} = \frac{1}{2}\log(\boldsymbol{F}^T\boldsymbol{F})\end{aligned} \tag{4.80}$$

where the elastic and hardening potentials $\psi_{\mathrm{el}}$ and $\psi_{\mathrm{h}}$ as well as the dissipation pseudo-potential $\phi$ are the convex potentials associated with a given small-strain behaviour, such as that in Section 4.6.1 for instance. As a result, problem (4.80) is non-convex only because of the non-convex constraint (4.78) defining the Hencky strain measure. The remaining terms, in particular the plastic dissipation, are still convex in the auxiliary variables $\boldsymbol{E}^{\mathrm{p}}, p$.

Problem (4.80) has been solved with a custom IPM capable of handling non-convex but smooth objectives or constraints. Obviously, proofs of convergence of the IPM algorithm will necessarily be lost in the non-convex case. However, our heuristic reasoning is that we will restrict to a case in which difficulties will be decoupled. On the one hand, non-smoothness is present only in conic constraints which we still consider to be convex (plastic dissipation), while, on the other hand, non-convexity concerns only terms which are smooth (stress-strain relation). Since the IPM can be seen as a Newton method with continuation along the so-called *central path*, we hope that smooth terms will be properly handled by the Newton method and that continuation along the central path will sill handle properly the non-smooth but convex conic constraints. Our proposed algorithm is therefore a simple extension of a classical IPM to the previously mentioned non-convex case.

As an illustration, we consider a fully clamped rectangular beam of length $L = 2.0\,\mathrm{m}$ oriented in direction $x$ and of height $h = 0.1\,\mathrm{m}$ and width $b = 0.04\,\mathrm{m}$. The beam consists of steel material (von Mises perfect plasticity, $\sigma_0 = 250$ MPa) and is subject to a uniformly distributed body force $\boldsymbol{f} = -f\boldsymbol{e}_z$.

The present implementation results have been compared with computations using the commercial finite-element software Abaqus (Smith, 2009) and also using the open-source finite-element platform FEniCS (Logg and Wells, 2010; Logg et al., 2012; Alnæs et al., 2015) coupled with MFront (Helfer et al., 2020) for the constitutive behaviour integration.

The FEniCS/MFront implementation consists in a total-Lagrangian implementation of logarithmic plasticity using a standard Newton-Raphson/return mapping procedure. The coupling between both libraries relies on the `MFrontGenericInterfaceSupport` project (Helfer et al., 2020).

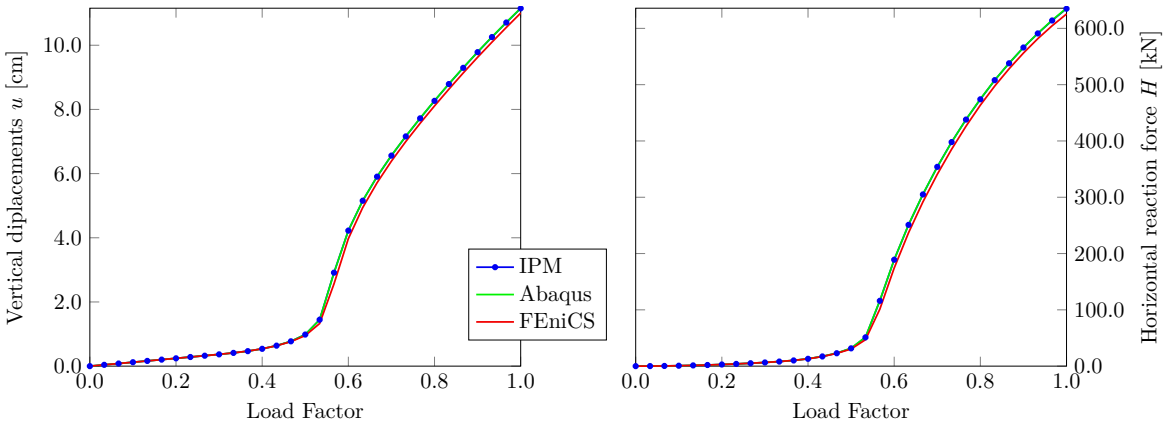


Figure 4.9: Evolution of the mid-span deflection $u$ and the horizontal support reaction $H$

Table 4.1: Total number of iterations for the different methods and load-stepping

| Method | Total iterations |
|---|---|
| FEniCS (30 steps) | 128 |
| IPM (30 steps) | 385 |
| IPM (15 steps) | 192 |
| IPM (5 steps) | 70 |

The Abaqus implementation relies on an updated-Lagrangian formulation using the Cauchy stress tensor and its work-conjugate rate of deformation. The integration technique for the total deformation gives the logarithmic strains (LE in Abaqus notation) which is used in the case of metal plasticity.

We monitor the evolution of the mid-span deflection $u$ and the horizontal support reaction $H$ when increasing the body force up to $f = 50\,\mathrm{MN/m^3}$. The evolutions of $u$ and $H$ have been represented in Fig. 4.9. It can first be observed that all three different implementations yield very similar results, the slight difference observed with respect to the FEniCS/MFront computations can be attributed to the fact that a different mesh, although of similar element size, was used. The obtained results clearly exhibit a first elastic then plastic stage (for a load factor below 0.5) when geometrical non-linear effects do not play an important role. A secondary stiffening stage (for load factor larger than 0.5) is then observed due to membrane catenary effect (see the increase of the horizontal reaction force) when geometrical non-linear effects become more and more important.

In order to assess the numerical solution procedure, we will compare the FEniCS solution with the proposed IPM solution since both approaches rely on a total-Lagrangian formulation. In particular, we compared the number of iterations per load step to reach convergence using the same relative residual tolerance. It must be recalled that, apart from the way boundary conditions are handled, the linear system size, and hence the cost per iteration, is similar for both methods.

Results are reported in Fig. 4.10 where it can be observed that the required number of iterations is much larger for the IPM than for the Newton method used in FEniCS for 30 load steps. This is by no means surprising due to the quadratic convergence of the Newton method close to a solution. It can also be observed that the required number of iterations increases in the second stage of the problem where plasticity and geometrically non-linear effects become much more dominant.

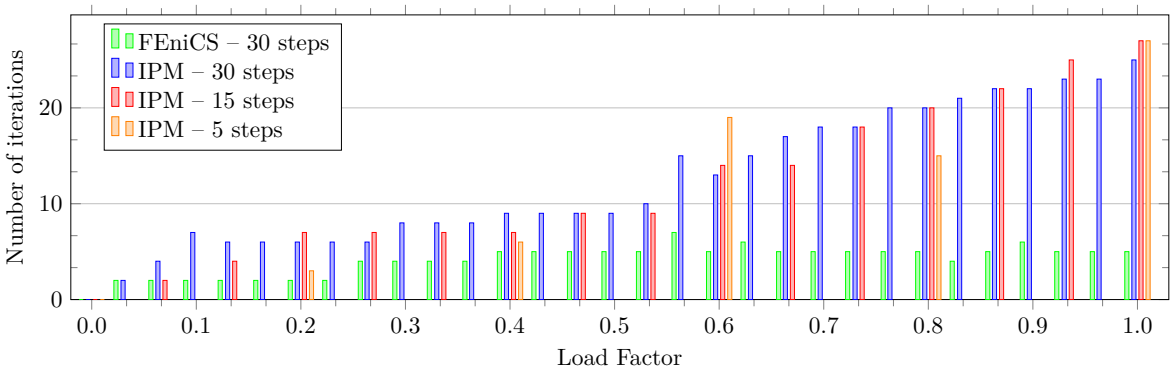


Figure 4.10: Number of iterations per load step

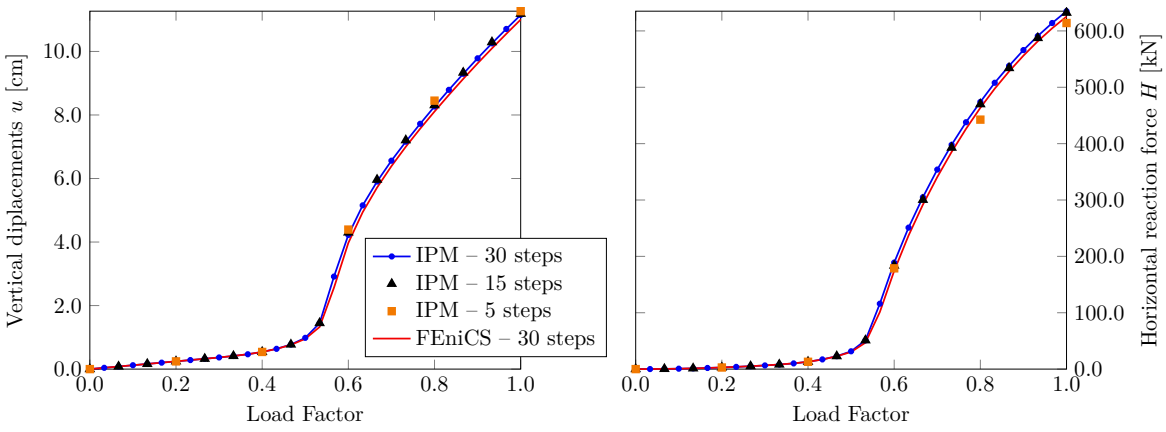


Figure 4.11: Comparison of the evolution of the mid-span deflection $u$ and the horizontal support reaction $H$ using 5 load steps

However, an extremely interesting feature of the IPM is its robustness over large load steps. Indeed, the Newton method was unable to converge with less than 20 load steps whereas the IPM method could converge using only 5 load steps. Besides, this robustness does not seem to deteriorate the convergence quality since roughly the same number of iterations is required for the same load level when using smaller load steps (see again Fig. 4.10). Overall, the total number of iterations (Table 4.1) using 5 load steps becomes competitive compared with the Newton method, whereas the Newton method is more efficient than the IPM with similar load-stepping. Moreover, Fig. 4.11 clearly shows that using fewer load steps yields similar values for the displacement and reaction forces.

## 4.7 Closing remarks

This chapter has shown that many problems in nonlinear mechanics enjoy a variational formulation which can be tackled using conic programming formulations. In particular, incremental variational principles of standard dissipative media offer a very generic framework for formulating thermodynamically consistent behaviours and working on the underlying variational evolution principles. Moreover, we have also seen that some finite-strain behaviours such as membranes can be formulated using convex principles. Obviously, in the general case, it is expected that finite-strain problems will remain non-convex.

On the numerical side, we have evidenced that IP solvers can deal without any problem with highly non-smooth behaviours as well as very large load steps without hindering convergence robustness, as opposed to Newton methods for instance. This can be further understood from the fact that considering large load steps does not fundamentally change the structure of the corresponding problem. Appendix B indeed investigates the behaviour of the primal and dual incremental variational problems such as (4.61) in the limit of very large load steps. This analysis shows that the solution at infinitely large load steps can be obtained by replacing the original incremental potential $j$ of (4.64) with its corresponding recession function $j_\infty$, see Definition 13. The latter encodes how $j$ behaves at infinity and is a convex homogeneous function by definition. Through this analysis, we recover intuitive results:

- the asymptotic problem of a perfectly elasto-plastic problem turns out to be rigid-plastic and therefore results in a standard limit analysis formulation;
- for elasto-plastic problems with unlimited hardening, the asymptotic problem is unbounded if hardening is not limited;
- with limited hardening, we recover a limit analysis problem with a yield strength corresponding to the ultimate strength obtained after complete hardening.

Overall, we can anticipate that a numerical method which is tailored to handle non-smooth homogeneous functions will perform well for large load steps. We have also seen promising results concerning non-convex IP solvers for finite-strain elastoplasticity.

To conclude, we should mention various aspects which have not been discussed in this chapter. First, we should mention the variational approach to fracture of Francfort and Marigo (1998) which revisits crack propagation as an energy minimization problem, see Marigo (2023) for a historical perspective of these developments. This approach extends Griffith's approach to brittle fracture by considering generic crack paths and topologies and provides a powerful framework for modeling crack propagation in brittle materials. Its numerical regularization

based on phase-field/damage-gradient approaches has found widespread use in many areas of engineering and materials science and will be discussed in Chapter 8, Section 8.2. Second, the framework of GSM can also be extended to models including gradient of state variables or other generalized continua, see for instance Maugin (1990); Frémond and Nedjar (1996). In particular, corresponding incremental variational principles can also be easily derived and an example will be discussed in Chapter 8, Section 8.3.

Finally, optimality conditions of variational formulations for plastic materials necessarily result in associated plastic flow rules. However, experimental measurements for many materials suggest that non-associated flow rules should be considered, which cannot be captured by an underlying variational formulation using standard convex analysis tools. To overcome this limitation, de Saxcé and Feng (1991); De Saxcé (1992) introduced the concept of a *bipotential*, which extends the Young-Fenchel inequality to a function $b(x, y)$ rather than a separable sum $f(x) + f^*(y)$. The bipotential provides a suitable modeling framework for a broad range of non-associated laws. Materials admitting a bipotential are called implicit standard materials (ISM), which include non-associated Drucker-Prager and Cam-Clay models in soil mechanics, non-linear kinematic hardening rules for cyclic plasticity and viscoplasticity, coupled plasticity-damage laws, Coulomb's friction law, and more. However, works devoted to an efficient numerical treatment of such frameworks remain very scarce at the moment, except concerning frictional contact, and should deserve more attention in the future.

# Chapter 5

# Computational limit analysis and civil engineering applications

This chapter gives an overview of one of my main research topics on limit analysis theory. We first expose a generic numerical framework in which limit analysis problems are very easily formulated using a domain-specific language based on FEniCS, the `fenics_optim` package. The latter enables to translate the abstract convex optimization problem into its discrete counterpart which is solved using the interior-point solver `Mosek`. The versatility of the numerical tools is illustrated on various academic problems, ranging from plate or shell models to generalized continua. In a second part, we review different applications of limit analysis approaches for civil engineering applications, including complex 3D steel or reinforced-concrete structures.

## Contents

## 5.1 Introduction

As discussed in Section 4.4.2, limit analysis (Hill, 1950), or more generally, yield design theory (Salençon, 1983, 2013), provides a direct way of computing the limit load without relying on incremental elasto-plastic analyses, and only requires a few mechanical parameters (i.e. the strength domain $G$), instead of a complete constitutive relation. By considering simple collapse mechanisms, analytical upper bounds for the exact collapse load can be obtained efficiently. The exact collapse load can be bracketed by the bounding status of the static lower bound and kinematic upper bound solutions. Limit analysis has found extensive applications in mechanical and civil engineering problems, such as soil slope stability, footing bearing capacity, and other geotechnical problems (Chen, 2013), masonry structures (Heyman, 1966), design of reinforced-concrete structures (e.g., through strut-and-tie methods (Schlaich et al., 1987) or yield-line analysis (Johansen, 1962)) (Chen, 2007; Nielsen and Hoang, 2016), the computation of collapse loads of frame, plate, or shell structures (Save, 1995; Save et al., 1997), etc. Analytical design formulas, obtained from hand-based solutions, have been implemented in different design codes.

### 5.1.1 Computational aspects

Limit analysis techniques have been somehow limited to hand-based solutions for quite a long time because of the difficulties encountered in the past when automating their resolution in a finite-element discrete setting for instance. This difficulty is mainly attributed to the non-smooth nature of the strength criterion which prevents from the use of gradient-based approaches as mentioned earlier. Fortunately, most strength criteria can be expressed using second-order cone or semi-definite constraints (Bisbos and Pardalos, 2007; Makrodimopoulos, 2010) so that the resulting limit analysis problem falls into the class of SOCP or SDP problems. Thanks to the efficiency of modern IP solvers, it now possible to solve complex and large-scale limit analysis problems (Krabbenhøft et al., 2008; Martin and Makrodimopoulos, 2008; Portioli et al., 2014; Vincent et al., 2018).

As regards numerical discretization techniques for limit analysis problem, the vast majority of works relies on the finite-element method (Lysmer, 1970; Anderheggen and Knöpfel, 1972; Pastor and Turgeman, 1976). The specificity of limit analysis problems, compared to more standard nonlinear computations with displacement-based FE discretizations, lies in the use of static equilibrium-based finite-elements for obtaining true lower bound (Sloan, 1988; Krabbenhoft and Damkilde, 2002) (and therefore safe) estimates of the limit load but also in the use of discontinuous finite-elements for the kinematic upper bound approach (Sloan and Kleeman, 1995; Makrodimopoulos and Martin, 2008, 2007). Indeed, most hand-based upper bound solutions have been obtained considering rigid-block mechanisms, thus involving no deformation but only displacement jumps in the plastic dissipation computation. Despite the higher computational cost compared to equivalent continuous interpolations, discontinuous interpolations provide more accurate limit load estimates (Pastor and Turgeman, 1976; Sloan and Kleeman, 1995; Krabbenhoft et al., 2005; Makrodimopoulos and Martin, 2008), especially if finite-element edges are well-oriented. They are also more robust for certain problems since they do not suffer from locking issues, see for instance Nagtegaal et al. (1974) for volumetric locking in pressure-insensitive materials or Bleyer and de Buhan (2016) for shear-locking in thin plates.

In the present chapter, we describe a general framework for the formulation of limit analysis problems for different mechanical models (2D/3D continua, plates/shells or generalized continua). Relying on the FEniCS finite-element library and symbolic representation of operators and code-generation capabilities, different FE discretization schemes (including

discontinuous or equilibrium elements) can be easily formulated and generalized to more advanced mechanical models. The proposed framework therefore offers four levels of generality in the problem formulation:

- choice of a *mechanical model*: limit analysis problems possess the same structure and can be formulated in a symbolic fashion through generalized stress/strain definitions (Section 5.2).
- choice of a *strength criterion*: the formulation of its conic representation at a local point suffices to completely characterize the strength criterion, its translation to the global optimization problem being automatically performed (Section 5.3.1).
- choice of a *FE discretization*: including element type, interpolation degree or quadrature rule, all compatible for a variable number of degrees of freedom related to the choice of the mechanical model (Section 5.2.4).
- choice of the *optimization solver*: although the accompanying FEniCS toolbox relies extensively on the `Mosek` optimization solver (MOSEK ApS, 2019b), once formulated in a standard conic programming form, the problem can then be written in a specific file format appropriate for another solver.

## 5.2 A general framework for limit analysis problems

In this section, we consider a material domain $\Omega \subset \mathbb{R}^d$ (with $d = 1, 2, 3$) associated with a specific mechanical model. In the subsequent applications, we will consider classical continuum theories such as 2D or 3D Cauchy continua or Reissner-Mindlin plate models for instance but also generalized continuum models encompassing higher-grade or higher-order theories. For this reason, the subsequent presentation will be made in a generalized continuum framework in which the mechanical stress or strain measures, equilibrium or continuity equations and boundary conditions will be written in an abstract fashion, their precise expression remaining to be specified for each particular mechanical theory. In particular, the presentation will make use of the virtual work principle following the works of Germain (1973b,a).

### 5.2.1 Virtual work principle for generalized continua

Let us therefore consider a generalized virtual velocity field $\boldsymbol{u}(\boldsymbol{x})$ of dimension $n$ and a set of strain measures $\boldsymbol{D}\boldsymbol{u}$ of dimension $m$ with $\boldsymbol{D}$ being a generalized strain operator. Following Germain (1973b,a), such strain measures must be objective i.e. null for any rigid body motion. The virtual power of internal forces is assumed to be given by an internal force density depending linearly upon the strain measures:

$$\mathcal{P}^{(i)}(\boldsymbol{\Sigma}, \boldsymbol{u}) = -\int_\Omega \boldsymbol{\Sigma} \cdot \boldsymbol{D}\boldsymbol{u} \, \mathrm{d}\Omega \tag{5.1}$$

in which $\boldsymbol{\Sigma}$ denotes the generalized stress measure associated with $\boldsymbol{D}\boldsymbol{u}$ by duality[1]. The above expression must in fact be understood in the sense of distributions i.e. $\boldsymbol{u}$ may exhibit discontinuities $\boldsymbol{J}\boldsymbol{u}$ (where $\boldsymbol{J}$ is a jump operator consistent with the definition of operator $\boldsymbol{D}$)

[1] We use the scalar product "·" to denote the inner product between the associated stress and strain measures

across some internal surface $\Gamma$. The power of internal forces therefore writes more explicitly as:

$$\mathcal{P}^{(i)}(\boldsymbol{\Sigma}, \boldsymbol{u}) = -\left(\int_{\Omega\setminus\Gamma} \boldsymbol{\Sigma} \cdot \boldsymbol{D}\boldsymbol{u} \, \mathrm{d}\Omega + \int_{\Gamma} \boldsymbol{\Sigma} \cdot \boldsymbol{J}\boldsymbol{u} \, \mathrm{d}S\right) \tag{5.2}$$

The power of external forces is given by:

$$\mathcal{P}^{(e)}(\boldsymbol{u}) = \int_{\Omega} \boldsymbol{f} \cdot \boldsymbol{u} \, \mathrm{d}\Omega + \int_{\partial\Omega} \boldsymbol{T} \cdot \boldsymbol{u} \, \mathrm{d}S \tag{5.3}$$

where $\boldsymbol{f}$ denotes body forces and $\boldsymbol{T}$ surface tractions.

According to the virtual power principle, the system is in equilibrium if and only if the sum of the internal and external virtual powers is zero for any virtual velocity field:

$$\mathcal{P}^{(i)}(\boldsymbol{\Sigma}, \boldsymbol{u}) + \mathcal{P}^{(e)}(\boldsymbol{u}) = 0 \quad \forall \boldsymbol{u} \tag{equilibrium}$$

### 5.2.2 General formulation of a limit analysis problem

Limit analysis (or yield design) theory amounts to finding the maximum loading a system can sustain considering only equilibrium and strength conditions for its constitutive material. The latter can be generally described by the fact that the generalized stresses $\boldsymbol{\Sigma}(\boldsymbol{x})$ must belong to a strength domain $G(\boldsymbol{x})$ for all points $\boldsymbol{x} \in \Omega$:

$$\boldsymbol{\Sigma}(\boldsymbol{x}) \in G(\boldsymbol{x}) \quad \forall \boldsymbol{x} \in \Omega \tag{strength condition}$$

The strength domain $G \subseteq \mathbb{R}^m$ is assumed to be a convex set (it may be unbounded and non-smooth) which usually contains the origin $0 \in G$.

Finding the maximum loading will be achieved with respect to a given loading *direction* i.e. by assuming that both volume and surface forces $\boldsymbol{f}$ and $\boldsymbol{T}$ are scaled by a single load factor $\lambda$. Let us mention that if one wants to describe the set of ultimate loads defined by multiple loading parameters, the ultimate load factor $\lambda^+$ must be computed independently for each fixed loading direction in the multiple loading parameter space. When repeating this process for different loading directions, one obtains the corresponding set of ultimate loads.

The limit analysis problem can finally be formulated as finding the maximum load factor $\lambda$ such that there exists a generalized stress field $\boldsymbol{\Sigma}(\boldsymbol{x})$ in equilibrium with $\lambda(\boldsymbol{f}, \boldsymbol{T})$ and complying with the material strength properties i.e. satisfying both (equilibrium) and (strength condition) which can also be written as:

$$\begin{aligned} \lambda^+ = \sup_{\lambda, \boldsymbol{\Sigma}} \quad & \lambda \\ \text{s.t.} \quad & \mathcal{P}^{(i)}(\boldsymbol{\Sigma}, \boldsymbol{u}) + \lambda \mathcal{P}^{(e)}(\boldsymbol{u}) = 0 \quad \forall \boldsymbol{u} \\ & \boldsymbol{\Sigma}(\boldsymbol{x}) \in G(\boldsymbol{x}) \quad \forall \boldsymbol{x} \in \Omega \end{aligned} \tag{5.4}$$

Formulation (5.4) is at the basis of the mixed finite-element formulation discussed in Bleyer and Hassen (2021) when choosing proper interpolation spaces for $\boldsymbol{\Sigma}$ and $\boldsymbol{u}$. We now turn to the general formulation of the static and kinematic approaches.

### Static approach

Starting from the weak formulation of equilibrium given by (equilibrium), strong balance equations, continuity conditions and boundary conditions can be obtained for the generalized stresses $\boldsymbol{\Sigma}$. These will generally take the following form:

$$\boldsymbol{\mathcal{E}}\boldsymbol{\Sigma} + \lambda \boldsymbol{f} = 0 \quad \text{in } \Omega \tag{5.5}$$

$$\boldsymbol{\mathcal{C}}\boldsymbol{\Sigma} = 0 \quad \text{on } \Gamma \tag{5.6}$$

$$\boldsymbol{\mathcal{T}}\boldsymbol{\Sigma} = \lambda \boldsymbol{T} \quad \text{on } \partial\Omega \tag{5.7}$$

where $\boldsymbol{\mathcal{E}}$ is an equilibrium operator (adjoint to $\boldsymbol{\mathcal{D}}$) and $\boldsymbol{\mathcal{C}}$ and $\boldsymbol{\mathcal{T}}$ are some continuity and trace operators related to $\boldsymbol{\mathcal{E}}$. A generalized stress field $\boldsymbol{\Sigma}(\boldsymbol{x})$ satisfying these conditions will be termed as *statically admissible* with a given loading $(\lambda \boldsymbol{f}, \lambda \boldsymbol{T})$.

The pure static formulation can therefore be generally written as:

$$\begin{aligned} \lambda^+ = \sup_{\lambda, \boldsymbol{\Sigma}} \quad & \lambda \\ \text{s.t.} \quad & \boldsymbol{\mathcal{E}}\boldsymbol{\Sigma} + \lambda \boldsymbol{f} = 0 \quad \text{in } \Omega \\ & \boldsymbol{\mathcal{C}}\boldsymbol{\Sigma} = 0 \quad \text{on } \Gamma \\ & \boldsymbol{\mathcal{T}}\boldsymbol{\Sigma} = \lambda \boldsymbol{T} \quad \text{on } \partial\Omega \\ & \boldsymbol{\Sigma}(\boldsymbol{x}) \in G(\boldsymbol{x}) \quad \forall \boldsymbol{x} \in \Omega \end{aligned} \tag{SA}$$

Obviously $\boldsymbol{\Sigma}$ must belong to an appropriate functional space $\mathcal{W}$ consistent with the nature of the above operators. If one restricts to a (finite-dimensional) subset $\mathcal{W}_h \subset \mathcal{W}$ such that all constraints of (SA) can be satisfied exactly, the corresponding solution $\lambda_s$ of the corresponding (finite) convex optimization problem will therefore be a lower bound to the exact limit load: $\lambda_s \leq \lambda^+$.

### Kinematic approach

The kinematic formulation of a limit analysis problem can be obtained after introducing the maximum resisting power as:

$$\mathcal{P}^{(mr)}(\boldsymbol{u}) = \sup_{\boldsymbol{\Sigma}(\boldsymbol{x}) \in G(\boldsymbol{x})} \{-\mathcal{P}^{(i)}(\boldsymbol{\Sigma}, \boldsymbol{u})\} = \int_{\Omega \setminus \Gamma} \pi_G(\boldsymbol{D}\boldsymbol{u}) \, \mathrm{d}\Omega + \int_{\Gamma} \pi_G(\boldsymbol{J}\boldsymbol{u}) \, \mathrm{d}S \tag{5.8}$$

in which $\pi_G$ is the support function of the convex set $G$:

$$\pi_G(\boldsymbol{d}) = \sup_{\boldsymbol{\Sigma} \in G} \{\boldsymbol{\Sigma} \cdot \boldsymbol{d}\} \tag{5.9}$$

The kinematic approach of limit analysis then reads as:

$$\begin{aligned} \lambda^+ = \inf_{\boldsymbol{u}} \quad & \mathcal{P}^{(mr)}(\boldsymbol{u}) \\ \text{s.t.} \quad & \mathcal{P}^{(e)}(\boldsymbol{u}) = 1 \end{aligned} \tag{KA}$$

Similarly to the static approach (SA), $\boldsymbol{u}$ must belong to an appropriate functional space $\mathcal{V}$. If one restricts to a (finite-dimensional) subset $\mathcal{V}_h \subset \mathcal{V}$, the corresponding solution $\lambda_u$ of the corresponding (finite) convex optimization problem will therefore be an upper bound to the exact limit load: $\lambda^+ \leq \lambda_u$.

### 5.2.3 Conic programming of strength criteria

As already mentioned in Bisbos and Pardalos (2007); Krabbenhøft et al. (2007); Makrodimopoulos (2010), a large class of classical strength criteria can be formulated in terms of second-order cone (SOC) constraints or semi-definite positive (SDP) matrix constraints. For some more advanced strength criteria, their conic representation may involve power or exponential cones. This is the case, for instance, for the Generalized Hoek-Brown (Kumar and Rahaman, 2020) or the Hosford yield criterion which are both power-cone representable (Bleyer and Hassen, 2021). Below, we illustrate how conic-representation is used for the case of a 3D Mohr-Coulomb criterion.

The Mohr-Coulomb criterion $G$ for a soil of cohesion $c$ and internal friction angle $\phi$ requires the stress state $\boldsymbol{\sigma} \in \mathbb{S}^3$ to satisfy:

$$\sigma_{\mathrm{M}} - a\sigma_{\mathrm{m}} \leq \frac{2c\cos\phi}{1+\sin\phi} \tag{5.10}$$

where $a = \frac{1-\sin\phi}{1+\sin\phi}$ and $\sigma_{\mathrm{M}} = \max_I \sigma_I$ (resp. $\sigma_{\mathrm{m}} = \min_I \sigma_I$) is the maximum (resp. minimum) principal stress. The quantity $k = \frac{2c\cos\phi}{1+\sin\phi}$ corresponds to the soil unixial tensile strength.

As the criterion involves the maximum and minimum principal stresses in its definition, it can be formulated using SDP constraints in the 3D case (Bisbos and Pardalos, 2007; Krabbenhøft et al., 2007; Martin and Makrodimopoulos, 2008). Note that in 2D, its formulation involves second-order cone constraints only. Let us introduce a scalar variables $t$ such that:

$$t\boldsymbol{I} \preccurlyeq \boldsymbol{\sigma} \tag{5.11}$$

so that $t \leq \sigma_{\mathrm{m}}$. Then, one replaces (5.10) with:

$$\sigma_{\mathrm{M}} \leq k + at \tag{5.12}$$

Both constraints (5.11) and (5.12) can then be rewritten using SDP constraints involving two additional matrix variables $\boldsymbol{X}_1$ and $\boldsymbol{X}_2$ as follows:

$$\boldsymbol{\sigma} \in G \Leftrightarrow \exists t, \boldsymbol{X}_1, \boldsymbol{X}_2 \text{ s.t. } \begin{cases} (k+at)\,\boldsymbol{I} - \boldsymbol{\sigma} = \boldsymbol{X}_1 \\ \boldsymbol{\sigma} - t\boldsymbol{I} = \boldsymbol{X}_2 \\ \boldsymbol{X}_1, \boldsymbol{X}_2 \succcurlyeq 0 \end{cases} \tag{5.13}$$

which provides the SDP representation of criterion $G$ defined by (5.10).

Conic convex duality can then be used to easily derive the corresponding conic-representation of the support function:

$$\begin{aligned} \pi_G(\boldsymbol{d}) &= \max_{\boldsymbol{\sigma}\in G} \boldsymbol{\sigma} : \boldsymbol{d} = \min_{\boldsymbol{Y}_1,\boldsymbol{Y}_2\succcurlyeq 0} \max_{\boldsymbol{\sigma},t} \boldsymbol{\sigma} : \boldsymbol{d} + \big((f_{\mathrm{c}}+at)\boldsymbol{I} - \boldsymbol{\sigma}\big) : \boldsymbol{Y}_1 + (\boldsymbol{\sigma} - t\boldsymbol{I}) : \boldsymbol{Y}_2 \\ &= \min_{\boldsymbol{Y}_1,\boldsymbol{Y}_2} \quad k\,\mathrm{tr}\,\boldsymbol{Y}_1 \\ &\quad \text{s.t.} \quad \boldsymbol{d} = \boldsymbol{Y}_1 - \boldsymbol{Y}_2 \\ &\qquad\quad a\,\mathrm{tr}\,\boldsymbol{Y}_1 = \mathrm{tr}\,\boldsymbol{Y}_2 \\ &\qquad\quad \boldsymbol{Y}_1, \boldsymbol{Y}_2 \succcurlyeq 0 \end{aligned} \tag{5.14}$$

We can show that the above conic formulation is equivalent to the more classical definition (Salençon, 1983) of Mohr-Coulomb's support function:

$$\pi_G(\boldsymbol{d}) = \begin{cases} c\,\mathrm{cotan}\,\phi\,\mathrm{tr}\,\boldsymbol{d} & \text{if } \mathrm{tr}\,\boldsymbol{d} \geq \sin\phi \sum_{I=1}^{3} |d_I| \\ +\infty & \text{otherwise} \end{cases} \tag{5.15}$$

### 5.2.4 Kinematic formulation for 2D/3D continua

Let us now consider the kinematic limit analysis of 2D or 3D continua for which $\boldsymbol{u}$ is a 2D or 3D velocity field and the associated strain is its symmetric gradient $\boldsymbol{D}\boldsymbol{u} = \nabla^s \boldsymbol{u}$. For a continuous velocity field $\boldsymbol{u}$, the finite-element kinematic limit analysis approach (KA), with body force $\boldsymbol{f}$ only, reads:

$$\begin{aligned} \lambda^+ \leq \inf_{\boldsymbol{u}\in\mathcal{V}_h} \quad & \int_\Omega \pi_G(\nabla^s \boldsymbol{u})\,\mathrm{d}\Omega \\ \text{s.t.} \quad & \int_\Omega \boldsymbol{f}\cdot\boldsymbol{u}\,\mathrm{d}\Omega = 1 \end{aligned} \tag{5.16}$$

where $\mathcal{V}_h$ is a finite-element subspace of Lagrange elements based on a given mesh of typical mesh size $h$. In the above problem, the computed objective function is an upper bound of the exact limit load factor $\lambda^+$ only if the integral of the objective function term is evaluated exactly. In general, this is not possible because of the non-linearity of function $\pi_G$, except in the special case of $\boldsymbol{u}$ being interpolated with $\mathbb{P}_1$-Lagrange elements so that the gradient is cell-wise constant and the integral becomes trivial.

In classical finite-element approaches, integrals are numerically evaluated using Gaussian quadrature rules. Doing so, one looses the upper-bound estimate of (5.16). It is however possible to obtain an upper-bound estimate when using $\mathbb{P}_2$-Lagrange elements for $\boldsymbol{u}$ on a mesh consisting of simplex (straight edges) triangles (or tetrahedra in 3D) by relying on a *vertex* quadrature rule (Makrodimopoulos and Martin, 2007):

$$\int_T F(\mathbf{r}(\boldsymbol{x}))\,\mathrm{d}T \lesssim \frac{|T|}{d+1}\sum_{i=1}^{d+1} F(\mathbf{r}(\boldsymbol{x}_i)) \tag{5.17}$$

where $F$ is a convex function and $\mathbf{r}$ is an affinely-varying function over the mesh cell $T$ (either a triangle in dimension $d = 2$ or a tetrahedron for $d = 3$ of area/volume $|T|$) with $\mathbf{r}(\boldsymbol{x}_i)$ being its value at the $d+1$ vertices.

In this case, we have:

$$\begin{aligned} \lambda^+ \leq \lambda_u = \inf_{\boldsymbol{u}\in\mathcal{V}_h} \quad & \sum_{T\in\mathcal{T}_h} \frac{|T|}{d+1}\sum_{i=1}^{d+1} \pi_G(\nabla^s \boldsymbol{u}(\boldsymbol{x}_i)) \\ \text{s.t.} \quad & \boldsymbol{F}^{\mathrm{T}}\boldsymbol{u} = 1 \end{aligned} \tag{5.18}$$

where $\mathcal{T}_h$ denotes the mesh and $\boldsymbol{F}$ the vector of nodal forces. The numerical resolution of (5.18) using general-purpose conic solvers requires to transform it into a canonical form such as (3.27). To do so, one must in particular express the objective function using the conic representation (5.14) after introducing additional auxiliary variables $\boldsymbol{Y}_1, \boldsymbol{Y}_2$ defined at all integration points. The process of converting all expressions and constraints into matrix format is rather cumbersome, especially if one aims at changing easily the strength criterion $G$ or the finite-element discretization, notably when using discontinuous interpolations for instance.

## 5.3 The `fenics_optim` package

For these reasons, I have developed a general-purpose domain-specific language (DSL) for automating the formulation and resolution of convex variational problems in a finite-element setting. The package is implemented as an add-on to the FEniCS Python interface and enables to easily formulate convex optimization problems using only a few lines of code and to discretize them in a very simple manner using various finite-element interpolation

spaces available in FEniCS. Their numerical resolution is performed efficiently using `Mosek` as the underlying conic programming solver (MOSEK ApS, 2019b). We describe below some of the key aspects at the core of the package implementation. For more details and additional examples, the reader can refer to (Bleyer, 2020a) and the online documentation https://fenics-optim.readthedocs.io/. At the time of writing this manuscript, this project is being adapted to the new FEniCSx version.

### 5.3.1 Conic-representable functions

One of the main feature of `fenics_optim` is to easily handle the representation of a convex function in a conic format, as (5.14) for instance. Indeed, given a convex function $f(\boldsymbol{x})$, we say that it is *conic-representable* if it can be written in the following form:

$$\begin{aligned} f(\boldsymbol{x}) = \inf_{\boldsymbol{y}} \quad & \boldsymbol{c}_x^{\mathrm{T}}\boldsymbol{x} + \boldsymbol{c}_y^{\mathrm{T}}\boldsymbol{y} \\ \text{s.t.} \quad & \boldsymbol{b}_l \leq \boldsymbol{A}\boldsymbol{x} + \boldsymbol{B}\boldsymbol{y} \leq \boldsymbol{b}_u \\ & \boldsymbol{y} \in \mathcal{K} \end{aligned} \tag{5.19}$$

where $\boldsymbol{c}_x$, $\boldsymbol{c}_y$, $\boldsymbol{b}_l$, $\boldsymbol{b}_u$ are given vectors of appropriate size, $\boldsymbol{A}$ and $\boldsymbol{B}$ are given matrices and $\mathcal{K} = \mathcal{K}_1 \times \ldots \times \mathcal{K}_n$ is a product of cones of the magic family (see Section 3.2). Note that the above representation is not necessarily unique. However, as soon as one equivalent form of (5.19) is available, minimizing $f(\boldsymbol{x})$ can be achieved using dedicated conic IP solvers. As mentioned in Juditsky and Nemirovski (2021), any given convex function does not necessarily possess an obvious conic reformulation and specific calculus rules must therefore be used in order to obtain such a representation. This process can be automated using Disciplined Convex Programming, as done for instance in the `CVX` software (Grant and Boyd, 2014). Without being exhaustive, we give in the following several examples of simple conic-representable functions and some convexity-preserving operations which also maintain conic representability inherited from the original function(s).

#### Simple conic-representable functions

Many interesting conic-representable functions can be obtained using simple building blocks such as:

- affine functions;
- convex quadratic functions;
- $p$-norms with $p \geq 1$: $p = 2$ requires quadratic cones, $p = 1$ or $\infty$ requires linear inequalities and $p \notin \{1, 2, \infty\}$ can be expressed using generic power cones;
- logarithm and exponential functions using exponential cones;
- maximum and minimum principal values of a symmetric matrix variable using SDP cones.

We refer for instance to MOSEK ApS (2019a) for more details on conic formulations of other usual functions.

**Operations on functions**

Based on the above simple functions, more complex functions can be obtained using simple operations on functions which all preserve the conic-representability. For instance, the sum $f_1(\boldsymbol{x}) + f_2(\boldsymbol{x})$ of two conic-representable functions is obviously also conic-representable. Without being exhaustive, other examples include:

- precomposition by a linear operator $A$:

$$(f \circ A)(\boldsymbol{x}) = f(\boldsymbol{A}\boldsymbol{x}) \tag{5.20}$$

- convex conjugate:

$$f^*(\boldsymbol{y}) = \sup_{\boldsymbol{x}} \boldsymbol{y}^{\mathrm{T}}\boldsymbol{x} - f(\boldsymbol{x}) \tag{5.21}$$

- perspective (Rockafellar, 1970):

$$\mathrm{persp}_f(\boldsymbol{x}, t) = t f(\boldsymbol{x}/t) \tag{5.22}$$

- inf-convolution $f_1 \square f_2$ between two functions $f_1$,$f_2$ (Rockafellar, 1970):

$$\begin{aligned}(f_1 \square f_2)(\boldsymbol{x}) = \inf_{\boldsymbol{x}_1, \boldsymbol{x}_2} \quad & f_1(\boldsymbol{x}_1) + f_2(\boldsymbol{x}_2) \\ \text{s.t.} \quad & \boldsymbol{x} = \boldsymbol{x}_1 + \boldsymbol{x}_2\end{aligned} \tag{5.23}$$

- the marginal $f \setminus \boldsymbol{A}$ of $f$ through a linear operator $\boldsymbol{A}$ (Fitzpatrick and Simons, 2001):

$$\begin{aligned}(f \setminus \boldsymbol{A})(\boldsymbol{x}) = \inf_{\boldsymbol{y}} \quad & f(\boldsymbol{y}) \\ \text{s.t.} \quad & \boldsymbol{x} = \boldsymbol{A}\boldsymbol{y}\end{aligned} \tag{5.24}$$

- a generalized marginal operator through a set of $n$ linear operators $\boldsymbol{A}_i$ and positive weights $c_i \geq 0$:

$$\begin{aligned}(f \setminus \{\boldsymbol{A}_i, c_i\})(\boldsymbol{x}) = \inf_{\boldsymbol{y}_1, \cdots, \boldsymbol{y}_n} \quad & \sum_{i=1}^{n} c_i f(\boldsymbol{y}_i) \\ \text{s.t.} \quad & \boldsymbol{x} = \sum_{i=1}^{n} \boldsymbol{A}_i \boldsymbol{y}_i\end{aligned} \tag{5.25}$$

By extension, we also say that a convex set $G$ is conic-representable if its indicator function $\delta_G$ is conic-representable. In this case, $G$ is conic-representable, its support function $\pi_G$ is also conic-representable. Moreover, if $f$ is conic-representable, its epigraph $\mathrm{epi}\, f$ is also conic-representable.

### 5.3.2 Conic-representable variational problems

As mentioned in Chapter 4, many convex variational problems consist in minimizing some potential $\Psi(\boldsymbol{u})$ with respect to a mechanical field $\boldsymbol{u}$. Often this potential can be expressed from a corresponding potential density $\psi(\boldsymbol{u})$ per unit volume. The resulting variational problem formulated on a domain $\Omega$ generally reads as:

$$\inf_{\boldsymbol{u} \in V} \int_{\Omega} \psi(\boldsymbol{u}) \, \mathrm{d}\Omega \tag{5.26}$$

where $V$ is some affine, or at least convex, space gathering various constraints on $\boldsymbol{u}$ e.g. boundary conditions, physical bounds, etc. After introducing an appropriate finite-element discretization space $V_h \subset V$ and quadrature rule for the integral, the discrete version will be of the form:

$$\min_{\bar{\boldsymbol{u}}=(\boldsymbol{u}_i)\in V_h} \sum_{g=1}^{G} \omega_g \psi(\boldsymbol{L}_g \bar{\boldsymbol{u}}) \tag{5.27}$$

where $\omega_g$ are positive quadrature weights and $\boldsymbol{L}_g$ are linear operators relating the vector of unknowns $\bar{\boldsymbol{u}} = (\boldsymbol{u}_i) \in V_h$ to the value of the continuous field $\boldsymbol{u}$ at the corresponding quadrature point.

When the potential density $\psi$ is conic-representable, one naturally obtains a conic-representable variational problem. The `fenics_optim` package therefore relies on FEniCS to transform abstract forms (5.26) into their discrete counterparts (5.27) for a generic conic-representable function $\psi$.

For this reason, in the following of the manuscript, we will write variational problems in their continuous form such as (5.26) rather than their discrete counterpart for the sake of notation simplicity. It is however implied that their concrete implementation and resolution is performed using a specific discretization such as (5.27). For the same reason, we will often ignore the definition of appropriate continuous function spaces for the different fields and do as if working in finite dimension.

## 5.4 Illustrative applications

### 5.4.1 Stability of a vertical cut-off

To illustrate the versatility of the `fenics_optim` package, we consider the stability of a vertical cut-off in a cohesive-frictional soil obeying the Mohr-Coulomb criterion. In 3D, the conic representation of its support function is easily defined as:

```
class MohrCoulomb(ConvexFunction):
    """SDP implementation of Mohr-Coulomb criterion."""
    def conic_repr(self, X):
        a = (1-sin(phi))/(1+sin(phi))
        k = 2*c*cos(phi)/(1+sin(phi))
        Y1 = self.add_var(6, cone=SDP(3))
        Y2 = self.add_var(6, cone=SDP(3))
        self.add_eq_constraint(X - Y1 + Y2)
        self.add_eq_constraint(tr(to_mat(Y2))-a*tr(to_mat(Y1)))
        self.set_linear_term(k*tr(to_mat(Y1)))
```

Then the corresponding function space `V` (continuous $\mathbb{P}_2$-Lagrange elements) is defined and fixed boundary conditions are imposed on the part named "`border`" of the boundary. A `MosekProblem` object is instantiated and a first optimization field `u` belonging to function space `V` is added to the problem and is constrained to satisfy the Dirichlet boundary conditions `bc`:

```
V = VectorFunctionSpace(mesh, "P", 2)
bc = DirichletBC(V, Constant((0.,0.,0.)), border)

prob = MosekProblem("Upper bound limit analysis")
u = prob.add_var(V, bc=bc)
```

The external work normalization constraint is then added by defining the function space for the Lagrange multiplier corresponding to the constraint (here it is scalar so we use a `"Real"` function space) and passing the corresponding constraint in its weak form as follows:

```
R = FunctionSpace(mesh, "Real", 0)
def Pext(lamb):
    return lamb*dot(f,u)*dx
prob.add_eq_constraint(R, A=Pext, b=1)
```

Finally, the Mohr-Coulomb support function is called as a function of the strain $\nabla^s \boldsymbol{u}$ written in terms of UFL operators. We also specify the choice for the quadrature scheme used for its numerical evaluation. Here the *vertex* scheme (5.17) is chosen. This convex function is then added to the problem before asking for its optimization by `Mosek`.

```
mc_support = MohrCoulomb(c, phi)
strain = sym(grad(u))
pi = mc_support(strain, quadrature_scheme="vertex")
prob.add_convex_term(pi)

prob.optimize()
```

Clearly, the package enables to express complex problems in very compact forms. Similar implementation can be obtained when dealing with static lower bound approaches. In this case, the main difference comes from the fact that discontinuous spaces are used for the stress interpolation and traction continuity must be enforced through element facets. This is however easily handled thanks to FEniCS modelling capabilities. Similarly, discontinuous interpolations for the velocity field in kinematic approaches can also be handled by defining convex function with facet integration measures.

As an illustration, we test on a plane strain vertical cut-off stability problem the convergence properties for various discretization choices. The latter include $\mathbb{P}_1$ and $\mathbb{P}_2$ upper bound elements, stress-based lower bound elements and non-upper bound displacement-based elements, we refer the reader to Bleyer and Hassen (2021) and references therein for more details on the finite-element formulations. Results are given in terms of the non-dimensional safety factor $(\gamma H/c)^+$ for a slope of self-weight $\gamma$ and height $H$ in Fig. 5.1-left as a function of the total number of elements. The concentration of the local dissipation $\pi_G(\nabla^s \boldsymbol{u})$ along the slip-line is represented on Fig. 5.1-right. We can see that we observe, as expected, convergence from below for lower-bound elements and from above for upper bound elements. Regarding the latter, the rate of convergence is faster for quadratic elements (`UB2`) than for linear elements (`UB1`). As often, displacement-based and mixed elements which are not supposed to yield an upper-bound estimate tend to converge from above with a better accuracy than true upper-bound elements.

### 5.4.2 Plate and shell models

#### Thin plate models

In this section, we discuss the limit analysis of thin plates in bending, a problem which has been studied in Demengel (1983); Bleyer et al. (2016) for instance. In the present case, we consider a unit square plate made of a von Mises material of uniform bending strength $m$ and subjected to a uniformly distributed transverse loading $f$. The thin plate limit analysis

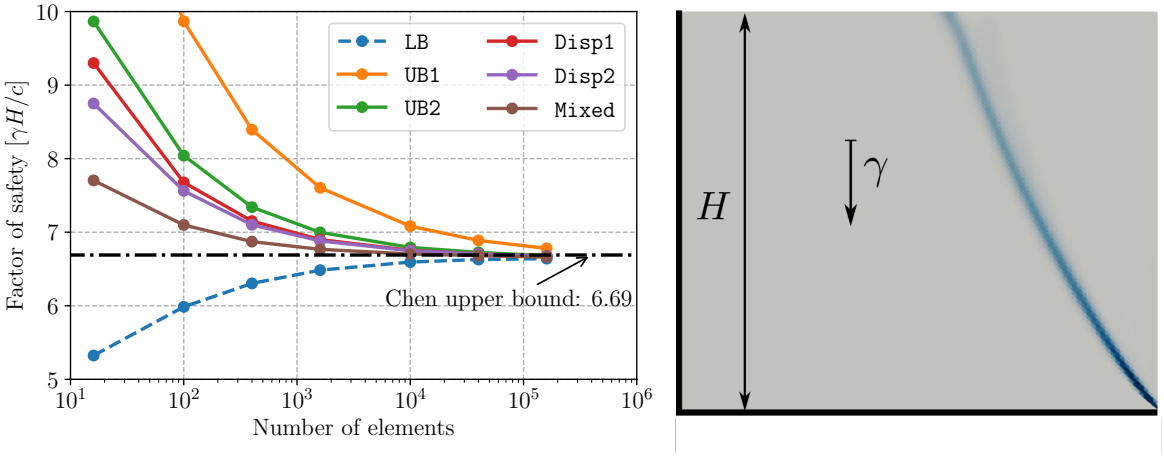


Figure 5.1: Left: Convergence of the vertical slope factor of safety for various finite element discretization: `UB1` (resp. `UB2`) are the $\mathbb{P}_1$ (resp. $\mathbb{P}_2$) Lagrange upper bound elements, `LB` the lower bound element and `Disp1`, `Disp2`, `Mixed` correspond to non-upper bound elements considered in (Krabbenhøft et al., 2007). Analytical upper bound from Chen (2013). Right: local dissipation map

problem consists in solving the following problem:

$$\begin{aligned} \inf_{u\in \mathrm{HB}_0(\Omega)} \quad & \int_\Omega \pi(\nabla^2 u)\,\mathrm{d}\Omega \\ \text{s.t.} \quad & \int_\Omega f u\,\mathrm{d}\Omega = 1 \end{aligned} \tag{5.28}$$

where $\mathrm{HB}_0$ is the space of *bounded Hessian functions* (Demengel, 1984) with zero trace on $\partial\Omega$ and $\pi(\boldsymbol{\kappa}) = \frac{2m}{\sqrt{3}}\sqrt{\kappa_{11}^2+\kappa_{22}^2+\kappa_{12}^2+\kappa_{11}\kappa_{22}}$ for any $\boldsymbol{\kappa}\in\mathbb{S}_2^+$ is the support function of the plane-stress von Mises criterion expressed in terms of bending curvatures $\boldsymbol{\kappa}$.

Contrary to elastic bending plate problems involving functions with $C^1$-continuity, we deal here with functions in HB which are continuous but may have discontinuities in their normal gradient $\partial_n u$. In particular, we can consider a $\mathbb{P}_2$-Lagrange interpolation for $u$ with jumps of $\partial_n u$ across all internal facets $F\in\Gamma_h$ of unit normal $\boldsymbol{n}$. In this case the objective function in (5.28) writes explicitly (Bleyer and de Buhan, 2013c) as:

$$\begin{aligned} \inf_{u\in \mathrm{HB}_0(\Omega)} \quad & \sum_{T\in\mathcal{T}_h}\int_T \pi(\nabla^2 u)\,\mathrm{d}\Omega + \sum_{F\in\Gamma_h}\int_F \pi(\llbracket\partial_n u\rrbracket \boldsymbol{n}\otimes\boldsymbol{n})\,\mathrm{d}S \\ \text{s.t.} \quad & \int_\Omega f u\,\mathrm{d}\Omega = 1 \end{aligned} \tag{5.29}$$

where $\mathcal{T}_h$ is the set of all triangular finite-elements. It happens that in fact $\pi(\llbracket\partial_n u\rrbracket\boldsymbol{n}\otimes\boldsymbol{n}) = |\llbracket\partial_n u\rrbracket|\pi(\boldsymbol{n}\otimes\boldsymbol{n}) = |\llbracket\partial_n u\rrbracket|\frac{2m}{\sqrt{3}}$ for the von Mises criterion.

The reference solution for this problem is known to be $25.02m/f$ (Capsoni and Corradi, 1999), whereas we find $25.05m/f$ for a $50\times 50$ structured mesh. The corresponding solutions for $u$ and $\pi(\nabla^2 u)$ are represented in Fig. 5.2.

We refer the reader to (Bleyer and de Buhan, 2013b)(Bleyer et al., 2015a) for a more thorough discussion on FE discretizations, to (Bleyer and de Buhan, 2014c; Bleyer et al., 2015b) for their extension to thick plate problems and to (Bleyer and de Buhan, 2014b,a) for homogenization of periodic thin plates in limit analysis.

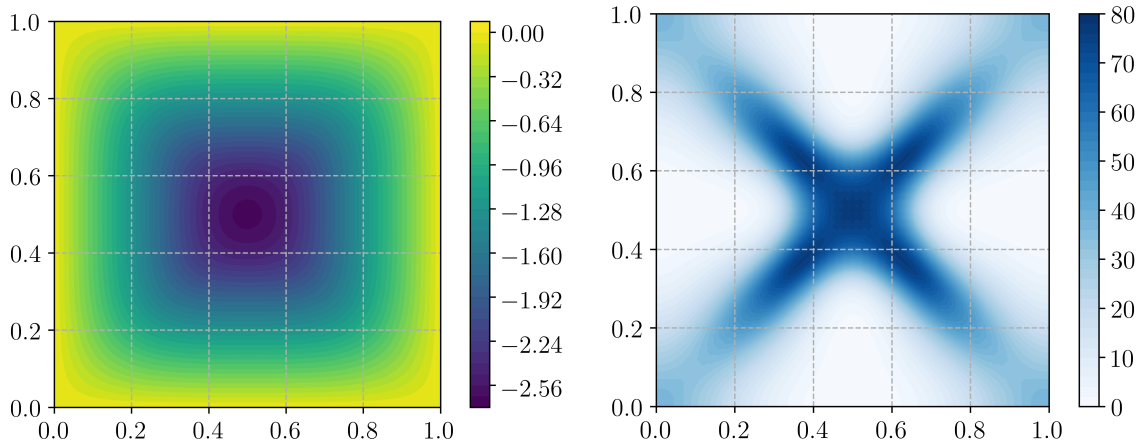


(a) Optimal collapse mechanism $u$

(b) Curvature dissipation density $\pi(\nabla^2 u)$

Figure 5.2: Results for the simply supported von Mises square plate

**Shell finite-element discretization**

Let us now briefly consider a lower bound approach for shell structures. We refer to (Bleyer and de Buhan, 2016) and references therein for more details concerning limit analysis of shells, especially the upper bound kinematic approach. The shell geometry will be approximated by a plane facet discretization into triangular elements and will be described locally by a unit normal $\boldsymbol{\nu}$ and a tangent plane spanned by two unit vectors $\boldsymbol{a}_1$ and $\boldsymbol{a}_2$. This local frame is therefore constant element-wise. The generalized internal forces of the shell model are described by a symmetric *membrane force* tensor $\boldsymbol{N} = N_{ij}\underline{a}_i \otimes \underline{a}_j$, a symmetric *bending moment* tensor $\boldsymbol{M} = M_{ij}\boldsymbol{a}_i \otimes \boldsymbol{a}_j$ and a *shear force* vector $\boldsymbol{Q} = Q_i \boldsymbol{a}_i$ $(i, j = 1, 2)$, the components of which are expressed in the local tangent plane. We will consider only thin shells, meaning that the shell strength criterion $G_{\text{shell}}$ is a convex set in the 6-dimensional $(\boldsymbol{N}, \boldsymbol{M})$ space (infinite shear strength assumption). Introducing $\boldsymbol{T} = \boldsymbol{N} + \boldsymbol{\nu} \otimes \boldsymbol{Q}$, the local equilibrium equations in a plane facet are given by:

$$\operatorname{div}_T \boldsymbol{T} + \lambda \boldsymbol{f} = 0 \tag{5.30}$$

$$\operatorname{div}_T \boldsymbol{M} + \boldsymbol{Q} = 0 \tag{5.31}$$

where $\operatorname{div}_T$ is the tangent plane divergence operator and $\lambda \boldsymbol{f}$ the distributed loading. In addition to local equilibrium, continuity equations of the force resultant $\boldsymbol{R} = \boldsymbol{T}\boldsymbol{n}$ and the normal bending moment $\boldsymbol{\mathcal{M}} = \boldsymbol{M}\boldsymbol{n} \times \boldsymbol{\nu}$ must be satisfied where $\boldsymbol{n}$ is the in-plane normal to a facet edge:

$$[\![\boldsymbol{R}]\!] = 0 \tag{5.32}$$

$$[\![\boldsymbol{\mathcal{M}}]\!] = 0 \tag{5.33}$$

Finite-element discretization relies on a discontinuous $\mathbb{P}_{1,d}$ interpolation for both membrane forces $\boldsymbol{N}$ and shear forces $\boldsymbol{Q}$ and a discontinuous $\mathbb{P}_{2,d}$ interpolation for the bending moments $\boldsymbol{M}$. Equilibrium (resp. continuity) equations are then satisfied using cell (resp. facet) Lagrange multipliers of appropriate polynomial degree. Again, all these constraints are easily implemented with UFL operators.

### General shell strength criterion

Even for the simple case of a homogeneous von Mises thin shell, the strength condition expressed in terms of $(\boldsymbol{N}, \boldsymbol{M})$ stress-resultant becomes extremely complicated (Ilyushin, 1956) so that simple SOC-representable approximations have been proposed in the past for the von Mises shell (Robinson, 1971). In (Bleyer and de Buhan, 2016), we proposed a general way of formulating an $(\boldsymbol{N}, \boldsymbol{M})$ shell strength criterion for a general multilayered shell through an up-scaling procedure. It is given by:

$$(\boldsymbol{N}, \boldsymbol{M}) \in G_{\text{shell}} \Longleftrightarrow \begin{cases} \exists\, \boldsymbol{\sigma}(z) \in \mathcal{G}_{\text{ps}} \quad \forall z \in [-h/2; h/2] \text{ and s.t.} \\ \boldsymbol{N} = \displaystyle\int_{-h/2}^{h/2} \boldsymbol{\sigma}(z)\, \mathrm{d}z \\ \boldsymbol{M} = \displaystyle\int_{-h/2}^{h/2} (-z)\boldsymbol{\sigma}(z)\, \mathrm{d}z \end{cases} \tag{5.34}$$

where $h$ is the shell thickness and $\mathcal{G}_{ps}$ is the material local plane-stress criterion, which may potentially depend on coordinate $z$ for a multilayered shell. To make formulation (5.34) usable in practice, the local plane-stress distribution $\boldsymbol{\sigma}(z)$ is replaced by a discrete set of plane-stress states $\boldsymbol{\sigma}_g = \boldsymbol{\sigma}(z_g)$ expressed at quadrature points $z_g$ which are used to approximate the two integrals:

$$(\boldsymbol{N}, \boldsymbol{M}) \in G_{\text{shell}}^{\text{approx}} \Longleftrightarrow \begin{cases} \exists\, \boldsymbol{\sigma}_g \in \mathcal{G}_{\text{ps}} \quad \forall g = 1, \ldots, n_z \text{ and s.t.} \\ \boldsymbol{N} = \displaystyle\sum_{g=1}^{n_z} \omega_g \boldsymbol{\sigma}_g \\ \boldsymbol{M} = \displaystyle\sum_{g=1}^{n_z} (-z_g)\omega_g \boldsymbol{\sigma}_g \end{cases} \tag{5.35}$$

where $\omega_g$ are the corresponding quadrature weights of the $n_z$-points quadrature rule. From (5.35) it can readily be seen that if $\mathcal{G}_{\text{ps}}$ is SOC-representable, so will be $G_{\text{shell}}^{\text{approx}}$.

The precise choice of the quadrature rule leads to different kinds of approximations to $G_{\text{shell}}$: e.g. an upper bound approximation is obtained with a trapezoidal quadrature rule, a Gauss-Legendre quadrature leads to an approximation with no lower or upper bound status, a rectangular rule will give a lower bound approximation. In the following, we choose the latter to be consistent with the lower bound status of the static approach. Let us finally remark that the approximation will converge to the shell criterion $G_{\text{shell}}$ when increasing $n_z$. In the following we took $n_z = 6$.

### Numerical example

As an illustrative application, we consider the problem of a cylindrical shell of length $2L$, radius $R$ and thickness $h = 0.01R$, clamped at both extremities and loaded by a self-weight uniform vertical loading $\boldsymbol{f} = -q\boldsymbol{e}_z$ (see Fig. 5.3a). The shape of the collapse mechanism varies depending on the cylinder slenderness $2L/R$. For sufficiently long cylinders, the computed limit load $q^+$ is well described by the one obtained when representing the cylinder as a 1D beam $q^+_{\text{beam}} = \frac{32}{\pi} N_0 \left(\frac{R}{2L}\right)^2$ with $N_0 = \sigma_0 h$ being the membrane uniaxial strength. The obtained limit loads agree very well with the lower bound result of Bleyer and de Buhan (2016). The obtained deformations have been represented in Fig. 5.3b along with the normal force magnitude distribution. It can be seen that the mechanisms agree well with those obtained from an upper bound kinematic approach, with a beam-like mechanism involving plastic hinges at the clamped supports and mid-span for the case $2L/R = 30$.

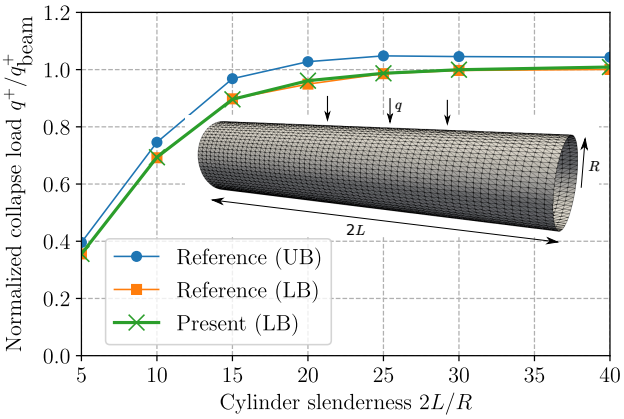


(a) Limit load results: reference LB and UB limit loads from Bleyer and de Buhan (2016), present LB from Bleyer and Hassen (2021)

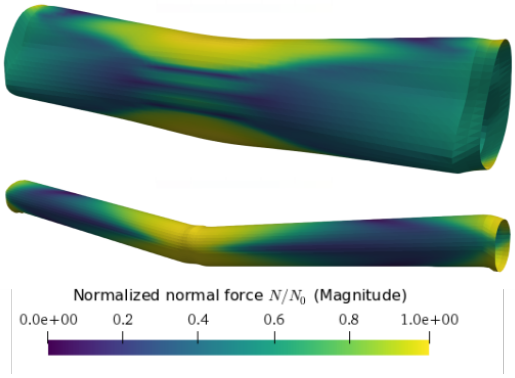


(b) Cylindrical shell pseudo-collapse mechanisms and normalized normal force magnitude $\|\boldsymbol{N}\|/N_0$. Top: slenderness $2L/R = 10$, bottom: slenderness $2L/R = 30$.

Figure 5.3: Cylindrical shell under self-weight

### 5.4.3 A Cosserat-continuum model for jointed rocks

We further illustrate the ability of the proposed framework to tackle generalized continua by considering a Cosserat model for jointed rocks, initially proposed in de Buhan et al. (2002). The governing equations of the model, in plane strain conditions, involve a non-symmetric stress tensor $\boldsymbol{\Sigma} = \begin{bmatrix} \Sigma_{11} & \Sigma_{12} \\ \Sigma_{21} & \Sigma_{22} \end{bmatrix}$ and a couple stress vector $\boldsymbol{H} = (H_1, H_2)$ both expressed in the local reference frame $(\boldsymbol{e}_1, \boldsymbol{e}_2)$ of the jointed rock mass (see Fig. 5.4). The corresponding equilibrium equations read as:

$$\operatorname{div} \boldsymbol{\Sigma} + \boldsymbol{f} = 0 \tag{5.36}$$

$$\operatorname{div} \boldsymbol{H} + \Sigma_{21} - \Sigma_{12} = 0 \tag{5.37}$$

the corresponding weak form obtained from the virtual work principle being:

$$\int_\Omega \left( \boldsymbol{\Sigma}^{\mathrm{T}} : (\nabla \boldsymbol{u} - \operatorname{skew} \omega) + \boldsymbol{H} \cdot \nabla \omega \right) \mathrm{d}\Omega = \int_\Omega \boldsymbol{f} \cdot \boldsymbol{u} \, \mathrm{d}\Omega \tag{5.38}$$

for any continuous test function $\boldsymbol{u}$ and $\omega$ with $\operatorname{skew} \omega = \omega(\underline{e}_2 \otimes \underline{e}_1 - \underline{e}_1 \otimes \underline{e}_2)$ and where we considered only body forces as loading parameters.

As regards strength properties, the rock mass is assumed to obey a Mohr-Coulomb criterion of cohesion $c_m$ and friction angle $\phi_m$. The joints are represented as an orthogonal array, spaced by a length $\ell$ and making an angle $\theta$ with the horizontal axis. They are assumed to also obey a Mohr-Coulomb condition with parameters $(c_j, \phi_j)$. The generalized strength condition for a jointed rock mass modeled as a Cosserat continuum is expressed as (de Buhan

et al., 2002):

$$(\boldsymbol{\Sigma}, \boldsymbol{H}) \in G_{\text{Cosserat}} \Longleftrightarrow \begin{cases} \Sigma_{11} \tan\phi_j + |\Sigma_{21}| \leq c_j \\ \Sigma_{22} \tan\phi_j + |\Sigma_{12}| \leq c_j \\ \dfrac{\ell}{2}\Sigma_{11} + |H_1| \leq \dfrac{\ell}{2}\dfrac{c_j}{\tan\phi_j} \\ \dfrac{\ell}{2}\Sigma_{22} + |H_2| \leq \dfrac{\ell}{2}\dfrac{c_j}{\tan\phi_j} \\ |H_1| \leq \dfrac{\ell}{2}\dfrac{c_j}{\cos\phi_j} \\ |H_2| \leq \dfrac{\ell}{2}\dfrac{c_j}{\cos\phi_j} \\ \operatorname{sym}\boldsymbol{\Sigma} \in G_{\text{MC,2D}}(c_m, \phi_m) \end{cases} \tag{5.39}$$

where the last condition expresses the rock mass Mohr-Coulomb criterion on $\operatorname{sym}\boldsymbol{\Sigma} = (\boldsymbol{\Sigma} + \boldsymbol{\Sigma}^{\mathrm{T}})/2$ and where all other conditions involve the joints resistance. Let us point out that the case $\ell = 0$ induces $H_i = 0$ and thus $\boldsymbol{\Sigma} = \boldsymbol{\Sigma}^{\mathrm{T}}$ due to (5.37), one therefore retrieves a Cauchy model with a strength criterion described by the first, second and last conditions of (5.39). Finally, $G_{\text{Cosserat}}$ involves only linear inequality constraints in addition to the Mohr-Coulomb criterion $G_{\text{MC,2D}}$. It is, therefore, SOC-representable, the part involving joints only being linear-representable.

We considered the stability problem of an excavation of height $H$, making a 25° angle with the vertical and subjected to its self-weight of intensity $\gamma$. The problem amounts to find the maximum value of the non-dimensional stability factor $K^+ = \left(\dfrac{\gamma H}{c_m}\right)^+$. For numerical applications, we took $c_j = 0.5c_m$, $\phi_j = 20°$, $\phi_m = 40°$, $\theta = 10°$ and varied the joint spacing $\ell$. The evolution of the stability factor estimates as a function of $\ell/H$ has been represented in Fig. 5.4b for two different mesh sizes. Strengthening of the stability factor is observed for increasing $\ell/H$ ratios. The obtained value in the standard Cauchy ($\ell = 0$) case is quite close to the analytical upper bound of $K^+ \leq 1.47$ derived for the same problem in de Buhan et al. (2002). Finally, collapse mechanisms and a measure of the pure Cosserat contribution $(\Sigma_{21} - \Sigma_{12})(u_{2,1} - u_{1,2} - \omega) + \boldsymbol{H} \cdot \nabla\omega$ to the total dissipation have been represented in Fig. 5.5. It can be observed that the shape of the collapse mechanism and the location of "shearing" zones involving Cosserat effects is quite dependent on the joint spacing. For $\ell = 0$, a triangular sliding block with a concentrated slip zone is obtained, approximately corresponding to the merging of the two slip bands of Fig. 5.5a.

## 5.5 Civil engineering applications

In this section, we will present some practical applications of finite-element based limit analysis for civil engineering problems. Examples of Section 5.5.1 and Section 5.5.2 are extracted from industrial PhD theses made in collaboration with the engineering company Strains[2]. The corresponding developments and results have been implemented in the company's internal software. The latter uses the same methodology, i.e. lower and upper-bound finite-element discretization, conic formulations and interior-point solver, as the one presented earlier in this chapter. In particular, I have helped the company to develop its own primal-dual interior point solver for SOCP and SDP problems.

[2] https://strains.fr/

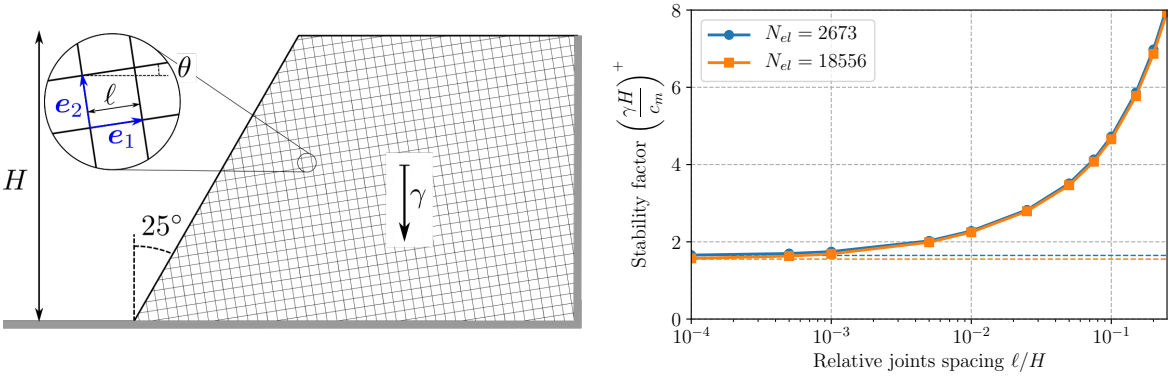


(a) Geometry

(b) Evolution of the stability factor as function of the joints spacing $\ell/H$ for two mesh sizes (dashed lines correspond to standard continuum limit analysis results $\ell = 0$).

Figure 5.4: Stability of a jointed rock excavation

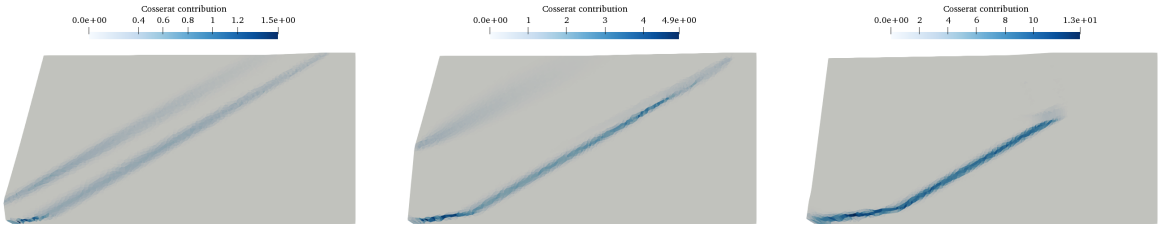


(a) $\ell/H = 0.001$ (b) $\ell/H = 0.01$ (c) $\ell/H = 0.1$

Figure 5.5: Collapse mechanism of the jointed rock excavation and pure Cosserat contribution to the total dissipation

### 5.5.1 Complex 3D steel connections

#### Introduction

The first application concerns complex 3D assemblies found in steel construction. Steel assemblies connect different parts of a structure using various topologies designed specifically to transmit a given type of force. In simple industrial buildings, connections can be modeled using simplifying hypothesis such as nominally-pinned or fully-rigid connections between the elements. However, engineers are facing today new 3D connection topologies where a large number of members converge to the same point in different angles and sizes (see Fig. 5.6).

Figure 5.6: A complex 3D steel structure - *Fondation Louis Vuitton*

The behavior of the steel connection is neither fully-rigid nor nominally-pinned. In reality, all steel assemblies are semi-rigid, and their stiffness and ultimate resistance varies due to the contact between the steel plates, bolts, welds and the possible yielding or buckling of some parts.

The Eurocode design rules provide some approximate methods to evaluate the mechanical characteristics of steel assemblies such as the sub-components method. However, these calculations are often extremely time-consuming and rely on simplified models with large safety coefficients therefore providing uneconomical designs.

The design of steel assemblies is to be considered one of the biggest challenges of steel structures engineering. Few software used in engineering practice can efficiently handle such intrinsically three-dimensional models using a first-order elastic analysis, let alone a full second-order plastic analysis coupling contact interfaces with material non-linearities and geometrical non-linearities.

The main objective of Chadi El Boustani's PhD work (El Boustani, 2020) was to provide engineers with a robust and efficient numerical tool for the ultimate state analysis of such assemblies. Note that this tool has also been extended to elastoplastic simulations, including contact, both in a small and finite-strain setting as discussed in Section 4.6.4.

#### Analysis of a column base plate

According to the Eurocodes (EC) (EN1993–1-1, 2005; EN1993–1-8, 2005), a typical steel assembly ultimate design analysis relies on the so-called *component method* where the complex assembly is divided into basic components (Fig. 5.7). Each of them is then checked against various failure mechanisms assembled to derive an estimate of the ultimate resistance of the connection. Note that computing the strength of even basic component can be sometimes

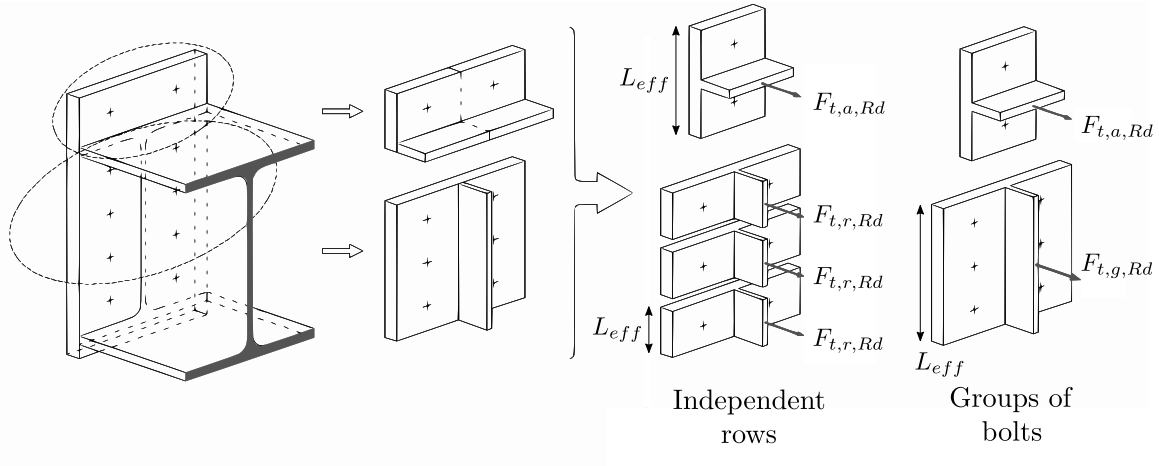


Figure 5.7: A descriptive explanation of the components method

difficult. In such cases, EC provides guidelines to replace the corresponding component with an equivalent T-stub (of effective length $L_{eff}$) which is simpler to analyse.

However, even for a classical base column under tensile loading as shown in Fig. 5.8, the component method requires more than 20 sub-components should be analysed (Fig. 5.9). This manual procedure quickly becomes impractical for more complex assemblies. As an alternative, we used a 3D finite-element model of the assembly to determine its ultimate strength. The HEB column is welded to a base plate which is bolted to its final support, fillet welds are explicitly modeled and contact conditions are enforced around the bolts. Both lower and upper-bound finite-element simulations are run, providing a bracketing of the assembly tensile strength between $F_{\text{T,lower}} = 335\,\text{kN}$ using the lower bound approach and $F_{\text{T,upper}} = 354\,\text{kN}$ using the upper bound approach. The associated 3D collapse mechanism represented in Fig. 5.10 involves yielding in bending of the base plate. As plastic dissipation mostly concentrates near the welds and the bolts, the obtained mechanism looks similar to a yield-line mechanism as commonly considered for plates in bending.

Indeed, the manual computation according to the Eurocode identifies the yield-line mechanism of Fig. 5.11a as the most critical one associated with a tensile strength of $F_{T,rd} = 312\,\text{kN}$. Clearly, both mechanisms are very close to each other. The small difference in terms of predicted strength is due to the fact that the Eurocode simplified approach does not take into consideration 3D effects, nor the complete curvature seen in the yield line, nor the contribution of the bolt heads to the assembly strength. The predicted strength is therefore slightly more conservative.

**More complex assemblies**

In this paragraph, we briefly describe two other complex assemblies that were analyzed using the industrial software developed by Strains. These assemblies are part of a large set of checks that were made for a structural engineering firm. Geometry details and load cases are omitted in order to simplify the presentation and preserve the confidentiality of the study.

Two complex assemblies are briefly presented:

- a 3D bracing assembly (Fig. 5.12a) in which the applied loads are mainly tension or compression forces in the converging bracing members obtained from a global 3D model of the whole structure;

- a moment transmitting assembly (Fig. 5.12b) in which the applied load is a combination

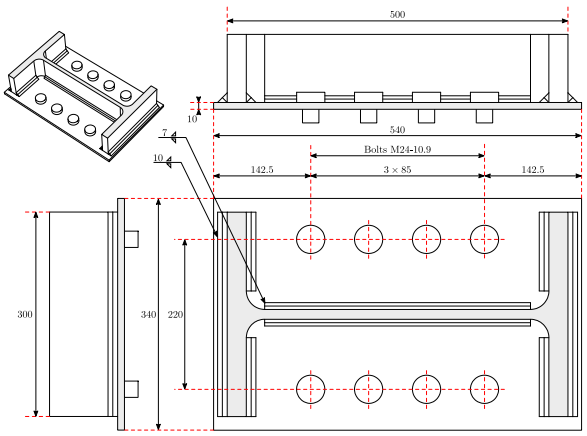


Figure 5.8: Description of the column base plate model

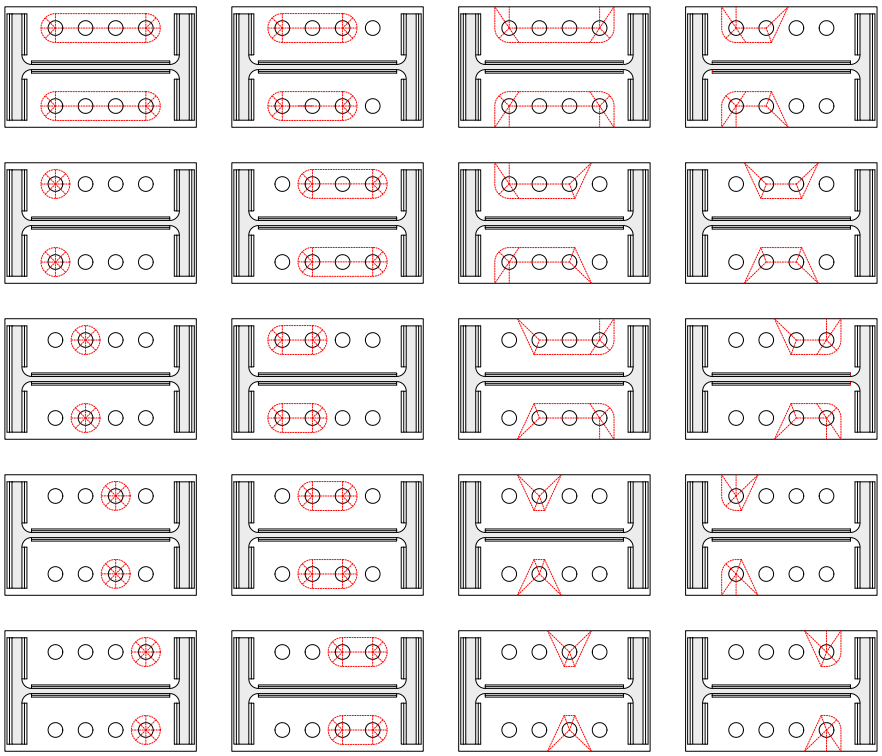

Figure 5.9: Illustration of all failure mechanisms to check (the dashed red lines represent yield lines)

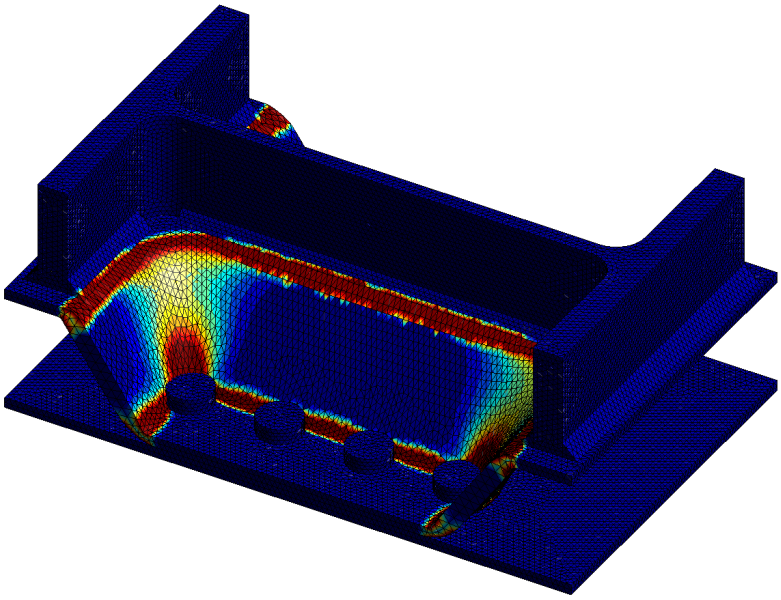

Figure 5.10: 3D failure mode obtained by the finite-element limit analysis (color indicates plastic dissipation)

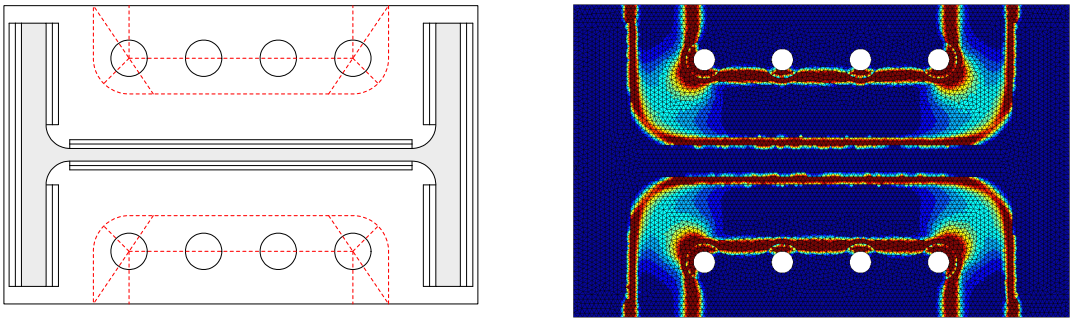

(a) Expected yield mechanism (the dashed red lines represent yield lines)

(b) Plastic dissipation concentration matches the expected shape of the yield lines in Fig. 5.11a

Figure 5.11: Top view of the critical failure mechanism

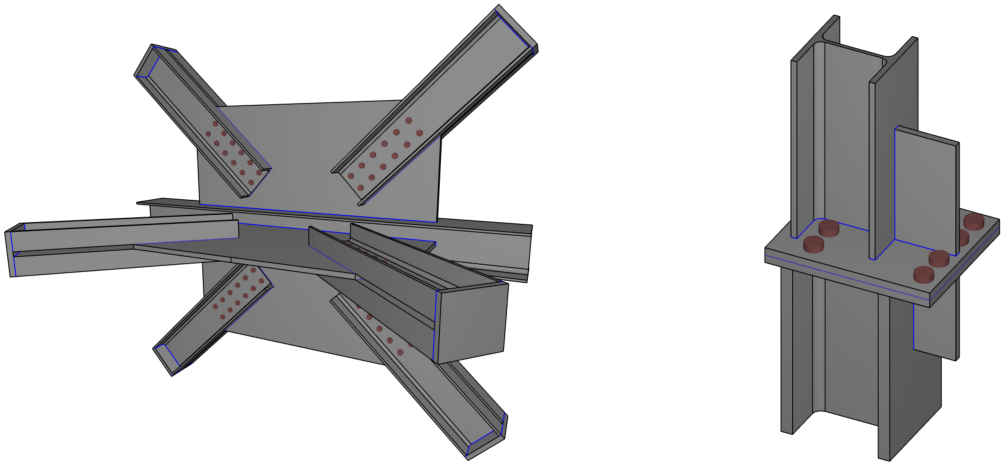

(a) A wind bracing assembly

(b) A continuity assembly

Figure 5.12: Complex 3D assemblies

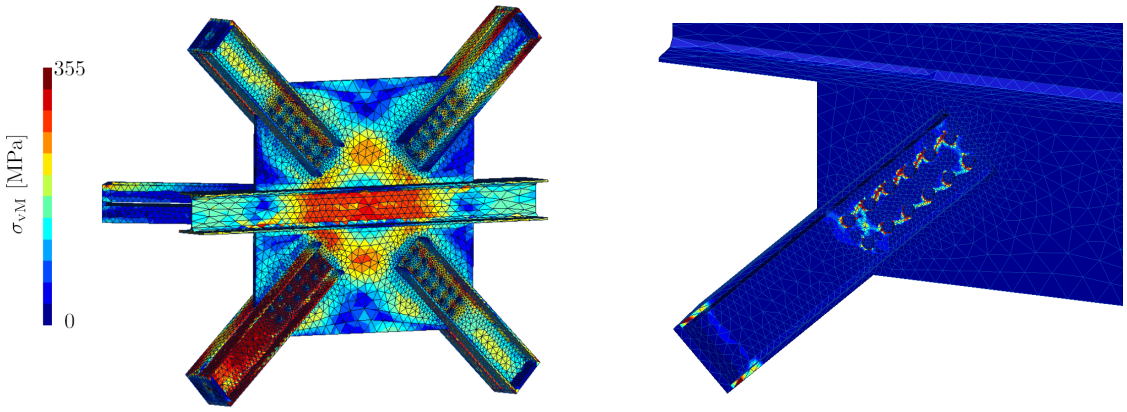


(a) Equivalent von Mises plastic stress isovalues (b) Plastic dissipation in the critical diagonal

Figure 5.13: Wind bracing analysis

of a uniaxial bending moment, normal and shear force.

In the case of the first assembly, failure occurs in one of the bracing members where the web plate fails in bearing due to a critical bearing pressure as shown in Fig. 5.13b. One can also see in Fig. 5.13a that the elastic limit, in this case $f_y = 355\,\text{MPa}$ is reached in the same diagonal member. The upper bound provides a load factor of 2.2 for the corresponding load case while the lower bound approach yields a load factor of 1.9. The gap between the two results can be reduced by reducing the mesh size in the failure area.

For the second assembly, the failure mechanism involves bending of the top beam as well as bending of the end-plate (Fig. 5.14a). As before, failure of the end-plate can be matched to a complex yield-line mechanism as shown in Fig. 5.14b.

The mesh used for both examples consisted of roughly 5.5 million degrees of freedom. The interior point method shows a very efficient behavior with a number of iteration remaining stable compared to smaller problems (22 to 24 iterations) and a CPU time of approximately 315 s per iteration (OpenMP parallelization over 8 cores), resulting in a computing time of 2h per analysis.

### 5.5.2 Massive reinforced-concrete structures

In this section, we consider the case of massive 3D reinforced-concrete structures. Contrary to steel, concrete is not a perfectly plastic material as it is brittle in tension and damageable in compression. However, including steel rebars reinforcements often provide enough ductility to reinforced-concrete structures so that limit analysis concepts can also be applied to this case. Nevertheless, one must keep in mind this fundamental difference and ensure that ductility requirements are satisfied, that the failure mechanism does not involve tensile failure of concrete, etc. This makes the analysis of concrete structure particularly difficult, accounting also for the fact that damage models are difficult to handle in practice due to damage localization and mesh dependence issues, see Chapter 8.

With such precautions in mind, the design of reinforced-concrete structures at ultimate state covered by Eurocode 2 essentially distinguishes two types of structural regions:

- so-called *B-regions* where beam theory applies and design is based the cross-section properties

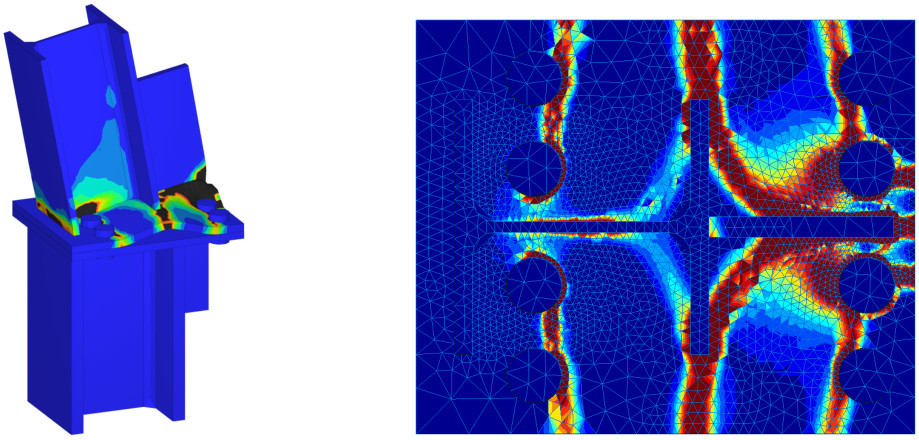

(a) 3D failure mechanisms (b) 2D view of plastic dissipation

Figure 5.14: Continuity assembly failure mechanism

- and so-called *D-regions* corresponding to regions of geometry or loading discontinuities, boundaries, etc.

The latter are much more involved to design as they require a local 2D/3D analysis. To simplify such an analysis, Eurocode 2 relies on a simplified approach called the *strut-and-tie method*, see also in Chapter 6. This method relies on an idealization of the flow of forces inside a structure in the form of a truss consisting of concrete struts in compression and steel reinforcements (or ties) in tension. Equilibrium conditions are enforced at nodes, strut and ties strength capacities are verified according to their corresponding cross-section and additional strength conditions are enforced at the nodes using 3D stress states. In this sense, the strut-and-tie method is a simplified lower-bound limit analysis which looks for a stress state in equilibrium satisfying the materials strength conditions. The main difference with a finite-element based lower bound limit analysis is that the stress state is not a general 3D field but is simplified in the form of a truss with members and nodes, resulting in a simplified analysis. However, the main difficulty when implementing such a method is to find a relevant truss layout for complex or non-conventional cases. In practice, a first 3D elastic analysis is often conducted in order to guide the engineer's intuition towards a relevant truss layout. Here, we advocate the use of 3D finite-element limit analysis of reinforced concrete structures to directly provide a relevant stress field and accurate estimate of the collapse load.

#### 3D limit analysis of reinforced-concrete structures

The PhD work of Hugues Vincent, again in collaboration with Strains, has been devoted to the implementation of a similar limit analysis tool for 3D RC structures (Vincent, 2018). Concrete is modeled using a Mohr-Coulomb or a Rankine strength criterion with very small tensile strength. As seen in Section 5.2.3, the corresponding 3D limit analysis problems result in large-scale semi-definite programs, which makes them inherently more challenging to solve than their SOCP counterparts for 3D steel structures. Again both lower and upper bound discretizations have been developed (Vincent et al., 2018, 2020).

A specific emphasis must however be put on the modeling of steel rebars. Indeed, modeling them explicitly as 3D cylinders often results in very fine mesh sizes and complex meshing densities. Fortunately, 3D reinforced-structures often consist of regions where steel reinforcement is arranged in a periodic array of identical steel rebars. In such regions, we can

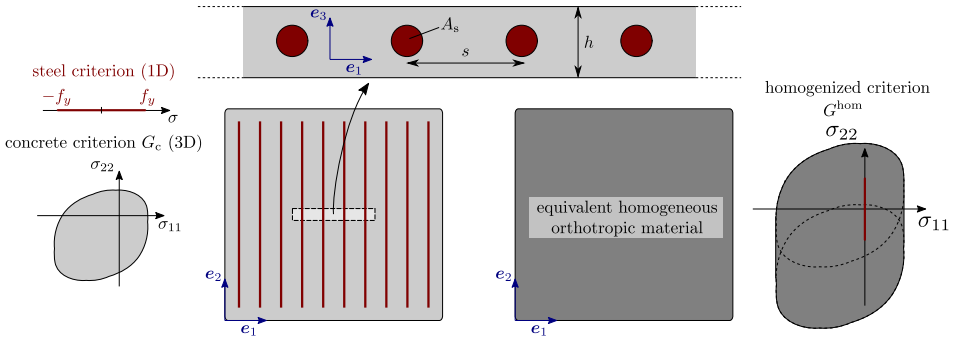


Figure 5.15: Homogenization of a periodic material (concrete in gray) reinforced by linear 3D inclusions (steel rebars in red).

resort to homogenization theory to replace individual rebars with an equivalent homogenized layer for which mesh size requirements will be much less stringent.

Let us consider a 2D region consisting of a periodic array of parallel rebars oriented along direction $\boldsymbol{e}_2$ as in Fig. 5.15. Accounting for the fact that rebars are in small volume fraction and assuming perfect bonding between concrete and steel rebars, the homogenized strength criterion can be written as:

$$\boldsymbol{\sigma} \in G^{\text{hom}} \quad \leftrightarrow \exists \boldsymbol{\sigma}^{\text{c}}, \sigma^{\text{r}} \text{ s.t. } \begin{cases} \boldsymbol{\sigma} = \boldsymbol{\sigma}^{\text{c}} + \sigma^{\text{r}} \boldsymbol{e}_2 \otimes \boldsymbol{e}_2 \\ \boldsymbol{\sigma}^{c} \in G^{\text{c}} \\ |\sigma^{r}| \leq \eta^{\text{r}} f_y \end{cases} \tag{5.40}$$

where the total stress $\boldsymbol{\sigma}$ can be decomposed as the sum of a 3D partial stress $\boldsymbol{\sigma}^{\text{c}}$ in the concrete phase and a 1D partial stress $\sigma^{r}$ in the reinforcement phase. The former must satisfy the reinforced concrete criterion $G^{\text{c}}$ whereas the latter should satisfy a uniaxial stress criterion involving the steel elastic limit $f_y$ and $\eta^{\text{r}}$ is the reinforcement volume fraction defined as:

$$\eta^{\text{r}} = \frac{A_{\text{s}}}{sh} \tag{5.41}$$

with $A_{\text{s}}$ being the cross-section of a single rebar, $s$ the rebar spacing and $h$ the layer thickness. The above composite criterion is therefore given by the Minkowski sum of the bulk concrete criterion $G^{\text{c}}$ and a segment $[-\eta^{\text{r}} f_y; \eta^{\text{r}} f_y]$ along direction 22. Geometrically, it can be obtained as the convex hull of two copies of $G^{\text{c}}$ translated by $\pm\eta^{\text{r}} f_y$ along direction 22 (see Fig. 5.15-right). Obviously, it can be extended to the case of non-symmetric strengths in tension and compression or another set of inclusions oriented, for instance, along $\boldsymbol{e}_1$.

**Remark 8.** Formula (5.40) heavily relies on the two assumptions of small volume fraction and perfect bonding. Relaxing the first one would imply solving a 3D limit analysis problem over the periodic unit cell. Our numerical tools enable to do such a computation quite easily. However, using the numerically computed criterion in a limit analysis problem at the structure scale is however much more difficult. Indeed, one needs to resort to approximation procedures to express the obtained numerical yield surface using conic constraints. The interested reader may refer to references (Bleyer and de Buhan, 2013a,d, 2014a) for more details on this aspect.

Relaxing the perfect bonding assumption would require to resort to a specific class of generalized continua called *multiphase continua* where both concrete and reinforcement phases are endowed with their own kinematics. A specific interfacial strength condition could then be considered to account for a possible loss of steel rebar anchorage. Again, the reader can refer to (de Buhan et al., 2017) and references therein.

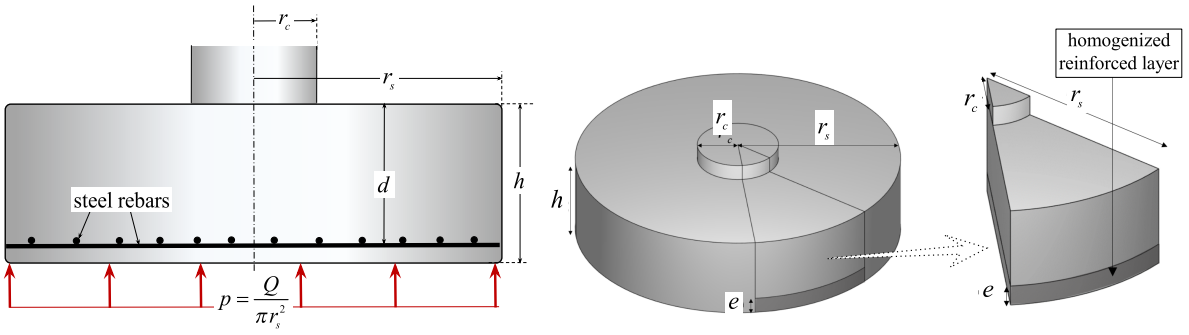


(a) 2D view and loading

(b) 3D view and 45° slice

Figure 5.16: Reinforced-concrete circular footing

Obviously, there are practical cases where homogenization cannot be used directly. In Vincent et al. (2018), we investigated a strategy in which a single rebar can be diluted in a larger region using the homogenized formulation. This approach requires a coarser mesh than meshing the real rebar diameter in 3D but needs to identify an appropriate smearing length scale. More recently, we worked on a specific finite-element formulation enabling to use embedded 1D bars in a 3D mesh (Ferradi et al., 2023). This approach is much more interesting regarding mesh generation but allows only for pseudo lower-bound estimates of the ultimate load.

**Load-bearing capacity of a reinforced-concrete footing**

As an illustration of 3D limit analysis in reinforced-concrete structures, we consider the computation of the load-carrying capacity of a circular slab (thickness $h$, radius $r_s$) used as a building or bridge foundation system (Fig. 5.16a). It is rigidly connected in its central upper part to a column (bridge pier for instance) of radius $r_c < r_s$. The action of the underlying soil is simply modeled by means of a uniform pressure applied on the footing base equal to: $p = Q/(\pi r_s^2)$ where $Q$ is the total resulting force applied by the foundation to the soil. The concrete footing has been reinforced in its lower part by a system of steel rebars which are homogenized as a uniform layer of orthotropic reinforced material (Fig. 5.16b). Finally, we model a 45° slice accounting for symmetry conditions. The objective of the analysis is to investigate, for a given geometry of the footing, the influence on the bearing capacity $Q^+$ of the reinforcement ratio $\omega$ defined as:

$$\omega = \frac{A_s}{2hr_s}\frac{f_y}{f_c} \tag{5.42}$$

where $A_s$ is the total area of reinforcement in a meridional ($x = 0$ or $y = 0$) cross-section and $f_y$, $f_c$ are the steel and concrete yield strengths.

The results of our analysis will be compared to those established by Simões et al. (2016) who implemented a semi-analytical kinematic approach in a simplified axisymmetric setting[3]. It is based upon two families of simple failure mechanisms, called M1 and M2, represented in Fig. 5.17 in any meridian plane passing through the symmetry axis, with the cylindrical coordinates $(r - z)$. The first kind of mechanism (M1, Fig. 5.17a) corresponds to a rigid body

[3]Note that the orthotropic reinforcement layout breaks the symmetry around the vertical axis. However, we verified numerically that the solution is essentially influenced by the reinforcement ratio $\omega$ but not by the exact reinforcement layout (orthogonal vs. orthoradial grid for instance).

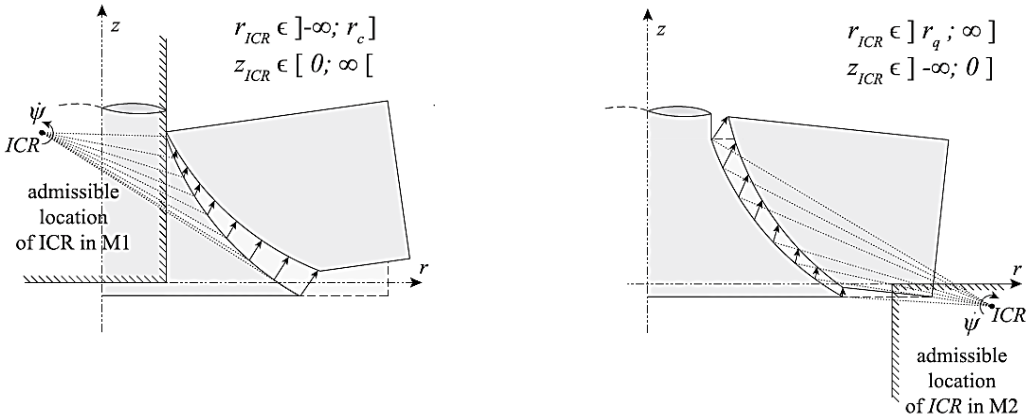


(a) Mechanism M1 (b) Mechanism M2

Figure 5.17: Failure mechanisms M1 and M2 used in the kinematic approach of limit analysis by Simões et al. (2016).

motion of an external part of the slab separated from its central part by a velocity discontinuity line, the instantaneous centre of rotation (ICR) being located in the upper left quarter of plane defined in the same figure. The second kind of mechanism (M2, Fig. 5.17b) corresponds to the situation when the ICR is located in the lower right quarter of plane. Simões et al. (2016) determined the optimal location of the ICR for each mechanism numerically and proposed simplified analytical expressions approximating the obtained results with satisfying accuracy.

The numerical bounds obtained from our 3D limit analysis are represented by the two red coloured (upper bound) and blue coloured (lower bound) curves of Fig. 5.18 for the following values of the strength parameters:

$$f_c = 30\,\text{MPa} \quad ; \quad f_t = 0.1\,\text{MPa} \quad ; \quad f_y = 500\,\text{MPa} \tag{5.43}$$

and a geometry of the footing defined by the following non-dimensional parameters:

$$r_c/d = 0.5 \quad ; \quad (r_s - r_c)/d = 1.5 \quad ; \quad r_s/r_c = 4 \tag{5.44}$$

The results are compared against the analytical predictions of Simões et al. (2016) who identified that failure is dictated by a *flexural-shear* mechanism for low values of the reinforcement ratio $\omega$ and by a "*punching shear*" failure for large values of the reinforcement ratio.

We can observe that our 3D predictions agree well with the analytical estimates of Simões et al. (2016). More precisely, while the flexural-shear predictions are higher that the 3D predictions, the punching-shear prediction (which is independent of the reinforcement ratio) lies within the interval formed by the 3D upper and lower bound estimates. It must however be kept in mind that the analytical predictions correspond to approximations of a purely kinematic approach in an axisymmetric setting.

Finally, deeper insight can be gained from analyzing the obtained velocity fields represented in Fig. 5.19 for three increasing reinforcement ratios: $\omega = 0.05; 0.20; 0.375$. It deserves the following comments:

- For the lowest reinforcement ratio ($\omega = 0.05$, Fig. 5.19a) where all calculation methods lead to very close estimates of the load-bearing capacity, the observed velocity field corresponds to a pure *flexural* mechanism, in which the external part of the footing is given, in the median plane, a rigid body motion with a centre of rotation located in the vicinity of the central supported column.

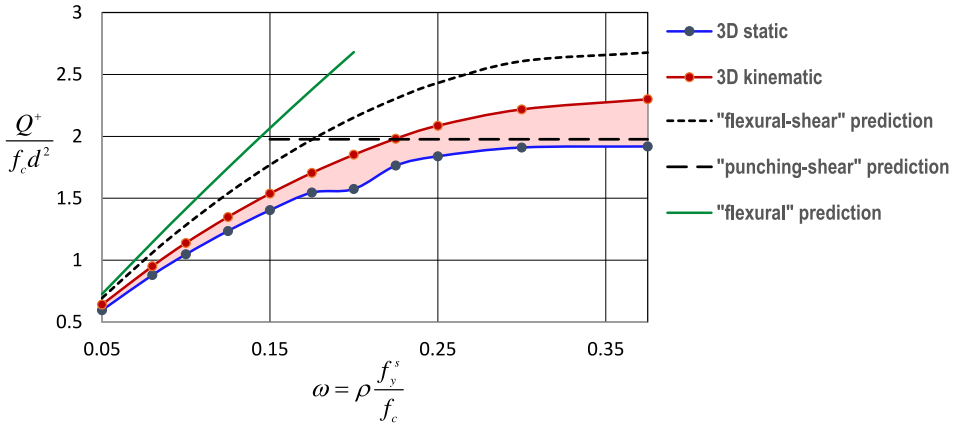


Figure 5.18: Comparison between different estimates of the footing load-bearing capacity as functions of the reinforcement ratio

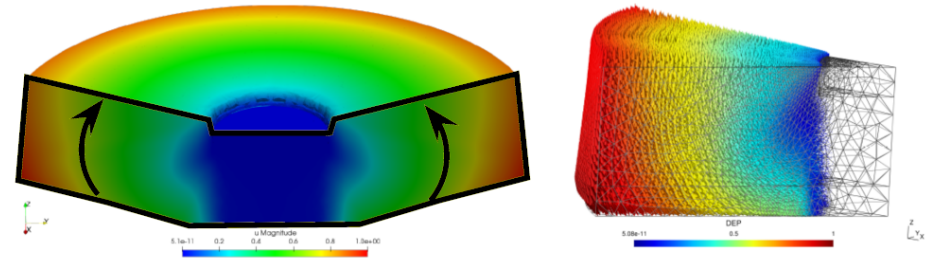

(a) $\omega = 0.05$

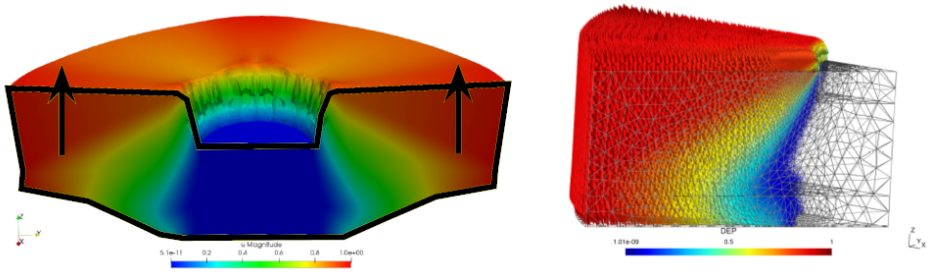

(b) $\omega = 0.20$

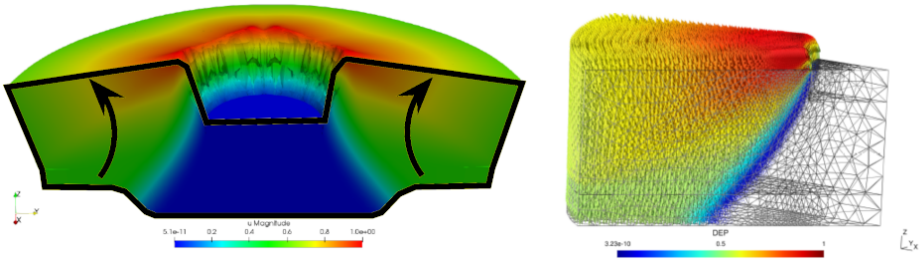

(c) $\omega = 0.375$

Figure 5.19: Optimal failure mechanisms obtained for three different reinforcement ratios

- Conversely, for an intermediate value of the reinforcement ratio ($\omega = 0.20$, Fig. 5.19b) the optimal velocity field corresponds to a *punching-shear* mechanism, that is to a uniform vertical translation of an external ring-shaped part of the footing, while the central part around the column remains motionless.
- Finally, for the highest value of the reinforcement ratio ($\omega = 0.375$, Fig. 5.19c), the optimal velocity field is also of *punching-shear* type but with a rigid body motion around of centre of rotation located outside the footing.

## 5.6 Conclusions

This chapter has discussed the numerical implementation of limit analysis theory in a finite-element setting. The structure ultimate load is estimated by accounting for a material strength criterion through the resolution of stress and displacement variational principles. Upon selection of appropriate finite-element discretization spaces and quadrature rules, their resolutions leads to guaranteed lower and upper bound estimates, respectively. However, such variational problems lead to complex, non-smooth, and large-scale convex optimization problems, which are addressed with conic programming and interior-point algorithms. The development of a Domain-Specific Language dedicated to formulating convex variational problem enables to automate limit analysis problems for various mechanical models.

This chapter also highlighted the usefulness of such computational tools for assessing the load-bearing capacity of complex civil engineering structures in various domains. For instance, limit analysis-based software have also recently emerged in the field of geotechnical engineering, see the Optum Computational Engineering[4] products for instance.

The next two chapters present more recent developments which were motivated by extending limit analysis concepts from their classical setting. In Chapter 6, we will present how limit analysis and topology optimization concepts can be used together to optimize a structure geometry with respect to its load-bearing capacity. In Chapter 7, we will discuss how limit analysis can be extended to account for uncertainties either in material properties or loading values.

[4] https://optumce.com/

# Chapter 6

# Optimal design of structures using convex shape optimization

This chapter is devoted to an extension of the previously introduced concepts and numerical tools to the problematic of shape optimization in structural mechanics. Our contribution to this domain is based on a convex optimization viewpoint of topology optimization formulations which can be extended to generic constitutive models. When applying the proposed approach to a limit analysis setting, we obtain a topology optimization formulation which looks for the optimal structure maximizing the overall load-bearing capacity, instead of the elastic compliance for instance. An important aspect of this setting is related to the choice of the corresponding strength criterion which we discuss. We then consider the case of multi-material optimization, focusing in particular on structures made of uniaxial reinforcements with either fixed or unknown orientations. Numerical applications show deep links with the strut-and-tie method used in practice for the design of reinforced concrete structures. This chapter ends with applying similar concepts to form-finding of optimal shell or vault structures subject to compression only.

## Contents

## 6.1 Introduction

*Shape optimization* covers the generic problem of finding an optimal shape or an optimal distribution of material which minimizes or maximizes a given objective function subject to some cost constraints (e.g. fixed total volume). Depending on the type of optimization variable and the set of admissible solutions, one obtains various classes of problems. The most basic is the *parametric optimization* where only a few parameters (e.g. length, width of a rectangular domain, elastic modulus, etc.) are optimized. *Geometric optimization* then amounts to find the optimal shape from an initial guess and then move its boundary towards an optimum. In this case, topological changes (addition of matter or holes) is not allowed. Finally, *topology optimization* allows for a generic optimization with topological changes and is thus more challenging.

Objective functions in shape optimization can be very diverse depending on the application e.g. maximum stiffness or target displacement in quasi-statics, target eigenfrequency in dynamics, maximum damping coefficient for viscous materials, etc. In the setting of static linear elasticity, the most simple problem consists in finding an optimal shape $\Omega$ which would maximize the structural stiffness for a given loading and an imposed volume of material. More formally, stiffness maximization or compliance minimization can be formulated as follows:

$$\begin{array}{lll} \min\limits_{\Omega,\boldsymbol{u}} & \displaystyle\int_{\partial\Omega} \boldsymbol{T}\cdot\boldsymbol{u}\,\mathrm{d}S & \\ \text{s.t.} & \boldsymbol{\sigma} = \mathbb{C}_0 : \nabla\boldsymbol{u} & \text{in } \Omega \\ & \operatorname{div}\boldsymbol{\sigma} = 0 & \text{in } \Omega \\ & \boldsymbol{\sigma}\boldsymbol{n} = \boldsymbol{T} & \text{on } \partial\Omega_{\mathrm{N}} \\ & \boldsymbol{u} = 0 & \text{on } \partial\Omega_{\mathrm{D}} \\ & |\Omega| = \eta|\mathcal{D}| & \end{array} \tag{6.1}$$

where $\mathbb{C}_0$ is the material stiffness, $\eta \in [0;1]$ is the imposed volume fraction, $\boldsymbol{T}$ an imposed external loading applied on the boundary and $\Omega$ belongs to some set of admissible shapes (typically contained inside a computational domain $\mathcal{D} \supseteq \Omega$). Note that in (6.1), the structural compliance has been written here as the work of external loads. Indeed, in the case of zero prescribed displacement, a stiff structure will correspond to minimal displacements under the imposed external loads. However, this definition of compliance does not work in the case of non-zero prescribed displacement as discussed in Barbarosie and Lopes (2011); Niu et al. (2011).

The difficulty of this formulation is obviously that one has to optimize over a *shape* $\Omega$. Moreover, there is no existence result of well-defined optimal shapes in general. Various methods have therefore been proposed in the literature to parameterize this optimization problem by enlarging the class of admissible solutions for which optimal solutions do exist.

One of them is the homogenization method (Allaire, 2012) which operates on a local volume fraction and an effective stiffness tensor which represents an underlying microstructure. Note that the microstructure can vary locally and adapt in an optimal fashion to the local stress distribution. To obtain manufacturable shapes, a specific penalization procedure is often introduced in order to produce black-and-white designs. Another class of methods relies on the introduction of a scalar fictitious densitiy field $\rho \in [0;1]$ defined on the computational domain $\mathcal{D}$, the most popular being by far the Solid Isotropic Material Penalization (SIMP) (Bendsøe and Sigmund, 2004). In this case, a specific assumption is made on the form $\mathbb{C}(\rho)$ of the stiffness tensor on $\rho$, namely:

$$\mathbb{C}(\rho) = \rho^p \mathbb{C}_0 \tag{6.2}$$

where $p > 1$ is progressively driven from 1 to $p_{\max}$ (typically around 3) in order to penalize intermediate densities. The corresponding minimization problem therefore reads:

$$\begin{array}{lll} \min\limits_{\rho,\boldsymbol{u}} & \displaystyle\int_{\partial\mathcal{D}} \boldsymbol{T}\cdot\boldsymbol{u}\,\mathrm{d}S & \\ \text{s.t.} & \boldsymbol{\sigma} = \rho^p\mathbb{C}_0 : \nabla\boldsymbol{u} & \text{in } \mathcal{D} \\ & \operatorname{div}\boldsymbol{\sigma} = 0 & \text{in } \mathcal{D} \\ & \boldsymbol{\sigma}\boldsymbol{n} = \boldsymbol{T} & \text{on } \partial\mathcal{D}_{\mathrm{N}} \\ & \boldsymbol{u} = 0 & \text{on } \partial\mathcal{D}_{\mathrm{D}} \\ & 0 \le \rho \le 1 & \text{in } \mathcal{D} \\ & \int_{\mathcal{D}} \rho\,\mathrm{d}\Omega = \eta|\mathcal{D}| & \end{array} \tag{6.3}$$

Note that the above problem is convex if $p = 1$ and non-convex as soon as $p > 1$. A typical solving strategy amounts to alternatively minimize with respect to $\boldsymbol{\sigma}$ and $\rho$. To avoid checkerboard instabilities, filtering strategies are generally introduced, e.g. non-local sensitivity filtering. Restriction methods aim at removing mesh dependency due to the emergence of finer and finer microstructure, one can mention for instance perimeter control, gradient control, Helmholtz filters, etc. The reader can refer to Sigmund and Petersson (1998) for a general review.

Finally, let us also mention other topology optimization approaches: the level-set method (Allaire et al., 2004) which relies on a level-set description of the shape $\Omega$ and uses shape derivatives to optimize for the location of the shape boundary; Evolutionary Structural Optimization (Xie and Steven, 1997) (ESO/BESO) which use element erosion (and insertion), free material optimization (Zowe et al., 1997), etc.

Note that, in most cases, the topology optimization pipeline consists in an iterative procedure involving a direct calculation with fixed values of the optimization variables (density field, homogenized stiffness tensor, etc.), followed by an evaluation of the gradient of the objective with respect to such parameters (the so-called *sensitivities computation*) and a gradient descent step to update the new parameters (potentially with some penalization and filtering steps as discussed before). In this numerical chain, the computation of sensitivities might be quite challenging, especially when extending the previous elastic compliance minimization setting to nonlinear behaviours. For instance, for non-smooth behaviours such as elasto-plasticity, sensitivities or shape derivatives are often computed by replacing the original non-smooth behaviour with a regularized smooth behaviour (Allaire et al., 2018). Overall, in such non-smooth cases, the convergence of the iterative procedure might therefore be more difficult to obtain.

In the following, we will depart from this usual strategy and propose instead a convex optimization formulation in a generic thermodynamic setting. This point of view offers new insights on topology optimization formulations for general material behaviours. Moreover, it makes it possible to optimize simultaneously over the mechanical fields and the density variable, thereby avoiding the need of computing sensitivities which will prove very useful for non-smooth behaviours.

## 6.2 A generic convex optimization formulation

### 6.2.1 Elastic compliance minimization

Let us first revisit the elastic compliance minimization problem (6.1). The latter benefits from a purely stress-based formulation since the work of external forces is related to the total

complementary elastic energy. Our forthcoming proposal will therefore rely on a topology optimization formulation based on the dual stress-based variational principle which reads here:

$$\begin{array}{lll} \min\limits_{\Omega,\boldsymbol{\sigma}} & \displaystyle\int_\Omega \frac{1}{2}\boldsymbol{\sigma} : (\mathbb{C}_0)^{-1} : \boldsymbol{\sigma}\,\mathrm{d}\Omega & \\ \text{s.t.} & \operatorname{div}\boldsymbol{\sigma} = 0 & \text{in } \Omega \\ & \boldsymbol{\sigma}\boldsymbol{n} = \boldsymbol{T} & \text{on } \partial\Omega_{\mathrm{N}} \\ & |\Omega| = \eta|\mathcal{D}| & \end{array} \tag{6.4}$$

Note that in the case of non-zero prescribed displacement $\boldsymbol{u} = \bar{\boldsymbol{u}}$ on $\partial\Omega_{\mathrm{D}}$, the compliance $C$, defined as the objective of the above minimization problem, would be in fact:

$$C = \int_\Omega \frac{1}{2}\boldsymbol{\sigma} : (\mathbb{C}_0)^{-1} : \boldsymbol{\sigma}\,\mathrm{d}\Omega - \int_{\partial\Omega_{\mathrm{D}}} (\boldsymbol{\sigma}\boldsymbol{n})\cdot\bar{\boldsymbol{u}}\,\mathrm{d}S \tag{6.5}$$

$$= -\int_\Omega \frac{1}{2}\boldsymbol{\varepsilon} : \mathbb{C}_0 : \boldsymbol{\varepsilon}\,\mathrm{d}\Omega + \int_{\partial\Omega_{\mathrm{N}}} \boldsymbol{T}\cdot\boldsymbol{u}\,\mathrm{d}S \tag{6.6}$$

recovering the definition proposed in Barbarosie and Lopes (2011); Niu et al. (2011).

Finally, the SIMP counterpart to (6.4) reads:

$$\begin{array}{lll} \min\limits_{\rho,\boldsymbol{\sigma}} & \displaystyle\int_\Omega \frac{1}{2}\rho^{-p}\boldsymbol{\sigma} : (\mathbb{C}_0)^{-1} : \boldsymbol{\sigma}\,\mathrm{d}\Omega & \\ \text{s.t.} & \operatorname{div}\boldsymbol{\sigma} = 0 & \text{in } \mathcal{D} \\ & \boldsymbol{\sigma}\boldsymbol{n} = \boldsymbol{T} & \text{on } \partial\mathcal{D}_{\mathrm{N}} \\ & 0 \le \rho \le 1 & \text{in } \mathcal{D} \\ & \int_{\mathcal{D}} \rho\,\mathrm{d}\Omega = \eta|\mathcal{D}| & \end{array} \tag{6.7}$$

which, again, is convex when $p = 1$ since $(\boldsymbol{\sigma}, \rho) \mapsto (\boldsymbol{\sigma} : (\mathbb{C}_0)^{-1} : \boldsymbol{\sigma})/\rho$ is a convex function of $(\boldsymbol{\sigma}, \rho)$.

### 6.2.2 Extension to convex stress potentials

In the following, we aim at extending the volume-constrained compliance minimization to a generic thermodynamic stress potential $\Psi^*(\boldsymbol{\sigma})$ representing a material behaviour which may be different than classical linear elasticity. For simplicity, we restrict to behaviours without internal state variables and consider a single load step only. We propose the following formulation:

$$\begin{array}{lll} \min\limits_{\rho,\boldsymbol{\sigma}} & \displaystyle\int_{\mathcal{D}} \rho\Psi^*(\boldsymbol{\sigma}/\rho)\,\mathrm{d}\Omega & \\ \text{s.t.} & \operatorname{div}\boldsymbol{\sigma} = 0 & \text{in } \mathcal{D} \\ & \boldsymbol{\sigma}\boldsymbol{n} = \boldsymbol{T} & \text{on } \partial\mathcal{D}_{\mathrm{N}} \\ & 0 \le \rho \le 1 & \text{in } \mathcal{D} \\ & \int_{\mathcal{D}} \rho\,\mathrm{d}\Omega = \eta|\mathcal{D}| & \end{array} \tag{6.8}$$

in which we introduced the *perspective function* $\mathrm{persp}_{\Psi^*}(\rho, \boldsymbol{\sigma}) = \rho\Psi^*(\boldsymbol{\sigma}/\rho)$ in the objective function, see Appendix A.2 for the definition and properties of the perspective function. The above problem is therefore convex owing to the convexity of the perspective. If $\eta = 1$, $\rho = 1$ everywhere is possible and we recover a standard stress-based variational principle. Moreover, this formulation coincides with the SIMP formulation (6.3) with $p = 1$ in the elastic case since $\rho\Psi^*(\boldsymbol{\sigma}/\rho) = \frac{1}{2}\rho(\frac{\boldsymbol{\sigma}}{\rho}) : \mathbb{C}_0^{-1} : (\frac{\boldsymbol{\sigma}}{\rho}) = \frac{1}{2}(\boldsymbol{\sigma} : \mathbb{C}_0^{-1} : \boldsymbol{\sigma})/\rho$.

One can also easily derive the corresponding dual displacement-based problem which reads (see Appendix C.1):

$$\min_{\boldsymbol{u},\Lambda} \int_{\mathcal{D}} \max\{\Psi(\boldsymbol{\varepsilon}); \Lambda\} \, \mathrm{d}\Omega - \int_{\partial\mathcal{D}_{\mathrm{N}}} \boldsymbol{T} \cdot \boldsymbol{u} \, \mathrm{d}S - (1-\eta)|\mathcal{D}|\Lambda \tag{6.9}$$

where $\Lambda \in \mathbb{R}$ is a scalar variable corresponding to the Lagrange multiplier associated with the volume constraint in (6.8). Interestingly, the dual problem (6.9) is similar to a classical potential energy minimum principle, except that a lower limit $\Lambda$ is set on the local potential energy density $\Psi(\boldsymbol{\varepsilon})$. The pseudo-density $\rho$ can be recovered from the optimal dual variables. Note that if $\eta = 1$, that is we allow the pseudo-density $\rho$ to fill the whole domain, $\Lambda$ can take any value and we recover the classical complementary and potential energy principles from (6.8) and (6.9) respectively.

### 6.2.3 Numerical aspects

#### Conic programming modeling

The benefit of having a convex formulation such as (6.8) or (6.9) is that one is guaranteed of the existence of an optimal solution. Moreover, the latter can be efficiently obtained numerically using conic programming solvers if the corresponding original variational problem (without any topology optimization) benefits from a conic formulation. The numerical resolution is slightly more costly (an additional scalar field $\rho$ to solve for) but similar robustness of the conic solver algorithm is expected. Finally, the use of a Domain-Specific Language for convex optimization makes the formulation of such a problem particularly easy. For instance, in the `fenics_optim` package, a `Perspective` operator has been introduced in order to easily model convex functions such as $\rho\Psi^*(\boldsymbol{\sigma}/\rho)$ from an existing convex function object $\Psi^*$.

#### Penalization procedure

In some instances, solving the convex topology optimization problem already provides very interesting results in term of optimal shapes. However, in general, one should expect the solution $\rho(\boldsymbol{x})$ to be a gray-level field with intermediate values which does not correspond to a real material. As discussed before, a penalization procedure must therefore be used in order to obtain black-and-white designs.

Inspired by the SIMP continuation strategy, we would like to replace $\rho$ in the objective of (6.8) with $\rho^p$ for $p > 1$ increasing. Unfortunately, the problem is no longer convex in this case. Akin to the procedure suggested in Mourad et al. (2021), we propose to consider instead a linear approximation of $\rho^p$ for iteration $n+1$, namely:

$$\rho^p \approx a_n + \rho b_n \tag{6.10}$$

where $a_n$ and $b_n$ are coefficients obtained from a previous estimate $\rho_n$ of the pseudo-density field. For instance, two strategies can be investigated:

- tangent approximation:

$$\rho^p \approx \rho_n^p + p\rho_n^{p-1}(\rho - \rho_n) \tag{6.11}$$

  that is:

$$a_n = \rho_n^p(1-p) \quad ; \quad b_n = p\rho_n^{p-1} \tag{6.12}$$

- secant approximation:

$$\rho^p \approx \rho_n^{p-1}\rho \tag{6.13}$$

that is:

$$a_n = 0 \quad ; \quad b_n = \rho_n^{p-1} \tag{6.14}$$

In doing so, we recover convex formulations with the corresponding stress-based problem being:

$$\begin{array}{lll} \min\limits_{\rho,\boldsymbol{\sigma}} & \displaystyle\int_{\mathcal{D}} (a_n + \rho b_n)\Psi^*(\boldsymbol{\sigma}/(a_n+\rho b_n))\,\mathrm{d}\Omega & \\ \text{s.t.} & \operatorname{div}\boldsymbol{\sigma} = 0 & \text{in } \mathcal{D} \\ & \boldsymbol{\sigma}\boldsymbol{n} = \boldsymbol{T} & \text{on } \partial\mathcal{D}_{\mathrm{N}} \\ & 0 \le \rho \le 1 & \text{in } \mathcal{D} \\ & \int_{\mathcal{D}} \rho\,\mathrm{d}\Omega = \eta|\mathcal{D}| & \end{array} \tag{6.15}$$

whereas, adapting the calculations in Appendix C.1, the dual problem now becomes:

$$\min_{\boldsymbol{u},\Lambda} \int_{\mathcal{D}} \left(\max\{b_n\Psi(\boldsymbol{\varepsilon});\Lambda\} - a_n\Psi(\boldsymbol{\varepsilon})\right)\,\mathrm{d}\Omega - \int_{\partial\mathcal{D}_{\mathrm{N}}} \boldsymbol{T}\cdot\boldsymbol{u}\,\mathrm{d}S - (1-\eta)|\mathcal{D}|\Lambda \tag{6.16}$$

The penalization procedure therefore amounts to solve iteratively a series of problems (6.15) by starting from the initial convex formulation (6.8) with $a_0 = 0, b_0 = 1$. At each step, coefficients $a_n$ and $b_n$ are updated and the SIMP penalization exponent $p$ is slightly increased with some heuristic up to reaching a maximum value $p_{\max}$ with $p_{\max} = 3$ typically.

**Filtering**

As discussed before, filtering strategies must be considered to remove checkerboard instabilities and remove mesh dependence of the obtained solutions. In our work, we tested in particular a filtering based on a slope-control constraint following Petersson and Sigmund (1998) :

$$\|\nabla\rho\|_2 \le 1/\ell \quad \text{in } \mathcal{D} \tag{6.17}$$

where $\ell$ is a user-defined minimal characteristic length. With such a constraint, strong gradients of the density field are prevented since $\rho$ is forced to vary between 0 and 1 on a distance which is at least $\ell$. As a result, mesh independent solutions are obtained when $\ell$ is larger than a few mesh sizes. Note that this constraint is convex and directly fits into the conic programming framework. It can be added at a small extra cost without impacting on the overall convergence of the interior-point algorithm.

## 6.3 Optimization of structural load-bearing capacity

The PhD of Leyla Mourad has been the initial motivation for working on topology optimization formulations. The main goal of this PhD was to propose novel methodologies for optimizing reinforced concrete structures. In this case, the overall geometry filled with concrete is generally given and engineers aim at proposing an optimal layout of reinforcements to sustain the applied load and prevent the occurrence of traction in the concrete phase. In order to optimize steel consumption, it therefore appears irrelevant to optimize with respect to a compliance objective function since steel reinforcements do not contribute to the global stiffness, which is essentially due to the concrete. Instead, they contribute, in an essential fashion, to the structure load-bearing capacity. To reach this goal, we first aimed at extending the concepts of limit analysis to the topology optimization setting by finding an optimal

structure which would have a maximum load-bearing capacity. Previously, Damkilde and Krenk (1997) determined an optimized material distribution in reinforced concrete slabs in bending. More recently, the works of Kammoun and Smaoui (2014); Fin et al. (2018); Herfelt et al. (2018) have proposed strength-based topology optimization of von Mises plastic materials using limit analysis formulations. Here, we provide a general formulation of topology optimization in a limit analysis context with a special emphasis on the choice of the strength criterion, including for instance materials with asymmetric tension/compression strengths.

### 6.3.1 LOAD-MAX and VOL-MIN formulations

We now particularize the previous formulations to a stress potential given by the indicator of a convex strength domain $G$ i.e. $\Psi^*(\boldsymbol{\sigma}) = \delta_G(\boldsymbol{\sigma})$ akin to limit analysis formulations. For this purpose, it will be more convenient to consider the displacement-controlled variant of (6.8), similar to (B.2):

$$\begin{array}{rll} \min\limits_{\rho,\boldsymbol{\sigma},\lambda} & \displaystyle\int_{\mathcal{D}} \rho\Psi^*(\boldsymbol{\sigma}/\rho)\,\mathrm{d}\Omega - \lambda U & = -\max\limits_{\rho,\boldsymbol{\sigma},\lambda} \quad \lambda U \\ \text{s.t.} & \operatorname{div}\boldsymbol{\sigma} = 0 \quad \text{in } \mathcal{D} & \boldsymbol{\sigma} \in \rho G \quad \text{in } \mathcal{D} \\ & \boldsymbol{\sigma}\boldsymbol{n} = \lambda \boldsymbol{T} \quad \text{on } \partial\mathcal{D}_{\mathrm{N}} & \operatorname{div}\boldsymbol{\sigma} = 0 \quad \text{in } \mathcal{D} \\ & 0 \le \rho \le 1 & \boldsymbol{\sigma}\boldsymbol{n} = \lambda \boldsymbol{T} \quad \text{on } \partial\mathcal{D}_{\mathrm{N}} \\ & \displaystyle\int_{\mathcal{D}} \rho\,\mathrm{d}\Omega = \eta|\Omega| & 0 \le \rho \le 1 \\ & & \displaystyle\int_{\mathcal{D}} \rho\,\mathrm{d}\Omega = \eta|\Omega| \end{array} \qquad \text{(LOAD-MAX)}$$

in which we can see that the imposed displacement amplitude $U$ becomes irrelevant and can be taken as $U = 1$. As a result, we obtain an extended limit analysis problem in which both $\rho$ and $\boldsymbol{\sigma}$ are optimized for and in which the strength condition corresponds to a strength criterion scaled by the pseudo-density $\rho$. The initial convex-potential topology optimization formulation therefore amounts to finding the structure $\Omega$ exhibiting the *maximum load-bearing capacity* which was initially proposed in Mourad et al. (2021). We introduce:

$$\lambda^+(\eta) = \mathrm{val}(\texttt{LOAD-MAX}) \tag{6.18}$$

as the maximum limit load for an imposed volume fraction. Note that for $\eta = 1$, one obtains the load factor $\lambda^+(1) = \Lambda^+$ of the original computational domain $\mathcal{D}$.

In (Mourad et al., 2021), we also proposed a variant of the above-problem in which we fix the load level $\lambda$ and rather look for the structure of minimum volume capable of sustaining the load level under the considered strength conditions. This *volume minimization* problem reads:

$$\begin{array}{rll} \eta^-(\lambda) = \min\limits_{\rho,\boldsymbol{\sigma}} & \dfrac{1}{|\mathcal{D}|}\displaystyle\int_{\mathcal{D}} \rho\,\mathrm{d}\Omega & \\ \text{s.t.} & \boldsymbol{\sigma} \in \rho G \quad \text{in } \mathcal{D} & \\ & \operatorname{div}\boldsymbol{\sigma} = 0 \quad \text{in } \mathcal{D} & \\ & \boldsymbol{\sigma}\boldsymbol{n} = \lambda \boldsymbol{T} \quad \text{on } \partial\mathcal{D}_{\mathrm{N}} & \\ & 0 \le \rho \le 1 & \end{array} \qquad \text{(VOL-MIN)}$$

Interestingly, one can show, see (Mourad et al., 2021), that both problems (LOAD-MAX) and (VOL-MIN) are in fact equivalent since $\lambda^+(\eta)$ and $\eta^-(\lambda)$ are inverses of each other.

In both problems, if $\rho = 1$ then the original strength constraint $\boldsymbol{\sigma} \in G$ is enforced, whereas for $\rho = 0$, a zero stress field is enforced $\boldsymbol{\sigma} = 0$. Finally, let us point out that we will always solve the above problems simultaneously for $\boldsymbol{\sigma}$ and $\rho$, in a monolithic fashion using conic

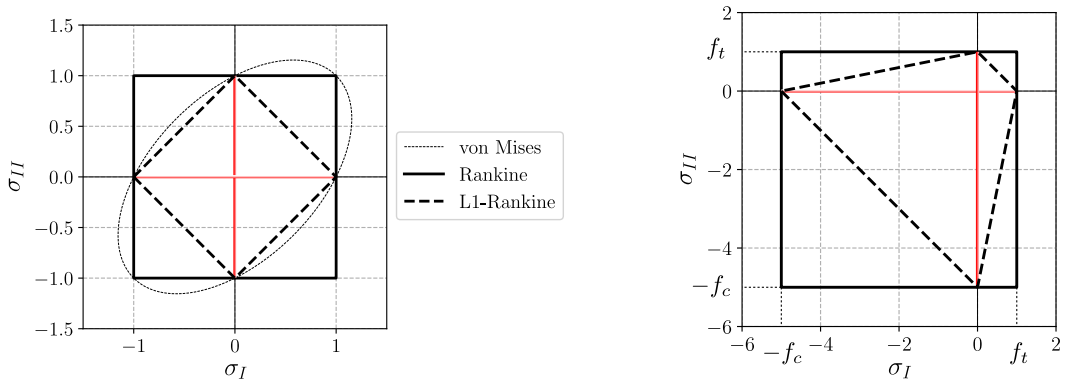


(a) Symmetric strengths $f_t = f_c = 1$ (b) Asymmetric strengths $f_c = 5$, $f_t = 1$

Figure 6.1: Strength criteria shapes in the principal stress space (the $L_0$-norm is represented in red).

solvers. Indeed, contrary to elastic-based topology optimization problems, solving the above problems for $\boldsymbol{\sigma}$ only, at fixed $\rho$, is already a difficult problem, since it is, in fact, a limit analysis problem. The coupled problem therefore adds only an extra scalar optimization variable compared to a standard limit analysis computation and avoids the need of alternate minimization between the problem on $\boldsymbol{\sigma}$ and the problem on $\rho$.

### 6.3.2 On the choice of the strength criterion

The strength criterion $G$ can be chosen based on the considered material strength properties. Various criteria can model the strength properties of materials exhibiting different behaviours in tension and compression, e.g. Drucker-Prager, Mohr-Coulomb, Rankine, etc.

However, in topology optimization, one expects to find optimal structures in the form of trusses consisting of individual members subjected to a uniform stress state so that $-f_c \leq \sigma_I \leq f_t$ and $\sigma_{II} = 0$ where $f_t$ (resp. $f_c$) is the tensile (resp. compressive) strength, see in particular the seminal work of Michell (1904). This condition is equivalent to saying that $\boldsymbol{\sigma}$ must be of rank 1 ($L_0$ Schatten norm). Unfortunately, the induced set is non-convex. The smallest convex set containing the sparsity-inducing $L_0$-norm is the nuclear $L_1$-ball: $\|\boldsymbol{\sigma}\|_1 = |\sigma_I| + |\sigma_{II}| \leq f_0$ for equal tension and compression strengths $f_t = f_c = f_0$. Indeed, the $L_1$-norm is the tightest convex relaxation norm of the $L_0$-norm and has been used in many applications for inducing sparse solutions (Bach et al., 2011) in compressed sensing or image processing applications. As a result, we advocate for the use of a $L_1$-Rankine criterion in order to promote *sparse* (i.e. as uniaxial as possible) principal stress states at the optimum. In the case of asymmetric tensile/compressive strengths, this $L_1$-Rankine criterion reads as (see Fig. 6.1 for a comparison of the criterion shapes in plane stress 2D):

$$\boldsymbol{\sigma} \in G_{\text{L1-Rankine}} \Leftrightarrow \sum_{J=I,II,III} \max\left\{-\frac{\sigma_J}{f_c}; \frac{\sigma_J}{f_t}\right\} \leq 1 \tag{6.19}$$

which can be easily expressed using a second-order cone formulation in the 2D case, see again Mourad et al. (2021).

We further justify this choice by relating it to volume-optimal trusses studied by Michell (1904). Continuous volume-optimal 2D trusses have indeed been characterized as finding a 2D stress state complying with equilibrium conditions and minimizing the quantity $\int_{\mathcal{D}}(|\sigma_I| + |\sigma_{II}|)\,\mathrm{d}\Omega$ in Strang and Kohn (1983); Allaire (2012). We see that, when removing the upper

bound $\rho \leq 1$ on the material density, problem (VOL-MIN) with a symmetric $L_1$-Rankine criterion can be written as:

$$\begin{aligned} \min_{\sigma,\rho} \quad & \frac{1}{|\mathcal{D}|}\int_{\mathcal{D}} \rho \, \mathrm{d}\Omega \\ \text{s.t.} \quad & \text{equilibrium} \\ & |\sigma_I| + |\sigma_{II}| \leq \rho f_0 \quad \text{in } \mathcal{D} \end{aligned} \tag{6.20}$$

which is also equivalent to:

$$\begin{aligned} \min_{\sigma} \quad & \frac{1}{f_0|\mathcal{D}|}\int_{\mathcal{D}} (|\sigma_I| + |\sigma_{II}|) \, \mathrm{d}\Omega \\ \text{s.t.} \quad & \text{equilibrium} \end{aligned} \tag{6.21}$$

which is exactly the characterization of volume-optimal continuous 2D trusses discussed in Strang and Kohn (1983); Kilian et al. (2017). A similar equivalence can be obtained for asymmetric strengths.

In the above problems, we removed the upper bound condition $\rho \leq 1$ so that there is no limit load anymore. A constrained version of the Michell truss design problem has also been proposed in Strang and Kohn (1983) although not being completely equivalent to our formulation. However, they share the similar feature of avoiding infinitely large truss member sections (and are thus unable to sustain concentrated forces) but also of exhibiting a maximum load level.

### 6.3.3 Illustrative applications

#### MBB beam

We first consider a MBB beam example (see inset of Fig. 6.2a) of length $l = 36$ and height $h = 6$ with simple supports on the left and roller supports on the right, a vertical force of reference intensity $P = 1$ is applied at the top. In the following, only one half of the model will be considered, taking symmetry into account. Both supports and force are distributed over a small distance $s = 0.5$ to mitigate stress concentrations.

In Fig. 6.2a, solutions to problems (LOAD-MAX) and (VOL-MIN) have been represented for varying load level and volume fractions. As expected, both problems yield the same solution in terms of $\lambda^+(\eta)$. The most interesting feature is the existence of a plateau where $\lambda^+(\eta) = \Lambda^+$ for $\eta \geq \eta_{\max} = \eta^-(\Lambda^+)$. This can be explained by the fact that, for a given geometry, limit analysis solutions do not necessarily involve optimal stress fields lying at the boundary of the strength criterion everywhere in the domain. Some regions are indeed only weakly stressed or even unstressed so that a smaller strength criterion can be used. This leads to a material distribution with significantly lower total density while preserving the maximum load-bearing capacity. Interestingly, in the present example the material volume savings are significant since $\eta_{\max} \approx 50\%$.

Moreover, the solutions to the convex load maximization problem (Fig. 6.2b obtained for $\eta = 20\%$ display a concentration of matter in the top and bottom region as one could expect. However, in the central region of the beam, the optimized material is much more diffused as evidenced by the principal stress fields. The latter is indeed reminiscent of continuous solutions of the Michell problem. In Mourad et al. (2021), it has been shown that the $L_1$-Rankine was the best option for promoting uniaxial stress states in such regions, as opposed to more classical criteria like a von Mises or Rankine criterion. Nevertheless, this solution shows the need for a penalization procedure to obtain a manufacturable truss-like design. The solution obtained after this penalization have been represented in Fig. 6.3 which

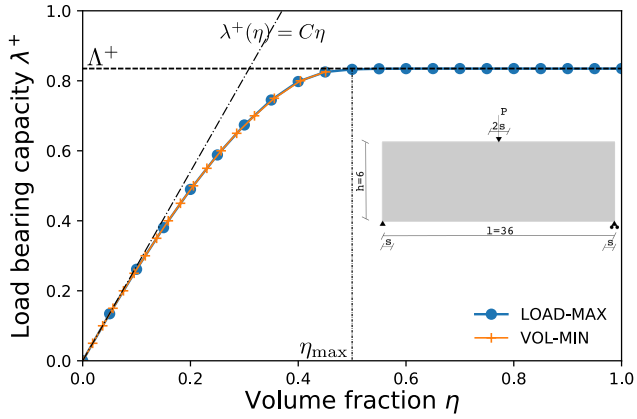


(a) Comparison between both formulations. The horizontal line corresponds to the standard limit analysis solution $\Lambda^+$ and the oblique line of equation $\lambda^+(\eta) = C\eta$ to the solution of (LOAD-MAX) when removing the upper bound constraint $\rho \leq 1$.

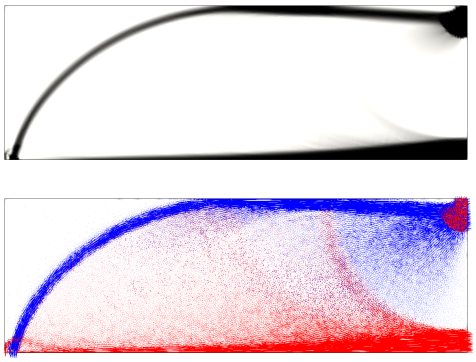

(b) Optimized design for $\eta = 0.20$. Top: pseudo-density field $\rho$. Bottom: principal stresses (blue: compression, red:traction)

Figure 6.2: Load maximization/volume minimization for the $L_1$-Rankine ($f_c = f_t = 1$) criterion on a MBB beam problem.

(a) (LOAD-MAX), $\eta = 0.2$

(b) (VOL-MIN), $\lambda = \lambda^+(0.2)$

Figure 6.3: Optimized design of the MBB-beam using either penalized load maximization or volume minimization.

clearly exhibit a truss-like topology. It should be noted that if a (LOAD-MAX) formulation is used (Fig. 6.3a), the penalization will result in a structure with a lower limit load than the continuous solution of Fig. 6.2b for the same volume fraction. Conversely, when using a (VOL-MIN) formulation (Fig. 6.3b), the penalized solution will sustain the same load level $\lambda$ but will require a larger volume $\eta_{\text{pen}} > 0.2$.

### No-tension material

We further illustrate the versatility of our formulation by tackling the important case of no-tension materials $f_t = 0$. The domain represented in Fig. 6.4 is subject to fixed supports on its bottom and lateral sides and uniformly distributed compressive $\boldsymbol{T} = -\boldsymbol{e}_y$ load on the top boundary. We investigate two different cases for the central region width with either $s = 0$ or $s = 0.3$. We set $\eta = 0.2$ and $\ell = 0.1$ for slope control.

First, the principal stress distributions obtained from the resolution of the unpenalized convex problem for the case $s = 0$ are represented in Fig. 6.5a. We can remark that the obtained stress field is indeed in a purely compressive state with a localized uniaxial field in the inclined strut which is supported by the bottom boundary. The central top region is subject

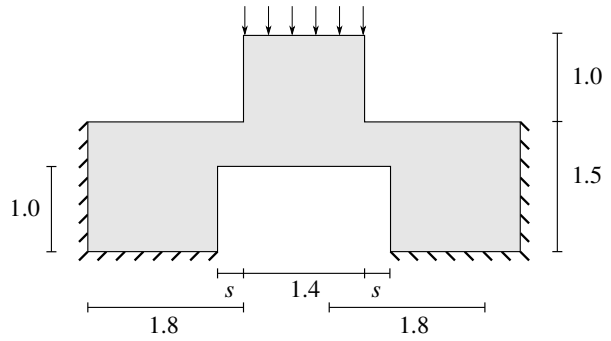


Figure 6.4: Geometrical domain for optimization of a no-tension material

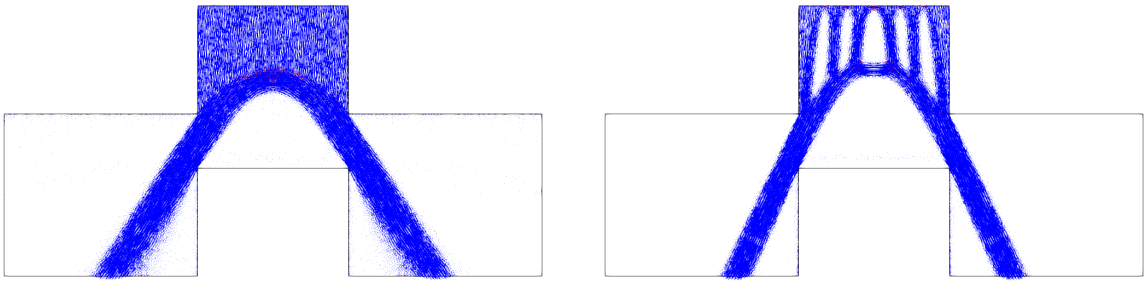

(a) Initial unpenalized solution (b) Final penalized solution

Figure 6.5: Principal stress distributions for the no-tension material example with $s = 0$

to a uniformly distributed uniaxial stress state. We can highlight that the obtained solution is therefore already extremely satisfying in terms of manufacturability. As a result, there is little use here for a penalization procedure, which will essentially replace the top uniform region by a series of columns and slightly modify the main struts inclination (Fig. 6.5b).

Interestingly, when increasing the central opening width (case $s = 0.3$). The previous solution now becomes impossible to sustain since the struts would have to kink to avoid the opening. Since this kink cannot be supported by a no-tension material, the final solution introduces a secondary strut which will be supported by the vertical boundaries in this case (Fig. 6.6a). Again, the obtained solution is remarkably well localized and the penalization procedure only modifies the top uniform region (Fig. 6.6b).

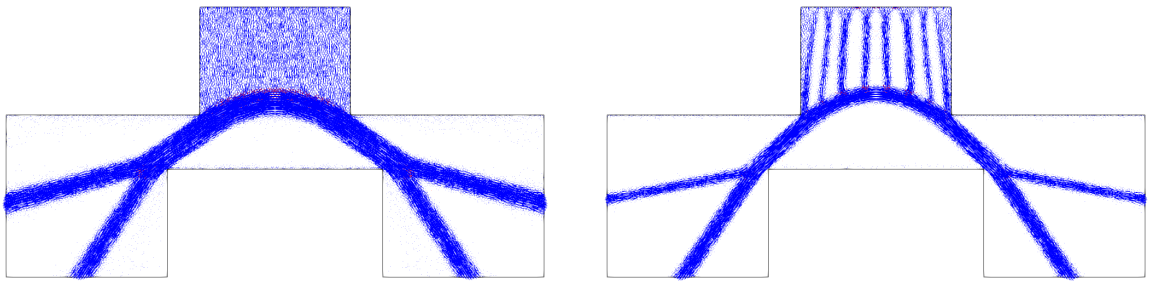

(a) Initial unpenalized solution (b) Final penalized solution

Figure 6.6: Principal stress distributions for the no-tension material example with $s = 0.3$

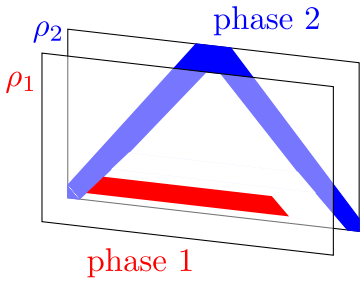


Figure 6.7: Bi-material optimization where we optimize over two materials and a void phase.

## 6.4 Generalization to multi-material optimization and application to reinforced concrete structures

In this section, we show how the previous formulation can be easily extended to the optimization of a structure in presence of reinforcements. In (Mourad et al., 2022), we investigated the case where the composite material consists of a matrix phase with a fixed geometry and a reinforcement phase the topology of which we want to optimize. Even if this situation seems more relevant for the practical application to reinforced concrete structures, we will see that it is more interesting to consider the situation where both phases, matrix (concrete) and reinforcement (steel), are simultaneously optimized as it will draw some links with the strut-and-tie method used in engineering practice. In the following, we will therefore treat only this second situation and we refer to (Mourad et al., 2022) for more details on the former case.

### 6.4.1 Problem formulation

We therefore investigate the concurrent optimization of two different materials (or phases) in addition to a void phase (Fig. 6.7). Both materials are indexed by $i = 1, 2$ whereas void is associated with $i = 0$. Each material possesses a corresponding strength criterion $G^i$. We aim at enforcing that a given point $\boldsymbol{x}$ belongs to either phase 1, phase 2 or to the void. In terms of strength conditions, we would therefore have $\boldsymbol{\sigma} \in G^1$, $\boldsymbol{\sigma} \in G^2$ or $\boldsymbol{\sigma} = 0$ which can be written as follows:

$$\exists \tilde{\boldsymbol{\sigma}}^0, \tilde{\boldsymbol{\sigma}}^1, \tilde{\boldsymbol{\sigma}}^2, \zeta_0, \zeta_1, \zeta_2 \text{ s.t. } \begin{cases} \boldsymbol{\sigma} = \zeta_0 \tilde{\boldsymbol{\sigma}}^0 + \zeta_1 \tilde{\boldsymbol{\sigma}}^1 + \zeta_2 \tilde{\boldsymbol{\sigma}}^2 \\ \tilde{\boldsymbol{\sigma}}^0 = 0 \\ \tilde{\boldsymbol{\sigma}}^1 \in G^1 \\ \tilde{\boldsymbol{\sigma}}^2 \in G^2 \\ \zeta_0 + \zeta_1 + \zeta_2 = 1 \\ \zeta_0, \zeta_1, \zeta_2 \in \{0, 1\} \end{cases} \tag{6.22}$$

where the binary variables $\zeta_i$ indicate the membership to the corresponding phase, the constraint $\sum \zeta_i = 1$ enforcing that one and only one of the $\zeta_i = 1$ while the others are zero.

Obviously, due to the binary constraints, the above strength condition is not convex which will result in the corresponding topology optimization problem being extremely difficult to solve. To alleviate this issue and following the same concept as the convex topology optimization formulation, a natural idea is to convexify the above condition with its tightest convex relaxation. To do so, we allow each $\zeta_i$ to take continuous values inside $[0; 1]$ instead of being binary. To make a clear distinction, we will replace each $\zeta_i$ with $\rho_i$, interpreting these

variables as the pseudo-density fields of topology optimization. Hence, we consider:

$$\exists \tilde{\boldsymbol{\sigma}}^1, \tilde{\boldsymbol{\sigma}}^2, \rho_0, \rho_1, \rho_2 \text{ s.t. } \begin{cases} \boldsymbol{\sigma} = \rho_1 \tilde{\boldsymbol{\sigma}}^1 + \rho_2 \tilde{\boldsymbol{\sigma}}^2 \\ \tilde{\boldsymbol{\sigma}}^1 \in G^1 \\ \tilde{\boldsymbol{\sigma}}^2 \in G^2 \\ \rho_0 + \rho_1 + \rho_2 = 1 \\ \rho_0, \rho_1, \rho_2 \in [0;1] \end{cases} \iff \exists \tilde{\boldsymbol{\sigma}}^1, \tilde{\boldsymbol{\sigma}}^2, \rho_1, \rho_2 \text{ s.t. } \begin{cases} \boldsymbol{\sigma} = \rho_1 \tilde{\boldsymbol{\sigma}}^1 + \rho_2 \tilde{\boldsymbol{\sigma}}^2 \\ \tilde{\boldsymbol{\sigma}}^1 \in G^1 \\ \tilde{\boldsymbol{\sigma}}^2 \in G^2 \\ \rho_1 + \rho_2 \leq 1 \\ \rho_1, \rho_2 \in [0;1] \end{cases} \tag{6.23}$$

This motivates the introduction of the following density-dependent strength condition $G(\rho_1, \rho_2)$:

$$\boldsymbol{\sigma} \in G(\rho_1, \rho_2) \Leftrightarrow \exists \boldsymbol{\sigma}^1, \boldsymbol{\sigma}^2 \text{ s.t. } \begin{cases} \boldsymbol{\sigma} = \boldsymbol{\sigma}^1 + \boldsymbol{\sigma}^2 \\ \boldsymbol{\sigma}^1 \in \rho_1 G^1 \\ \boldsymbol{\sigma}^2 \in \rho_2 G^2 \end{cases} \tag{6.24}$$

in which we made the change of variable $\boldsymbol{\sigma}^i = \rho_i \tilde{\boldsymbol{\sigma}}^i$.

In particular, if both $\rho_1(\boldsymbol{x}) = \rho_2(\boldsymbol{x}) = 0$ at a given point $\boldsymbol{x}$, we have $\boldsymbol{\sigma}(\boldsymbol{x}) = 0$ i.e. $\boldsymbol{x}$ is in a void phase. If $\rho_1(\boldsymbol{x}) = 1$, then $\rho_2(\boldsymbol{x}) = 0$ and $\boldsymbol{\sigma}(\boldsymbol{x}) \in G^1$ i.e. $\boldsymbol{x}$ belongs to material 1 and vice versa. Note that it is possible to find states where $\rho_1(\boldsymbol{x}) \neq 0$ and $\rho_2(\boldsymbol{x}) \neq 0$, which results in $\boldsymbol{x}$ belonging to a fictitious material averaging the strength properties of both phases. Indeed, in the case where $\rho_1 + \rho_2 = 1$, $G(\rho_1, \rho_2)$ corresponds to the *convex hull* of $G_1$ and $G_2$. Finally, in the case where $G^1 = G^2 = G$, we have $G(\rho_1, \rho_2) = (\rho_1 + \rho_2)G = \rho G$ and we recover the single material formulation of (Mourad et al., 2021).

The two corresponding load-maximization (LOAD-MAX) and volume minimization (VOL-MIN) problems are therefore respectively given by:

$$\begin{aligned} \lambda^+ = \max_{\lambda, \boldsymbol{\sigma}^1, \boldsymbol{\sigma}^2, \rho_1, \rho_2} \quad & \lambda & & \\ \text{s.t.} \quad & \operatorname{div}(\boldsymbol{\sigma}^1 + \boldsymbol{\sigma}^2) = 0 & & \text{in } \mathcal{D} \\ & (\boldsymbol{\sigma}^1 + \boldsymbol{\sigma}^2)\boldsymbol{n} = \lambda \boldsymbol{T} & & \text{on } \partial\mathcal{D}_T \\ & \boldsymbol{\sigma}^1 \in \rho_1 G^1 & & \text{in } \mathcal{D} \\ & \boldsymbol{\sigma}^2 \in \rho_2 G^2 & & \text{in } \mathcal{D} \\ & \int_{\mathcal{D}} (\rho_1 + \rho_2) \, \mathrm{d}\Omega \leq \eta |\mathcal{D}| & & \\ & 0 \leq \rho_1 \leq 1 & & \\ & 0 \leq \rho_2 \leq 1 & & \\ & \rho_1 + \rho_2 \leq 1 & & \end{aligned} \tag{BIMAT-LOAD-MAX}$$

and

$$\begin{aligned} \eta^- = \min_{\boldsymbol{\sigma}^1, \boldsymbol{\sigma}^2, \rho_1, \rho_2} \quad & \frac{1}{|\mathcal{D}|} \int_{\mathcal{D}} (\rho_1 + \rho_2) \, \mathrm{d}\Omega & & \\ \text{s.t.} \quad & \operatorname{div}(\boldsymbol{\sigma}^1 + \boldsymbol{\sigma}^2) = 0 & & \text{in } \mathcal{D} \\ & (\boldsymbol{\sigma}^1 + \boldsymbol{\sigma}^2)\boldsymbol{n} = \lambda \boldsymbol{T} & & \text{on } \partial\mathcal{D}_T \\ & \boldsymbol{\sigma}^1 \in \rho_1 G^1 & & \text{in } \mathcal{D} \\ & \boldsymbol{\sigma}^2 \in \rho_2 G^2 & & \text{in } \mathcal{D} \\ & 0 \leq \rho_1 \leq 1 & & \\ & 0 \leq \rho_2 \leq 1 & & \\ & \rho_1 + \rho_2 \leq 1 & & \end{aligned} \tag{BIMAT-VOL-MIN}$$

where we used $c(\rho_1, \rho_2) = \rho_1 + \rho_2$ as a cost function measuring the amount of both materials. Note that in (Mourad et al., 2022), we also investigated the use of a non-symmetric cost

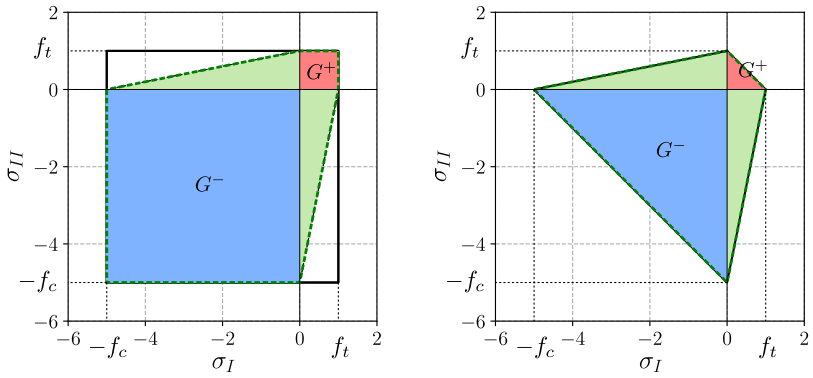


Figure 6.8: Splitting of a nominal strength criterion $G$ (in black) into a purely compressive part $G^-$ (in blue) and a purely tensile part $G^+$ (in red) and the corresponding convex hull $\text{conv}\{G^+, G^-\}$ (in green). Left: a Rankine strength criterion, right: a $L_1$-Rankine strength criterion in the plane of principal stresses

function $c_\omega(\rho_1, \rho_2)$ which introduces a weighting factor $\omega \in [0; 1]$ to give more or less weight to the cost associated with the presence of material 1 over material 2. Finally, both problems can be solved using a similar conic programming formulation and penalization procedure as the single material case.

### 6.4.2 No-tension and no-compression materials

An important case of application of the previous bi-material formulation is concerned with the optimization of a no-tension and a no-compression phase. Practically, this could correspond to two different materials respectively possessing negligible tensile strength (e.g. concrete, rocks, masonry, etc.) and negligible compressive strength (e.g. thin membrane which would buckle under compression). Another possibility is to consider a single material for which we would like to distinguish members in tension from members in compression in the optimization process, for example in order to assign a different cost between the tensile and compressive "phase".

As regards this last point of view, one could define, for a single material of nominal strength properties $G$, the *no-tension strength criterion* $G^1 = G^- = G \cap S^-$ and the *no-compression strength criterion* $G^2 = G^+ = G \cap S^+$ where:

$$S^\pm = \{\boldsymbol{\sigma} \text{ s.t. } \pm\boldsymbol{\sigma} \succcurlyeq 0\} \tag{6.25}$$

represent the cone of symmetric positive/negative stress tensors. In this case, since $G^\pm \subset G$ and $G$ is convex, we have that $\text{conv}\{G^+, G^-\} \subseteq G$. Again, this formulation will tend to promote stress states either in pure tension or in pure compression. Fig. 6.8 illustrates this construction in the case of a Rankine and $L_1$-Rankine criterion. Note that we have that $\text{conv}\{G^+, G^-\} = G_{L_1\text{-Rankine}}$ in this latter case.

Finally, as already discussed, the use of a $L_1$-Rankine strength criterion will even further promote uniaxial stress states. If the original material is isotropic and possesses a characteristic tensile strength $f_t$ and compressive strength $f_c$, a natural modeling strategy for obtaining truss-like designs when distinguishing the optimization of tensile and compressive members

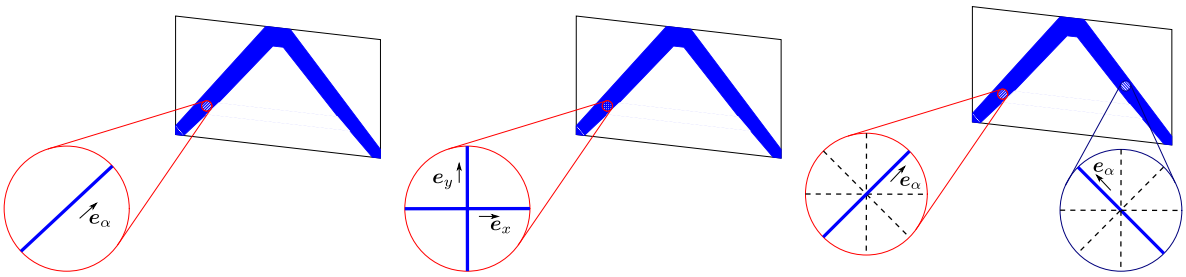


(a) Reinforcement along a single prescribed direction

(b) Reinforcement along two prescribed directions

(c) Reinforcement along one direction among a set of potential orientations

Figure 6.9: Modelling the reinforcement phase with uniaxial reinforcements

is therefore to consider:

$$G^1 = G_{L_1\text{-Rankine}(f_c,0)} \tag{6.26}$$

$$G^2 = G_{L_1\text{-Rankine}(0,f_t)} \tag{6.27}$$

where $G_{L_1\text{-Rankine}(f_c,f_t)}$ denotes the isotropic $L_1$-Rankine strength criterion of compressive (resp. tensile) strength $f_c$ (resp. $f_t$).

### 6.4.3 Reinforcement phase with prescribed orientations

Finally, the above choice can also be adapted to the situation in which the reinforcement phase consists of uniaxial reinforcement members which have fixed or unknown orientations instead of the isotropic $L_1$-Rankine criterion.

Let us first consider the case where the reinforcing phase (here denoted with $i = 2$ by convention) consists of uniaxial members of tensile strength $f_t$[1] oriented along a given direction $\boldsymbol{e}_\alpha$ as in Fig. 6.9a. The corresponding strength condition will therefore read:

$$G^2 = \{\boldsymbol{\sigma}^2 = \sigma^{\mathrm{r}} \boldsymbol{e}_\alpha \otimes \boldsymbol{e}_\alpha \text{ s.t. } 0 \leq \sigma^{\mathrm{r}} \leq f_t\} \tag{6.28}$$

The latter also easily generalizes to a reinforcing material made of multiple reinforcement directions by summing the corresponding uniaxial stress contributions. For instance, an important practical case of interest is that of orthogonal reinforcements aligned with the global $x, y$ directions (and possibly $z$ in 3D) as in Fig. 6.9b. In this case, the strength criterion for two reinforcement directions $\boldsymbol{e}_x$ and $\boldsymbol{e}_y$ generalizes to:

$$G^2 = \{\boldsymbol{\sigma}^2 = \sigma^{\mathrm{r},x} \boldsymbol{e}_x \otimes \boldsymbol{e}_x + \sigma^{\mathrm{r},y} \boldsymbol{e}_y \otimes \boldsymbol{e}_y \text{ s.t. } 0 \leq \sigma^{\mathrm{r},x}, \sigma^{\mathrm{r},y} \leq f_t\} \tag{6.29}$$

Now, instead of considering that the reinforcing material is made of a fixed distribution of predefined orientations, we can consider a reinforcing material consisting of uniaxial reinforcements but with a locally unknown orientation *a priori*, with the goal that the topology optimization process would naturally select the locally optimal orientation. Finding such an optimal microstructure for the reinforcing phase at each material point is reminiscent of the concepts of the homogenization method in topology optimization (Allaire et al., 2004), with respect to strength conditions instead of the elastic stiffness tensor.

Let us indeed consider that the reinforcing material is made of a distribution of uniaxial reinforcements belonging to a certain family $\mathcal{A}$ of orientations $\alpha$ as in Fig. 6.9c. In order to

[1] Note that considering a non-zero compressive strength $f_c$ is also possible.

enforce that only one orientation is active at a given material point, we can write the following strength condition:

$$\exists \sigma^{\mathrm{r},\alpha}, \zeta_\alpha \text{ s.t. } \begin{cases} \boldsymbol{\sigma}^2 = \sum_{\alpha\in\mathcal{A}} \zeta_\alpha \sigma^{\mathrm{r},\alpha} \boldsymbol{e}_\alpha \otimes \boldsymbol{e}_\alpha & \\ 0 \leq \sigma^{\mathrm{r},\alpha} \leq f_t & \forall \alpha \in \mathcal{A} \\ \zeta_\alpha \in \{0;1\} & \forall \alpha \in \mathcal{A} \\ \sum_{\alpha\in\mathcal{A}} \zeta_\alpha = 1 & \end{cases} \tag{6.30}$$

where we introduced the binary variables $\zeta_\alpha$ which describe the activation or not of a specific orientation, the last constraint enforcing that one and only one of such orientations can be active.

Again, criterion (6.30) is non-convex due to the binary constraint on the $\zeta_\alpha$. As before, we consider instead the following convexified formulation by relaxing the binary constraint:

$$\boldsymbol{\sigma}^2 \in G^2 \Leftrightarrow \exists \sigma^{\mathrm{r},\alpha}, \zeta_\alpha \text{ s.t. } \begin{cases} \boldsymbol{\sigma}^{\mathrm{r}} = \sum_{\alpha\in\mathcal{A}} \zeta_\alpha \sigma^{\mathrm{r},\alpha} \boldsymbol{e}_\alpha \otimes \boldsymbol{e}_\alpha & \\ 0 \leq \sigma^{\mathrm{r},\alpha} \leq f_t & \forall \alpha \in \mathcal{A} \\ 0 \leq \zeta_\alpha \leq 1 & \forall \alpha \in \mathcal{A} \\ \sum_{\alpha\in\mathcal{A}} \zeta_\alpha = 1 & \end{cases} \tag{6.31}$$

which we recognize as the definition of the *convex hull* of the individual uniaxial strength conditions $G^\alpha = \{\sigma^{\mathrm{r},\alpha} \boldsymbol{e}_\alpha \otimes \boldsymbol{e}_\alpha \text{ s.t. } 0 \leq \sigma^{\mathrm{r},\alpha} \leq f_t\}$ i.e.

$$G^2 = \mathrm{conv}_{\alpha\in\mathcal{A}}\{G^\alpha\} \tag{6.32}$$

which is indeed the tightest convexification of the union of all the $G^\alpha$. Finally, in the case where $\mathcal{A}$ spans all the possible directions in space, we can easily show that $G^2$ is in fact equal to the $L_1$-Rankine criterion with tensile strength $f_t$. This result justifies that the $L_1$-Rankine is the tightest convex criterion promoting uniaxial stress states in an isotropic fashion.

The main interest of the above construction in the case of a fixed family of discrete orientations $\mathcal{A} = \{\alpha_1, \ldots, \alpha_N\}$ is that the resulting strength condition will be anisotropic, exhibiting a larger strength in the corresponding directions. We therefore expect the strength-based topology optimization procedure to naturally result in designs locally oriented in one of these favorable directions.

By way of illustration, Fig. 6.10 displays the maximum uniaxial tensile stress $\sigma^+$ in direction $\boldsymbol{e}_\theta = \cos\theta \boldsymbol{e}_x + \sin\theta \boldsymbol{e}_y$ for a material consisting of such a family of discrete orientations obeying criterion (6.31). As expected, when the reinforcement material is made of only two reinforcement directions, the material possesses no shear strength so that the uniaxial strength is always zero except if $\theta$ is perfectly aligned with one of the two directions. For more than two directions, the material possesses a shear strength and, therefore, a non-zero tensile strength for any $\theta$. Again, we observe that the uniaxial strength is equal to $f_t$ when the loading direction is aligned with one of the reinforcement direction and is less than $f_t$ in-between. The resulting material therefore possesses anisotropic strength properties. In the limit of an isotropic continuous distribution of reinforcement direction, the uniaxial strength becomes a constant equal to $f_t$ since the resulting material strength properties are equivalent to an isotropic $L_1$-Rankine strength criterion.

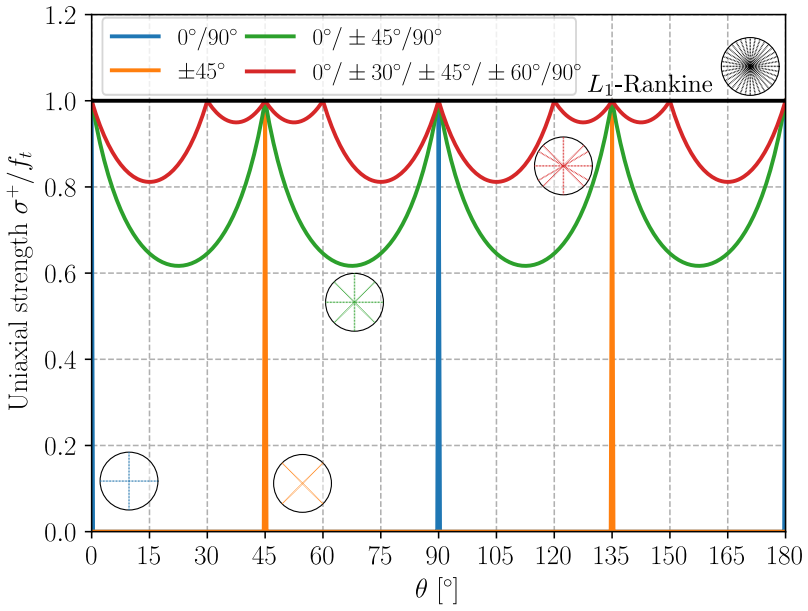


Figure 6.10: Anisotropic uniaxial tensile strength for a material reinforced by a family of reinforcements of discrete orientations obeying criterion (6.31)

### 6.4.4 Example

We revisit here the MBB example with the two-material formulation where phase 1 (resp. phase 2) corresponds to a pure compression (resp. pure tension) phase of strength $f_c$ (resp. $f_t$) as in (6.27). Fig. 6.11 represents the corresponding optimized densities for both phases and various imposed volume fractions $\eta$. Clearly, each truss member belongs to a single phase, depending on its state of tension or compression. The resulting distribution of tensile and compression agrees with structural intuition. We can see that regions where both phases are simultaneously active correspond to joints where members connect to each other.

We assume now that the tensile phase (phase 2) enjoys anisotropic strength properties of the form (6.31). We recall that if the set of allowed orientations $\mathcal{A}$ spans all directions, then the corresponding strength criterion is equivalent to a $L_1$-Rankine strength criterion so that we recover the results of Fig. 6.11. In Fig. 6.12, we report the results obtained when considering a tensile phase with allowed orientations of $\alpha = 0°$, $\alpha \in \{0°; \pm 30°\}$, $\alpha \in \{0°; \pm 45°\}$ or $\alpha \in \{0°; 90°\}$. As expected, if tensile members can be aligned horizontally only (Fig. 6.12a), the most efficient design is obtained with tensile members located at the bottom of the beam and with inclined compressive struts transmitting the load to the supports. Interestingly, we obtain two individual tensile members in this case. When we further allow for inclined directions along ±30° or ±45°, we obtain, in addition to a horizontal tensile member, secondary inclined members to which additional compressive struts can be connected. Note that the case $\alpha \in \{0°; \pm 45°\}$ (Fig. 6.12c) is quite close to the isotropic case obtained with the $L_1$-Rankine criterion in Fig. 6.11c. Finally, the case with $\alpha \in \{0°; 90°\}$ (Fig. 6.12d) indeed produces tensile members aligned either horizontally or vertically. Interestingly, despite the fact that tensile orientations are constrained, one still has freedom in the length and location of those members which enables to reach a design where compressive struts can more or less follow the same paths as in the isotropic case. Also note that the convexified formulation (6.31) authorizes in theory a superposition of the different orientations at a given point. Clearly, this is not observed since each tensile members is in a pure uniaxial stress state corre-

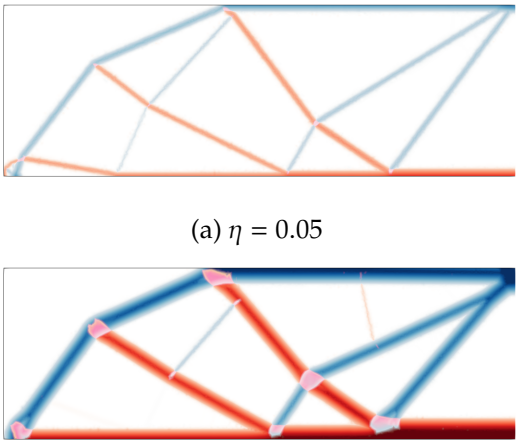

(a) $\eta = 0.05$

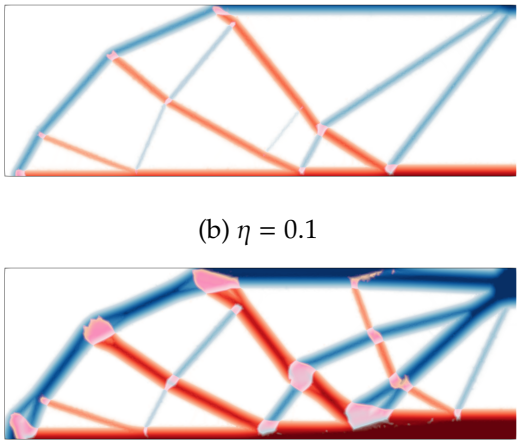

(b) $\eta = 0.1$



(c) $\eta = 0.2$



(d) $\eta = 0.3$

Figure 6.11: Bi-material load-maximization of the MBB example with tension/compression splitting ($f_c = f_t = 1$) and various maximum volume fraction $\eta$

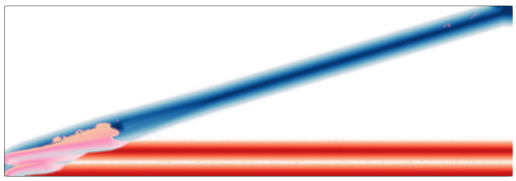

(a) Orientations along 0°

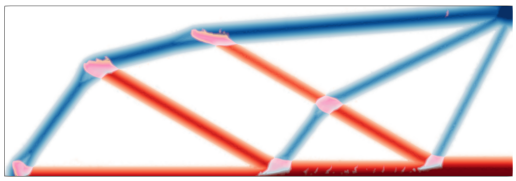

(b) Orientations along 0° and ±30°

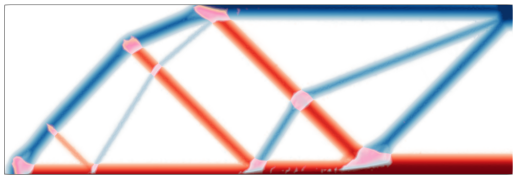

(c) Orientations along 0° and ±45°

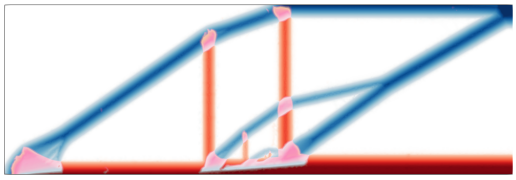

(d) Orientations along 0° and 90°

Figure 6.12: Bi-material load-maximization ($\eta = 0.2$) of the MBB example with discrete orientations for the tensile phase

Figure 6.13: Optimized reinforced concrete beam [courtesy of S. Maitenaz, Laboratoire Navier]

sponding to a single well-defined orientation. It is only at points corresponding to junctions between tensile and/or compressive members that different orientations may coexist locally.

### 6.4.5 A link with the strut-and-tie method for reinforced concrete structures

As mentioned earlier, it may appear strange to apply the previous bi-material formulation to the optimization of steel layout in reinforced concrete structures since the concrete phase occupies the whole domain in practice. However, this could pave the way to a systematic optimization of concrete consumption in standard reinforced concrete structures such as beams or slabs. For instance, the work of Maitenaz et al. (2020) has shown that classical beams can indeed be optimized and fabricated using additive manufacturing, without impairing their overall mechanical performance. In this work, optimization has been based on the normative design code which relies on the strut-and-tie method.

The latter bears similarities with the proposed bi-material formulation. Indeed, rather than considering the topology optimization formulation as a tool for obtaining an optimal shape with minimal volume, one could also view it as a way of obtaining a simplified flow of stresses in equilibrium with a given load and satisfying strength conditions of the concrete and reinforcement phase. With this point of view, the stress field is indeed simplified towards a set of regions in which it is essentially uniaxial, except for joint regions. Moreover, since volume is also optimized, one can expect that among all the possible stress fields in equilibrium with a given loading, the resulting layout will be the most simple possible, i.e. consisting of a minimal number of members. This philosophy is exactly that on which the strut-and-tie method is based. One looks indeed for a simplified mechanical system to transmit forces, in the form of a truss, while satisfying strength conditions, both in the members and in the truss nodes.

To further test the analogy between both methods, a more quantitative comparison has been made on a reinforced concrete corbel (Fig. 6.14a). The reference strut-and-tie (ST) model, shown in Fig. 6.14b, essentially involves a vertical and an horizontal tie connected to an inclined strut going from the point of load application to the column vertical edge. The strut inclination angle is denoted by $\theta$. A secondary strut connects the first one to the two ties. When looking at the optimized topology of concrete (in blue) and steel (in red) phases, one can see in Fig. 6.14c that a similar layout is obtained. The main difference is that the steel ties makes a round corner and is sustained by a fan of concrete struts. This is due to the fact that an isotropic distribution of steel orientations was possible in this case. A much closer layout is obtained when considering only orthogonal steel orientations along the vertical and horizontal directions, as shown in Fig. 6.14d. More quantitatively, Table 6.1 reports the measured forces in the strut and tie as well as the strut inclination in the case of orthogonal steel. Different values are measured from the topology optimization result, depending on the chosen value for the concrete strength $f_c$: either the characteristic strength $f_{ck} = 45\,\text{MPa}$, the design strength $f_{cd} = 30\,\text{MPa}$ or the effective strength accounting for a reduction due to potential cracking $\nu' f_{cd}$ with $\nu' = 1 - f_{ck}/(250\,\text{MPa}) = 0.82$. We can see that the measured values agree very well with the strut-and-tie result. It can be noted that the retained value

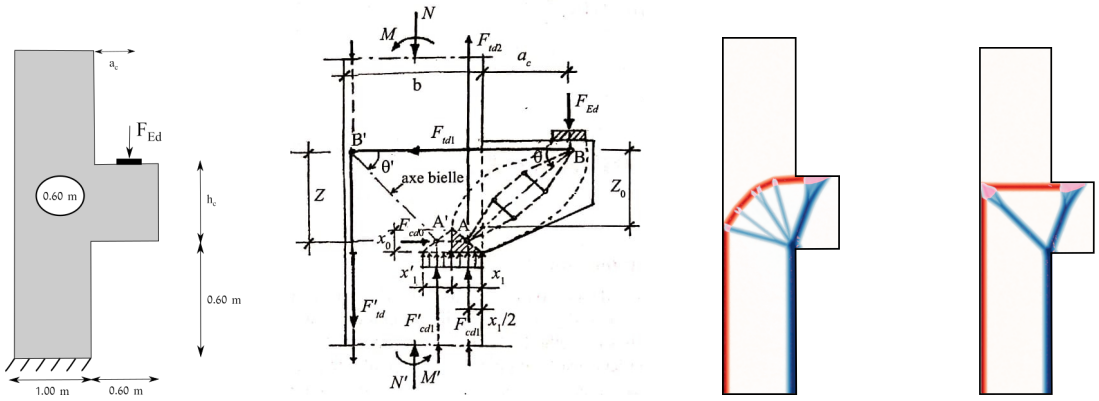


(a) Geometry and loading (b) Strut-and-tie model, taken from Bosc (2008) (c) Optimized, isotropic steel (d) Optimized, orthogonal steel

Figure 6.14: Reinforced-concrete corbel: comparison between strut-and-tie model and bi-material optimization

| | $f_c = f_{ck}$ | $f_c = f_{cd}$ | $f_c = \nu' f_{cd}$ | ST |
|---|---|---|---|---|
| $F_{\text{strut}}$ | 2.37 MN | 2.37 MN | 2.39 MN | 2.43 MN |
| $\theta$ | 65.60 ° | 64.30 ° | 62.90 ° | 68 ° |
| $F_{\text{tie}}$ | 0.82 MN | 0.88 MN | 0.87 MN | 0.9 MN |

Table 6.1: Estimated forces and strut inclination with respect to the strut-and-tie (ST) result depending on the chosen concrete strength $f_c$

for the concrete strength does not play an important role, which can be explained by the fact that steel rebars are the limiting factor for this case.

Finally, the attractiveness of this methodology as a design aid for the structural engineer is further illustrated by investigating situations for which the ST model is much more difficult to imagine. For instance, Fig. 6.15a considers a deep beam with a square opening which has been investigated in (Muttoni et al., 2015). In this work, quite complex ST models have been imagined based on the combination of engineering intuition and practice and finite-element computations, guiding towards an idea about the flow of stresses in this structure. With our approach, we are able to obtain the strut-and-tie layout of Fig. 6.15b. Clearly, the obtained solution is very close to the imagined ST model, even when looking at small details around the opening for instance. An alternative ST model including only horizontal and vertical reinforcements has also been proposed (Fig. 6.16a) and compared against our prediction (Fig. 6.16b). Again, the agreement between the ST model and the optimization procedure is striking.

## 6.5 Optimization of funicular shells

In this section, we will analyze funicular shell structures i.e. curved 2D structures in an ambient 3D space which are subjected to a compressive membrane state only for a given loading. Clearly, it is quite straightforward to extend the methodology described in the previous sections to such a situation for which the shell mid-surface is given a priori. However, one is usually more interested in finding an optimal shell mid-surface and the corresponding

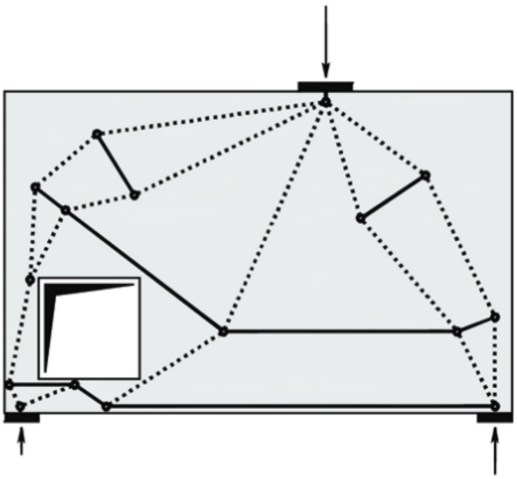

(a) ST model based on elastic stress fields: solid lines: ties in tension; dashed lines: struts in compression

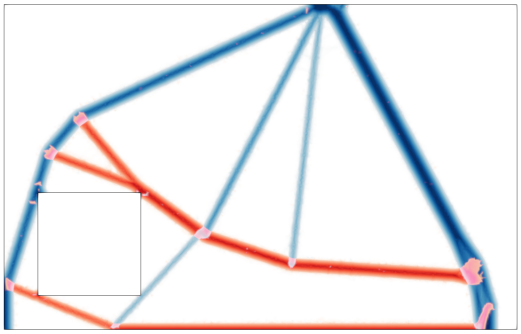

(b) Optimized design from the bimaterial volume minimization

Figure 6.15: Comparison of the proposed methodology with strut-and-tie models with inclined reinforcements, taken from (Muttoni et al., 2015)

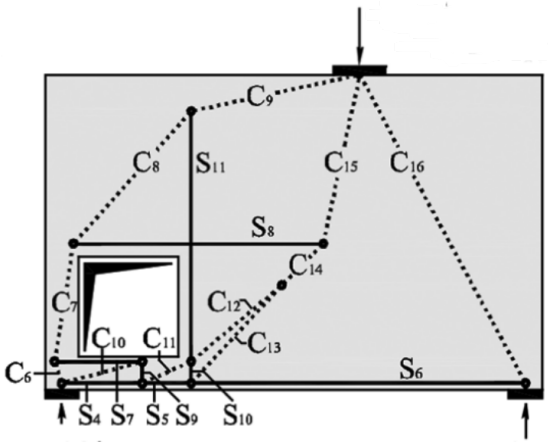


(a) ST model based on elastic stress fields: solid lines: ties in tension; dashed lines: struts in compression

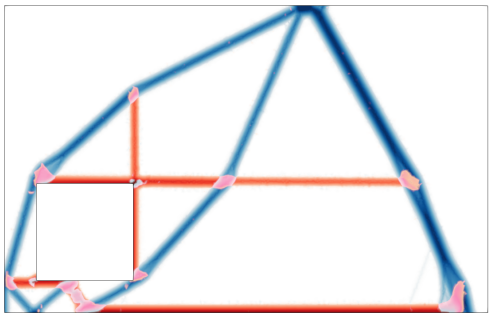

(b) Optimized design from the bimaterial volume minimization

Figure 6.16: Comparison of the proposed methodology with strut-and-tie models with orthogonal reinforcements, taken from (Muttoni et al., 2015)

thickness distribution in an automatic manner. For this purpose, multiple form-finding methods can be found in the literature including dynamic relaxation, thrust-network analysis, etc.

In the following, various formulations will be presented when considering pure tensile states rather than compressive ones. Following the hanging chain analogy, compressive solutions can be obtained by a simple change of sign of loadings and optimal shapes. Illustrative applications will however be given in the form of arch or vault-like structures.

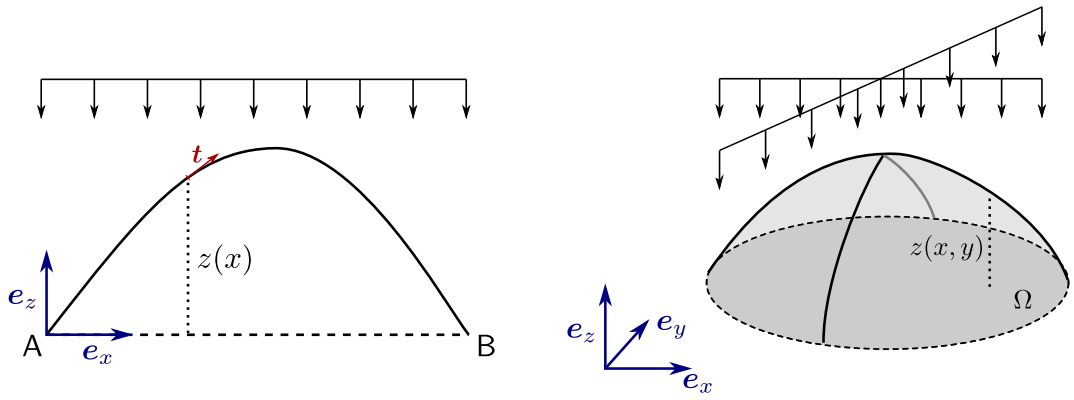


Figure 6.17: Left: optimal arch problem. Right: optimal vault problem

### 6.5.1 Optimal arch

Let us consider the case of an arch constrained to lie in a 2D $(Oxz)$ plane and supported by two supports A at $x = 0$ and B at $x = l$ (Fig. 6.17-left). We consider a distributed loading of intensity $\boldsymbol{f} = p\boldsymbol{e}_z$ which is constant per horizontal unit length $x$. A classical result of structural mechanics for such a load case is that funicular arches are parabolic. Indeed, owing to equilibrium, one has for the internal force:

$$\boldsymbol{R}(x) = H_x\boldsymbol{e}_x + (H_y - px)\boldsymbol{e}_z \tag{6.33}$$

where $H_x$ and $H_y$ are the opposite of the horizontal and vertical reactions at A, $H = -H_x$ being the so-called arch *thrust*. The arch will be funicular if the internal force consist only of a normal force i.e. $\boldsymbol{R}(x) = N(x)\boldsymbol{t}(x)$ with $N(x) \geq 0$ and $\boldsymbol{t}(\boldsymbol{x}) = \dfrac{1}{\sqrt{1 + (z'(x))^2}}(\boldsymbol{e}_x + z'(x)\boldsymbol{e}_z)$ is the unit tangent vector for an arch of elevation $z(x)$. Hence, one has:

$$H_x = \frac{N(x)}{\sqrt{1 + (z'(x))^2}} \tag{6.34}$$

$$H_y - px = \frac{N(x)z'(x)}{\sqrt{1 + (z'(x))^2}} = H_x z'(x) \tag{6.35}$$

which yields:

$$z(x) = \frac{p}{2H_x}x(l - x) \tag{6.36}$$

with $H_y = \dfrac{pl}{2}$. As a result, there exists an infinite number of funicular arches depending on the value of the thrust $H$. Among all of them, we can find an arch of minimum volume if we consider that its constitutive material cannot sustain a stress larger than $\sigma_0$. Indeed, the volume of the arch is given by:

$$\mathcal{V} = \int A(s)\,\mathrm{d}s = \int_0^l A(x)\sqrt{1 + (z'(x))^2}\,\mathrm{d}x \tag{6.37}$$

where $A$ is the cross-section at a given point. The minimum volume arch is obtained by choosing the latter such that the material is fully stressed at its tensile limit i.e.

$$N(x) = \sigma_0 A(x) = H_x\sqrt{1 + (z'(x))^2} \tag{6.38}$$

One then has:

$$\mathcal{V} = \frac{1}{\sigma_0}\int_0^l H_x\left(1+(z'(x))^2\right)\mathrm{d}x = \frac{1}{\sigma_0}\int_0^l \left(H_x + \frac{p^2(x-l/2)^2}{H_x}\right)\mathrm{d}x \tag{6.39}$$

The minimal volume arch is therefore given by the solution to the following scalar convex problem:

$$\begin{array}{ll}\min\limits_{H_x} & \dfrac{1}{\sigma_0}\displaystyle\int_0^l \left(H_x + \frac{p^2(x-l/2)^2}{H_x}\right)\mathrm{d}x \\ \text{s.t.} & H_x \geq 0\end{array} \tag{6.40}$$

for which we easily find the optimal solution to be:

$$H_x = \frac{pl}{2\sqrt{3}} \tag{6.41}$$

$$\mathcal{V} = \frac{pl}{\sqrt{3}\sigma_0} \tag{6.42}$$

The optimal arch is therefore parabolic with a maximum rise at $x = l/2$ of $z_{\max} = (\sqrt{3}/4)l$.

Note that the total volume $\mathcal{V}$ in (6.40) can be decomposed into the sum of a thrust contribution $H_x$ and a rise contribution $p^2(x-l/2)^2/H_x$. Interestingly, the optimal arch is characterized by an equipartition property since, at the optimum, both contributions are equal.

### 6.5.2 Optimal archgrids and optimal vaults

Extension of the above reasoning to systems consisting of two sets of orthogonal arches led to the study of *optimal archgrids* (Rozvany and Prager, 1979). Further progress was made by recognizing that finding optimal archgrid continua can be formulated as a convex optimization program similar to (6.40) (Czubacki and Lewiński, 2020). However, archgrids cannot sustain any in-plane shear and so that stable solutions may fail to exist in general, apart from particular configurations of boundary conditions and loadings. Very recently, Bołbotowski (2022); Bołbotowski and Bouchitté (2022) extended the above reasoning to an isotropic setting in which an optimal vault is characterized by an elevation function $z(\boldsymbol{x})$ defined over a reference planar domain $\Omega$ (Fig. 6.17-right). The corresponding primal stress-based formulation akin to (6.40) is given by:

$$\begin{array}{ll}\inf\limits_{\boldsymbol{\Sigma},\boldsymbol{q}} & \dfrac{2}{\sigma_0}\displaystyle\int_\Omega c(\boldsymbol{\Sigma},\boldsymbol{q})\,\mathrm{d}\Omega \\ \text{s.t.} & \operatorname{div}\boldsymbol{\Sigma} = 0 \\ & \operatorname{div}\boldsymbol{q} + f = 0\end{array} \tag{6.43}$$

where div refers to the planar divergence operator on $\Omega$ and where $c(\boldsymbol{\Sigma},\boldsymbol{q})$ is defined as[2]:

$$c(\boldsymbol{\Sigma},\boldsymbol{q}) = \sup_{\boldsymbol{\varepsilon},\boldsymbol{\theta}}\{\boldsymbol{\Sigma}:\boldsymbol{\varepsilon}+\boldsymbol{\theta}\cdot\boldsymbol{q} \quad \text{s.t.} \quad 2\boldsymbol{\varepsilon}+\boldsymbol{\theta}\otimes\boldsymbol{\theta} \preccurlyeq \boldsymbol{I}\} \tag{6.44}$$

$$= \begin{cases}\frac{1}{2}\operatorname{tr}\boldsymbol{\Sigma} + \frac{1}{2}\boldsymbol{q}\boldsymbol{\Sigma}^{-1}\boldsymbol{q} & \text{if } \boldsymbol{\Sigma}\succcurlyeq 0 \\ +\infty & \text{otherwise}\end{cases} \tag{6.45}$$

Note that notations and numerical coefficients have been changed compared to the original publication (Bołbotowski, 2022) in order to be consistent throughout all sections. The above

[2]Note that expression (6.45) should be written more carefully when $\boldsymbol{\Sigma}$ has a zero eigenvalue.

formulation is reminiscent of plate theory as it involves an in-plane membrane force tensor $\boldsymbol{\Sigma}$ and a vertical force vector $\boldsymbol{q}$ which is in equilibrium with the out-of-plane loading $f$. The objective function in (6.43) yields the vault optimal volume so that $2c(\boldsymbol{\Sigma}, \boldsymbol{q})/\sigma_0$ corresponds to the projected shell thickness per unit area in the reference plane $\Omega$.

Clearly, (6.43) is a convex optimization problem which enjoys a corresponding dual variational problem given by:

$$\begin{array}{ll} \sup\limits_{\xi,z} & \dfrac{2}{\sigma_0}\displaystyle\int_\Omega f z \,\mathrm{d}\Omega \\ \text{s.t.} & \boldsymbol{\varepsilon} = \nabla^s \boldsymbol{\xi} \\ & \boldsymbol{\theta} = \nabla z \\ & 2\boldsymbol{\varepsilon} + \boldsymbol{\theta}\otimes\boldsymbol{\theta} \preccurlyeq \boldsymbol{I} \\ & \boldsymbol{\xi} = 0 \text{ and } z = 0 \quad \text{on } \partial\Omega_{\mathrm{D}} \end{array} \tag{6.46}$$

where $z$ is the wanted optimal vault elevation. Indeed, at the optimum, one has $\boldsymbol{q} = \boldsymbol{\Sigma}\nabla z$ at the optimum which is reminiscent of (6.35) in the case of an arch.

The primal (6.43) and dual (6.46) formulations are conic programs which are representable using quadratic cones. In (Bołbotowski, 2022), numerical examples have been given using a ground structure discretization method. In the following, we will rather rely on a finite-element discretization.

**Remark 9.** The constraint

$$2\boldsymbol{\varepsilon} + \boldsymbol{\theta}\otimes\boldsymbol{\theta} \preccurlyeq \boldsymbol{I} \tag{6.47}$$

can be also rewritten as follows:

$$2\varepsilon_{\tau\tau} + \theta_\tau^2 \leq 1 \quad \forall \boldsymbol{\tau} \in \mathbb{R}^2 \text{ with } \|\boldsymbol{\tau}\| = 1 \tag{6.48}$$

where $\boldsymbol{\tau}\cdot\boldsymbol{\varepsilon}\boldsymbol{\tau} = \varepsilon_{\tau\tau}$, $\theta_\tau = \boldsymbol{\theta}\cdot\boldsymbol{\tau}$ and $\boldsymbol{\tau}$ denotes any in-plane unit vector. The above constraint is therefore isotropic.

Interestingly, this isotropic constraint can be relaxed by considering a finite set of prescribed directions $\boldsymbol{\tau}^k$ for $k = 1, \ldots, N$. With $(\boldsymbol{\tau}^k) = \{\boldsymbol{e}_1, \boldsymbol{e}_2\}$ consisting of two in-plane orthogonal directions, one obtains an orthotropic formulation which coincides with the archgrid formulation studied in (Rozvany and Prager, 1979; Czubacki and Lewiński, 2020).

### 6.5.3 Optimal shells

In this section, we aim at providing various improvements over the formulations discussed in the previous sections. The first main improvement is the ability to properly account for in-plane loading components which does not seem to have been considered so far. Doing so, we will no longer assume that the optimal surface is given by a single elevation function $z(\boldsymbol{x})$ with respect to the reference plane $\Omega$ which *de facto* excludes overhanging parts for instance. Instead, we consider that the optimal surface is given from a generic 3D displacement field $\boldsymbol{u}(\boldsymbol{x}) = (u(\boldsymbol{x}), v(\boldsymbol{x}), w(\boldsymbol{x}))$. This will also make it possible to consider surfaces with supports which are not necessarily aligned on a fixed plane. In order to distinguish our proposal from the previous optimal vault formulation, we will rather speak of an *optimal shell* formulation.

#### Extension to the optimal arch problem

Let us momentarily go back to the optimal arch problem of Section 6.5.1. We consider an arch supported by two supports A and B lying on the $x$-axis and subjected to a generic 3D

loading $\boldsymbol{f}$, thereby consisting of both longitudinal and transversal components.

Assuming that the optimal arch is transformed via a generic 3D displacement field $\boldsymbol{u}$, the tangent vector now becomes

$$\boldsymbol{t}(x) = \frac{1}{J}\left((1+u'(x))\boldsymbol{e}_x + v'(x)\boldsymbol{e}_y + w'(x)\boldsymbol{e}_z\right) \tag{6.49}$$

$$\text{where } J(x) = \frac{ds}{dx} = \sqrt{(1+u'(x))^2 + (v'(x))^2 + (w'(x))^2} \tag{6.50}$$

We have the equilibrium equation:

$$\frac{d\boldsymbol{R}}{dx} + \boldsymbol{f} = 0 \tag{6.51}$$

with $\boldsymbol{R}(x) = N(x)\boldsymbol{t}(x)$ and $N(x) \geq 0$ so that the arch is funicular. In particular, one has:

$$R_x = \frac{N}{J}(1+u'(x)) \quad R_y = \frac{N}{J}v'(x) \quad R_z = \frac{N}{J}w'(x) \tag{6.52}$$

Introducing $\Sigma(x) = N(x)/J(x)$, the total volume is:

$$\mathcal{V} = \int A(s)ds = \frac{1}{\sigma_0}\int_0^l N\frac{ds}{dx}dx = \frac{1}{\sigma_0}\int_0^l \Sigma J^2 dx \tag{6.53}$$

$$= \frac{1}{\sigma_0}\int_0^l \left(\frac{R_x^2}{\Sigma} + \frac{R_z^2}{\Sigma} + \frac{R_y^2}{\Sigma}\right)dx \tag{6.54}$$

where we can see that the obtained expression for the arch volume is close to the original expression (6.39) for a single elevation function.

Unfortunately, minimizing the total volume $\mathcal{V}$ subject to the equilibrium condition (6.51) will always produce a null solution since $\Sigma(x)$ can be as large as possible, contrary to before where $J \geq 1$. We therefore need to impose additional constraints on $\Sigma(x)$ to prevent this. For now, let us fix a maximum value $\Sigma_0 > 0$ for $\Sigma(x)$. This will enforce the normal force to satisfy $N(x) \leq \Sigma_0 J(x)$ as an additional design constraint. We will see later that such a constraint can have a different interpretation. We therefore consider the following convex optimization problem:

$$\begin{aligned} \min_{\Sigma,\boldsymbol{R}} \quad & \frac{1}{\sigma_0}\int_0^l \frac{\|\boldsymbol{R}\|^2}{\Sigma}\,\mathrm{d}x \\ \text{s.t.} \quad & \frac{d\boldsymbol{R}}{dx}(x) + \boldsymbol{f} = 0 \\ & 0 \leq \Sigma \leq \Sigma_0 \end{aligned} \tag{6.55}$$

Obviously, the solution will depend on the imposed value for $\Sigma_0$ which produces arches of different rise-to-span ratios. In fact, problem (6.55) belongs to the class of problems described in Appendix C.2 where the objective function is a homogeneous function of degree -1 and where the cost constraint $j(\Sigma) = \sup_{x\in[0;l]} \Sigma(x) = \|\Sigma\|_\infty$ is homogeneous of degree 1. As a result, one can show that the solution $(\Sigma, \boldsymbol{R})$ of (6.55) for any $\Sigma_0$ can be obtained from the solution to the following reference problem:

$$\begin{aligned} \min_{\Sigma,\boldsymbol{R}} \quad & \int_0^l \left(\frac{1}{\sigma_0}\frac{\|\boldsymbol{R}\|^2}{\Sigma} + \|\Sigma\|_\infty\right)\mathrm{d}x \\ \text{s.t.} \quad & \frac{d\boldsymbol{R}}{dx}(x) + \boldsymbol{f} = 0 \end{aligned} \tag{6.56}$$

More precisely, denoting by $(\Sigma^\star, \boldsymbol{R}^\star)$ the optimal solution to the reference problem (6.56) and $\mathcal{V}^\star$ the corresponding optimal volume, the solution $(\Sigma, \boldsymbol{R})$ and optimal value $\mathcal{V}$ to (6.55) is given by:

$$\Sigma = \frac{2\Sigma_0}{\mathcal{V}^\star}\Sigma^\star \tag{6.57}$$

$$\boldsymbol{R} = \boldsymbol{R}^\star \tag{6.58}$$

$$\mathcal{V} = \frac{(\mathcal{V}^\star)^2}{4\Sigma_0} \tag{6.59}$$

Let us now derive the dual problem to (6.55) which reads:

$$\begin{array}{ll} \inf\limits_{\boldsymbol{u}} & \dfrac{2}{\sigma_0}\displaystyle\int_0^l \left(\frac{1}{2}\Sigma_0\|\boldsymbol{u}'(x)\|^2 - \boldsymbol{f}\cdot\boldsymbol{u}\right)\mathrm{d}x \\ \text{s.t.} & \boldsymbol{u} = 0 \quad \text{at } x = 0, l \end{array} \tag{6.60}$$

where the displacement field $\boldsymbol{u}$ describes the optimal shape. Interestingly, the objective function can be interpreted (up to the unimportant factor $2/\sigma_0$) as the geometric stiffness energy of a perfectly flexible chain, minus the work of external loads. Assuming that its elastic energy is negligible compared to the geometric stiffness, the above formulation is therefore equivalent to finding the equilibrium position of such a chain with an initial prestress $\Sigma_0$.

Similarly, we can show that the optimal displacement solution $\boldsymbol{u}$ is given as:

$$\boldsymbol{u} = \frac{\mathcal{V}^\star}{2\Sigma_0}\boldsymbol{u}^\star \tag{6.61}$$

where $\boldsymbol{u}^\star$ solves the reference problem:

$$\begin{array}{ll} \inf\limits_{\boldsymbol{u}} & \dfrac{1}{\sigma_0}\displaystyle\int_0^l \boldsymbol{f}\cdot\boldsymbol{u}\,\mathrm{d}x \\ \text{s.t.} & \displaystyle\int_0^l \|\boldsymbol{u}'(x)\|^2 \le l \\ & \boldsymbol{u} = 0 \quad \text{at } x = 0, l \end{array} \tag{6.62}$$

which is the dual to (6.56). The above formulation is reminiscent of the mean-squared slope condition discussed in (Rozvany and Prager, 1979; Czubacki and Lewiński, 2020).

In order to validate the above extended optimal arch formulations, a 1D finite-element implementation of the reference problems (6.56)-(6.62) has been solved using `CVXPY`. We first consider a transversal load of the form $\sin\theta g\boldsymbol{e}_y - \cos\theta g\boldsymbol{e}_z$ for which we expect to find the optimal parabolic arch for a uniform load of intensity $g$ in the vertical plane rotated by the angle $\theta$. This is indeed verified in Fig. 6.18, we also check that we recover the same volume for all $\theta$. Second, in Fig. 6.19, we consider an in-plane load of the form $g(\gamma_x\boldsymbol{e}_x - \boldsymbol{e}_z)$ corresponding for instance to an earthquake-induced horizontal acceleration. We see that the formulation (6.62) makes it possible to consider an inplane deformation, including overhanging parts for very large horizontal accelerations.

Finally, Fig. 6.20 illustrates the set of optimal arches when varying the volume/prestress ratio $\eta = \mathcal{V}^\star/(2\Sigma_0)$ for the in-plane loading case. Note that when $\eta = 1$, one obtains the solution to the reference problem (6.56)-(6.62). Solutions for $\eta < 1$ corresponds to solution for which having a smaller volume is preferred over the prestress cost which is required to reach such an equilibrium. On the contrary, solutions with $\eta > 1$ prefer reducing prestress cost at the expense of a larger volume. The former therefore correspond to small rise-to-span ratios whereas the latter correspond to large rise-to-span ratios.

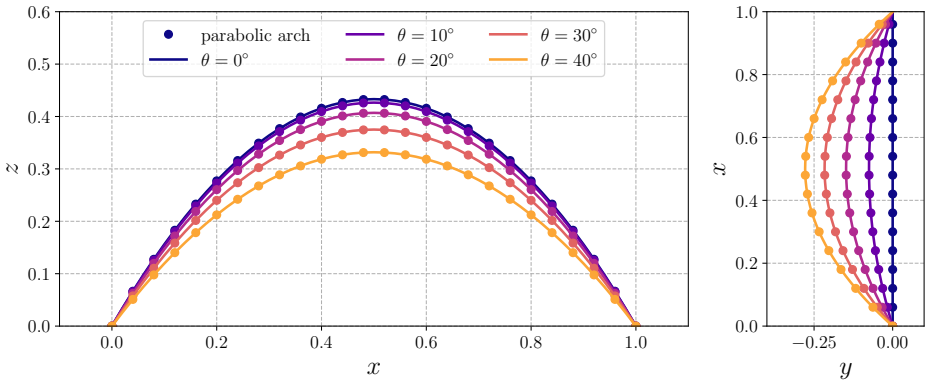


Figure 6.18: Optimal arch solutions with inclined transversal load $\sin\theta g\boldsymbol{e}_y - \cos\theta g\boldsymbol{e}_z$

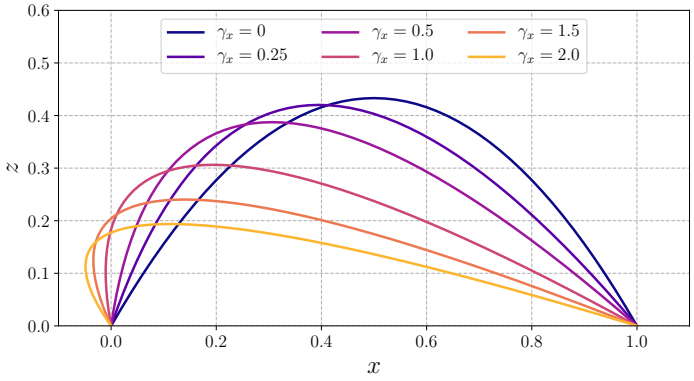


Figure 6.19: Optimal arch solutions with in-plane load $g(\gamma_x \boldsymbol{e}_x - \boldsymbol{e}_z)$

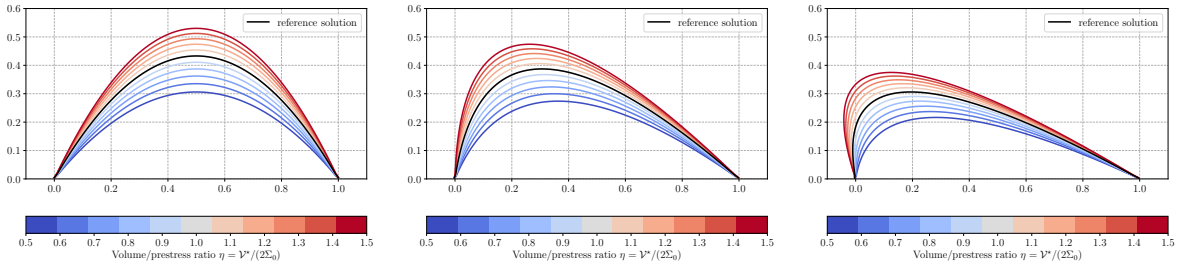


(a) $\gamma_x = 0$ (b) $\gamma_x = 0.5$ (c) $\gamma_x = 1$

Figure 6.20: Series of optimal arches for variable volume/prestress ratios $\eta = \mathcal{V}^\star/(2\Sigma_0)$ (in-plane loading case)

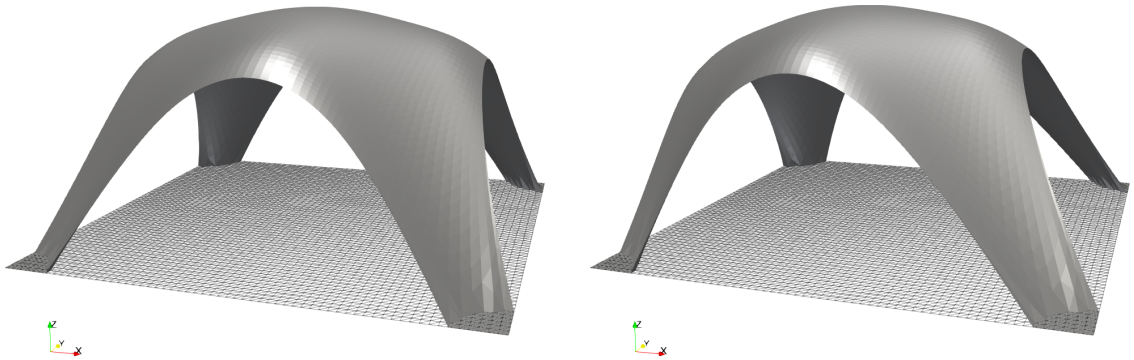

(a) $\gamma_x = 0$ (b) $\gamma_x = 0.25$

Figure 6.21: 3D view of the optimal groin vault for a uniform horizontal + vertical loading $\boldsymbol{f} = (\gamma_x g, 0, -g)$.

**Extension to optimal shells**

At the time of writing this manuscript, we are currently working on the generalization of the previous ideas to a formulation of optimal shells. It turns out that the interpretation of the problem as maximizing the geometric stiffness of membrane is particularly useful. Skipping the technical details, we illustrate the obtained optimal forms found by this process in the case of a groin vault in Fig. 6.21 for a loading $\boldsymbol{f} = (\gamma_x g, 0, -g)$ for two values of horizontal acceleration $\gamma_x$. We also illustrate in Fig. 6.22 results of an optimal shell for a more complex boundary and for which the inner circles are supported at a different prescribed height.

## 6.6 Conclusions

This chapter has discussed various convex optimization formulations in the context of shape optimization. In this field, convex problems are usually the exception rather than the rule. Indeed, common practice usually considers highly non-convex problems which are solved by a specific optimization procedure, sometimes involving a series of convex approximations such as the method of moving asymptotes (MMA) or sequential quadratic programming (SQP). In this chapter, we follow a somehow opposite path as we start from generic convex topology optimization formulations involving convex thermodynamic potentials. Such convex problems are then used with a continuation procedure involving a penalty exponent in order to obtain better-defined black-and-white designs.

Thereby, we introduced a general formulation of topology optimization in a limit analysis setting, focusing on optimizing the limit load rather than the elastic compliance. In particular, the proposed formulation reduces to the Michell plastic design setting in the limit of infinitely small imposed volume fraction. For higher volume fractions, one tends to recover limit analysis solutions associated with the full computational domain but with important potential savings of material for a similar load-bearing capacity.

One key aspect of our formulation is also related to the choice of a specific strength criterion for the considered material. This enables us to tackle not only materials with different properties in tension and compression, up to no-tension materials, but also to introduced preferred reinforcement orientations in anisotropic formulations. The latter are particularly

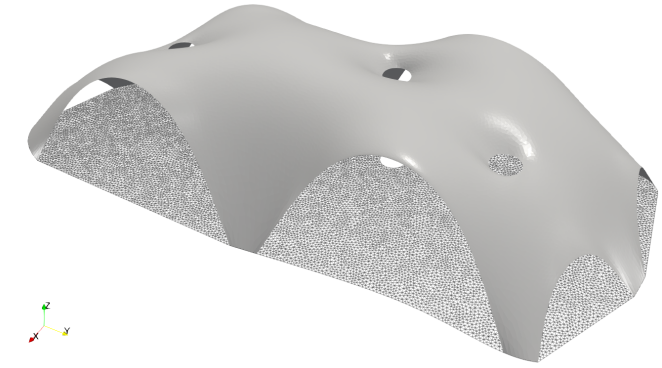

(a) 3D view

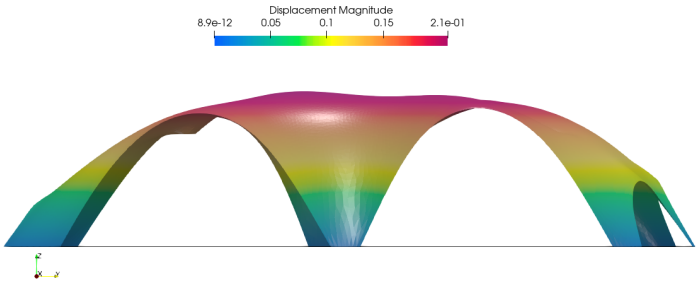


(b) Elevation view

Figure 6.22: Complex optimal shell structure

useful when optimizing two phases simultaneously, e.g. a concrete pure-compression and a steel pure-tension phase. The obtained topologies then become extremely close to strut-and-tie models which are particularly relevant for reinforced-concrete engineers.

Finally, we have also seen how the problem of finding optimal funicular arches or shells can be formulated using convex programs which is not necessarily obvious at first sight. Akin to topology optimization, form-finding problems rarely fit into a convex optimization framework. Interestingly, such formulations can also be related to a minimum compliance problem involving the geometric stiffness of a prestressed membrane. This point of view remains largely unexplored as of now and offers interesting perspectives for future research.

# Chapter 7

# Handling uncertainties using robust and stochastic optimization

In this chapter, we explore recent developments in the mathematical optimization and finance communities to account for uncertainties in non-linear mechanics problems. Instead of deriving the average value of a structure response with respect to such uncertainties, we rather aim at evaluating the worst-case behavior of the structure which should be accounted for in a safe design process. In particular, we propose a robust optimization formulation of limit analysis problems which aims at finding the worst-case limit load for any realization of the uncertain parameters among a given uncertainty set. Second, we also propose a risk-averse optimization approach for deriving best and worst-case estimates of the mechanical response of standard dissipative media using the Conditional Value-at-Risk (CVaR) measure.

## Contents

## 7.1 Introduction

When modeling and simulating real materials, it is important to account for uncertainties in material properties that are inevitable. In traditional deterministic constitutive modeling, material models are typically calibrated using a set of experimental data. However, even though these experimental data sets generally exhibit statistical distribution, the models are often calibrated based solely on the mean of the data, disregarding any information about uncertainties.

Advanced techniques of *uncertainty quantification* (UQ) aim to propagate the uncertainties in material properties from the material scale to the structural scale. These techniques are particularly important for designing and optimizing structures under uncertain operating conditions or environmental loads. They can be classified into two different categories: *intrusive* and *non-intrusive* ones. Non-intrusive approaches are a class of techniques used to propagate uncertainties through computational models without modifying the models themselves. The basic idea behind non-intrusive UQ methods is to use the model as a black box and construct a surrogate model, which is a computationally efficient approximation of the original model. The surrogate model is then used to perform the uncertainty quantification. The main advantage of non-intrusive UQ is that it can be applied to any existing computational model without the need for additional code development. Typical techniques involve Monte-Carlo sampling, polynomial chaos expansion, surface response methods or machine-learning techniques.

Conversely, intrusive UQ methods involve modifying the original computational model by including additional terms to propagate uncertainty through the system. They are called *intrusive* because they require direct modification of the original simulation code, which may be computationally expensive and time-consuming. However, they might be more accurate than non-intrusive approaches. A typical example is stochastic finite element method (Ghanem and Spanos, 2003), which involves introducing probabilistic models for material properties, loads, and boundary conditions into the finite element model of the structure. The probabilistic models are then propagated through the finite element analysis to obtain probabilistic estimates of the structural response. This approach is however difficult to generalize to highly non-linear material behaviour such as elastoplasticity. This is notably due to the important coupling between elasticity, plastic yield surfaces and hardening which can all be stochastic but also due to the history-dependent character of elastoplastic behaviour.

In the following, we describe two approaches based on robust and stochastic optimization to account for uncertainties in a rather simplified manner for the robust case or in a more detailed manner for the stochastic optimization case.

## 7.2 Robust optimization approach

In many cases, uncertainties are not necessarily known in great details. In particular, most stochastic approaches, including the one in Section 7.3 rely on *a priori* knowledge of the uncertain parameters probability distribution. In this first section, we instead aim at describing the uncertainties in a simpler manner. We assume that the uncertain material parameters, described by a general vector $\zeta$, belong to some known convex set $\mathcal{U}$, called an *uncertainty set*. The goal of *robust optimization* (Ben-Tal et al., 2009; Bertsimas et al., 2011) is then to find an optimal solution among all possible realizations of the problem data inside this uncertainty set. Such problems therefore often turn into min/max problems as they amount to optimizing with respect to the worst-case scenario among the uncertainty set.

### 7.2.1 Application to uncertain limit analysis

In the context of limit analysis, let us consider here the case where the loading is certain but the material may possess uncertain material properties. The strength criterion is now written as $G(\zeta)$ where $\zeta \in \mathcal{U} \subseteq \mathbb{R}^m$ is a vector of uncertain parameters in the uncertainty set. Obviously, the choice of the uncertainty set is an important modeling step in such approaches and depends on our knowledge of the origins of the considered uncertainty. If probability distributions are known, uncertainty sets can be based on the size of the support or the shape of the probability distribution. For instance, its size can correspond to a certain confidence level of the probability distribution. It can also be built from available data. Here, we can assume, for simplicity, that $\mathcal{U}$ is a convex ball of unit radius for some norm i.e. $\mathcal{U} = \{\zeta \in \mathbb{R}^m \text{ s.t. } \|\zeta\| \leq 1\}$. In particular, we will note by $\mathcal{U}_p$ uncertainty sets corresponding to the $L_p$-ball (typically with $p = 1, 2$ or $\infty$).

The maximum load factor now becomes uncertain i.e. it depends on the value $\zeta$ of the uncertainty realization:

$$\begin{aligned} \lambda^+(\zeta) = \max_{\lambda,\boldsymbol{\sigma}} \quad & \lambda \\ \text{s.t.} \quad & \operatorname{div} \boldsymbol{\sigma} + \lambda \boldsymbol{f}^{\mathrm{r}} + \boldsymbol{f}^{\mathrm{f}} = 0 \\ & \boldsymbol{\sigma} \cdot \boldsymbol{n} = \lambda \boldsymbol{t}^{\mathrm{r}} + \boldsymbol{t}^{\mathrm{f}} \\ & \boldsymbol{\sigma} \in G(\zeta) \end{aligned} \tag{7.1}$$

where $\boldsymbol{f}^{\mathrm{r}}$ (resp. $\boldsymbol{f}^{\mathrm{f}}$) is a variable (resp. fixed) body force and $\boldsymbol{t}^{\mathrm{r}}$ (resp. $\boldsymbol{t}^{\mathrm{f}}$) a variable (resp. fixed) surface traction.

### 7.2.2 Adjustable robust optimization

For a given loading and two different given realizations of the uncertainty, one expects that the corresponding optimal stress fields will be different depending on the uncertainty realizations. The most natural approach therefore consists in considering the stress field and the corresponding load factor to be *recourse variables*, i.e. variables which depend on the realization $\zeta$ of the uncertainty. Thus, we are faced with an *adjustable robust counterpart* (ARC) to problem (7.1) defined as follows:

$$\begin{aligned} \lambda_{\mathrm{ARC}} = \min_{\zeta \in \mathcal{U}} \lambda^+(\zeta) = \min_{\zeta \in \mathcal{U}} \max_{\boldsymbol{\sigma}(\zeta), \lambda(\zeta)} \quad & \lambda(\zeta) \\ \text{s.t.} \quad & \operatorname{div} \boldsymbol{\sigma}(\zeta) + \lambda(\zeta) \boldsymbol{f}^{\mathrm{r}} + \boldsymbol{f}^{\mathrm{f}} = 0 \\ & \boldsymbol{\sigma}(\zeta) \cdot \boldsymbol{n} = \lambda(\zeta) \boldsymbol{t}^{\mathrm{r}} + \boldsymbol{t}^{\mathrm{f}} \\ & \boldsymbol{\sigma}(\zeta) \in G(\zeta) \end{aligned} \tag{ARC}$$

i.e. we find the smallest maximum load factor for each realization of the uncertainty within the uncertainty set.

### 7.2.3 Static robust optimization

Unfortunately, adjustable recourse problem are numerically challenging. Indeed, formulation (ARC) involves a min/max problem and can be equivalently formulated as a max problem involving an infinite number of constraints. To solve adjustable recourse problem, one typically makes a simplifying assumption on how recourse variables depend on the uncertainty, the so-called *decision rules*.

The most simple of such rules is to assume that recourse variables are in fact static, i.e. they do not depend on the uncertainty. This yields to a conservative static robust counterpart

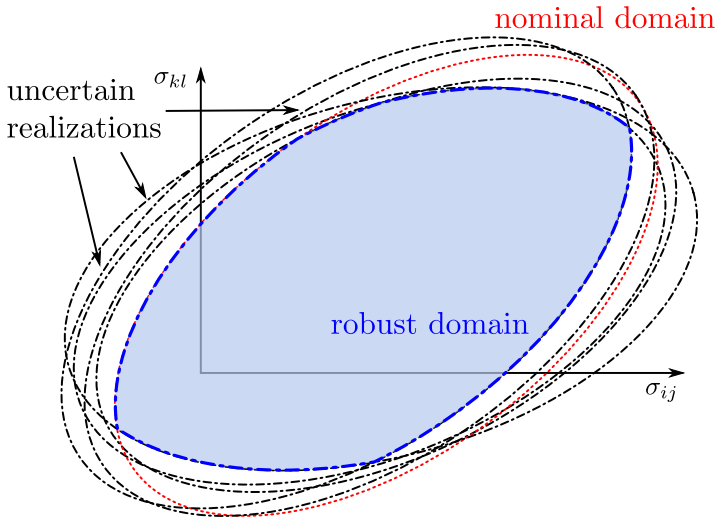


Figure 7.1: Robust strength domain $G_{\text{RC}}$ (in blue) obtained as the intersection of various uncertain realizations $G(\boldsymbol{\zeta})$ (in black) of a nominal domain (in red).

(RC) in which we look for a stress field $\boldsymbol{\sigma}$ and a load factor $\lambda$, independent of the exact realization of the uncertainty, which satisfy the strength condition $G(\boldsymbol{\zeta})$ for all $\boldsymbol{\zeta} \in \boldsymbol{\mathcal{U}}$. The corresponding problem can be formulated as follows:

$$\begin{aligned} \lambda_{\text{RC}} = \max_{\lambda,\boldsymbol{\sigma}} \quad & \lambda \\ \text{s.t.} \quad & \operatorname{div} \boldsymbol{\sigma} + \lambda \boldsymbol{f}^{\text{r}} + \boldsymbol{f}^{\text{f}} = 0 \\ & \boldsymbol{\sigma} \cdot \boldsymbol{n} = \lambda \boldsymbol{t}^{\text{r}} + \boldsymbol{t}^{\text{f}} \\ & \boldsymbol{\sigma} \in G(\boldsymbol{\zeta}) \qquad\qquad \forall \boldsymbol{\zeta} \in \boldsymbol{\mathcal{U}} \end{aligned} \tag{RC}$$

What makes problem (RC) a *robust optimization* problem is the condition $\forall \boldsymbol{\zeta} \in \boldsymbol{\mathcal{U}}$ in the last constraint. This implies that the constraint $\boldsymbol{\sigma} \in G(\boldsymbol{\zeta})$ must be fulfilled for any possible value of $\boldsymbol{\zeta} \in \boldsymbol{\mathcal{U}}$. It is therefore an infinite-dimensional constraint. One of the main goals of robust optimization theory is to make such a problem tractable using standard convex optimization algorithms.

For instance, the robust constraint can be reformulated as:

$$\boldsymbol{\sigma} \in G(\boldsymbol{\zeta}) \quad \forall \boldsymbol{\zeta} \in \boldsymbol{\mathcal{U}} \quad \Leftrightarrow \quad \boldsymbol{\sigma} \in G_{\text{RC}} \tag{7.2}$$

when introducing:

$$G_{\text{RC}} = \bigcap_{\boldsymbol{\zeta} \in \boldsymbol{\mathcal{U}}} G(\boldsymbol{\zeta}) \tag{7.3}$$

the robust counterpart to the uncertain strength criterion. In order for a stress field to be admissible with respect to any possible realization of the uncertain strength criterion $G(\boldsymbol{\zeta})$, it has to belong to the intersection of all such domains (see Fig. 7.1).

As a result, problem (RC) is a classical limit analysis problem with a different strength criterion given by (7.3). This makes problem (RC) very appealing provided that a simple expression for $G_{\text{RC}}$ can be found. It is however very hard to determine a simple expression for the infinite-dimensional set intersection appearing in (7.3). Fortunately, exact or approximate reformulation of strength criteria robust counterparts can be obtained in many cases, see Bleyer and Leclère (2022).

### 7.2.4 Affinely adjustable robust optimization

Unfortunately, if RC problems are numerically tractable, the obtained approximation might be unreasonably conservative (Bertsimas and Sim, 2004). A middle ground is the *affinely adjustable robust counterpart* (AARC), which consists in looking for adjustable variables $\boldsymbol{\sigma}(\boldsymbol{\zeta})$ and $\lambda(\boldsymbol{\zeta})$ that are affine functions of the uncertain variable, the so-called *affine decision rule* (Ben-Tal et al., 2004):

$$\boldsymbol{\sigma}(\boldsymbol{\zeta}) = \boldsymbol{\sigma}_0 + \sum_{j=1}^{m} \boldsymbol{\sigma}_j \zeta_j \tag{7.4a}$$

$$\lambda(\boldsymbol{\zeta}) = \lambda_0 + \sum_{j=1}^{m} \lambda_j \zeta_j \tag{7.4b}$$

where the $\boldsymbol{\sigma}_i$ (resp. $\lambda_i$) represent $1+m$ different stress fields (load factor variables) which are now static optimization variables. Inserting the affine decision rules (7.4a)-(7.4b) into (ARC), the corresponding AARC reads:

$$\begin{aligned}
\lambda_{\text{AARC}} = \max_{\boldsymbol{\sigma}_i, \lambda_i} \min_{\boldsymbol{\zeta} \in \mathcal{U}} \quad & \lambda_0 + \sum_{j=1}^{m} \lambda_j \zeta_j \\
\text{s.t.} \quad & \operatorname{div}\left(\boldsymbol{\sigma}_0 + \sum_{j=1}^{m} \boldsymbol{\sigma}_j \zeta_j\right) + \left(\lambda_0 + \sum_{j=1}^{m} \lambda_j \zeta_j\right) \boldsymbol{f}^{\mathrm{r}} + \boldsymbol{f}^{\mathrm{f}} = 0 \\
& \left(\boldsymbol{\sigma}_0 + \sum_{j=1}^{m} \boldsymbol{\sigma}_j \zeta_j\right) \cdot \boldsymbol{n} = \left(\lambda_0 + \sum_{j=1}^{m} \lambda_j \zeta_j\right) \boldsymbol{t}^{\mathrm{r}} + \boldsymbol{t}^{\mathrm{f}} \\
& \left(\boldsymbol{\sigma}_0 + \sum_{j=1}^{m} \boldsymbol{\sigma}_j \zeta_j\right) \in G(\boldsymbol{\zeta})
\end{aligned} \tag{7.5}$$

which can also be reformulated as follows:

$$\begin{aligned}
\lambda_{\text{AARC}} = \max_{\bar{\lambda}, \boldsymbol{\sigma}_i, \lambda_i} \quad & \bar{\lambda} \\
\text{s.t.} \quad & \operatorname{div}(\boldsymbol{\sigma}_j) + \lambda_j \boldsymbol{f}^{\mathrm{r}} + \boldsymbol{f}^{\mathrm{f}} = 0 && \forall j = 0, \dots, m \\
& \boldsymbol{\sigma}_j \cdot \boldsymbol{n} = \lambda_j \boldsymbol{t}^{\mathrm{r}} + \boldsymbol{t}^{\mathrm{f}} && \forall j = 0, \dots, m \\
& \left(\boldsymbol{\sigma}_0 + \sum_{j=1}^{m} \boldsymbol{\sigma}_j \zeta_j\right) \in G(\boldsymbol{\zeta}) && \forall \boldsymbol{\zeta} \in \mathcal{U} \\
& \bar{\lambda} \leq \lambda_0 + \sum_{j=1}^{m} \lambda_j \zeta_j && \forall \boldsymbol{\zeta} \in \mathcal{U}
\end{aligned} \tag{AARC}$$

in which we removed the uncertainty from the objective function and replaced the minimization over $\boldsymbol{\zeta}$ with robust constraints. Note that equality constraints depending on $\boldsymbol{\zeta}$ have been re-expressed by identifying the corresponding terms of the expansion in terms of $\zeta_i$ since $\mathcal{U}$ is full dimensional.

### 7.2.5 Comparison between the different approaches

Summarizing, (RC) is the most conservative formulation yielding the smallest limit load. (AARC) is more flexible since it considers additional static variables $\boldsymbol{\sigma}_j, \lambda_j$ for $j = 1, \dots, m$ and

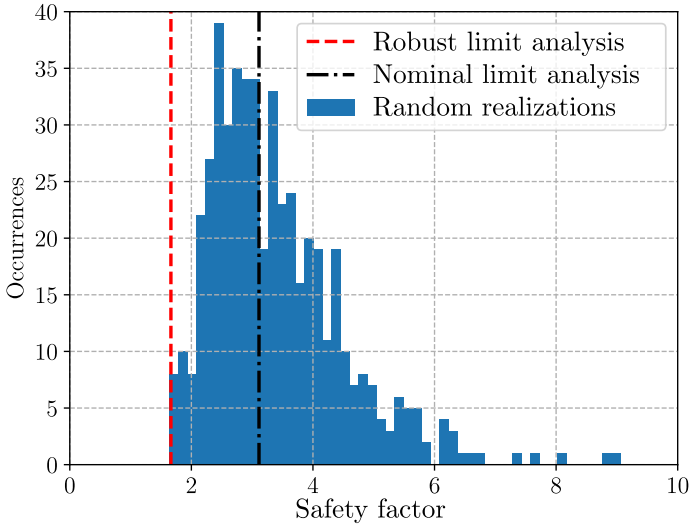


Figure 7.2: Empirical distribution of the slope stability safety factor. The vertical black and red lines correspond to a single deterministic limit analysis with either nominal strength properties or using the corresponding robust strength condition.

reduces to (RC) if we fix all $\sigma_j = 0$. As mentioned, (ARC) is less conservative than (AARC) since we allow for more general decision rules but is generally untractable. Finally, all of these formulations guard against all possible realizations of the uncertainty such that we have the following ordering:

$$\lambda_{\mathrm{RC}} \leq \lambda_{\mathrm{AARC}} \leq \lambda_{\mathrm{ARC}} \leq \lambda^+(\boldsymbol{\zeta}) \quad \forall \boldsymbol{\zeta} \in \mathcal{U} \tag{7.6}$$

### 7.2.6 Illustrative example

As an illustration, we consider a slope stability problem for a cohesive-frictional soil with uncertain values for the cohesion and friction angle ($c = 1 \pm 0.1$ MPa and $\phi = (30 \pm 10)°$) for a pseudo-static earthquake loading $\boldsymbol{f} = (0.2g, -g)$. In this case, the robust criterion $G_{\mathrm{RC}}$ can be well approximated by the intersection of two Mohr-Coulomb cones, see Bleyer and Leclère (2022), each of them having the minimal value for the cohesion i.e. $c_{\min} = 0.9$ MPa and one cone being associated with the smallest friction angle $\phi_{\min} = 20°$ and the other with the largest friction angle $\phi_{\max} = 40°$.

The problem has been formulated using a finite-element discretization using the `fenics_optim` package described in Bleyer (2020a) and solved using Mosek (MOSEK ApS, 2019b). Fig. 7.2 represents the empirical distribution of the slope safety factor obtained for 200 random realizations of the material parameters. The nominal safety factor is slightly larger than 3 whereas the robust estimate is slightly less than 2 and indeed corresponds to the lower bound of the empirical distribution. It can be seen from Fig. 7.3 that the collapse mechanism in the robust case involves a much larger volume of soil than the nominal case since the most critical scenario corresponds to a smaller friction angle.

## 7.3 Risk-averse behaviour of standard dissipative media

In this section, we present our contribution to develop a stochastic variational formulation accounting for non-smooth material behaviour under uncertainty. Using the concepts of

(a) Nominal collapse mechanism

(b) Robust collapse mechanism

Figure 7.3: Collapse mechanism and concentrated dissipation in slip lines for the nominal and robust case.

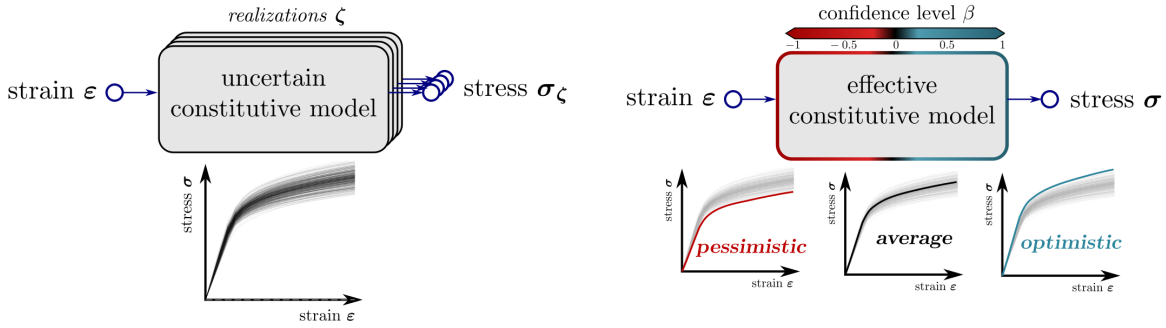


Figure 7.4: A stochastic material resulting in a stochastic stress-strain response (left) is replaced with an effective constitutive behavior (right), depending on a confidence level $\beta$. Average, optimistic and pessimistic effective behavior are obtained depending on the choice of the confidence level when evaluating the effective behavior.

*stochastic programming*, we provide a thermodynamically consistent formulation of stochastic Generalized Standard Materials. We will discuss in particular how to define an effective behaviour to obtain the average response of the material. More importantly, we will be interested in obtaining optimistic and pessimistic effective responses of the material, see Fig. 7.4. To do so, we borrow from the concepts of risk measures in mathematical finance and study the use of the *Conditional Value-at-Risk* in this context. This section is extracted from Bleyer (2023b).

### 7.3.1 Stochastic approach of material behaviour

#### Formulation of an effective behaviour

Let us first investigate the formulation of material behaviour in the stochastic setting. For simplicity, we restrict ourselves to rate-independent behaviours. As we have seen before, dissipative materials can be described by the primal incremental variational principle (4.62) involving the generic incremental convex potential $j(\varepsilon)$.

We now assume that it depends upon random parameters $\zeta$ which have a known probability distribution i.e. $j(\varepsilon;\zeta)$ is now a random field. We are interested in the *effective behaviour* of the material with respect to the variability of $\zeta$ and therefore consider the following effective potential:

$$j^{\text{eff}}(\varepsilon) = \mathcal{R}\left[j(\varepsilon;\zeta)\right] \tag{7.7}$$

where $\mathcal{R}$ refers to some effective measure of $j$ over all realizations $\zeta$. Since $j$ is defined as a minimum problem involving an uncertain objective function, its computation therefore falls into the scope of *stochastic programming*. The most classical choice for the effective measure is the expected value $\mathcal{R}[j] = \mathbb{E}\left[j\right]$ which only considers the average behaviour of the material. For engineering applications, one is instead interested in events of low probability which might be more detrimental to the structural safety. In such a context, it becomes interesting to rely on the notion of *risk measures* which will be later introduced in Section 7.3.2.

**Internal state variables in the stochastic setting**

Before that, let us first discuss the classical case where $\mathcal{R}[j] = \mathbb{E}\left[j\right]$. In the stochastic setting, the first question which arises concerns the dependency of the internal state variables with respect to the uncertainty. Since we are interested in computing an effective behaviour of the material, we consider the total strain $\boldsymbol{\varepsilon}$ to be imposed by the external observer. In a global structural analysis, $\boldsymbol{\varepsilon}$ will for instance be obtained by minimizing the effective potential associated with $j^{\text{eff}}$. In the stochastic programming setting, $\boldsymbol{\varepsilon}$ is therefore referred to as a *first-stage variable* since its value is chosen independently from the exact realization of the uncertainty. On the contrary, the implicit state variables $\boldsymbol{\alpha}$ are referred to as *second-stage variables* i.e. their value directly depends on the uncertainty realization. To make this dependency more explicit, we will now use the subscripted notation $\boldsymbol{\alpha}_\zeta$.

In the stochastic setting where the different potentials are now random, we can wonder about how to select the appropriate internal state variables in addition to the effective observable strain $\boldsymbol{\varepsilon}$. A first possibility is to consider that we control the total strain $\boldsymbol{\varepsilon}_\zeta$ in all observations i.e.:

$$\boldsymbol{\varepsilon} = \boldsymbol{\varepsilon}_\zeta \quad \text{a.s.} \tag{7.8}$$

This assumption results in the fact that the total stress is controlled on average only i.e.:

$$\boldsymbol{\sigma} = \mathbb{E}\left[\boldsymbol{\sigma}_\zeta\right] \tag{7.9}$$

where $\boldsymbol{\sigma}_\zeta$ is the individual stress response of each realization.

Conversely, we can also decide to impose the total stress for each realization, while controlling the strain on average only i.e.:

$$\boldsymbol{\sigma} = \boldsymbol{\sigma}_\zeta \quad \text{a.s.} \tag{7.10}$$

$$\boldsymbol{\varepsilon} = \mathbb{E}\left[\boldsymbol{\varepsilon}_\zeta\right] \tag{7.11}$$

Both approaches are obviously not equivalent. For instance, in the case of linear elasticity, the first approach yields:

$$j^{\text{eff}}(\boldsymbol{\varepsilon}) = \mathbb{E}\left[\frac{1}{2}\boldsymbol{\varepsilon} : \mathbb{C}_\zeta : \boldsymbol{\varepsilon}\right] = \frac{1}{2}\boldsymbol{\varepsilon} : \mathbb{E}\left[\mathbb{C}_\zeta\right] : \boldsymbol{\varepsilon} \tag{7.12}$$

whereas the second approach yields:

$$\begin{aligned} j^{\text{eff}}(\boldsymbol{\varepsilon}) = \min_{\boldsymbol{e}_\zeta} \quad & \mathbb{E}\left[\frac{1}{2}(\boldsymbol{\varepsilon} + \boldsymbol{e}_\zeta) : \mathbb{C}_\zeta : (\boldsymbol{\varepsilon} + \boldsymbol{e}_\zeta)\right] \quad = \frac{1}{2}\boldsymbol{\varepsilon} : \mathbb{E}\left[\mathbb{C}_\zeta^{-1}\right]^{-1} : \boldsymbol{\varepsilon} \\ \text{s.t.} \quad & \mathbb{E}\left[\boldsymbol{e}_\zeta\right] = 0 \end{aligned} \tag{7.13}$$

We therefore see that the first approach will produce an elastic behaviour characterized by the average elastic moduli whereas the second expression is associated with the harmonic average of the elastic moduli. Note that both quantities are not equal in general, as we only have $\mathbb{E}\left[\mathbb{C}_\zeta\right] \succcurlyeq \mathbb{E}\left[\mathbb{C}_\zeta^{-1}\right]^{-1}$ where inequality is understood in the sense of quadratic forms. Note that a result similar to (7.13) can also be found in Junker and Nagel (2019).

**Numerical application**

We now illustrate the more general stochastic formulations on the example of a one-dimensional elasto-plastic behaviour with isotropic power-law hardening. The corresponding 1D potentials are given by:

$$\psi(\varepsilon, \varepsilon^p, p) = \psi_{\text{el}}(\varepsilon, \varepsilon^{\text{p}}) + \psi_{\text{h}}(p) \tag{7.14}$$

$$\psi_{\text{el}}(\varepsilon, \varepsilon^{\text{p}}) = \frac{1}{2}E(\zeta)(\varepsilon - \varepsilon^{\text{p}})^2 \tag{7.15}$$

$$\psi_{\text{h}}(p) = \frac{1}{1+1/m}H(\zeta)p^{1+1/m} \tag{7.16}$$

$$\phi(\dot{\varepsilon}^p, \dot{p}) = \begin{cases} \sigma_0(\zeta)\dot{p} & \text{for } |\dot{\varepsilon}^p| \leq \dot{p} \\ +\infty & \text{otherwise} \end{cases} \tag{7.17}$$

We consider that the Young modulus $E(\zeta)$, hardening modulus $H(\zeta)$ and yield stress $\sigma_0(\zeta)$ are independent random variables following a lognormal distribution. We assume the power-law exponent $m$ to be deterministic ($m = 3$ in the following numerical simulations).

The stochastic programming formulation where we consider the total strain to be fully deterministic reads:

$$\begin{aligned} j^{\text{eff}}(\varepsilon) = \min_{\varepsilon^{\text{p}}_\zeta, p_\zeta} \quad & \frac{1}{2}\mathbb{E}\left[E(\zeta)(\varepsilon - \varepsilon^{\text{p}}_\zeta)^2\right] + \frac{1}{1+1/m}\mathbb{E}\left[H(\zeta)p_\zeta^{1+1/m}\right] + \mathbb{E}\left[\sigma_0(\zeta)(p_\zeta - p_{n,\zeta})\right] \\ \text{s.t.} \quad & |\varepsilon^{\text{p}}_\zeta - \varepsilon^{\text{p}}_{n,\zeta}| \leq p_\zeta - p_{n,\zeta} \end{aligned} \tag{7.18}$$

The corresponding dual potential is given by:

$$\begin{aligned} (j^{\text{eff}})^*(\sigma) = \min_{\sigma_\zeta, R_\zeta} \quad & \frac{1}{2}\mathbb{E}\left[\frac{1}{E(\zeta)}\sigma_\zeta^2\right] + \frac{1}{1+m}\mathbb{E}\left[\frac{1}{H(\zeta)^m}R_\zeta^{1+m}\right] + \mathbb{E}\left[\sigma_\zeta \varepsilon^{\text{p}}_{n,\zeta} - R_\zeta p_{n,\zeta}\right] \\ \text{s.t.} \quad & |\sigma_\zeta| \leq \sigma_0(\zeta) \quad \forall \zeta \\ & \sigma = \mathbb{E}\left[\sigma_\zeta\right] \end{aligned} \tag{7.19}$$

The second stochastic programming formulation where we consider the total stress to be deterministic reads:

$$\begin{aligned} j^{\text{eff}}(\varepsilon) = \min_{e_\zeta, \varepsilon^{\text{p}}_\zeta, p_\zeta} \quad & \frac{1}{2}\mathbb{E}\left[E(\zeta)(\varepsilon + e_\zeta - \varepsilon^{\text{p}}_\zeta)^2\right] + \frac{1}{1+1/m}\mathbb{E}\left[H(\zeta)p_\zeta^{1+1/m}\right] + \mathbb{E}\left[\sigma_0(\zeta)(p_\zeta - p_{n,\zeta})\right] \\ \text{s.t.} \quad & |\varepsilon^{\text{p}}_\zeta - \varepsilon^{\text{p}}_{n,\zeta}| \leq p_\zeta - p_{n,\zeta} \end{aligned} \tag{7.20}$$

The corresponding dual potential is given by:

$$\begin{aligned} (j^{\text{eff}})^*(\sigma) = \min_{R_\zeta} \quad & \frac{1}{2}\mathbb{E}\left[\frac{1}{E(\zeta)}\sigma^2\right] + \frac{1}{1+m}\mathbb{E}\left[\frac{1}{H(\zeta)^m}R_\zeta^{1+m}\right] + \mathbb{E}\left[\sigma \varepsilon^{\text{p}}_{n,\zeta} - R_\zeta p_{n,\zeta}\right] \\ \text{s.t.} \quad & |\sigma| \leq \sigma_0(\zeta) \quad \forall \zeta \end{aligned} \tag{7.21}$$

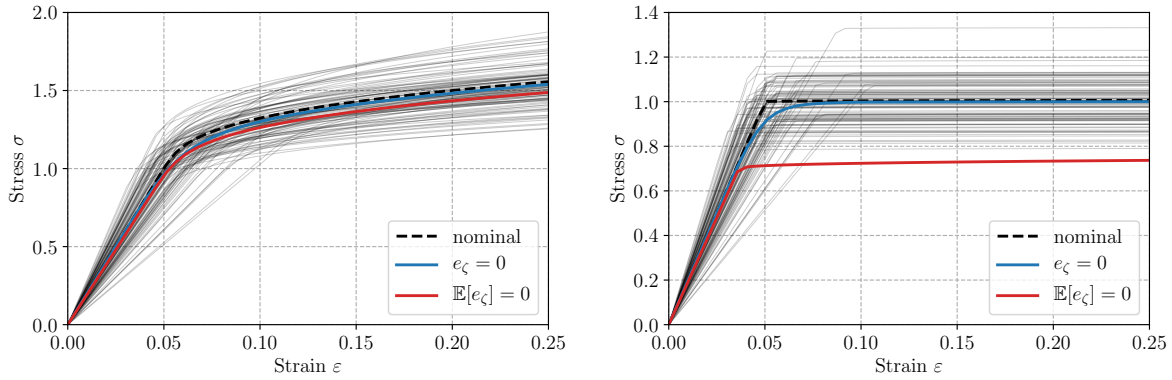


(a) Hardening case with $\mathbb{E}[H] = 1$

(b) Nearly perfectly plastic case with $\mathbb{E}[H] = 0.01$

Figure 7.5: Effective behaviour of a stochastic hardening elastoplastic material. The black dashed line corresponds to the nominal deterministic case where all parameters take their average value. Thin black lines correspond to 100 independent realizations of the stochastic behaviour.

Fig. 7.5a represents the corresponding effective behaviour for both formulations in the case where $\mathbb{E}[E] = 20$, $\mathbb{E}[H] = 1$ and $\mathbb{E}[\sigma_0] = 1$ and a 20% standard deviation for both $E$ and $H$ and 10% for $\sigma_0$. The effective behaviour is obtained either using formulation (7.18) (in blue) or (7.20) (in red). In both cases, expectations have been computed using a Monte-Carlo sampling approximation with a sample size $N = 500$. Minimization over the $N$ different state variables is performed using the `cvxpy` package (Diamond and Boyd, 2016; Agrawal et al., 2018). First, it can be seen that both approaches lead to a very similar behaviour, the second formulation (7.20) being slightly softer than the first one due to the presence of additional total strain variables. Interestingly, the obtained effective behaviour is close to the nominal deterministic behaviour except that it exhibits an earlier and progressive onset of plasticity since it accounts for a distribution of yield stress with different values.

This is further confirmed in Fig. 7.5b which corresponds to an almost perfectly-plastic behaviour with $\mathbb{E}[H] = 0.01$. We can observe that the effective behaviour corresponding to (7.18) admits an initial hardening phase before reaching a perfectly plastic plateau. Moreover, in the ultimate perfectly plastic regime, the elastic term vanishes so that $\varepsilon_\zeta^{\mathrm{p}} = \varepsilon$. One can then see that (7.18) gives approximately $j^{\mathrm{eff}}(\varepsilon) \approx \mathbb{E}[\sigma_0]|\varepsilon - \varepsilon_n|$ in the asymptotic regime of the perfectly plastic case. The final plastic plateau is therefore given by the average yield stress $\mathbb{E}[\sigma_0] = 1$.

Conversely, formulation (7.20) clearly fails in reproducing a reasonable effective behaviour. This can indeed be well understood when inspecting the dual formulation (7.21) in which the last constraint will enforce the observable stress to satisfy the plasticity criterion for any possible realization of the yield stress $\sigma_0(\boldsymbol{\zeta})$. As a result, this constraint can in fact be reformulated as $|\sigma| \leq \min_\zeta \sigma_0(\boldsymbol{\zeta})$ which is overly conservative. Note that we obtain here a non-zero yield stress due to the fact that we have a finite set of samples but, in theory for a lognormal distribution, this minimum should be zero.

We might therefore be tempted to conclude that the second formulation imposing a deterministic stress is not relevant. However, when inspecting again the dual formulation (7.21), we can see that a minor modification could lead to a relevant effective estimate, yet

different from (7.18)-(7.19). Indeed, the last constraint can also be formulated as $g(\sigma;\zeta) \leq 1$ $\forall\zeta$ where $g(\sigma;\zeta) = |\sigma|/\sigma_0(\zeta)$ is the gauge function of the corresponding yield criterion. Since the second formulation involves a deterministic stress, we then see that satisfying the yield condition almost surely is too restrictive. Another classical approach in stochastic programming is to replace such a hard constraint by a soft counterpart such as imposing that the constraint is satisfied on average only, hence $\mathbb{E}\left[g(\sigma;\zeta)\right] \leq 1$. In the present case, this amounts to imposing $|\sigma| \leq \dfrac{1}{\mathbb{E}\left[\dfrac{1}{\sigma_0(\zeta)}\right]}$. The new dual formulation therefore reads:

$$\begin{aligned}(j^{\text{eff}})^*(\sigma) = \min_{R_\zeta} \quad & \frac{1}{2}\mathbb{E}\left[\frac{1}{E(\zeta)}\sigma^2\right] + \frac{1}{1+m}\mathbb{E}\left[\frac{1}{H(\zeta)^m}R_\zeta^{1+m}\right] + \mathbb{E}\left[\sigma\varepsilon^{\text{p}}_{n,\zeta} - R_\zeta p_{n,\zeta}\right] \\ \text{s.t.} \quad & \mathbb{E}\left[|\sigma|/\sigma_0(\zeta)\right] \leq 1 \quad \forall\zeta\end{aligned} \tag{7.22}$$

Going back to the corresponding primal formulation, (7.22) is the dual to the following primal formulation:

$$\begin{aligned}j^{\text{eff}}(\varepsilon) = \min_{e_\zeta,\varepsilon^{\text{p}}_\zeta,p_\zeta} \quad & \frac{1}{2}\mathbb{E}\left[E(\zeta)(\varepsilon + e_\zeta - \varepsilon^{\text{p}}_\zeta)^2\right] + \frac{1}{1+1/m}\mathbb{E}\left[H(\zeta)p_\zeta^{1+1/m}\right] + \max_\zeta[\sigma_0(\zeta)(p_\zeta - p_{n,\zeta})] \\ \text{s.t.} \quad & |\varepsilon^{\text{p}}_\zeta - \varepsilon^{\text{p}}_{n,\zeta}| \leq p_\zeta - p_{n,\zeta}\end{aligned} \tag{7.23}$$

where the only difference with (7.20) is that the effective measure of the dissipation potential is no longer the expectation but the worst-case value. Fig. 7.6 shows the obtained effective estimate using this third formulation involving soft yield constraints. Clearly, we can see that this formulation removes the deficiencies of (7.20) which we identified earlier. Besides, it yields an effective behaviour which is close to formulation (7.18), the main difference being that there is no progressive onset of plasticity in this case. Note that for a lognormal variable $X$ we have:

$$\mathbb{E}\left[X^{-1}\right]^{-1} = \mathbb{E}[X]\left(1 + \frac{\text{var}[X]}{\mathbb{E}[X]^2}\right)^{-1} \approx \mathbb{E}[X] \tag{7.24}$$

when the variance is small as in the present case. This explains for instance in Fig. 7.6b why the effective yield stress are very close for both formulations (only 1% difference since we have a 10% standard deviation on $\sigma_0$). However, let us point out that we might see more differences for other types of distributions than a lognormal one.

To conclude, we have seen that there exist different possible formulations of an effective behaviour for a stochastic dissipative material. Depending on the chosen hypothesis regarding whether total strain is considered as a first-stage or second-stage variable, the associated thermodynamic stress should be respectively considered as a second-stage or a first-stage variable. Depending on the chosen hypothesis, we have also seen that the retained effective measure plays an important role, especially concerning the dissipation potential. These various formulations seem to yield very close effective behaviour which can question the usefulness of having such a discussion. However, we considered here the expectation as an effective measure of the behaviour. In the following, we will now discuss other choices, in particular risk measures which can take into account low probability events rather than average behaviour. In such a case, the distinction between these different formulations will be crucial.

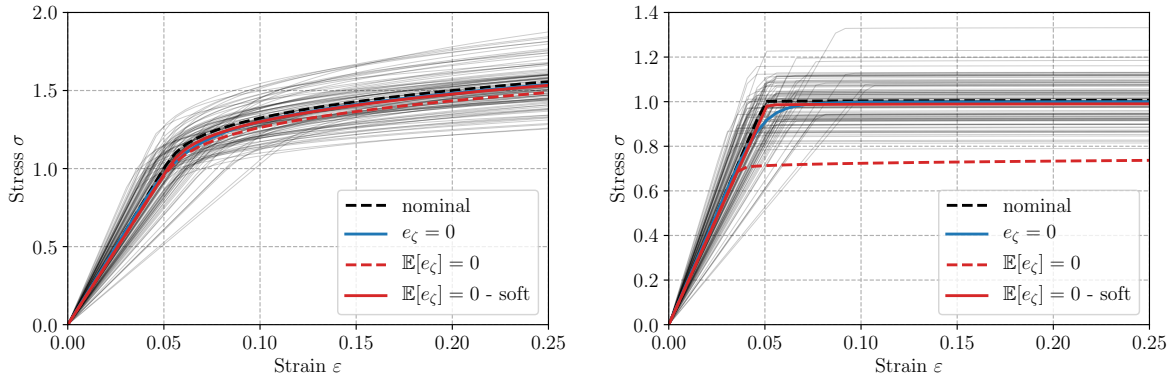


(a) Hardening case with $\mathbb{E}[H] = 1$

(b) Nearly perfectly plastic case with $\mathbb{E}[H] = 0.01$

Figure 7.6: Effective behaviour of a stochastic hardening elastoplastic material using the soft constraint formulations (7.23).

### 7.3.2 Coherent risk measures

In financial mathematics, a risk measure is a functional which amounts to quantify the level of risk of a given random variable $X$ where $X$ can be, for instance, some financial loss or cost, see (Rockafellar, 2007) for a broad overview. In the subsequent presentation, we follow the tradition in optimization where costs should be minimized. Therefore, we consider that large positive values of $X$ are disliked. The choice of a proper risk measure will aim at guarding against large values of $X$. Many possibilities of risk measures can be considered, depending on how the decision-maker evaluates risks. Typical examples are for instance:

- the expected value:
$$\mathcal{R}[X] = \mathbb{E}[X] \tag{7.25}$$
- the safety margin using $k$ standard deviations:
$$\mathcal{R}[X] = \mathbb{E}[X] + k\,\mathrm{std}[X], \quad \text{for } k > 0 \tag{7.26}$$
- the worst-case value:
$$\mathcal{R}[X] = \sup X \tag{7.27}$$
- the *Value-at-Risk* (VaR) for a confidence level $\beta \in [0;1]$ (or the $\beta$-quantile):
$$\mathcal{R}[X] = \mathrm{VaR}_\beta(X) = \inf\{Z \text{ s.t. } \mathbb{P}[Z \geq X] \geq \beta\} \tag{7.28}$$
- and many more...

Recently, attention has been devoted to the use of so-called *coherent risk measures* which are a specific class of risk measures benefiting from desirable properties proposed by Artzner et al. (1999) such as translational invariance, monotonicity and convexity. For instance, the expected value is a coherent risk measure but it is not very useful in quantifying the amount of risk since it does not take into account events in the distribution tail. This measure is therefore termed *risk-neutral*. Risk measures satisfying $\mathcal{R}[X] > \mathbb{E}[X]$ are instead called *risk-averse* measures.

The safety margin measure (7.26) is for instance risk-averse but is not coherent. Conversely, the worst-case value fulfills both coherency and risk-aversion but is not useful in

practice due to being severely conservative. The $\mathrm{VaR}_\beta(X)$ might be an interesting risk-averse measure as it gives an estimate of $X$ which is exceeded only with probability $1-\beta$. It is however not convex and hence does not fall into the class of coherent risk measures. As a result, stochastic programs in which an uncertain convex function $j(\boldsymbol{\varepsilon}, \boldsymbol{\zeta})$ is replaced with $\mathrm{VaR}_\beta(j)(\boldsymbol{\varepsilon})$ would not be convex anymore which is extremely undesirable from the computational and theoretical perspective. A very popular risk-averse measure closely linked to the VaR and which overcomes this drawback is the *Conditional Value-at-Risk* (CVaR).

### 7.3.3 Conditional Value-at-Risk and risk-averse estimates

For a continuous distribution, the CVaR is defined as the expected value of $X$ above $\mathrm{VaR}_\beta$:

$$\mathrm{CVaR}_\beta(X) = \mathbb{E}\left[X \text{ s.t. } X \geq \mathrm{VaR}_\beta(X)\right] \tag{7.29}$$

The above definition is slightly more technical when considering discrete distributions, we refer the reader to (Rockafellar and Uryasev, 2002) for a rigorous definition.

The CVaR is then a coherent risk measure and a key result due to Rockafellar et al. (2000) is that CVaR benefits from the following convex optimization characterization:

$$\mathrm{CVaR}_\beta(X) = \inf_\lambda \lambda + \frac{1}{1-\beta}\mathbb{E}\left[\langle X-\lambda\rangle_+\right] \tag{7.30}$$

where $\langle\star\rangle_+ = \max\{\star, 0\}$ denotes the positive part. From this definition, it is clear that $\mathrm{CVaR}_0(X) = \mathbb{E}[X]$. Let us also point out that, if the minimum of (7.30) is unique, then the optimal value is exactly $\lambda = \mathrm{VaR}_\beta(X)$.

The $\mathrm{CVaR}_\beta$ of $|\mathbf{x}|$ for a vector $\mathbf{x} \in \mathbb{R}^N$ can also be interpreted as a norm parameterized by $\beta$. Indeed, for $\beta = 0$, it reduces to the geometric average of all entries, whereas for $\beta = 1$ it reduces to the maximum norm. For intermediate values, it can be seen as an average of the $k$ largest values of $|\mathbf{x}|$ where $k/N = 1-\beta$, see Mafusalov and Uryasev (2013); Pavlikov and Uryasev (2014) for a more precise definition.

Applying such concepts from financial optimization to mechanics requires to decide on what would be the "loss" function against which we want to be immunized. This not necessarily an obvious question to answer. Let us first investigate what would be obtained when considering the CVaR as an effective measure $\mathcal{R}$ in (7.7) in the simple case where the behaviour is linear elastic, hence here $j(\boldsymbol{\varepsilon}) = \psi(\boldsymbol{\varepsilon}) = \frac{1}{2}\boldsymbol{\varepsilon} : \mathbb{C} : \boldsymbol{\varepsilon}$. We assume that uncertainty affects only the material Young modulus so that $E(\boldsymbol{\zeta})$ is a random variable and $\mathbb{C}(\boldsymbol{\zeta}) = E(\boldsymbol{\zeta})\mathbb{C}_0$ for some reference $\mathbb{C}_0$ material with unit Young modulus (see Fig. 7.7a). Then, one easily sees that:

$$\psi^{\mathrm{eff}}(\boldsymbol{\varepsilon}) = \mathrm{CVaR}_\beta\left(\psi\right)(\boldsymbol{\varepsilon}) = \frac{1}{2}\boldsymbol{\varepsilon} : \mathrm{CVaR}_\beta(E)\,\mathbb{C}_0 : \boldsymbol{\varepsilon} \tag{7.31}$$

i.e. one obtains a linear elastic material with an effective Young modulus $E^{\mathrm{eff}} = \mathrm{CVaR}_\beta(E)$. In the following, we use the notation $E_{\overline{\beta}} = \mathrm{CVaR}_\beta(E)$ which has the following properties:

$$E_{\overline{0}} = \mathbb{E}[E] \tag{7.32}$$

$$E_{\overline{1}} = \sup E \tag{7.33}$$

$$E_{\overline{\beta}} \geq \mathrm{VaR}_\beta(E) \tag{7.34}$$

$$E_{\overline{\beta}} \leq E_{\overline{\beta}'} \quad \forall \beta \leq \beta' \tag{7.35}$$

For $\beta \in [0;1]$, the effective modulus therefore varies from its mean value to its supremum (which can be infinite). In practice, $\beta$ is often chosen close to 1 e.g. $\beta = 0.95, 0.99$ so that $E_{\overline{\beta}}$ provides a best-case estimate of the material Young modulus. It might therefore appear strange to consider this stiff estimate as being a useful risk measure from the engineering point of view, since stiff materials are generally looked for. As it will be clear later, considering a CVaR in a primal displacement-based principle will yield an overestimation of the mechanical performance compared to its mean value. Structural performance underestimation will instead be obtained through duality. The confidence level $\beta$ will enable us to reach tail behaviours (both left and right) when $\beta$ is close to 1. We will therefore use in the following the term *risk* or *risk-averse* measure to denote a measure of the deviation from the mean value, irrespective of the fact that such a value can be beneficial or detrimental from the engineering point of view.

### 7.3.4 Dual CVaR

#### Quadratic elastic potentials

In Bleyer (2023a), we proposed to obtain the worst-case estimate of an elastic potential $\psi$ by taking the conjugate function of the CVaR of the conjugate i.e. $(\psi^*)^*_{\overline{\beta}}$. In the elastic case, we easily see that:

$$(\psi^*)_{\overline{\beta}}(\boldsymbol{\sigma}) = \frac{1}{2}\boldsymbol{\sigma} : \mathrm{CVaR}_\beta\left(E^{-1}\right)\mathbb{S}_0 : \boldsymbol{\sigma} \tag{7.36}$$

$$(\psi^*)^*_{\overline{\beta}}(\boldsymbol{\varepsilon}) = \frac{1}{2}\boldsymbol{\varepsilon} : (\mathrm{CVaR}_\beta\left(E^{-1}\right))^{-1}\mathbb{C}_0 : \boldsymbol{\varepsilon} \tag{7.37}$$

where $\mathbb{S}_0 = (\mathbb{C}_0)^{-1}$. This defines an elastic material with an effective Young modulus given by:

$$E^{\text{eff}} = E_{\underline{\beta}} = \mathrm{CVaR}_\beta\left(E^{-1}\right)^{-1} = ((E^{-1})_{\overline{\beta}})^{-1} \tag{7.38}$$

where we introduced the dual CVaR notation $E_{\underline{\beta}}$ which enjoys the following properties:

$$E_{\underline{0}} = \mathbb{E}\left[E^{-1}\right]^{-1} \tag{7.39}$$

$$E_{\underline{1}} = \inf E \tag{7.40}$$

$$E_{\underline{\beta}} \leq \mathrm{VaR}_\beta(E^{-1})^{-1} \tag{7.41}$$

$$E_{\underline{\beta'}} \leq E_{\underline{\beta}} \quad \forall \beta \leq \beta' \tag{7.42}$$

In the generic case of a convex function $f(\boldsymbol{x})$, one has the following convex formulation:

$$\begin{aligned} (f^*)^*_{\overline{\beta}}(\boldsymbol{x}) = \inf_{\widehat{\boldsymbol{x}},z} \quad & \mathbb{E}\left[z f(\widehat{\boldsymbol{x}}/z)\right] \\ \text{s.t.} \quad & \mathbb{E}\left[\widehat{\boldsymbol{x}}\right] = \boldsymbol{x} \\ & 0 \leq z \leq \frac{1}{1-\beta} \\ & \mathbb{E}\left[z\right] = 1 \end{aligned} \tag{7.43}$$

Unfortunately, we see that this definition is not suitable for all convex functions. Indeed, for positive homogeneous functions for instance, the objective simplifies to $\mathbb{E}\left[f(\widehat{\boldsymbol{x}})\right]$ and the auxiliary variable $z$, and thus $\beta$, play no role anymore. For instance, in the case where $f(\boldsymbol{x}) = k(\boldsymbol{\zeta})\|\boldsymbol{x}\|_p$ is the support function of a $L_q$-ball of radius $k(\boldsymbol{\zeta})$ with $\frac{1}{p} + \frac{1}{q} = 1$, one can

easily see that (7.43) yields the ball of smallest radius i.e. $(f^*)^*_{\underline{\beta}}(\boldsymbol{x}) = \{\inf k(\boldsymbol{\zeta})\}\|\boldsymbol{x}\|_p$. This is obviously not what we are looking for as this worst-case estimate is way too conservative and does not depend on $\beta$. We can remark that we recover an issue similar to that encountered previously with formulation (7.21) of the effective behaviour.

### Polar-based definition

Instead, we propose to obtain the worst-case estimate of a positive convex function $f$ by taking the polar function of the CVaR of the polar function:

$$f_{\underline{\beta}}(\boldsymbol{x}) = (f^\circ)^\circ_{\underline{\beta}}(\boldsymbol{x}) \tag{7.44}$$

where the polar is defined as Rockafellar (1970, Th. 15.4):

$$f^\circ(\boldsymbol{y}) = \inf\{\mu \geq 0 \text{ s.t. } (\boldsymbol{x},\boldsymbol{y}) - \mu f(\boldsymbol{x}) \leq 1 \quad \forall \boldsymbol{x}\} \tag{7.45}$$

In the case of quadratic convex functions, $f^\circ = f^*$ so that the polar definition (7.44) coincides with that given in Bleyer (2023a) in the context of linear elasticity.

Moreover, we have the following convex representation of $f_{\underline{\beta}}(\boldsymbol{x})$:

$$\begin{aligned} f_{\underline{\beta}}(\boldsymbol{x}) = \inf_{v\geq 0} \quad & \max\{\mathbb{E}\left[vf(\boldsymbol{x}/v)\right]; (1-\beta)\sup\{vf(\boldsymbol{x}/v)\}\} \\ \text{s.t.} \quad & \mathbb{E}[v] \leq 1 \end{aligned} \tag{7.46}$$

### The case of homogeneous functions

Suppose now that $f$ is homogeneous, then $f^\circ = g_G$ i.e. it is the gauge function of the convex set $G$ from which $f$ is the support function. For the previous support function $f(\boldsymbol{x}) = k(\boldsymbol{\zeta})\|\boldsymbol{x}\|_p$, $G = \{\boldsymbol{y} \text{ s.t. } \|\boldsymbol{y}\|_q \leq k(\boldsymbol{\zeta})\}$ so that $f^\circ(\boldsymbol{y}) = g_G(\boldsymbol{y}) = \dfrac{1}{k(\boldsymbol{\zeta})}\|\boldsymbol{y}\|_q$. Thus:

$$f^\circ_{\overline{\beta}}(\boldsymbol{y}) = (k^{-1})_{\overline{\beta}}\|\boldsymbol{y}\|_q = \frac{1}{k_{\underline{\beta}}}\|\boldsymbol{y}\|_q \tag{7.47}$$

$$\Rightarrow \quad f_{\underline{\beta}}(\boldsymbol{x}) = (f^\circ)^\circ_{\underline{\beta}}(\boldsymbol{x}) = k_{\underline{\beta}}\|\boldsymbol{x}\|_p \tag{7.48}$$

Finally, $f_{\underline{\beta}}$ defines a $p$-norm scaled by the worst-case estimate $k_{\underline{\beta}}$ which is typically what was expected. This result can be generalized in the sense that $f^\circ_{\overline{\beta}} = (g_G)_{\overline{\beta}}$ is homogeneous and therefore defines a new convex set $G_{\underline{\beta}}$ such that $(g_G)_{\overline{\beta}} = g_{G_{\underline{\beta}}}$. Hence, $(g_{G_{\underline{\beta}}})^\circ = f_{\underline{\beta}}$ is the support function of $G_{\underline{\beta}}$.

### Properties

Note that one has:

$$f_{\underline{\beta'}} \leq f_{\underline{\beta}} \leq f_{\underline{0}} = \mathbb{E}\left[f^\circ\right]^\circ \leq f_{\overline{0}} = \mathbb{E}\left[f\right] \leq f_{\overline{\beta}} \leq f_{\overline{\beta'}} \qquad \forall\, 0 \leq \beta \leq \beta' < 1 \tag{7.49}$$

Let us also recall that the optimal value of $\lambda$ in the CVaR definition (7.30) corresponds to the VaR. Then, $g^\circ = \text{VaR}_\beta(f^\circ)$ is such that $F_{f^\circ}(g^\circ) = \beta$. But one also has $F_{f^\circ}(g^\circ) = \mathbb{P}\left[f^\circ \leq g^\circ\right] = \mathbb{P}\left[f \geq g\right]$ so that:

$$F_{f^\circ}(g^\circ) = 1 - F_f(g) = \beta \quad \Rightarrow \quad F_f(g) = 1 - \beta \tag{7.50}$$

We conclude that $g = \text{VaR}_\beta(f^\circ)^\circ$ corresponds to the $(1-\beta)$-quantile of $f(\boldsymbol{x};\boldsymbol{\zeta})$. However, $f_{\underline{\beta}}$ does not correspond to the expectation below this $(1-\beta)$-quantile but rather the "polar expectation" $\mathbb{E}\left[f^\circ\right]^\circ$ below this quantile.

#### Illustration on one-dimensional behaviours

All these results concerning the CVaR best-case and worst-case estimates of simple behaviours are illustrated in Fig. 7.7 in the one-dimensional case. Thin black lines denote independent realizations of the corresponding potential and stress-strain curve assuming a lognormal distribution of the corresponding material coefficient with a unit mean and a 10% standard deviation. $\mathrm{CVaR}_\beta^+$ (resp. $\mathrm{CVaR}_\beta^-$) denotes the corresponding best-case (resp. worst-case) estimate obtained using $\psi_{\overline{\beta}}$ (resp. $\psi_\beta$) as the corresponding convex potential. Numerical results have been represented for a $95\overline{\%}$ confidence level.

### 7.3.5 Risk-averse stochastic programming of the structural response

#### A truss example

In this section, we investigate the global response of a structure in the previous stochastic behaviour framework. We will illustrate the proposed formulations on the 2D truss structure of Fig. 7.8 made of $M = 30$ members. Each member is of identical cross-section $S = 1$ and assumed to follow the hardening elastoplastic behaviour of (7.14)-(7.17). As before, the Young modulus $E$, the hardening modulus $H$ and the yield stress $\sigma_0$ for each member are assumed to be independent random variables following a lognormal distribution of mean $\mathbb{E}[E] = 20$, $\mathbb{E}[H] = 1$ and $\mathbb{E}[\sigma_0] = 1$. Unless stated otherwise, the corresponding standard deviations are again taken to be of 20% for the elastic moduli $E$ and $H$ and 10% for the yield stress $\sigma_0$. The reference loading $\boldsymbol{F}$ represented in Fig. 7.8 consists of vertical forces applied to the upper face. We will use a displacement-controlled path-following strategy by driving the associated work-conjugate displacement $U = \boldsymbol{F}^{\mathrm{T}}\boldsymbol{u}$ and report the corresponding load factor.

To fix ideas, Fig. 7.9 represents the bundle of structural responses for each of $N = 500$ realizations. It also reports the resolution of the corresponding deterministic problem when each bar property is affected its best-case CVaR value ($\mathrm{CVaR}_\beta^+$) of level $\beta$ or its worst-case dual CVaR value ($\mathrm{CVaR}_\beta^-$). For instance, $\mathrm{CVaR}_0^+$ corresponds to the nominal case and $\mathrm{CVaR}_0^-$ to the case where each property $X$ is of value $1/\mathbb{E}[1/X]$. Clearly, we see that simply taking the CVaR (resp. dual CVaR) value for each bar is way too optimistic (resp. pessimistic) since it assumes that each bar will take its best (resp. worst) case value simultaneously which is highly unlikely.

#### Effective structural response

In Section 7.3.1, we investigated the effective behaviour of a stochastic material by introducing an effective measure of the incremental potential density $j$. We now aim at extending the same concepts to investigate the effective structural response.

When using the risk-neutral measure $\mathcal{R} = \mathbb{E}$, we equivalently have:

$$\mathcal{R}[J](\boldsymbol{\varepsilon}) = \mathbb{E}\left[\int_\Omega j(\boldsymbol{\varepsilon};\boldsymbol{\zeta})\,\mathrm{d}\Omega\right] = \int_\Omega \mathbb{E}\left[j\right](\boldsymbol{\varepsilon})\,\mathrm{d}\Omega = \int_\Omega \mathcal{R}[j](\boldsymbol{\varepsilon})\,\mathrm{d}\Omega \tag{7.51}$$

In this case, the expectation is additive so that the effective global potential $J^{\mathrm{eff}} = \mathcal{R}[J]$ is equal to the global potential associated with the effective density $j^{\mathrm{eff}}$. However, this is no longer true when considering more complex nonlinear risk measures such as CVaR.

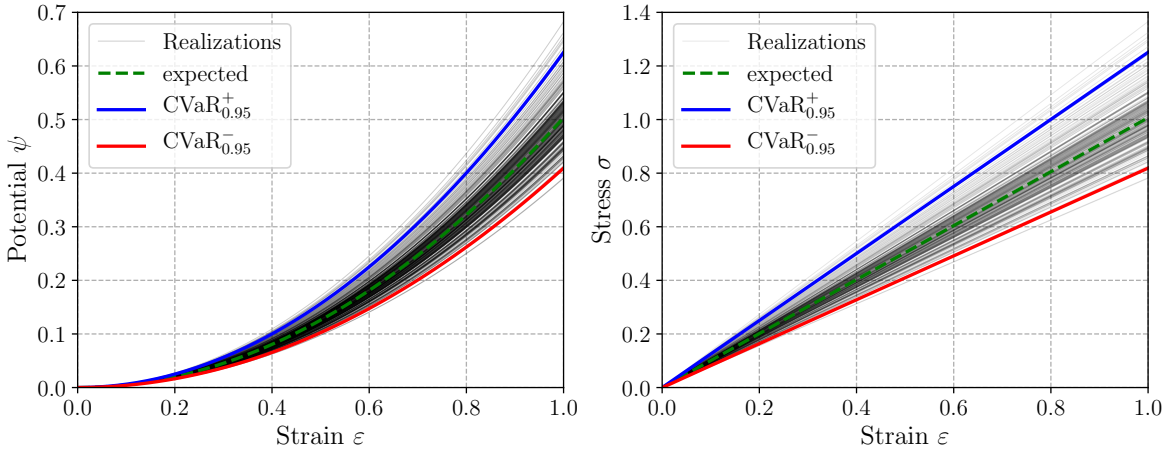


(a) Linear elastic behaviour $f(\varepsilon;\zeta) = E(\zeta)\frac{1}{2}\varepsilon^2$.

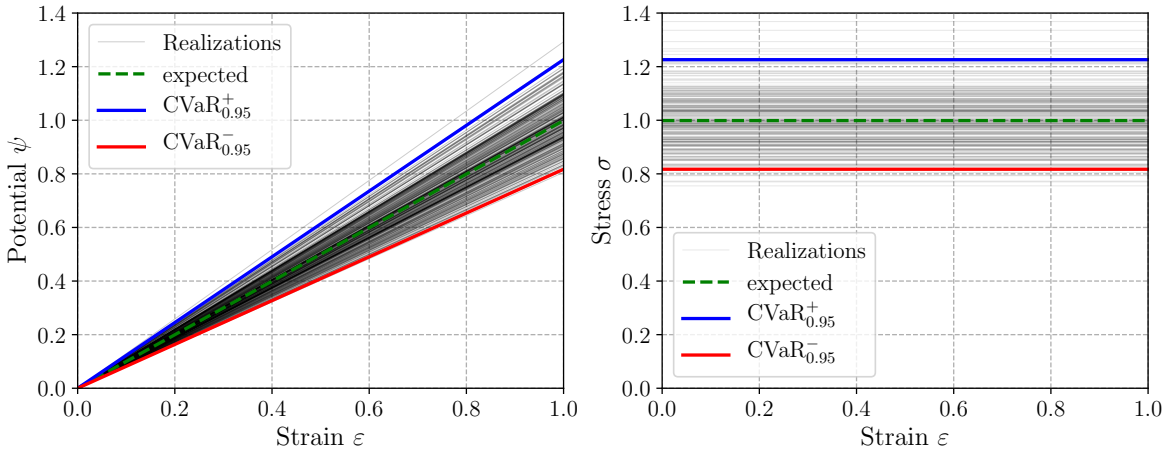


(b) Perfectly plastic behaviour $f(\varepsilon;\zeta) = k(\zeta)|\varepsilon|$.

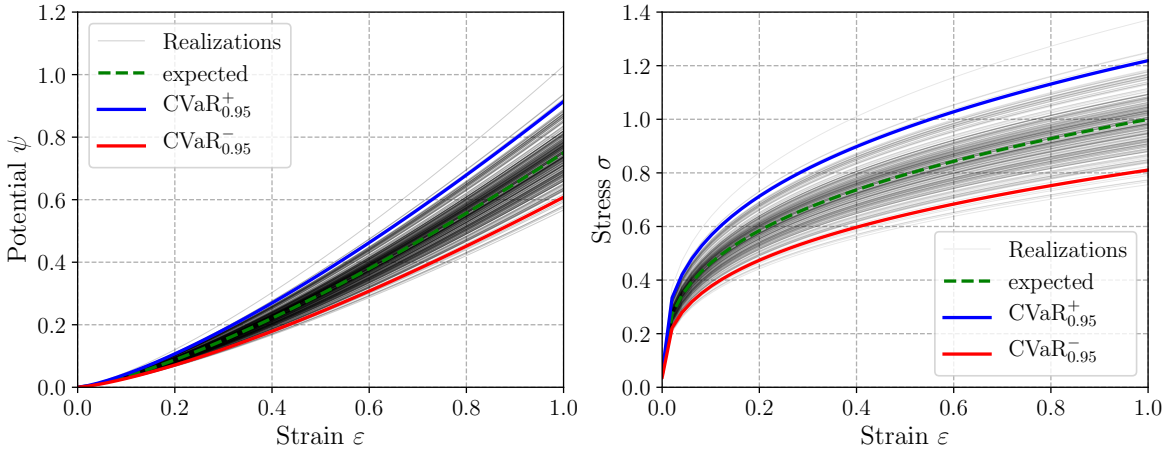


(c) Power-law behaviour $f(\varepsilon;\zeta) = H(\zeta)\frac{3}{4}|\varepsilon|^{4/3}$.

Figure 7.7: Risk-averse estimates of various 1D behaviours with lognormal distributions of unit mean and 10% standard deviations for $E(\zeta)$, $k(\zeta)$ and $H(\zeta)$.

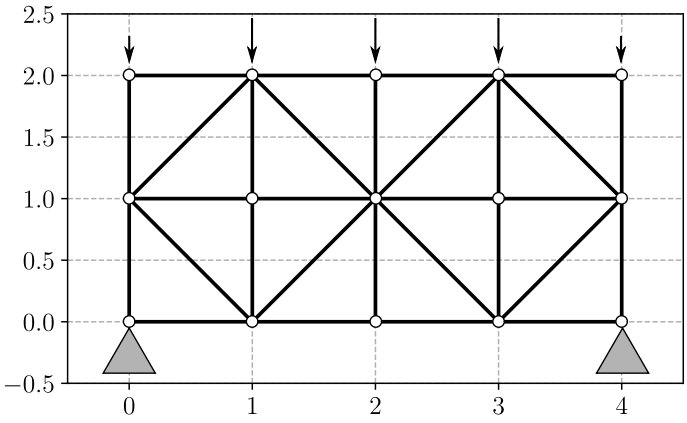


Figure 7.8: Truss structure with reference loading consisting of downwards vertical forces of intensity 1 on the middle nodes and 0.5 on the end nodes.

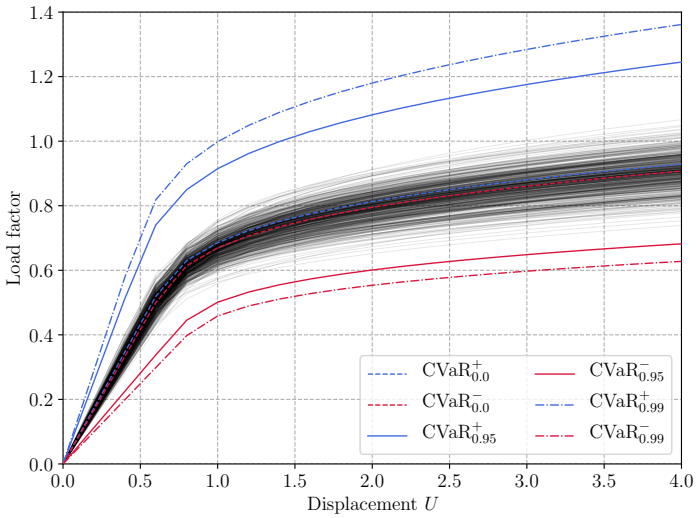


Figure 7.9: Stochastic structural response for 500 realizations and deterministic responses using the CVaR and dual CVaR value of each material property.

**Primal risk-averse formulation**

The extension of the previous risk-averse material response will rely on introducing the global free-energy and dissipation pseudo-potentials:

$$\Psi(\boldsymbol{\varepsilon}, \boldsymbol{\alpha}; \beta) = \int_\Omega \psi(\boldsymbol{\varepsilon}, \boldsymbol{\alpha}; \boldsymbol{\zeta}) \, \mathrm{d}\Omega \tag{7.52}$$

$$\Phi(\boldsymbol{\varepsilon}, \boldsymbol{\alpha}; \beta) = \int_\Omega \phi(\boldsymbol{\varepsilon}, \boldsymbol{\alpha}; \boldsymbol{\zeta}) \, \mathrm{d}\Omega \tag{7.53}$$

These are now stochastic global potentials and we apply the same formulation as before on the *global* potentials rather than on the local potentials:

$$\begin{aligned} \mathcal{R}_{\overline{\beta}}[J] &= \min_{\boldsymbol{\alpha}_\zeta} \mathrm{CVaR}_\beta \left( \Psi(\boldsymbol{\varepsilon}, \boldsymbol{\alpha}_\zeta; \boldsymbol{\zeta}) \right) + \mathrm{CVaR}_\beta \left( \Phi(\boldsymbol{\varepsilon} - \boldsymbol{\varepsilon}_n, \boldsymbol{\alpha}_\zeta - \boldsymbol{\alpha}_{\zeta,n}; \boldsymbol{\zeta}) \right) \\ &= \min_{\boldsymbol{\alpha}_\zeta} \Psi_{\overline{\beta}}(\boldsymbol{\varepsilon}, \boldsymbol{\alpha}_\zeta) + \Phi_{\overline{\beta}}(\boldsymbol{\varepsilon} - \boldsymbol{\varepsilon}_n, \boldsymbol{\alpha}_\zeta - \boldsymbol{\alpha}_{\zeta,n}) \end{aligned} \tag{7.54}$$

In the case where $\boldsymbol{\varepsilon}$ is not a dissipative variable, this leads to the following stochastic variational program:

$$\boldsymbol{u}_{n+1} = \arg\min_{\boldsymbol{u} \in \mathrm{KA}} \min_{\boldsymbol{\alpha}_\zeta} \Psi_{\overline{\beta}}(\boldsymbol{\varepsilon}, \boldsymbol{\alpha}_\zeta) + \Phi_{\overline{\beta}}(\boldsymbol{\alpha}_\zeta - \boldsymbol{\alpha}_{n,\zeta}) - \mathcal{P}_{\mathrm{ext}}(\boldsymbol{u}) \tag{7.55}$$

Note that $\mathcal{R}_{\overline{\beta}}$ is still a convex function of $\boldsymbol{\varepsilon}$ and reduces to $\mathbb{E}[J]$ for $\beta = 0$. Let us also point out that the notation used in (7.54) and (7.55) is slightly abusive in the sense that $\boldsymbol{\alpha}_\zeta$ is a second-stage optimization variable and therefore depends on $\boldsymbol{\zeta}$. In any case, introducing the convex formulation (7.30) in lieu of the CVaR operator in expression will result in (7.55) being a convex stochastic program where $\boldsymbol{\alpha}_\zeta$ are second-stage variables and $\boldsymbol{u}$, $\boldsymbol{\varepsilon}$ and the two $\lambda$ parameters associated with each CVaR terms are first-stage variables. The introduction of the two CVaR measures only adds these two additional scalar variables compared to a formulation based on the expectation. It introduces some additional non-linearity in the problem due to the presence of the positive part in (7.30). The latter can however be considered as very minor compared to the material non-linearity.

As discussed before, this risk-averse stochastic program can be solved by adopting a Monte-Carlo sampling approximation, yielding the following equivalent deterministic problem:

$$\begin{aligned} \underset{\boldsymbol{u} \in \mathrm{KA}, \boldsymbol{\alpha}^{(1)}, \ldots, \boldsymbol{\alpha}^{(N)}, \lambda_\Psi, \lambda_\Phi}{\arg\min} \quad & \lambda_\Psi + \frac{1}{1-\beta} \frac{1}{N} \sum_{k=1}^{N} \Psi_+^{(k)} + \lambda_\Phi + \frac{1}{1-\beta} \frac{1}{N} \sum_{k=1}^{N} \Phi_+^{(k)} - \mathcal{P}_{\mathrm{ext}}(\boldsymbol{u}) \\ \text{s.t.} \quad & \int_\Omega \psi(\boldsymbol{\varepsilon}, \boldsymbol{\alpha}^{(k)}; \boldsymbol{\zeta}^{(k)}) \, \mathrm{d}\Omega - \lambda_\Psi \leq \Psi_+^{(k)} \qquad \forall k = 1, \ldots, N \\ & \int_\Omega \phi(\boldsymbol{\varepsilon} - \boldsymbol{\varepsilon}_n, \boldsymbol{\alpha}^{(k)} - \boldsymbol{\alpha}_n^{(k)}; \boldsymbol{\zeta}^{(k)}) \, \mathrm{d}\Omega - \lambda_\Phi \leq \Phi_+^{(k)} \\ & 0 \leq \Psi_+^{(k)} \\ & 0 \leq \Phi_+^{(k)} \end{aligned} \tag{7.56}$$

which is conic-representable when both $\psi$ and $\phi$ are conic-representable. This problem is often called a *deterministic equivalent* of the original stochastic problem. Obviously, solving the above effective problem is computationally intensive since a large number of realizations must be considered in order for the Monte-Carlo sampling approximation to converge and the problem size scales with $N$. A large body of works in the literature is therefore devoted to improving the efficiency of computing the corresponding effective behaviour using various techniques such as variance reduction, adaptive sampling, kriging methods, etc.

Clearly, for $\beta > 0$, the solution to (7.56) will result in a "stiffer/stronger" response than the corresponding risk-neutral problem with $\beta = 0$.

**Dual risk-neutral formulation**

Following the developments of Section 7.3.4, it would make sense to replace in (7.54) the CVaR measure of $\Psi$ and $\Phi$ with their dual CVaR measure. However, we also need to provide some supplementary freedom by considering that the total strain is controlled on average only in order to derive correct worst-case estimates. Hence, we consider the following risk-averse measure:

$$\mathcal{R}_{\underline{\beta}}[J] = \min_{\boldsymbol{\varepsilon}_\zeta, \boldsymbol{\alpha}_\zeta} \Psi_{\underline{\beta}}(\boldsymbol{\varepsilon}_\zeta, \boldsymbol{\alpha}_\zeta) + \Phi_{\underline{\beta}}(\boldsymbol{\varepsilon}_\zeta - \boldsymbol{\varepsilon}_{n,\zeta}, \boldsymbol{\alpha}_\zeta - \boldsymbol{\alpha}_{\zeta,n}) \tag{7.57}$$

to be used in the stochastic program:

$$\boldsymbol{u}_{n+1} = \arg\min_{\boldsymbol{u}\in\mathcal{U}_{\text{ad}}} \min_{\boldsymbol{\alpha}_\zeta} \Psi_{\underline{\beta}}(\boldsymbol{\varepsilon}, \boldsymbol{\alpha}_\zeta) + \Phi_{\underline{\beta}}(\boldsymbol{\alpha}_\zeta - \boldsymbol{\alpha}_{n,\zeta}) - W_{\text{ext},n+1}(\boldsymbol{u}) \tag{7.58}$$

Note that in the case of a rate-independent material, the stress formulation involves a yield criterion of the form $g(\boldsymbol{Y}_\zeta; \boldsymbol{\zeta}) \leq 1$ to be satisfied at all $\boldsymbol{x} \in \Omega$. With the corresponding formulation, the latter is transformed into the following yield criterion:

$$\text{CVaR}_\beta \left( \sup_\Omega g(\boldsymbol{Y}_\zeta) \right) \leq 1 \tag{7.59}$$

We therefore see that the corresponding risk-averse yield criterion will involve the CVaR of the maximum value of the gauge function $g$ attained on $\Omega$. If we particularize this expression to the case of a single material point, we therefore have $\text{CVaR}_\beta \left( g(\boldsymbol{Y}_\zeta) \right) \leq 1$. In the risk-neutral case $\beta = 0$, this reduces to $\mathbb{E}\left[ g(\boldsymbol{Y}) \right] \leq 1$ which coincides with the yield constraint proposed in (7.22).

As before, its numerical resolution is obtained by a Monte-Carlo sampling approximation resulting in a convex program involving $N$ state variables. It is important to differentiation our approach from a Monte-Carlo sampling evaluation of various realizations of the structural response. Here, instead of evaluating $N$ times the full structural response associated with a classical constitutive law, we evaluate only once (for a given value of $\beta$) the effective structural response which is now associated with a more complex constitutive law (the classical constituive law being basically duplicated $N$ times). Our motivation is that, for large-scale problems, solving for the displacement field in a Newton-Raphson method is much more time-consuming than evaluating the constitutive equation. Therefore, despite an additional complexity in solving the constitutive model, we expect this formulation to be way more efficient computationally than a direct sampling.

### 7.3.6 Illustrative application

We first analyze the effective response of the truss structure in the risk-neutral $\beta = 0$. Fig. 7.10 shows the corresponding response obtained when solving the risk-neutral stochastic programs (7.55) and (7.58). We see that there is indeed a duality gap between both formulations since the dual CVaR risk measure is not equivalent to the CVaR measure for $\beta = 0$. This gap is however moderate. In particular, both formulations yield a good approximation of the average structural response when comparing with the empirical distribution of load-displacement curves.

We then consider the resolution of both problems in the risk-averse case with $\beta = 0.95$. Fig. 7.11 shows the different obtained responses when considering different types of uncertainty. On Fig. 7.11a, we assume that uncertainty affects only the Young modulus. In this case, the bundle of responses is quite thin and the behaviour has much less variance in the final

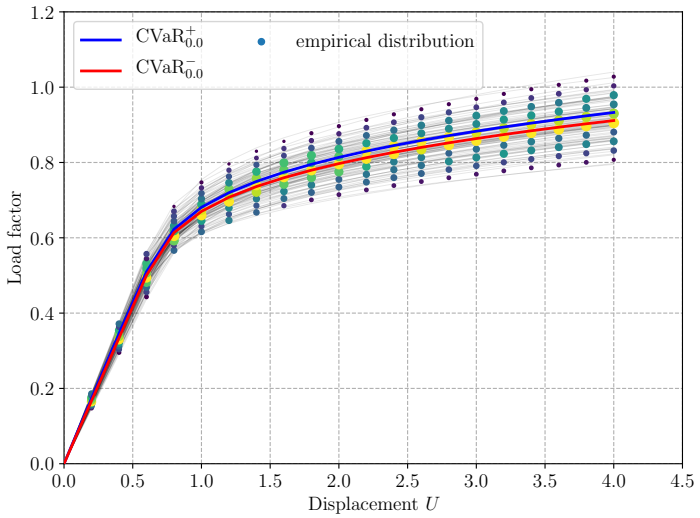


Figure 7.10: Risk-neutral $\beta = 0$ structural responses using the primal CVaR measure (7.55) and the dual CVaR measure (7.58).

hardening stage of the response. Both formulations are however able to correctly account for a best-case and a worst-case estimate of the response. On Fig. 7.11b, uncertainty affects only the hardening modulus which results in a much wider spread of the responses after a first deterministic elastic stage. Again, both risk-averse estimates are of very good quality compared to the empirical distribution. They coincide in the first deterministic elastic stage and then exhibit a hardening behaviour with a different slope, following that of the response distribution. A similar observation can also be made concerning Fig. 7.11c which considers only a yield strength uncertainty. Here, the difference is that both risk-averse estimates show a similar hardening response but the onset of plasticity occurs at different load levels, closely matching that of the empirical distribution. Finally, Fig. 7.11d is the most interesting since it considers a simultaneous uncertainty on all three mechanical parameters. Again, the agreement is also excellent in this case.

As regards this last case, Fig. 7.12 displays the deformed configurations of the truss structure for two different load levels corresponding to a displacement $U = 2$ and $U = 4$. The effective responses obtained from the resolution of both risk-averse formulations (7.55) and (7.58) have been compared against 25 of the uncertain realizations. First, we can see that the spread of nodal displacements can be quite large for some nodes and such a spread increases with the load level. Let us point out that, since we have a displacement control, all deformed configuration have the same equivalent displacement $U$ which corresponds to a weighted-average of the vertical displacement of the top surface. However, each deformed configuration will be associated with a very different state of internal forces. This is particularly highlighted by Fig. 7.12b which shows that the worst-case effective response using the dual CVaR measure (in red) is close to a collapsed state where its vertical members on both supports experience a very strong deformation. On the contrary, the best-case estimate in blue seems to be much stiffer for the same load level.

Fig. 7.13 investigates the influence on the confidence level $\beta$ on the obtained risk-averse estimate. As expected, going from 0 to 1 yields a stiffer and stronger response for the estimate obtained with the CVaR measure whereas one obtains a softer and weaker response for that obtained with the dual CVaR measure. One can see that going from $\beta = 0.95$ to $\beta = 0.995$ does not have too much of an influence here. However, we must moderate this observation

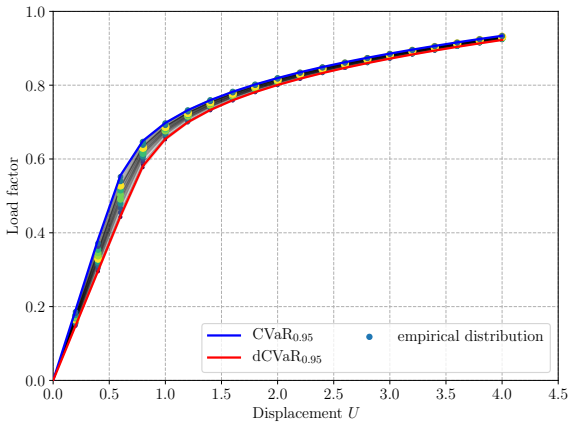


(a) Uncertainty on $E$ only

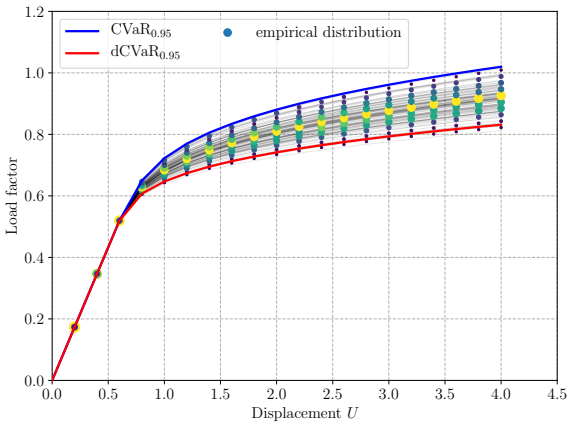


(b) Uncertainty on $H$ only

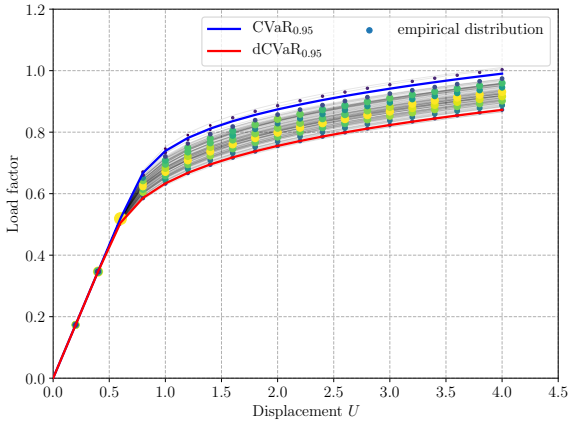


(c) Uncertainty on $\sigma_0$ only

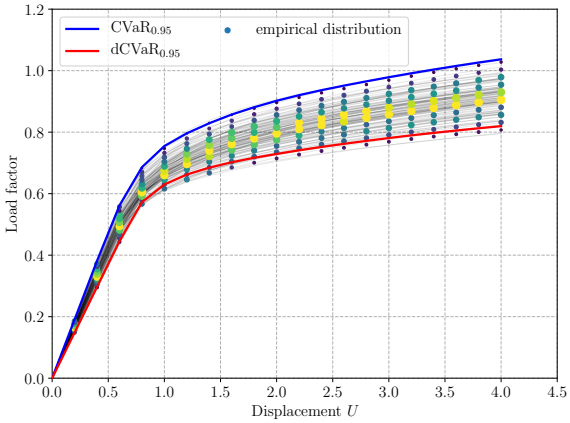


(d) Uncertainty on $E, H$ and $\sigma_0$

Figure 7.11: Risk-averse estimates for various types of uncertainty

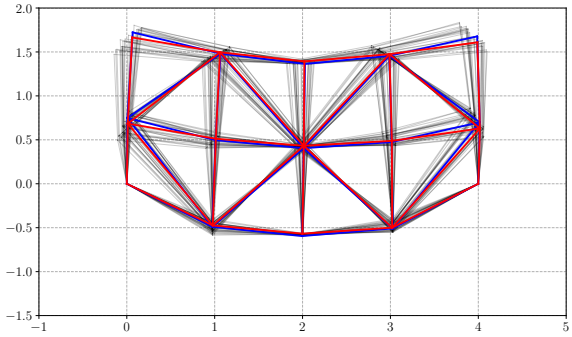

(a) $U = 2$

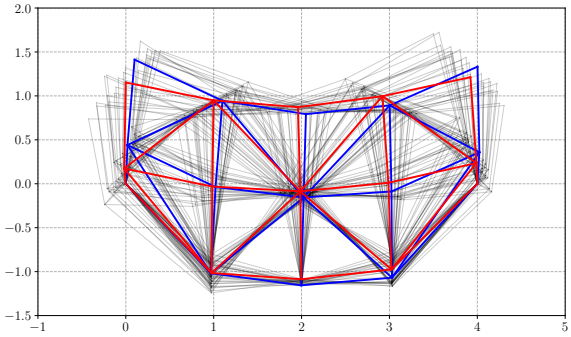

(b) $U = 4$

Figure 7.12: Effective deformed configurations: primal CVaR (blue), dual CVaR (red) and 25 random realizations

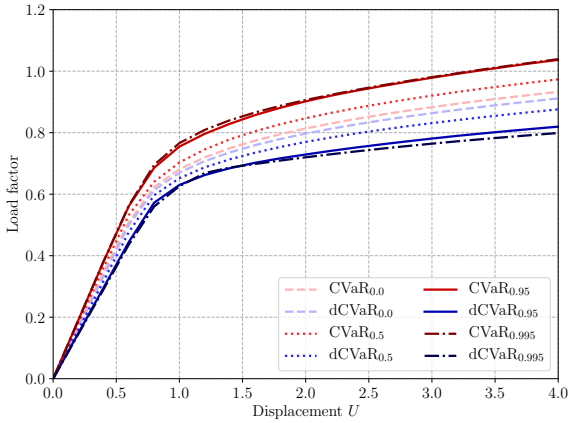


(a) Influence of confidence level $\beta$ for $N = 100$

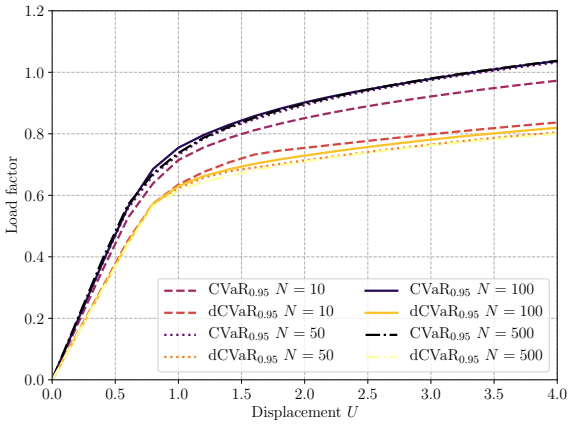


(b) Influence of number of realizations $N$ for $\beta = 0.95$

Figure 7.13: Influence of confidence level and number of sampling realizations on risk-averse estimates

since we used only a very small sample size in order to limit the computational cost. To further asses this aspect, Fig. 7.13b assesses the influence of the sample size $N$ for $\beta = 0.95$. It seems that reasonable estimates are already obtained with $N = 50$. In particular, it does not seem that one formulation is more sensitive than the other to the chosen sample size.

Finally, we further assess the efficiency of the proposed formulations on the much more challenging problem of a cyclic loading. In Fig. 7.14, the displacement amplitude is varied as $U : 0 \rightarrow 3 \rightarrow 0 \rightarrow 5 \rightarrow 0$. We can first observe that the cyclic behaviour of the truss is correctly reproduced. Moreover, in the plastic evolution phases, both formulation indeed produce the correct worst-case and best-case estimates, even after load direction has flipped signs. However, we can notice that in the elastic unloading/reloading phases, there is a crossover between the worst-case and best-case estimates. To explain this, let us consider the first unloading from $U = 3$ to 0. Even if the best-case estimate is stiffer than the worst-case one, at $U = 3$, the best-case response is associated with smaller plastic strain levels than the worst-case. Elastic unloading therefore occurs at different levels of plastic strain and this strain difference is then later compensated by stiffer/stronger response in the unloading stage. In the subsequent plastic yielding phases, the clearer separation between the optimistic and pessimistic responses is however quickly recovered.

## 7.4 Conclusions

This chapter introduced the theory of robust and stochastic optimization in the field of nonlinear mechanics. To our opinion, this approach is rather new in this field and offers very promising developments in the future. Regarding the stochastic approach of GSM materials, one key practical challenge is the numerical cost associated with an extensive number of internal state variables when using Monte-Carlo sampling. To overcome this difficulty, one potential strategy is to identify the set of active scenarios, for instance during global Newton iterations, which would significantly reduce the cost of evaluating the constitutive law. Indeed, when using the CVaR with a large risk-aversion level, we should expect only a small fractions of scenarios to be active at a given increment. Additionally, using linear or non-linear decision rules (Georghiou et al., 2015) for second-stage variables instead of sampling

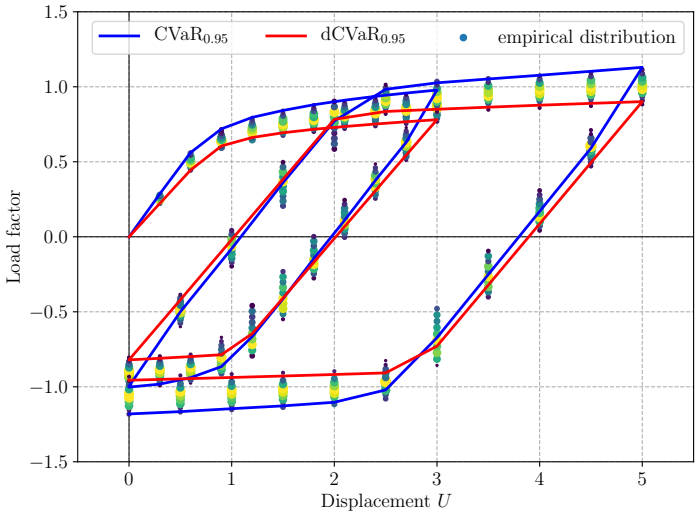


Figure 7.14: Risk-averse structural responses for a cylic loading.

could be a viable alternative to reduce this cost. More generally, it would be interesting to adapt this stochastic framework to a more classical treatment of constitutive laws in standard solvers.

# Chapter 8

# Variational regularization through gradient-based models

This chapter is devoted to non-convex problems which exhibit some kind of softening such as brittle fracture and damage models as well as softening plasticity problems. Section 8.2 first discusses the use of damage gradient or *phase-field* models used to regularize brittle fracture. We focus in particular on our contributions related to dynamic and anisotropic fracture. Finally, Section 8.3 presents a novel regularization method for elasto-plastic problems involving softening. The proposed approach departs from classical strain gradient plasticity models by including gradient regularization terms in the plastic dissipation potential.

**Contents**

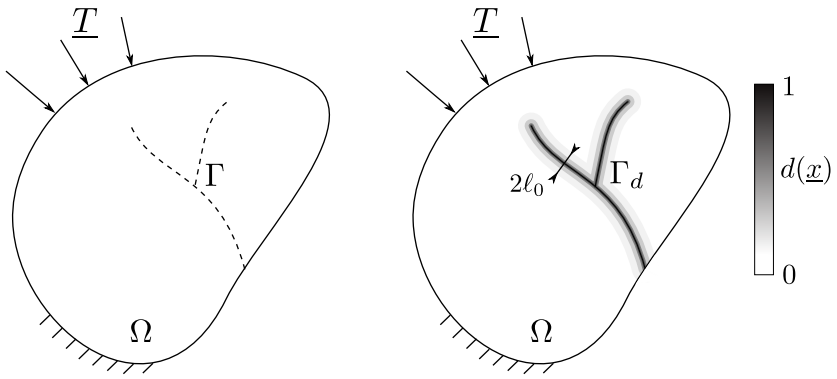


Figure 8.1: Regularization of a sharp crack problem with a phase-field/damage gradient model with regularization length $\ell_0$

## 8.1 Introduction

In practical applications, many materials exhibit, after a given load level, some form of degradation process, reducing its mechanical properties for increasing loading. This type of behavior is generally termed as *softening* in the sense that stress/strain relations are no longer monotonic increasing. Damage mechanics is the archetypal softening behavior model in which elastic properties are reduced through the evolution of a damage variable. Softening plasticity, in which elastic properties remain intact but plastic yield strength is reduced is another example. Finally, coupled elasto-plastic damage models can also be considered.

In all cases, softening behaviors are associated with a lack of convexity of the underlying energy potential and will result in localization of mechanical fields. Such models are therefore ill-posed and any discretization scheme will induce mesh-dependent results in which localization will occur over a band of one element width and dissipate zero energy in the limit of very fine meshes. Regularization strategies are therefore needed to remove such deficiencies.

Among the large number of possible strategies, all of them have in common of introducing *nonlocality*. Typical examples include:

- *ad hoc* regularization of local variables using integral or gradient-based averaging;
- generalized continua such as higher-order (e.g. strain gradient) or higher-grade (e.g. Cosserat) models;
- models base on gradients of internal state variables.

For more details, we refer to our chapter in the MEALOR II book (Besson et al., 2023, Chap. 11) and references therein.

The forthcoming discussion will focus on models based on gradients of internal state variables for both brittle and ductile fracture.

## 8.2 Variational models of brittle fracture

### 8.2.1 Introduction

It has always been notoriously difficult to accurately simulate the nucleation, propagation, kinking, branching of cracks in brittle materials. One of the main achievements of the

last decades has been the introduction of the variational approach to fracture by Francfort and Marigo (1998) who generalized the classical Griffith model of crack propagation in a variational energy minimization setting. In this setting, the displacement solution $\boldsymbol{u}$ and crack topology $\Gamma$ is obtained as the global minimum of a total energy $\mathcal{E}$ consisting of an elastic $\mathcal{E}_{\text{el}}$ and a fracture $\mathcal{E}_{\text{f}}$ energy:

$$\mathcal{E}(\boldsymbol{u},\Gamma) = \mathcal{E}_{\text{el}}(\boldsymbol{u},\Gamma) + \mathcal{E}_{\text{f}}(\Gamma) = \int_{\Omega\setminus\Gamma} \frac{1}{2}\boldsymbol{\varepsilon} : \mathbb{C} : \boldsymbol{\varepsilon}\, \mathrm{d}\Omega + G_{\text{c}}|\Gamma| \tag{8.1}$$

where the crack set is constrained to satisfy an irreversible evolution constraint: $\Gamma \supseteq \Gamma_n$ with respect to the previous time step $t_n$. Although this setting is formally appealing since crack path selection can be deduced from a global energy minimization principle, this model cannot account for crack nucleation and is challenging to implement numerically because of the geometrical nature of the crack set variable $\Gamma$.

To answer both challenges, a mathematical regularization has been proposed by Bourdin et al. (2000) based on a Ambrosio-Tortorelli regularization. The latter introduces an auxiliary field $d \in [0;1]$ where $d = 1$ represents the crack location and an internal length scale $\ell_0$ which limits via a gradient term localization effects. Evolution is still governed by a minimization principle over the pair $(\boldsymbol{u}, d)$ of the following total energy:

$$\mathcal{E}(\boldsymbol{u},d) = \mathcal{E}_{\text{el}}(\boldsymbol{u},d) + \mathcal{E}_{\text{f}}(d) = \int_{\Omega} g(d)\frac{1}{2}\boldsymbol{\varepsilon} : \mathbb{C} : \boldsymbol{\varepsilon}\, \mathrm{d}\Omega + \int_{\Omega} \frac{G_{\text{c}}}{c_w \ell_0}\left(w(d) + \ell_0^2 \|\nabla d\|^2\right) \mathrm{d}\Omega \tag{8.2}$$

where $g(d)$ is a degradation stiffness function, typically $g(d) = (1-d)^2$, and $w(d)$ is a local fracture energy density (e.g. $w(d) = d$ for the AT1 model, $w(d) = d^2$ for the AT2 model, etc.). Finally, $c_w$ is a normalization constant related to the specific choice of $w(d)$. It is chosen to ensure that the energy spent to create 1d localization profiles is exactly related to the input fracture energy $G_{\text{c}}$.

Such models have been initially introduced as a regularization of the variational approach to fracture and $\Gamma$-convergence towards the original model as $\ell_0 \to 0$ can be proved in various settings. However, it also turns out that such regularized models are able to predict crack nucleation with respect to a critical stress $\sigma_c \propto \sqrt{EG_c/\ell_0}$. In this sense, the numerical parameter $\ell_0$ can also be viewed as a physical material parameter and model (8.2) can be interpreted as a *gradient-damage model* (Pham et al., 2011; Tanné et al., 2018). Despite this historical perspective, the community eventually chose the term *phase-field* to describe this class of model, borrowing from similarities with models used in physics to describe phase changes in materials with diffuse interfaces.

One of the main success of such approaches is that crack path selection, including branching events, is automatically derived from an energy minimization principle without any additional criterion. Its prediction capabilities is continuously tested, favorably, against fracture experiments, see Figure 8.2.

### 8.2.2 Dynamic crack propagation and crack branching

Understanding the various mechanisms governing the dynamic propagation of a crack in a brittle medium is still an open challenge due to numerous phenomena occurring around the crack tip, including non-linear effects, dynamic stress redistribution due to crack front waves, crack tip splitting or crack surface instabilities. Dynamic linear fracture mechanics predicts that the Rayleigh wave speed $c_R$ is the limiting velocity of a mode I propagating crack (Stroh, 1957). However, various experimental results have shown that this simple picture of dynamic brittle fracture is far from being complete (Ravi-Chandar and Knauss, 1984a,b; Fineberg and

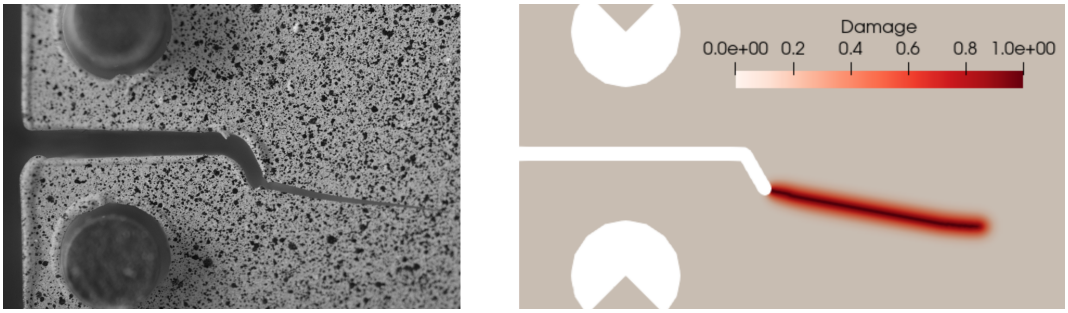


Figure 8.2: Crack propagation in a compact tension specimen: experimental crack path (left) vs numerical crack path with gradient-damage model (right). Source: MEALOR II Summer School

Marder, 1999). In particular, the existence of limiting velocities well below $c_R$, microscopic and macroscopic crack branching phenomena and a dependence of the fracture energy on the crack velocity have been observed experimentally.

We have worked with an extended version of the previous gradient damage models to a dynamic setting to investigate whether they were able to reproduce parts of the complex physical aspects of dynamic crack propagation. In Bleyer et al. (2017), we performed various numerical tests in a 2D pre-strained plate setting. Our results showed in particular that such models reproduce mode I cracks accelerating up to a certain limit velocity $v_{\max} \approx 0.7 c_R$ above which macroscopic crack branching can occur Fig. 8.3a. Interestingly, if we constrain the crack on a weaker path (e.g. with holes or along a weaker interface), branching is suppressed and cracks can accelerate to much larger velocities close to $c_R$. Before branching, the acceleration phase is associated with a broadening of the localized 1D crack solutions until enough energy is available for the crack tip to split into two main branches. This branching event seems to be related to a dynamic energy release rate $\Gamma$ reaching the value $2G_c$ (Fig. 8.3c). Interestingly, the link between damage dissipation and crack velocity before the first branching event was found to be roughly independent on the loading level (Fig. 8.3d), which reproduces experimental observation of velocity-toughening mechanisms.

Finally, experimental observations also reported that cracks exhibit dynamic instabilities characterized by crack velocity oscillations and frustrated branching attempts called *micro-branches*. Such microbranching events result in highly localized roughness events along post-mortem crack surfaces. In PMMA, at the onset of the microbranching instability, micro-branches initially localize along the width direction but rapidly merge, forming an almost invariant pattern across the width and showing a periodic alternance of up and down micro-branches with a well-defined length scale. As regards numerical simulations, we did not find any work which was capable of reproducing this kind of observation in a 2D setting. Since microbranching seems to be intrinsically 3D, we attempted to reproduce such an instability using dynamic explicit 3D simulations. Our results were in line with experimental observations in the sense that microbranching instability occurs at low velocities as a transition between strain crack propagation and macroscopic branching, see Fig. 8.4a. Moreover, it was also previously observed experimentally that this microbranching phase can be suppressed if the plate was made thinner and thinner. Our results also reproduce the same observation (Fig. 8.4b) and, conversely, they lead to much more localized branching events across the plate width for thicker plates. We must highlight that all simulations have been performed with the same regularization length $\ell_0$ which has an influence on the typical size of such microbranches.

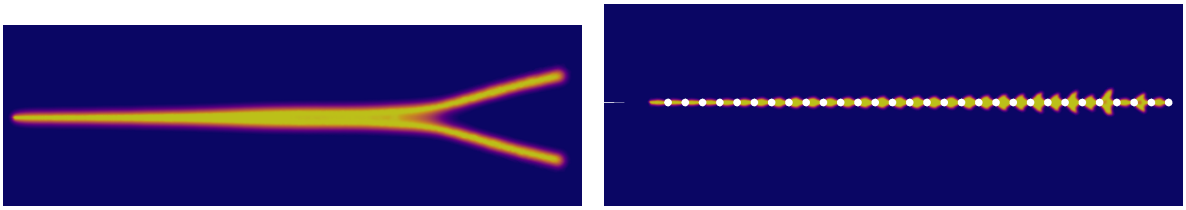

(a) Damage band broadening before branching (b) Suppressed branching on a weak path

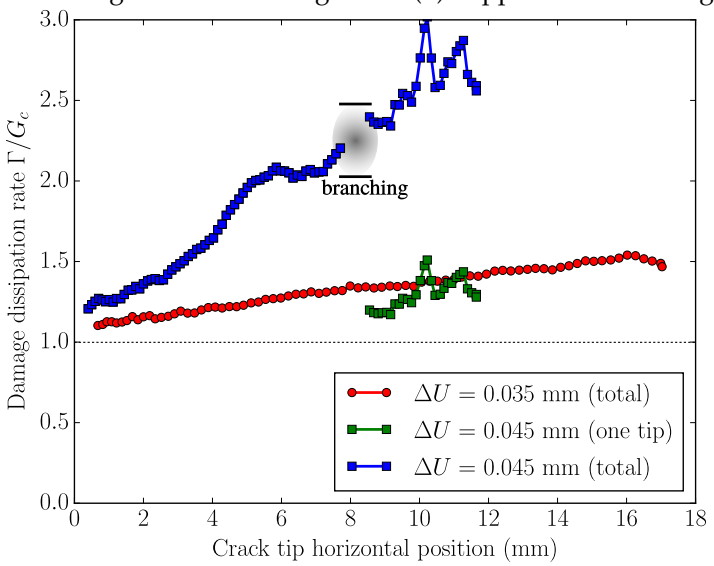


(c) Evolution of the normalized damage dissipation rate $\Gamma/G_c$ during crack propagation for different loading levels. For the low prestrain level ($\Delta U = 0.035\,\text{mm}$), the evolution is regular with $G_c \leq \Gamma \leq 1.5G_c$ and no branching is observed. For a higher loading ($\Delta U = 0.045\,\text{mm}$), branching is observed slightly after $\Gamma \geq 2G_c$. After branching, the dissipation associated with a single crack tip ($\Gamma/2$) is close to its initial value, slightly above $G_c$.

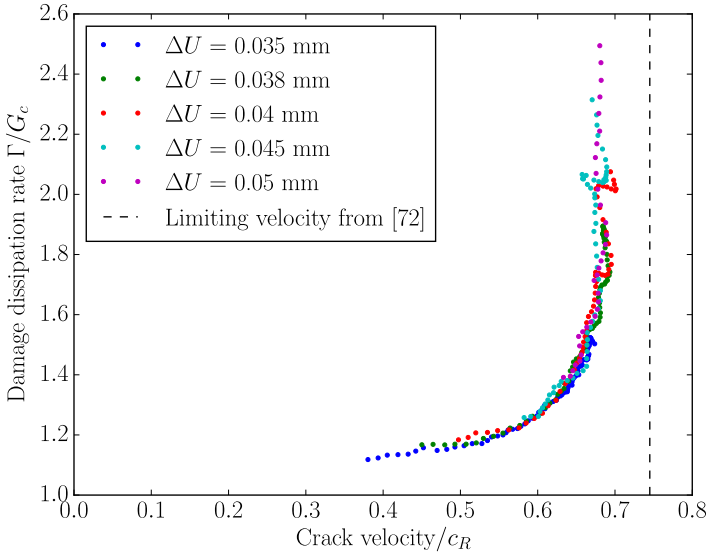


(d) The damage dissipation rate $\Gamma$ is a well-defined increasing function of the crack speed for all initial loadings. The points correspond to instantaneous values of $v$ and $\Gamma$ during the single crack propagation phase i.e. after initiation phase and before branching for high loadings. The dotted line corresponds to the experimentally observed limiting velocity in Zhou (1996).

Figure 8.3: Some results of dynamic phase-field models in 2D, from Bleyer et al. (2017)

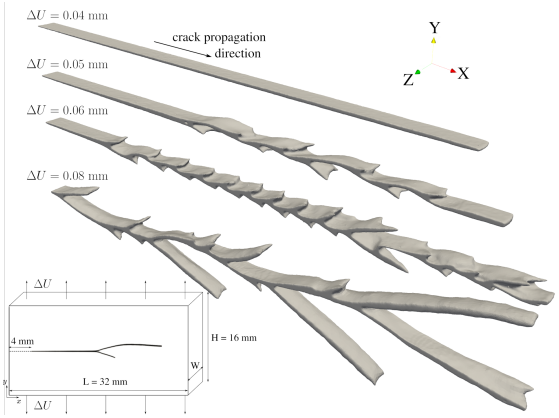


(a) Crack surface patterns for different loading levels $\Delta U$ for the same plate width ($W = 1mm$). The crack propagates as a single straight crack for low loading levels (top), the microbranching instability appears for higher loading with longer branches and shorter distance between successive branches for increasing loading (middle). For even higher loading (bottom), macroscopic branches are formed and are very close to 2D simulation patterns.

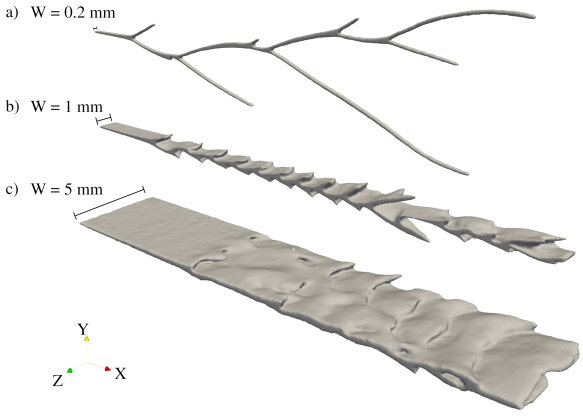


(b) Crack surface patterns for different plate widths $W$ for the same loading level ($\Delta U = 0.06$ mm). The microbranching instability is clearly suppressed for the thin plate (a), the macrobranching crack pattern being reminiscent of 2D simulations. The up-and-down quasi-periodic regime of small microbranching is obtained for the intermediate width (b) whereas more localization in the z-direction is obtained for the larger width (c) without exhibiting any well-structured feature.

Figure 8.4: 3D microbranching crack surfaces in various configurations.

Overall, even though theoretical results on such dynamic-extended models are still lacking at the moment, we believe that non-trivial physical instabilities can be well reproduced, at least qualitatively, by these models which further assess their versatility for accounting for fracture in various contexts.

### 8.2.3 Anisotropic fracture

Another rich extension of phase-field models of brittle fracture concerns the setting of anisotropic fracture. In such a context, one is typically interested in reproducing the fact that crack surface energy is no longer isotropic but depends on the crack propagation direction. In some extreme cases, one may even consider directions where crack propagation is entirely forbidden. Many works have focused on the anisotropic fracture energy setting where elastic properties are supposed isotropic. In this case, an important distinction must be made between the *weak anisotropy* case and the *strong anisotropy* case which correspond to the situation where the reciprocal fracture energy $\dfrac{1}{G_c(\theta)}$ is, respectively, a convex or a non-convex function of the crack direction $\theta$. Weak anisotropy with two-fold symmetry can be well-reproduced using an extended anisotropic version of the fracture energy $\mathcal{E}_f$ such as:

$$\mathcal{E}_f(d) = \int_\Omega \frac{G_c}{c_w \ell_0} \left( w(d) + \ell_0^2 \nabla d \cdot \boldsymbol{A} \cdot \nabla d \right) \, d\Omega \tag{8.3}$$

where $\boldsymbol{A}$ is a structural tensor characterizing the anisotropy. For four-fold symmetry and/or strong anisotropy, more advanced models must be proposed such as high-order models relying on the second-gradient $\nabla^2 d$, see Li and Maurini (2019).

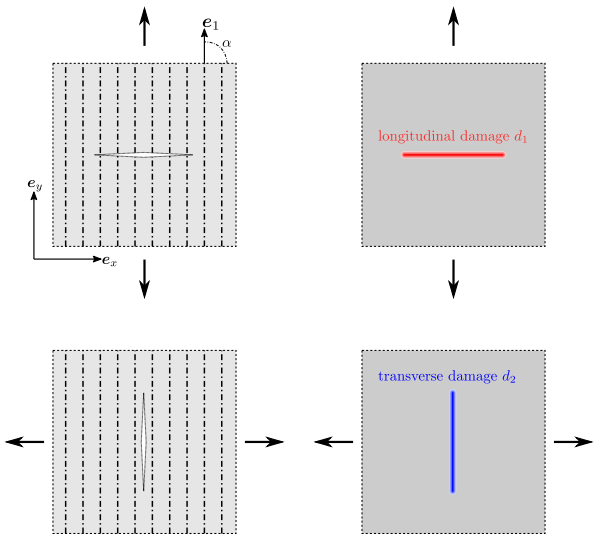


Figure 8.5: Schematics of the multi-mechanism anisotropic damage gradient model

**Multi-damage models**

Alternatively, we have been motivated by developing phase-field models of brittle fracture for fiber-reinforced composites in which two main fracture mechanisms seem to dominate, see Fig. 8.5: transverse fracture where cracks are parallel to the fiber orientation, splitting the matrix only, and longitudinal fracture where cracks are perpendicular to the fibers and break both the fiber and the matrix phases. For such purposes, we proposed a model accounting for two different damage variables $d_1, d_2$ associated with each mechanism. Assuming that no interaction exists in terms of dissipated energy, we posit the following total fracture energy:

$$\mathcal{E}_{\mathrm{f}}(d_1, d_2) = \int_\Omega \left[ \frac{G_{\mathrm{c}}^1}{c_w \ell_0} \left( w(d_1) + \ell_0^2 \|\nabla d_1\|^2 \right) + \frac{G_{\mathrm{c}}^2}{c_w \ell_0} \left( w(d_2) + \ell_0^2 \|\nabla d_2\|^2 \right) \right] \mathrm{d}\Omega \tag{8.4}$$

where $G_{\mathrm{c}}^1, G_{\mathrm{c}}^2$ are the surface fracture energies corresponding to both fracture mechanisms. Note that for simplicity, we considered the same regularization length $\ell_0$ and local energy $w(d)$ for both contributions. Regarding the elastic energy, our approach consists in introducing a specific anisotropic degradation function which will promote crack nucleation along the corresponding directions, a typical example in 2D would be for instance:

$$\mathcal{E}_{\mathrm{el}}(\boldsymbol{u}, d_1, d_2) = \int_\Omega \frac{1}{2} \boldsymbol{\varepsilon} : \mathbb{C}(d_1, d_2) : \boldsymbol{\varepsilon} \, \mathrm{d}\Omega \tag{8.5}$$

$$\text{where } \mathbb{C}(d_1, d_2) = \mathbb{D}(d_1, d_2) : \mathbb{C}_0 : \mathbb{D}(d_1, d_2) \tag{8.6}$$

$$= \begin{bmatrix} (1-d_1)^2 C_{11} & (1-d_1)(1-d_2) C_{12} & 0 \\ (1-d_1)(1-d_2) C_{12} & (1-d_2)^2 C_{22} & 0 \\ 0 & 0 & (1-d_1)(1-d_2) C_{66} \end{bmatrix} \tag{8.7}$$

The numerical resolution then follows the classical alternate minimization strategy with the main difference that the damage problem now involves a vectorial field $(d_1, d_2)$.

This kind of model is capable of reproducing the preferential crack orientation of anisotropic fiber reinforced materials as illustrated in Fig. 8.6 for a Single-Edge Notch Test in mode I loading. Moreover, a similar mode I setting with a pre-crack at 0° and fibers oriented at 90° has been analyzed theoretically by Leguillon (1993) using LEFM. Assuming that cracks other than

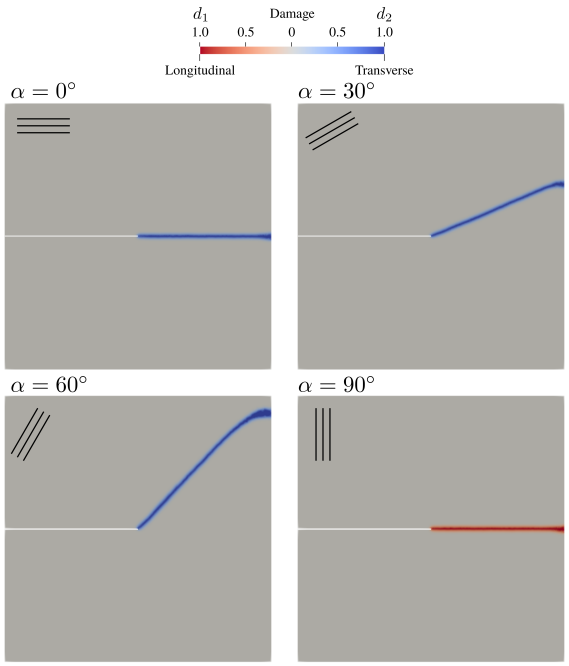


(a) Crack paths.Transverse cracks (damage variable $d_2$) are shown in blue, longitudinal cracks (damage variable $d_1$) are shown in red.

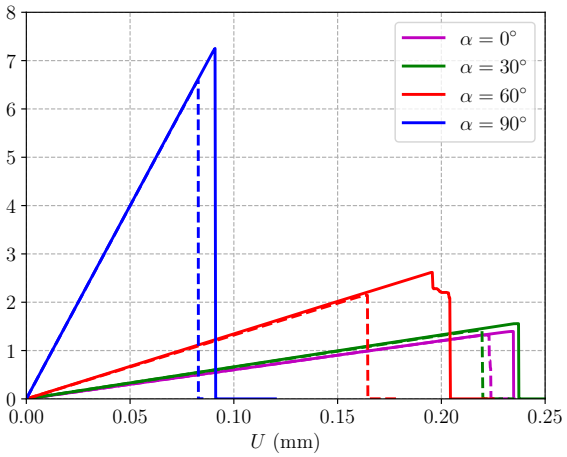


(b) Load-displacement curves

Figure 8.6: Longitudinal/Transverse Damage (LTD) model results for mode I loading for different principal orthotropic direction orientations $\alpha$.

0° or ±90° are forbidden, the author showed that straight propagation occurs if the contrast $\chi = G_c(90°)/G_c(0°)$ between both fracture energies is above a critical threshold $\chi_c$. Below this threshold, a crack kinking at ±90° is expected. For the retained values of the elastic properties, the theoretical threshold is estimated to be $\chi_c \approx 0.09$. Our simulations reveal the correct abrupt transition between the two failure modes: straight propagation or kinked propagation, see Fig. 8.7. By varying the imposed ratio between both fracture energies, we found the transition to happen between $\chi = 0.09$ and $\chi = 0.11$ for a length scale $\ell_0 = 10$ mm. For even smaller length scale, we found the critical contrast to approach the predicted value of $\chi_c \approx 0.09$. Interestingly, classical damage models with a single variable and a weakly anisotropic fracture energy are unable to reproduce this phenomenon.

In the work of Scherer et al. (2022), we further explored the difference between such models on more complex settings. In particular, we investigated the possibility of reproducing complex zig-zag crack paths which can occur in brittle crystals under certain conditions. Our approach indeed manages to exhibit nice zig-zag patterns as in Fig. 8.8 without relying on sophisticated higher-order phase-field models.

**Multi-layered plate models and inter/intra-laminar damage interaction**

These models have also been used in the context of modeling damage mechanisms arising in low-velocity impact of composites laminates for the aeronautic industry. The PhD thesis of Paul Bouteiller funded by Dassault Aviation focused on developing a generalized multi-layered plate model to reduce the computational burden of 3D simulations. As discussed in Section 2.2.4, the goal was to represent the complex 3D kinematics of a multilayered laminate with a generalized plate model formulated on a reference 2D plate, each node containing

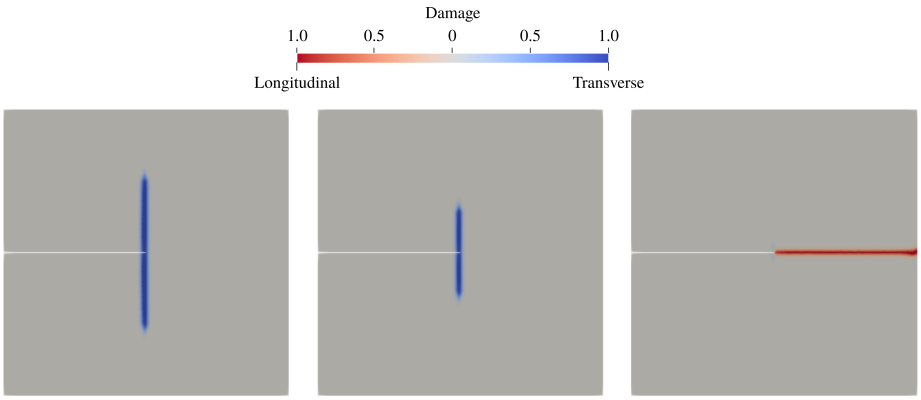


Figure 8.7: Crack path of the LTD model for the kinking problem for varying values of the surface energy constrast : left $\chi = 0.05$, middle $\chi = 0.09$, right $\chi = 0.11$.

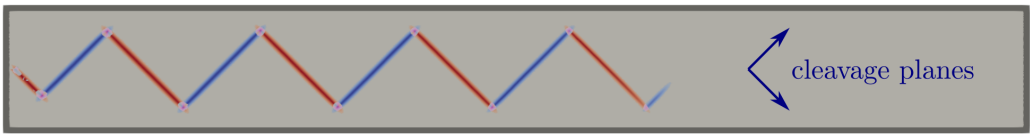


Figure 8.8: Zig-zag crack paths along two cleavage planes in a brittle crystal.

multiple degrees of freedom associated with each layer displacement and rotation for instance. The originality of the approach stems from the fact that the model is based on a stress expansion (rather than on a displacement expansion) inside each ply along the vertical coordinates to perform the 3D-2D dimension reduction. This choice is particularly relevant since we then have access to quantities of physical interest such as interfacial shear and opening stresses which play a pivotal role in simulating debonding mechanisms. The final model resulted in having, in each ply, two intra-laminar damage variables corresponding to the LTD anisotropic model and in each interface, two inter-laminar damage variables capable of modeling mode I and mode II debonding mechanisms. Note that intra-laminar damage fields will tend to produce localized cracks and must therefore be regularized as presented before, whereas inter-laminar damage is constrained to lie along the interface and can be seen as a damage field of a cohesive-zone model and does not require any regularization.

Fig. 8.9 shows an example of a four-point bending test of a 90°/0°/90° laminate investigated

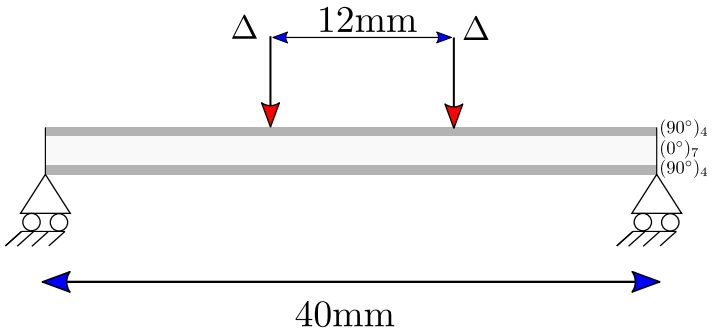


Figure 8.9: Four-point bending test from Quintanas-Corominas et al. (2020)

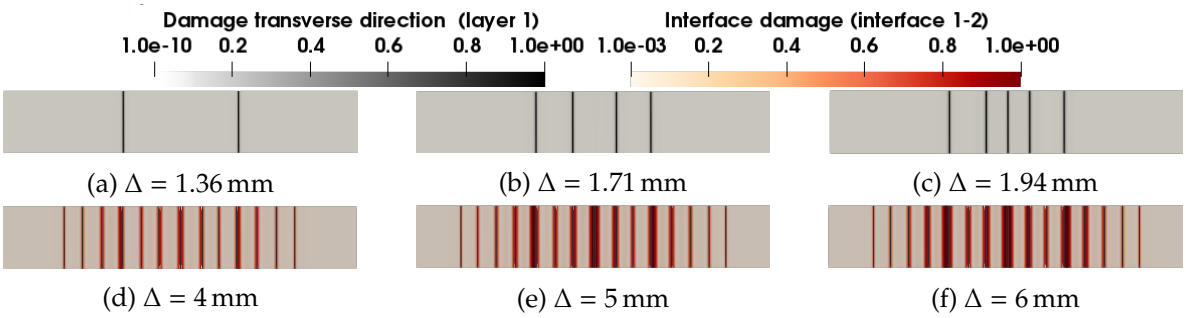


(a) $\Delta = 1.36\,\text{mm}$ (b) $\Delta = 1.71\,\text{mm}$ (c) $\Delta = 1.94\,\text{mm}$

(d) $\Delta = 4\,\text{mm}$ (e) $\Delta = 5\,\text{mm}$ (f) $\Delta = 6\,\text{mm}$

Figure 8.10: Matrix multi-cracking in the bottom 90° ply (in black) and debonding at the 90°/0° interface (in red) – top view.

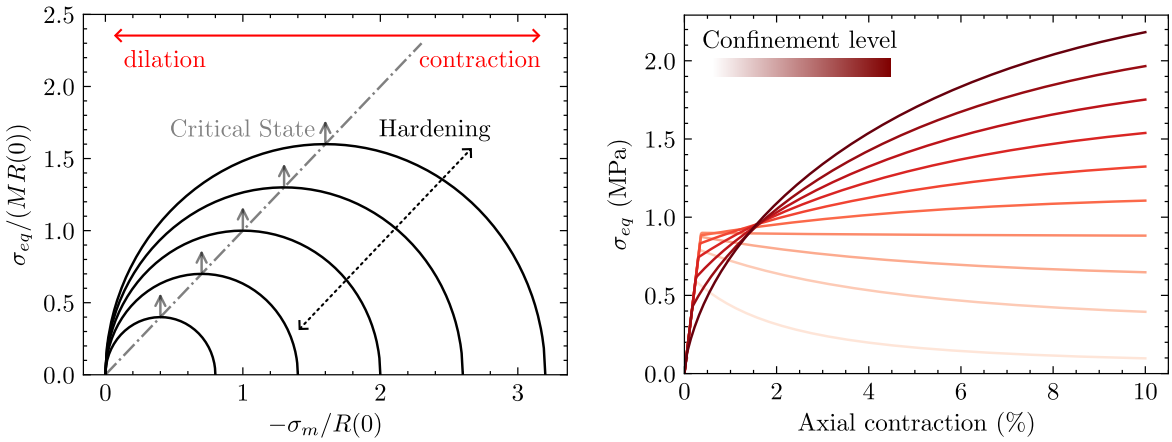


(a) Modified Cam-Clay yield surface (b) Typical stress/strain curves

Figure 8.11: Illustration of the Modified Cam-Clay model for granular soils

in Quintanas-Corominas et al. (2020). With our multilayered model (Bouteiller, 2022), this problem is modeled using a 2D mesh representing the plate reference plane in the $x, y$ direction and 3 layers which possess Reissner-Mindlin kinematics (in-plane and out-of-plane displacements and rotation) in interaction with each other. Fig. 8.10 represents the evolution of the intra-laminar and inter-laminar damage fields at different loading levels. For this configuration, matrix cracks first appear in the bottom 90° layer under the loading region and are followed by further matrix cracking events in the central zone. In this initial stage, delamination does not occur. For larger loading levels, multi-cracking stops and delamination propagates from the location of the matrix cracks. This kind of behavior is in line with experimental observations and more complex simulations using solid elements. The loading levels of crack nucleation and the obtained crack density also agree quantitatively with previous references.

## 8.3 Gradient regularization of softening plasticity models

### 8.3.1 Motivations

Recently, in the thesis of Goustan Bacquaert in collaboration with EDF, we investigated novel formulations for describing the behavior of granular soils. The main focus was put on developing simple models in order to favor robustness of structural computations. Indeed,

many elastoplastic models found in soil mechanics exhibit some form of softening which is detrimental to reliable engineering computations at the structural scale. One of the archetypal models found in this community is the so-called Modified Cam-Clay (MMC) model which can be described as an elastoplastic model characterized by an elliptic yield surface and a combined isotropic/kinematic hardening driven by the volumetric plastic strain (Fig. 8.11a). Depending on the loading path, the stress-strain curve can exhibit either a hardening or a softening response as in Fig. 8.11b.

In such a case, plastic strain localization and mesh-dependency problems will necessarily emerge when solving problems at the structure scale. Among many of the possible ways of solving these issues in softening plasticity, a common approach is due to Aifantis (1987) in which the free energy is supplemented with a quadratic term of the cumulated plastic strain gradient:

$$\psi_{\text{reg}}(\boldsymbol{\varepsilon}, p, \nabla p) = \psi_{\text{loc}}(\boldsymbol{\varepsilon}, p) + \frac{A}{2}\|\nabla p\|^2 \tag{8.8}$$

where $\psi_{\text{loc}}$ is the original free energy of the local (non-regularized) model and $A > 0$ a new material parameter which sets a typical length scale to control plastic strain localization.

To illustrate this model, let us consider an elasto-plastic material characterized by a convex yield domain and an isotropic hardening controlled by the cumulated plastic strain. The plastic yield surface can therefore be described by the convex set $G(p) = \rho(p)G_0$ where $G_0$ is the initial convex yield domain and $\rho(p)$ a positive scalar-valued function such that $\rho(0) = 1$. In the case where $\rho$ is a decreasing function of $p$, we are in presence of a softening plasticity model. The quadratic plastic gradient regularization proposed by Aifantis (1987) has been studied by many authors as a means of controlling plastic localization. However, many works (De Borst and Pamin, 1996; Jirásek and Rolshoven, 2009; Scherer et al., 2019; Abatour and Forest, 2023) have also pointed out some inherent deficiencies of this approach since localized plastic bands eventually thicken in an uncontrolled manner. This is illustrated in Fig. 8.12 for the case of a 1D bar in traction using a linear softening model which has been studied in detail by Jirásek and Rolshoven (2009). In this setting, one can derive an exact analytical solution and show that plastic strain profiles have a controlled support in an initial phase where the yield stress is between $\sigma_0$ and $\sigma_0/2$. When the yield stress becomes lower than $\sigma_0/2$, the plastic strain profile exhibits an increasingly larger support with the strain level. If this uncontrolled spreading of plastic bands is already problematic, such solutions will also eventually dissipate a larger energy than the homogeneous solution, which is another important fundamental issue. To overcome these issues some authors have recently proposed to rely either on adding an *ad hoc* evolution equation of the internal length scale (Scherer et al., 2019) or to rely on the concept of saturating state variables (Abatour and Forest, 2023).

### 8.3.2 A novel regularization framework

In our work, we are currently investigating the possibility of solving these issues without relying on the Aifantis model or its extended versions. Instead, we propose to control plastic localization using the dissipation pseudo-potential instead of the free energy. Without regularization, the dissipation pseudo-potential is simply the support function of the yield surface:

$$\phi_{\text{loc}}(\dot{\boldsymbol{\varepsilon}}^{\text{p}}, \dot{p}; p) = \rho(p)\pi_{G_0}(\dot{\boldsymbol{\varepsilon}}^{\text{p}}, \dot{p}) \tag{8.9}$$

where $\pi_{G_0}$ is the support function of the initial yield surface $G_0$, given for instance by Eq. (4.72) for $J_2$-plasticity. Here, the main specificity is related to the fact that the dissipation potential is state-dependent since the radius $\rho$ depends on the current plastic strain $p$.

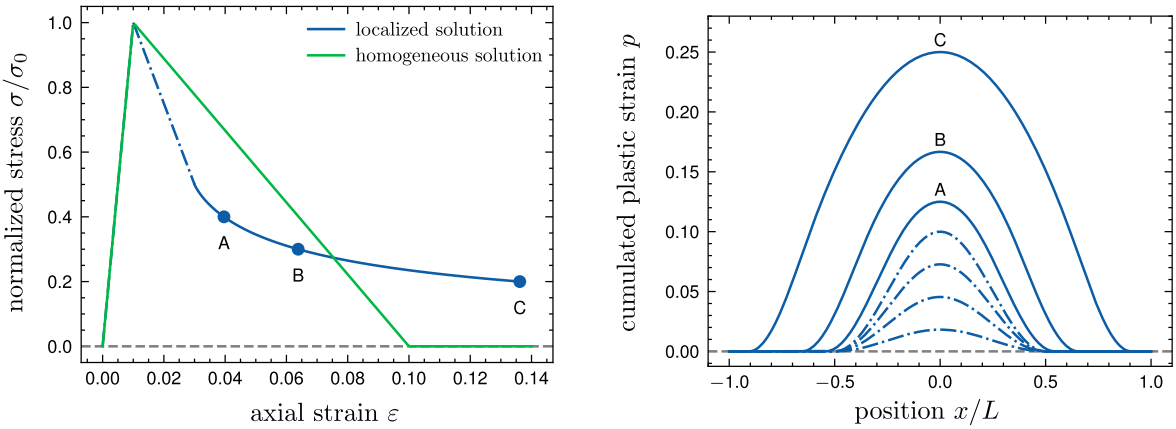


Figure 8.12: Response of a 1D bar in traction for a linear softening model and Aifantis (1987) regularization: (left) stress/strain response ; (right) plastic strain profiles

We now propose to extend the above dissipation potential with a nonlocal term depending on the gradient of the cumulated plastic strain rate as follows:

$$\phi_{\text{ref}}(\dot{\boldsymbol{\varepsilon}}^{\text{p}}, \dot{p}, \nabla\dot{p}; p) = \phi_{\text{loc}}(\dot{\boldsymbol{\varepsilon}}^{\text{p}}, \dot{p}; p) + \phi_{\text{nloc}}(\dot{p}, \nabla\dot{p}) \tag{8.10}$$

where $\phi_{\text{nloc}}$ is a state-independent non-local dissipation potential which we require to satisfy certain properties.

First, we require $\phi_{\text{nloc}}(\dot{p}, \nabla\dot{p})$ to depend on $\nabla\dot{p}$ through the non-dimensional gradient plasticity variable $\dot{P} = \ell_0\nabla\dot{p}$ where $\ell_0$ is an additional material parameter which is interpreted as a regularization length-scale. We thus make the following change of variable:

$$\phi_{\text{nloc}}(\dot{p}, \nabla\dot{p}) = \varphi(\dot{p}, \ell_0\nabla\dot{p}) \tag{8.11}$$

Furthermore, we require the auxiliary function $\varphi(\dot{p}, \dot{P})$ to satisfy the following properties:

- $\varphi(\dot{p}, \dot{P})$ is convex and positive homogeneous of degree 1 to ensure rate-independence;
- $\varphi(\dot{p}, 0) = 0 \ \forall\dot{p}$ so that there is no gradient contribution when plastic evolution is homogeneous (i.e. $\nabla\dot{p} = 0$) or when the regularization length $\ell_0 = 0$).

There exist many functions which may satisfy such properties. In the isotropic case, we also enforce $\varphi$ to depend on $\dot{P}$ via its norm $\|\dot{P}\|_2$ only. In such a case, typical examples which may satisfy such properties are:

- coupled quadratic norm:

$$\varphi(\dot{p}, \dot{P}) = \kappa\left(\sqrt{\dot{p}^2 + \|\dot{P}\|_2^2} - \dot{p}\right) \tag{8.12}$$

- coupled max norm:

$$\varphi(\dot{p}, \dot{P}) = \kappa\left(\max\{\dot{p}, \|\dot{P}\|_2\} - \dot{p}\right) = \kappa\left\langle\|\dot{P}\|_2 - \dot{p}\right\rangle_+ \tag{8.13}$$

- *QuadOverLin* function:

$$\varphi(\dot{p}, \dot{P}) = \kappa\frac{\|\dot{P}\|_2^2}{2\dot{p}} \tag{8.14}$$

where $\kappa > 0$ is an additional material parameter.

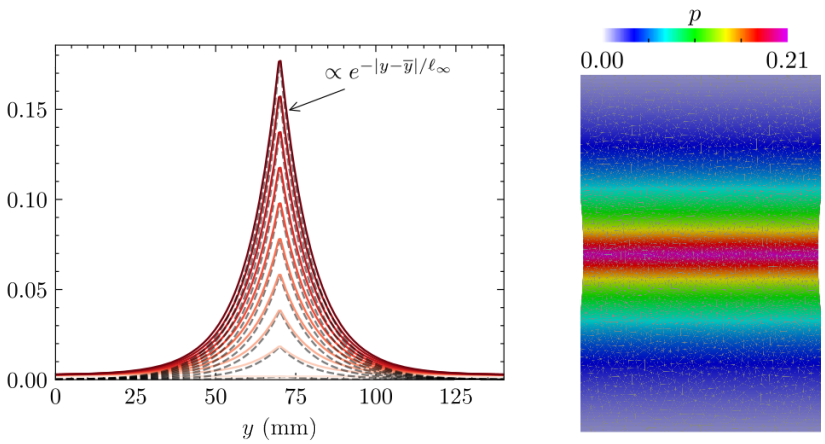


Figure 8.13: Regularization of plastic bands in the softening MCC model for a tensile loading using Eq. (8.13): (left) numerical profile in red and analytical solution in dotted black at various loading levels; (right) final 2D plastic profile

### 8.3.3 Preliminary results

The proposed model can then fit into the incremental variational schemes discussed in Chapter 4. It is important to note that the model is now non-local with respect to the plastic strain variable $p$. Classical strategies of constitutive integration combining return mapping procedures at the material point and global Newton-Raphson schemes can no longer be used in such a context. Instead we rely on the conic programming tools discussed earlier in this manuscript to solve the global variational problem associated with $p$. We must point out that, using a fixed-point strategy to freeze the state-dependent radius $\rho$ at a previous iteration, this global problem is non-smooth in the plastic strain variable and its gradient. Finally, all of the forms proposed for the function $\varphi$ are representable using simple conic constraints and can therefore be implemented easily in the `fenics_optim` package.

In Fig. 8.13 we show some preliminary results when applying the above methodology to the softening MCC model for a tensile loading test. In this case, we used the non-local function Eq. (8.13) as it allowed us to derive an analytical solution for the 1D localized profiles. These profiles exhibit a decaying exponential form with a fixed typical length scale $\ell_\infty = \ell_0$. As a result, we never observe any spreading of the localized plastic bands as evidenced in Fig. 8.13-left for different loading levels. Moreover, the analytical solution shows that dissipation is well controlled and always bounded above by that of the homogeneous solutions, thereby avoiding the two issues identified with Aifantis model of gradient plasticity.

Moreover, these good properties do not seem to be specific to the particular choice of (8.13). For instance, using (8.12) we are no longer able to derive an analytical solution but numerical simulations show that the localized plastic solutions exhibit a similar behavior, see Fig. 8.14. The main differences come from the shape of the profile and its support. In this case, the profile is smoother and the support of the last plastic increments seems finite.

Finally, Fig. 8.15 illustrates the difference between the energy regularization with a quadratic gradient term as proposed by Aifantis (1987) and the proposed approach with the *QuadOverLin* function Eq. (8.14) in the case of a softening von Mises plasticity model for a tension loading on a plate. As we can see, plastic band widths are well controlled in the proposed approach whereas for the energetic regularization, uncontrolled spreading of the

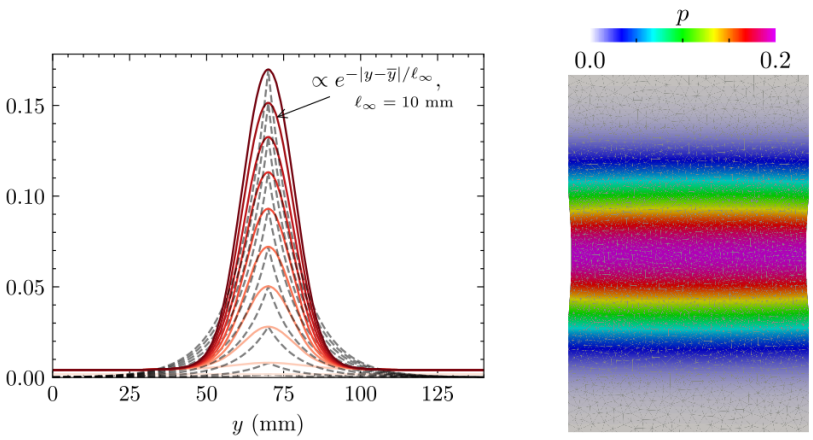


Figure 8.14: Regularization of plastic bands in the softening MCC model for a tensile loading using Eq. (8.12): (left) numerical profile in red at various loading levels; (right) final 2D plastic profile

bands occurs. We check that we easily reach mesh-independent results when the mesh size is sufficiently small with respect to the band width. Finally, we observe that the choice of the regularization length $\ell_0$ influences the post-peak softening regime of the load-displacement curve, the smaller $\ell_0$, the stronger is the softening regime.

### 8.3.4 Conclusions

The proposed model of regularization of softening plasticity seems extremely promising in controlling the plastic band localization, without any spurious spreading and with a consistent value for the dissipated energy. Interestingly, we tested the approach on various types of softening behaviors and various plastic yield surfaces and found the same behavior in all cases. Similarly, the dissipation regularization offers a certain freedom in choosing the non-local pseudo-potential $\varphi$. Importantly, similar results were obtained using various forms of such potential provided that we respect certain properties regarding convexity and homogeneity. The main difference between these different choices is related to the shape of the plastic localization profile. This suggests that the approach is very general and versatile. However, the approach relies on conic programming to be solved efficiently as its implementation into a standard nonlinear FE solver does not seem straightforward at first sight.

Obviously, this work is quite recent and will deserve more study in the future to better understand the role of this regularizing gradient term in the dissipation. Moreover, comparison with experimental plastic band localization profile could pave the way to identifying the relevant form of the potential $\varphi$ for a given material.

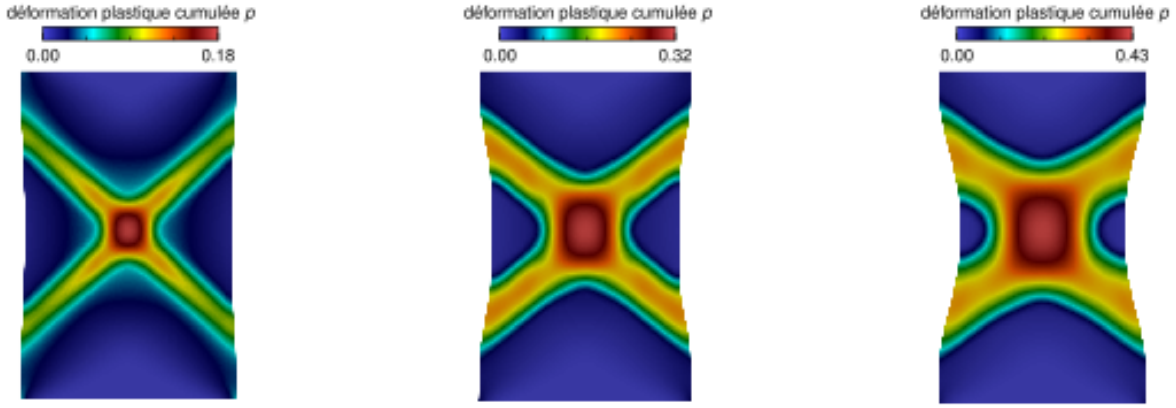


(a) Energy regularization $\|\nabla p\|^2$

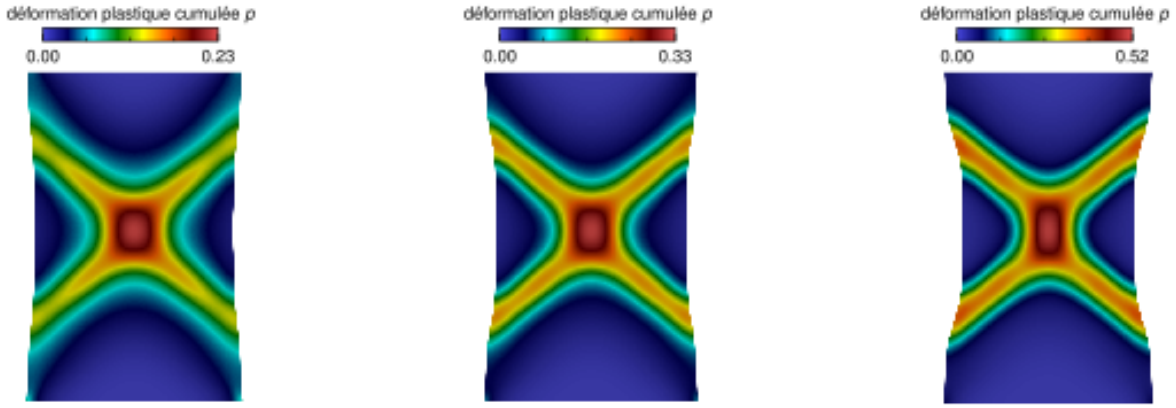


(b) Proposed dissipation regularization (8.12)

Figure 8.15: Regularization of softening von Mises plasticity for different load levels

# Chapter 9

# General research perspectives

This chapter discusses various research perspectives, focusing either on applications, theoretical aspects or computation techniques.

## 9.1 Avanced mechanical models in novel construction systems

In the near future, my goal is to advance the use of phase-field models for modeling brittle fracture of civil engineering materials in two PhD theses which started in Fall 2023. These projects aim to develop advanced mechanical and computational models for 3D-printed concrete thin-walled structures (PhD of Alice Gribonval) and wooden multilayered plates such as Cross-Laminated Timber (PhD of Gaspard Blondet), respectively.

The first project focuses on the development of high-performance 3D-printed concrete material that is planned to be used in pre-stressed structures with an optimized geometry to reduce construction material consumption. However, the 3D-printing process results in thin layered structures with anisotropic mechanical properties, making the modeling of brittle failure phenomena a challenge (Fig. 9.1a). To qualify projects using 3D-printed structures, it is necessary to correctly account for such phenomena, as these structures are not currently covered in design codes. Thus, the project will develop efficient and accurate simulation techniques for modeling brittle failure, contributing to better design and optimization of 3D-printed structures.

The second project aims to develop layerwise plate models to simulate failure in wooden multilayered plates such as CLT (Fig. 9.1b), which is increasingly popular in high-rise wooden buildings. Currently, there is no available model to correctly account for the interaction between the various damage mechanisms characterizing their failure, including rolling shear failure, tensile splitting, and ply debonding, see Fig. 9.1c. The project will also extend the layerwise models to a large displacement setting to account for buckling-induced failure. Such developments will result in advanced numerical models which will be key for better design and optimization of CLT structures to possibly reduce wood consumption.

## 9.2 Optimization under uncertainty

The line of work described in Chapter 7 opens a large range of possible applications of stochastic and robust optimization approaches to mechanical problems involving uncertainty. One interesting application would be to compute pessimistic crack paths in brittle fracture to improve the design of industrial parts which can be sensitive to brittle fracture. Moreover, as we have discussed in Chapter 6, I believe that topology optimization can only be relevant for practical engineering applications if we adopt a robust approach accounting for the possibility of uncertainties in the design loads. One of the main challenge in combining the concepts of Chapter 6 and Chapter 7 together lies in reducing the computational cost which is induced both by the topology optimization formulation and by the stochastic/robust optimization

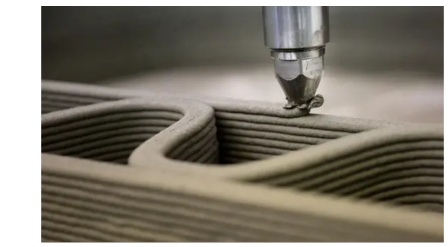

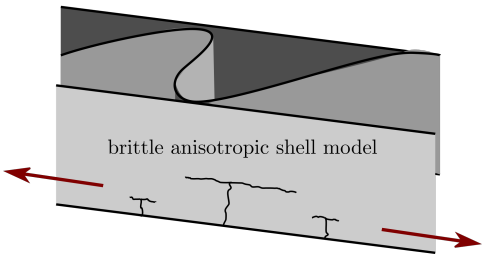


(a) 3D-printed concrete thin-walled structure (XtreeE)

(b) 5-layer CLT panel

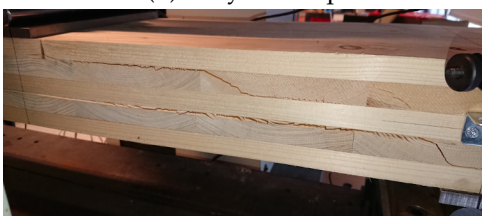

(c) Rolling shear failure and debonding

Figure 9.1: Current research projects

approach. Bridging these developments with limit-analysis based topology optimization on concrete structures may pave the way to designing innovative 3D-printed concrete structures of excellent structural performance.

## 9.3 Automated numerical tools

The advent of automated numerical tools, including just-in-time compilation (JIT) and automatic differentiation (AD), is significantly enhancing efficiency and flexibility across various scientific computing domains. JIT compilation facilitates dynamic code generation at runtime, optimizing performance through tailored machine-specific instructions. Concurrently, automatic differentiation enables the calculation of derivatives concerning input parameters, streamlining gradient-based optimization and sensitivity analysis. This proves especially beneficial in computational mechanics, where constitutive models and structural simulations often involve complex and computationally intensive operations. In automated tools such as MFront or FEniCS, the computational burden of implementation is left to the machine while the user can dedicate time to build more complex models using a simple Domain-Specific Language. I believe that scientific computing is currently in a period of excitement, with the emergence of many powerful tools, often open-source and driven by the development of machine learning. For instance, JAX is an open-source numerical computing library developed by Google. It is designed to provide a high-performance machine learning framework for transforming numerical functions while being flexible and composable. It provides various functionalities such as accelerated linear algebra, just-in-time compilation, automatic differentiation, auto-vectorization, etc. Currently we are exploring how to couple such tools for implementing material constitutive models at a much smaller cost from the user's perspective, see Fig. 9.2[1].

[1]See also the Linear viscoelasticity with JAX numerical tour

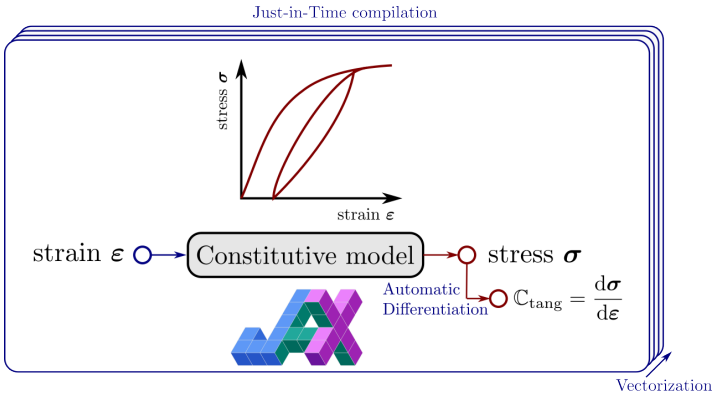


Figure 9.2: Automated constitutive modeling with JAX

## 9.4 Optimal Transport

Optimal Transport theory is an extremely active research field lying at the intersection between probabilities, PDEs and optimization. It essentially relies on the notion of a distance between probability distributions. For instance, it makes it possible to interpolate between probability distributions with minimal cost. Thereby, it has fundamental links with least action principles that can be found in various physical systems. I have been particularly amazed by the work of Benamou and Brenier (2000) who exhibited the link between a fluid mechanics least action principle and the Monge problem of optimal transport. I used this beautiful link as a computational example (Fig. 9.3) for the `fenics_optim` package where an initial Gaussian distribution $\rho_0$ (Fig. 9.3a) defined on the unit square $\Omega = [0;1] \times [0;1]$ is mapped onto 4 Gaussian distributions $\rho_1$ (Fig. 9.3f) by solving the following convex problem:

$$\begin{aligned} \inf_{\rho,\boldsymbol{m}} \quad & \int_0^1 \int_\Omega \frac{\|\boldsymbol{m}\|^2}{2\rho} \, \mathrm{d}\Omega \, \mathrm{d}t \\ \text{s.t.} \quad & \partial_t \rho + \operatorname{div}_x \boldsymbol{m} = 0 \\ & \rho(\boldsymbol{x}, t = 0) = \rho_0(\boldsymbol{x}) \\ & \rho(\boldsymbol{x}, t = 1) = \rho_1(\boldsymbol{x}) \\ & \boldsymbol{m} \cdot \boldsymbol{n} = 0 \text{ on } \partial\Omega \end{aligned} \tag{9.1}$$

As evidenced by previous works, optimal transport is also closely linked to shape optimization problems which we investigated in Section 6.5. I think that such a connection is extremely fruitful and should be further explored in the future. Finally, optimal transport is also widely used in the field of machine learning and more specifically distributional robust learning which explicitly accounts for uncertainty in the data distribution. Instead of optimizing for a single distribution, distributional robust optimization considers a set of possible distributions, often represented as a Wasserstein ball in the Wasserstein space defined by optimal transport. Exploring how such type of approaches can find interesting applications in mechanics seems also very interesting for the future.

## 9.5 Computational optimization

As evidenced in this manuscript, optimization numerical solvers, especially conic programming solvers, lie at the center of my computational toolbox. Even though such solvers showcase very interesting computational performances, many aspects would deserve to be

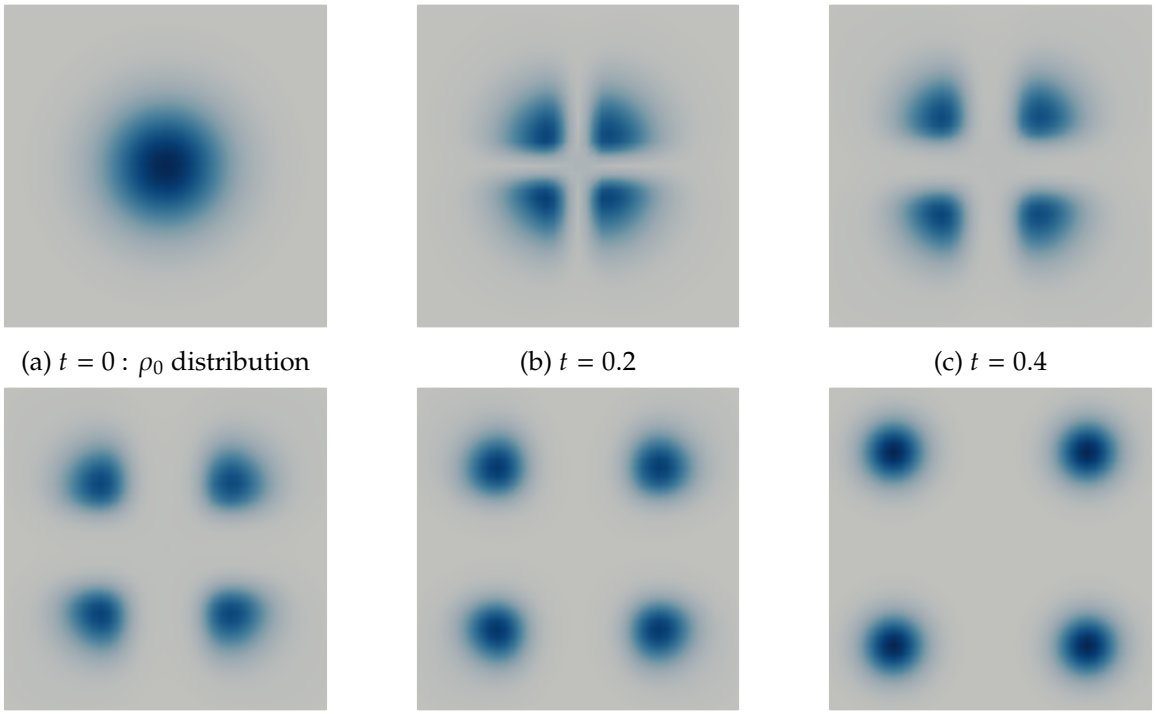

(a) $t = 0$ : $\rho_0$ distribution (b) $t = 0.2$ (c) $t = 0.4$

(d) $t = 0.6$ (e) $t = 0.8$ (f) $t = 1.0$ : $\rho_1$ distribution

Figure 9.3: Optimal transport between two distributions

developed in the future.

First, although conic representation of convex functions offers a versatile framework for composing operations on convex functions, it requires the user to formulate his problem in a somewhat rigid format. For instance, current black-box conic solvers cannot account for any prior knowledge of the problem mathematical structure such as composite objective containing smooth and non-smooth terms, cones acting only on local variables which can be condensed from the global linear system, etc. For this reason, it appears interesting to work on an open-source implementation of such solvers which would offer increased flexibility and which could account for the typical structure of problems arising in mechanics.

Second, knowing how an optimal solution depends on the data of the underlying problem is essential in many cases of application such as sensitivity analysis, uncertainty quantification, outer optimization, etc. As of today, there is very little work dedicated to computing sensitivities of convex optimization problems, a notable exception being Agrawal et al. (2019).

Finally, using such solvers on large scale problems is still challenging because of the use of direct solvers for solving the linear system involved at each iteration. The use of iterative solvers would definitely be necessary to improve the computational efficiency. However, the current challenge is that the linear system conditioning strongly deteriorates during the iterations when approaching the solution. A possible remedy to this issue would be to devise a hybrid algorithm which would combine during the course of the solution procedure different types of solvers (first and second order for instance).

# Appendix A

# Convex optimization results

## A.1 Recession function

The *recession function* corresponds, in some sense, to the asymptotic behaviour of a convex function $f$ at infinity. More precisely, it is defined as follows (Combettes, 2018):

**Definition 13** (Recession function)**.** The recession function $f_\infty$ of $f$ is defined as:

$$f_\infty(\boldsymbol{x}) = \sup_{\boldsymbol{y} \in \operatorname{dom} f} f(\boldsymbol{x}+\boldsymbol{y}) - f(\boldsymbol{y}) \tag{A.1}$$

In particular, it is a positively homogeneous convex function.

For a closed function $f$, we have:

$$f_\infty(\boldsymbol{x}) = \lim_{t \to 0^+} t f(\boldsymbol{x}/t) \tag{A.2}$$

We also have:

$$(f^*)_\infty(\boldsymbol{y}) = \pi_{\operatorname{dom} f}(\boldsymbol{y}) \tag{A.3}$$

$$(f_\infty)^*(\boldsymbol{y}) = \delta_{\operatorname{dom} f^*}(\boldsymbol{y}) \tag{A.4}$$

## A.2 Perspective function

### A.2.1 Definition

We start by noticing that for any convex function $f$, the function:

$$p_f(t, \boldsymbol{x}) = \begin{cases} t f(\boldsymbol{x}/t) & \text{if } t > 0 \\ +\infty & \text{otherwise} \end{cases} \tag{A.5}$$

is convex with respect to $(t, \boldsymbol{x})$. Some authors call this function the perspective of $f$. Others consider that the perspective is the lower semi-continuous envelope of $p_f$. We make this latter choice in this manuscript and define the perspective as:

**Definition 14** (Perspective)**.** The perspective function of a convex function $f(\boldsymbol{x})$:

$$\operatorname{persp}_f(t, \boldsymbol{x}) = \begin{cases} t f(\boldsymbol{x}/t) & \text{if } t > 0 \\ f_\infty(\boldsymbol{x}) & \text{if } t = 0 \\ +\infty & \text{otherwise} \end{cases} \tag{A.6}$$

### A.2.2 Conjugate

A result from convex analysis (Bauschke et al., 2011) establishes that:

$$(\text{persp}_f)^*(s, \boldsymbol{y}) = \delta_{\text{epi } f^*}(-s, \boldsymbol{y}) = \begin{cases} 0 & \text{if } f^*(\boldsymbol{y}) + s \leq 0 \\ +\infty & \text{otherwise} \end{cases} \tag{A.7}$$

### A.2.3 Application to the `QuadOverLin` function

**Definition 15.** The `QuadOverLin` function is defined as the perspective of the quadratic function $g(\boldsymbol{x}) = \frac{1}{2}\|\boldsymbol{x}\|_2^2$:

$$\texttt{QuadOverLin}(t, \boldsymbol{x}) = \begin{cases} \dfrac{\|\boldsymbol{x}\|_2^2}{t} & \text{if } t > 0 \\ 0 & \text{if } (t, \boldsymbol{x}) = 0 \\ +\infty & \text{otherwise} \end{cases} \tag{A.8}$$

Moreover:

$$f^*(s, \boldsymbol{y}) = \begin{cases} 0 & \text{if } g^*(\boldsymbol{y}) + s = \dfrac{1}{2}\|\boldsymbol{y}\|_2^2 + s \leq 0 \\ +\infty & \text{otherwise} \end{cases} \tag{A.9}$$

using (A.7).

# Appendix B

# Asymptotic analysis of rate-independent dissipative materials

In this section, we aim at studying the behaviour of the incremental variational problem discussed in Section 4.5.2 in an asymptotic regime of large loadings.

## B.1 Displacement-controlled formulation

In the following, we will consider a displacement-controlled setting. Let us thus assume zero Dirichlet boundary conditions $\boldsymbol{u}_{\mathrm{D}} = 0$ and a proportional loading of fixed direction $(, \boldsymbol{T})$ but with an unknown amplitude $\lambda$. The loading will be controlled via the value $U$ of the corresponding work-conjugate displacement. The condensed primal variational principle (4.62) is changed to:

$$J(U) := \min_{\boldsymbol{u} \in \mathcal{U}_{\mathrm{ad}}} \quad \begin{array}{l} \displaystyle\int_\Omega j(\boldsymbol{\varepsilon}) \, \mathrm{d}\Omega \\ \boldsymbol{\varepsilon} = \nabla^s \boldsymbol{u} \\ W_{\mathrm{ext}}(\boldsymbol{u}) = U \end{array} \tag{B.1}$$

In this problem, the unknown loading amplitude $\lambda$ is retrieved as the scalar Lagrange multiplier associated with the last constraint. The corresponding complementary energy principle indeed reads:

$$-J(U) = \min_{\boldsymbol{\sigma}, \lambda} \quad \begin{array}{l} \displaystyle\int_\Omega j^*(\boldsymbol{\sigma}) \, \mathrm{d}\Omega - \lambda U \\ \text{s.t.} \quad \operatorname{div} \boldsymbol{\sigma} + \lambda \boldsymbol{f} = 0 \quad \text{in } \Omega \\ \qquad \boldsymbol{\sigma} \boldsymbol{n} = \lambda \boldsymbol{T} \quad \text{on } \partial\Omega_{\mathrm{N}} \end{array} \tag{B.2}$$

## B.2 Asymptotic behaviour via recession functions

Let us now study the behaviour of problem (B.1) for large values of the imposed displacement $U$. Introducing a rescaled variable $\widehat{\boldsymbol{u}} = \boldsymbol{u}/U$, one has:

$$\frac{J(U)}{U} := \min_{\widehat{\boldsymbol{u}} \in \mathcal{U}_{\mathrm{ad}}} \quad \begin{array}{l} \displaystyle\frac{1}{U} \int_\Omega j(U\widehat{\boldsymbol{\varepsilon}}) \, \mathrm{d}\Omega \\ \widehat{\boldsymbol{\varepsilon}} = \nabla^s \widehat{\boldsymbol{u}} \\ W_{\mathrm{ext}}(\widehat{\boldsymbol{u}}) = 1 \end{array} \tag{B.3}$$

At the limit $U \to \infty$, the above problem then becomes:

$$J_\infty := \min_{\widehat{\boldsymbol{u}} \in \mathcal{U}_{\mathrm{ad}}} \quad \begin{array}{l} \displaystyle\int_\Omega j_\infty(\widehat{\boldsymbol{\varepsilon}}) \, \mathrm{d}\Omega \\ \widehat{\boldsymbol{\varepsilon}} = \nabla^s \widehat{\boldsymbol{u}} \\ W_{\mathrm{ext}}(\widehat{\boldsymbol{u}}) = 1 \end{array} \tag{B.4}$$

where we introduced the *recession function* $j_\infty$ of $j$ defined in Definition 13. The latter characterizes the asymptotic behaviour of the incremental potential at large loadings.

## B.3 Example on hardening elastoplasticity

Depending on the expression of $j$, the above problem may be unbounded i.e. $J_\infty = +\infty$. This is for instance the case if $j$ is a purely elastic quadratic potential, then $j_\infty = \delta_{\{\varepsilon=0\}}$. Conversely, let us consider the elastoplastic model with isotropic hardening introduced in Section 4.6.1 where:

$$\Psi(\boldsymbol{\varepsilon}) = \min_{\boldsymbol{\varepsilon}^{\mathrm{p}},p} \psi_{\mathrm{el}}(\boldsymbol{\varepsilon}-\boldsymbol{\varepsilon}^{\mathrm{p}}) + \psi_{\mathrm{h}}(p) + \phi(\boldsymbol{\varepsilon}^{\mathrm{p}}-\boldsymbol{\varepsilon}_n, p-p_n) \tag{B.5}$$

We recall that $\psi_{\mathrm{el}}$ is the elastic quadratic potential so that its recession function will be infinite except if $\boldsymbol{\varepsilon}^{\mathrm{p}} = \boldsymbol{\varepsilon}$, that is, we recover a rigid-plastic behaviour. As regards the hardening potential, its recession function will be finite only if the hardening is limited that is if $\psi_{\mathrm{h}} \sim H_\infty p$ for some constant $H_i n f t y$ when $p \to \infty$. In such a case, $(\psi_{\mathrm{h}})_\infty(p) = H_i n f t y p$. Finally, the plastic dissipation potential is positively homogeneous so that $\phi = \phi_\infty$. Therefore:

$$j_\infty(\widehat{\boldsymbol{\varepsilon}}) = \min_p H_\infty p + \phi(\widehat{\boldsymbol{\varepsilon}}, p) \tag{B.6}$$

As a result we recover a potential akin to a *rigid-plastic finite deformation* formulation of elastoplasticity where the dependency on the previous state variable vanishes.

As an example for the von Mises plastic behaviour with exponential hardening (4.77), we have $H\infty = \sigma_{\mathrm{u}} - \sigma_0$ and:

$$j_\infty(\widehat{\boldsymbol{\varepsilon}}) = \min_{p,\sqrt{\frac{2}{3}}\|\widehat{\boldsymbol{\varepsilon}}\| \le p} (\sigma_{\mathrm{u}}-\sigma_0)p + \sigma_0 p = \sqrt{\frac{2}{3}}\sigma_u \|\widehat{\boldsymbol{\varepsilon}}\| \tag{B.7}$$

Problem (B.1) then becomes:

$$\begin{aligned} J_\infty := \min_{\widehat{\boldsymbol{u}} \in \mathcal{U}_{\mathrm{ad}}} \quad & \int_\Omega \sqrt{\frac{2}{3}}\sigma_u \|\widehat{\boldsymbol{\varepsilon}}\| \,\mathrm{d}\Omega \\ & \widehat{\boldsymbol{\varepsilon}} = \nabla^{\mathrm{s}} \widehat{\boldsymbol{u}} \\ & W_{\mathrm{ext}}(\widehat{\boldsymbol{u}}) = 1 \end{aligned} \tag{B.8}$$

As a result, our asymptotic analysis through recession functions yields a limit analysis problem of a von Mises material with a tensile strength corresponding to the ultimate strength $\sigma_{\mathrm{u}}$. This analysis therefore formalizes the rigid-plastic analogy which is made for limit analysis problems. It however extends it by taking into account more complex evolution of internal state variables such as isotropic hardening in the previous simple example.

## B.4 Dual recession principle

Similarly, (B.2) admits a corresponding stress-based recession principle which is the dual problem to (B.4) and is given by:

$$\begin{aligned} -J_\infty = \min_{\boldsymbol{\sigma},\lambda} \quad & \int_\Omega (j_\infty)^*(\boldsymbol{\sigma}) \,\mathrm{d}\Omega - \lambda \\ \text{s.t.} \quad & \operatorname{div} \boldsymbol{\sigma} + \lambda \boldsymbol{f} = 0 \quad \text{in } \Omega \\ & \boldsymbol{\sigma}\boldsymbol{n} = \lambda \boldsymbol{T} \quad \text{on } \partial\Omega_{\mathrm{N}} \end{aligned} \tag{B.9}$$

Note that from (A.4), $(j_\infty)^*$ is the indicator of the convex set:

$$G = \{\boldsymbol{\sigma} \text{ s.t. } j^*(\boldsymbol{\sigma}) < +\infty\} \tag{B.10}$$

so that one has:

$$\begin{aligned} J_\infty = \max_{\boldsymbol{\sigma},\lambda} \quad & \lambda \\ \text{s.t.} \quad & \operatorname{div} \boldsymbol{\sigma} + \lambda \boldsymbol{f} = 0 \quad \text{in } \Omega \\ & \boldsymbol{\sigma}\boldsymbol{n} = \lambda \boldsymbol{T} \quad \text{on } \partial\Omega_{\mathrm{N}} \\ & \boldsymbol{\sigma} \in G \quad \text{in } \Omega \end{aligned} \tag{B.11}$$

Again, we recover the classical form of a limit analysis problem. As before, for an elastic potential $G$ is not bounded and problem (B.11) does not admit a finite solution.

# Appendix C

# Convex optimization results for topology optimization

## C.1 Derivation of the dual problem

Using classical convex duality, we can derive the dual problem associated with (6.8). Introducing first the weak form of the equilibrium conditions (first two constraints):

$$\int_\Omega \boldsymbol{\sigma} : \boldsymbol{\varepsilon} \, \mathrm{d}\Omega = \int_{\partial\Omega_N} \boldsymbol{T} \cdot \boldsymbol{u} \, \mathrm{d}S \tag{C.1}$$

where $\boldsymbol{u}$ is a kinematically admissible displacement field, we then form the following saddle-point problem:

$$\max_{\boldsymbol{u}, r\geq 0, s\geq 0, \Lambda} \min_{\rho, \boldsymbol{\sigma}} \mathcal{L}(\rho, \boldsymbol{\sigma}, \boldsymbol{u}, r, s, \Lambda) \tag{C.2}$$

where $r(\boldsymbol{x})$, $s(\boldsymbol{x})$ are positive scalar fields on $\Omega$, $\Lambda$ is a single scalar Lagrange multiplier. The Lagrangian is given by:

$$\mathcal{L} = \int_\Omega \left( \rho \Psi^*(\boldsymbol{\sigma}/\rho) - \boldsymbol{\sigma} : \boldsymbol{\varepsilon} - (\rho - \rho_\mathrm{m}) s - (\rho_\mathrm{M} - \rho) r + \Lambda(\rho - \eta) \right) \mathrm{d}\Omega + \int_{\partial\Omega_N} \boldsymbol{T} \cdot \boldsymbol{u} \, \mathrm{d}S \tag{C.3}$$

in which we replaced the inequality constraints $0 \leq \rho \leq 1$ present in (6.8) with the more general constraint $\rho_\mathrm{m} \leq \rho \leq \rho_\mathrm{M}$. Rearranging terms and transforming the min into a max, one has:

$$\min_{\rho, \boldsymbol{\sigma}} \mathcal{L} = -\max_{\rho, \boldsymbol{\sigma}} \left\{ \int_\Omega \left( \boldsymbol{\sigma} : \boldsymbol{\varepsilon} + \rho(s - r - \Lambda) - \rho \Psi^*(\boldsymbol{\sigma}/\rho) \right) \mathrm{d}\Omega \right\} - \int_\Omega (\rho_\mathrm{M} r - \rho_\mathrm{m} s + \eta\Lambda) \, \mathrm{d}\Omega + \int_{\partial\Omega_N} \boldsymbol{T} \cdot \boldsymbol{u} \, \mathrm{d}S \tag{C.4}$$

We now recognize that the maximization problem corresponds to the definition of the Legendre-Fenchel conjugate of the perspective function $\mathrm{persp}_{\Psi^*} : (\rho, \boldsymbol{\sigma}) \mapsto \rho \Psi^*(\boldsymbol{\sigma}/\rho)$.

Here, using (A.7) with $f = \Psi^*$, thus $f^* = \Psi$, one has finally:

$$\begin{aligned} \max_{\boldsymbol{u}, r\geq 0, s\geq 0, \Lambda} \quad & -\int_\Omega (\rho_\mathrm{M} r - \rho_\mathrm{m} s + \eta\Lambda) \, \mathrm{d}\Omega + \int_{\partial\Omega_N} \boldsymbol{T} \cdot \boldsymbol{u} \, \mathrm{d}S \\ \text{s.t.} \quad & \Psi(\boldsymbol{\varepsilon}) \leq r + \Lambda - s \leq r + \Lambda \end{aligned} \tag{C.5}$$

Again transforming the max into a min and eliminating auxiliary variables yields:

$$\min_{\boldsymbol{u}, \Lambda} \int_\Omega \left( (\rho_\mathrm{M} - \rho_\mathrm{m}) \max\{\Psi(\boldsymbol{\varepsilon}); \Lambda\} + \rho_\mathrm{m} \Psi \right) \mathrm{d}\Omega - \int_{\partial\Omega_N} \boldsymbol{T} \cdot \boldsymbol{u} \, \mathrm{d}S - (\rho_\mathrm{M} - \rho_\mathrm{m} - \eta)|\Omega|\Lambda \tag{C.6}$$

The latter expression then reduces to (6.9) in the specific case $\rho_\mathrm{M} = 1$, $\rho_\mathrm{m} = 0$.

## C.2 A specific class of convex problems

We consider below a specific class of convex problems:

$$\begin{aligned} \inf_{x\in S} \quad & c(x) \\ \text{s.t.} \quad & j(x) \leq j_0 \end{aligned} \tag{$P_{j_0}$}$$

where the objective function $c(x)$ is assumed to be positive homogeneous of degree $-1$ and where the constraint function $j(x)$ is assumed to be positive homogeneous of degree 1 and $S$ is a vectorial space (or a cone). Moreover, $j_0$ is a given constant. Hence, the solution to ($P_{j_0}$) is parametrized by the value of the constraint constant $j_0$.

We can show in fact that the whole range of solutions of ($P_{j_0}$) can be entirely characterized by the solution of a single reference problem. We have indeed the following lemma:

**Lemma 2.** *Consider the following problem:*

$$\inf_{x\in S} \quad c(x) + j(x) \tag{$P^*$}$$

*Let $x^*$ denote an optimal solution to ($P^*$) and let $Q = c(x^*) + j(x^*)$ be the corresponding optimal value. Then*

$$x = \frac{Q^2}{4j_0} x^* \tag{C.7}$$

*is also an optimal solution to ($P_{j_0}$).*

*Proof.* Let us introduce $C(j_0) = \text{val}(P_{j_0})$. From the homogeneity hypothesis, we easily see that $C(j_0)$ is also $-1$-homogeneous. Moreover, if $x_0$ is an optimum solution to ($P_{j_0}$), then necessarily $j(x_0) = j_0$, otherwise the optimum could be improved.

Now, let us conside an optimal solution $x^*$ to ($P^*$). Then, $c(x^*) + j(x^*) \leq c(\lambda x^*) + j(\lambda x^*)$ $\forall \lambda > 0$. Thus, the function $f(\lambda) := \lambda^{-1} c(x^*) + \lambda j(x^*)$ attains its minimum at $\lambda = 1$. But the minimum is characterized by $j(x^*) = c(x^*)/\lambda^2$. This shows that $j(x^*) = c(x^*) = \dfrac{Q}{2}$.

Moreover $x^*$ is also admissible for ($P_{Q/2}$) so that $C(Q/2) \leq c(x^*) = Q/2$. Let us then consider $x_{Q/2}$ the optimal solution to ($P_{Q/2}$), then we have $j(x_{Q/2}) = Q/2$ and $c(x_{Q/2}) + j(x_{Q/2}) = C(Q/2) + Q/2 \leq Q$. Thus $x_{Q/2}$ is also a solution to ($P^*$) and we have that $C(Q/2) = Q/2$. Also $C(j_0) = C\left(\dfrac{2j_0}{Q}\dfrac{Q}{2}\right) = \dfrac{Q^2}{4j_0}$.

Similarly, $\frac{2j_0}{Q}x^*$ is also admissible for ($P_{j_0}$) so that $C(j_0) \leq c(\frac{2j_0}{Q}x^*) = \dfrac{Q^2}{4j_0}$. Hence $\frac{2j_0}{Q}x^*$ is an optimal solution to ($P_{j_0}$). Considering now $x^\sharp = \dfrac{Q}{2j_0} x_{j_0}$ where $x_{j_0}$ is an optimal solution of ($P_{j_0}$), then $j(x^\sharp)$ and $c(x^\sharp) = Q/2$ so that $x^\sharp$ is also optimal for ($P^*$). □

# Bibliography


Abatour, M. and Forest, S. (2023). Strain gradient plasticity based on saturating variables. *European Journal of Mechanics-A/Solids*, page 105016.

Acary, V., Brémond, M., and Huber, O. (2018). On solving contact problems with coulomb friction: formulations and numerical comparisons. *Advanced Topics in Nonsmooth Dynamics: Transactions of the European Network for Nonsmooth Dynamics*, pages 375–457.

Agrawal, A., Barratt, S. T., Boyd, S. P., Busseti, E., and Moursi, W. M. (2019). Differentiating through a cone program.

Agrawal, A., Verschueren, R., Diamond, S., and Boyd, S. (2018). A rewriting system for convex optimization problems. *Journal of Control and Decision*, 5(1):42–60.

Aifantis, E. C. (1987). The physics of plastic deformation. *International journal of plasticity*, 3(3):211–247.

Alizadeh, F. and Goldfarb, D. (2003). Second-order cone programming. *Mathematical Programming*, 95(1):3–51.

Allaire, G. (2012). *Shape optimization by the homogenization method*, volume 146. Springer Science & Business Media.

Allaire, G., Geoffroy-Donders, P., and Pantz, O. (2018). Topology optimization of modulated and oriented periodic microstructures by the homogenization method. *Computers & Mathematics with Applications*, 78.

Allaire, G., Jouve, F., and Toader, A.-M. (2004). Structural optimization using sensitivity analysis and a level-set method. *Journal of computational physics*, 194(1):363–393.

Alnæs, M. S., Blechta, J., Hake, J., Johansson, A., Kehlet, B., Logg, A., Richardson, C., Ring, J., Rognes, M. E., and Wells, G. N. (2015). The fenics project version 1.5. *Archive of Numerical Software*, 3(100).

Anderheggen, E. and Knöpfel, H. (1972). Finite element limit analysis using linear programming. *International Journal of Solids and Structures*, 8(12):1413–1431.

Andersen, E. D., Roos, C., and Terlaky, T. (2003). On implementing a primal-dual interior-point method for conic quadratic optimization. *Mathematical Programming*, 95(2):249–277.

Arnold, D. N. and Brezzi, F. (1985). Mixed and nonconforming finite element methods: implementation, postprocessing and error estimates. *ESAIM: Mathematical Modelling and Numerical Analysis*, 19(1):7–32.

Artzner, P., Delbaen, F., Eber, J.-M., and Heath, D. (1999). Coherent measures of risk. *Mathematical finance*, 9(3):203–228.

Bach, F., Jenatton, R., Mairal, J., Obozinski, G., et al. (2011). Convex optimization with sparsity-inducing norms. *Optimization for Machine Learning*, 5:19–53.

Balmforth, N. J., Frigaard, I. A., and Ovarlez, G. (2014). Yielding to stress: recent developments in viscoplastic fluid mechanics. *Annual Review of Fluid Mechanics*, 46:121–146.

Barbarosie, C. and Lopes, S. (2011). A generalized notion of compliance. *Comptes Rendus Mécanique*, 339(10):641–648.

Bauschke, H. H., Combettes, P. L., et al. (2011). *Convex analysis and monotone operator theory in Hilbert spaces*, volume 408. Springer.

Bedford, A. (1985). *Hamilton's principle in continuum mechanics*, volume 139. Pitman advanced publishing program Boston, MA.

Ben-Tal, A., El Ghaoui, L., and Nemirovski, A. (2009). *Robust optimization*. Princeton university press.

Ben-Tal, A., Goryashko, A., Guslitzer, E., and Nemirovski, A. (2004). Adjustable robust solutions of uncertain linear programs. *Mathematical programming*, 99(2):351–376.

Benamou, J.-D. and Brenier, Y. (2000). A computational fluid mechanics solution to the monge-kantorovich mass transfer problem. *Numerische Mathematik*, 84(3):375–393.

Bendsøe, M. P. and Sigmund, O. (2004). *Topology optimization: theory, methods, and applications*. Engineering online library. Springer, 2. ed., corr. printing edition. OCLC: 249399186.

Bercovier, M. and Engelman, M. (1980). A finite-element method for incompressible non-Newtonian flows. *Journal of Computational Physics*, 36(3):313–326.

Bertsimas, D., Brown, D. B., and Caramanis, C. (2011). Theory and applications of robust optimization. *SIAM review*, 53(3):464–501.

Bertsimas, D. and Sim, M. (2004). The price of robustness. *Operations research*, 52(1):35–53.

Besson, J., Bleyer, J., Feld-Payet, S., Gourgues-Lorenzon, A.-F., Hannard, F., Helfer, T., Hure, J., Kondo, D., Lazarus, V., Le Bourlot, C., Maitournam, H., Maurini, C., Moes, N., Morgeneyer, T., Morin, L., Petit, T., and Simar, A. (2023). *MEALOR II Damage Mechanics and Local Approach to Fracture*. Zenodo.

Bilotta, A., Leonetti, L., and Garcea, G. (2012). An algorithm for incremental elastoplastic analysis using equality constrained sequential quadratic programming. *Computers & structures*, 102:97–107.

Bisbos, C. and Pardalos, P. (2007). Second-order cone and semidefinite representations of material failure criteria. *Journal of Optimization Theory and Applications*, 134(2):275–301.

Bleyer, J. (2017). Viscoplastic flows : supplementary code for "Advances in the simulation of viscoplastic fluid flows using interior-point methods".

Bleyer, J. (2018a). Advances in the simulation of viscoplastic fluid flows using interior-point methods. *Computer Methods in Applied Mechanics and Engineering*, 330:368–394.

Bleyer, J. (2018b). Multiphase continuum models for fiber-reinforced materials. *Journal of the Mechanics and Physics of Solids*.

Bleyer, J. (2018c). Numerical tours of computational mechanics with FEniCS. https://comet-fenics.readthedocs.io.

Bleyer, J. (2020a). Automating the formulation and resolution of convex variational problems: applications from image processing to computational mechanics. *ACM Transactions on Mathematical Software*, 46(3):27.

Bleyer, J. (2020b). fenics_optim – Convex optimization interface in FEniCS. Version 2.0.

Bleyer, J. (2021). A novel upper bound finite-element for the limit analysis of plates and shells. *European Journal of Mechanics - A/Solids*, 90:104378.

Bleyer, J. (2022). Applications of conic programming in non-smooth mechanics. *Journal of Optimization Theory and Applications*, pages 1–33.

Bleyer, J. (2023a). Risk-averse estimates of effective properties in heterogeneous elasticity. *Comptes Rendus. Mécanique*, 351(G1):29–42.

Bleyer, J. (2023b). Stochastic generalized standard materials and risk-averse effective behavior. working paper or preprint.

Bleyer, J., Carlier, G., Duval, V., Mirebeau, J.-M., and Peyré, G. (2015a). A Γ-Convergence Result for the Upper Bound Limit Analysis of Plates. *ESAIM: Mathematical Modelling and Numerical Analysis*.

Bleyer, J., Carlier, G., Duval, V., Mirebeau, J.-M., and Peyré, G. (2016). A $\gamma$-convergence result for the upper bound limit analysis of plates. *ESAIM: Mathematical Modelling and Numerical Analysis*, 50(1):215–235.

Bleyer, J. and de Buhan, P. (2013a). A greedy algorithm for yield surface approximation. *Comptes Rendus Mécanique*, 341(8):605–615.

Bleyer, J. and de Buhan, P. (2013b). On the performance of non-conforming finite elements for the upper bound limit analysis of plates. *International Journal for Numerical Methods in Engineering*, 94(3):308–330. This is a preprint version of an article accepted for publication in International Journal for Numerical Methods in Engineering Copyright © 2012 John Wiley & Sons, Ltd.

Bleyer, J. and de Buhan, P. (2013c). On the performance of non-conforming finite elements for the upper bound limit analysis of plates. *International Journal for Numerical Methods in Engineering*, 94(3):308–330.

Bleyer, J. and de Buhan, P. (2013d). Yield surface approximation for lower and upper bound yield design of 3d composite frame structures. *Computers & Structures*, 129:pp. 86–98.

Bleyer, J. and de Buhan, P. (2014a). A computational homogenization approach for the yield design of periodic thin plates. Part I: Construction of the macroscopic strength criterion. *International Journal of Solids and Structures*, 51(13):2448–2459.

Bleyer, J. and de Buhan, P. (2014b). A computational homogenization approach for the yield design of periodic thin plates. Part II : Upper bound yield design calculation of the homogenized structure. *International Journal of Solids and Structures*, 51(13):2460–2469.

Bleyer, J. and de Buhan, P. (2014c). Lower bound static approach for the yield design of thick plates. *International Journal for Numerical Methods in Engineering*, 100(11):814–833.

Bleyer, J. and de Buhan, P. (2016). A numerical approach to the yield strength of shell structures. *European Journal of Mechanics - A/Solids*, 59:178–194.

Bleyer, J. and Hassen, G. (2021). Automated formulation and resolution of limit analysis problems. *Computers & Structures*, 243:106341.

Bleyer, J., Le, C. V., and de Buhan, P. (2015b). Locking-free discontinuous finite elements for the upper bound yield design of thick plates. *International Journal for Numerical Methods in Engineering*, 103(12):894–913.

Bleyer, J. and Leclère, V. (2022). Robust limit analysis theory for computing worst-case limit loads under uncertainties. working paper or preprint.

Bleyer, J., Maillard, M., de Buhan, P., and Coussot, P. (2015c). Efficient numerical computations of yield stress fluid flows using second-order cone programming. *Computer Methods in Applied Mechanics and Engineering*, 283:599 – 614.

Bleyer, J., Roux-Langlois, C., and Molinari, J.-F. (2017). Dynamic crack propagation with a variational phase-field model: limiting speed, crack branching and velocity-toughening mechanisms. *International Journal of Fracture*, 204(1):79–100.

Bołbotowski, K. (2022). Optimal vault problem–form finding through 2d convex program. *Computers & Mathematics with Applications*, 109:280–324.

Bołbotowski, K. and Bouchitté, G. (2022). Optimal design versus maximal monge–kantorovich metrics. *Archive for Rational Mechanics and Analysis*, 243(3):1449–1524.

Bosc, J.-L. (2008). Dimensionnement des constructions selon l'eurocode 2 à l'aide des modèles bielles et tirants. *Presses de l'ENPC*.

Bourdin, B., Francfort, G. A., and Marigo, J.-J. (2000). Numerical experiments in revisited brittle fracture. *Journal of the Mechanics and Physics of Solids*, 48(4):797–826.

Bouteiller, P. (2022). *Simulation de la rupture des composites stratifiés dans le cadre de modèles de plaques multicouches*. PhD thesis, Ecole des Ponts ParisTech.

Bouteiller, P., Bleyer, J., and Sab, K. (2022). Consistent derivation of stress-based generalized models in elastodynamics: application to layerwise plate models. *International Journal of Solids and Structures*, 234:111077.

Boyd, S. P. and Vandenberghe, L. (2004). *Convex optimization*. Cambridge University Press, Cambridge, UK ; New York.

Bruno, H., Barros, G., Menezes, I. F., and Martha, L. F. (2020). Return-mapping algorithms for associative isotropic hardening plasticity using conic optimization. *Applied Mathematical Modelling*, 78:724–748.

Buliga, M. and de Saxcé, G. (2017). A symplectic brezis–ekeland–nayroles principle. *Mathematics and Mechanics of Solids*, 22(6):1288–1302.

Cao, X., Oueslati, A., Nguyen, A. D., and de Saxcé, G. (2020). Numerical simulation of elastoplastic problems by brezis–ekeland–nayroles non-incremental variational principle. *Computational Mechanics*, 65(4):1005–1018.

Capsoni, A. and Corradi, L. (1999). Limit analysis of plates- a finite element formulation. *Structural Engineering and Mechanics*, 8(4):325–341.

Chen, W.-F. (2007). *Plasticity in reinforced concrete*. J. Ross Publishing.

Chen, W.-F. (2013). *Limit analysis and soil plasticity*. Elsevier.

Christensen, P. W. (2002). A nonsmooth newton method for elastoplastic problems. *Computer Methods in Applied Mechanics and Engineering*, 191(11-12):1189–1219.

Cockburn, B., Gopalakrishnan, J., and Lazarov, R. (2009). Unified hybridization of discontinuous galerkin, mixed, and continuous galerkin methods for second order elliptic problems. *SIAM Journal on Numerical Analysis*, 47(2):1319–1365.

Combettes, P. L. (2018). Perspective functions: Properties, constructions, and examples. *Set-Valued and Variational Analysis*, 26:247–264.

Coussot, P. (2016). Bingham's heritage. *Rheologica Acta*, 6(3):163–176.

CPLEX, I. I. (2018). CPLEX User's Manual 12.8.

Czubacki, R. and Lewiński, T. (2020). Optimal archgrids: a variational setting. *Structural and Multidisciplinary Optimization*, 62(3):1371–1393.

da Rocha, H. B., Bleyer, J., and Turlier, H. (2022). A viscous active shell theory of the cell cortex. *Journal of the Mechanics and Physics of Solids*, 164:104876. 33 pages, 13 figures, 1 appendix.

Damkilde, L. and Krenk, S. (1997). Limits—a system for limit state analysis and optimal material layout. *Computers & structures*, 64(1-4):709–718.

Dantzig, G., Orden, A., and Wolfe, P. (1955). The generalized simplex method for minimizing a linear form under linear inequality restraints. *Pacific Journal of Mathematics*, 5(2):183–195.

de Almeida, J. M. and Maunder, E. A. (2017). *Equilibrium finite element formulations*. John Wiley & Sons.

De Angelis, F. and Cancellara, D. (2017). Multifield variational principles and computational aspects in rate plasticity. *Computers & Structures*, 180:27–39.

De Borst, R. and Pamin, J. (1996). Some novel developments in finite element procedures for gradient-dependent plasticity. *International Journal for Numerical Methods in Engineering*, 39(14):2477–2505.

de Buhan, P., Bleyer, J., and Hassen, G. (2017). *Elastic, plastic and yield design of reinforced structures*. Elsevier.

de Buhan, P., Freard, J., Garnier, D., and Maghous, S. (2002). Failure properties of fractured rock masses as anisotropic homogenized media. *Journal of Engineering Mechanics*, 128(8):869–875.

de Rooij, R. and Abdalla, M. (2015). A finite element interior-point implementation of tension field theory. *Computers & Structures*, 151:30–41.

De Saxcé, G. (1992). Une généralisation de l'inégalité de fenchel et ses applications aux lois constitutives. *Comptes rendus de l'Académie des sciences. Série 2, Mécanique, Physique, Chimie, Sciences de l'univers, Sciences de la Terre*, 314(2):125–129.

de Saxcé, G. and Feng, Z.-Q. (1991). New inequality and functional for contact with friction: the implicit standard material approach. *Journal of Structural Mechanics*, 19(3):301–325.

Dean, E. J., Glowinski, R., and Guidoboni, G. (2007). On the numerical simulation of Bingham visco-plastic flow: old and new results. *Journal of non-newtonian fluid mechanics*, 142(1):36–62.

Demengel, F. (1983). Problemes variationnels en plasticité parfaite des plaques. *Numerical Functional Analysis and Optimization*, 6(1):73–119.

Demengel, F. (1984). Fonctions à hessien borné. *Annales de l'institut Fourier*, 34(2):155–190.

Diamond, S. and Boyd, S. (2016). CVXPY: A Python-embedded modeling language for convex optimization. *Journal of Machine Learning Research*, 17(83):1–5.

Domahidi, A., Chu, E., and Boyd, S. (2013). Ecos: An socp solver for embedded systems. In *2013 European control conference (ECC)*, pages 3071–3076. IEEE.

Dunning, I., Huchette, J., and Lubin, M. (2017). Jump: A modeling language for mathematical optimization. *SIAM Review*, 59(2):295–320.

El Boustani, C. (2020). *Innovative optimization-based numerical methods for modeling the non-linear behavior of steel structures*. PhD thesis, Université Paris-Est.

El Boustani, C., Bleyer, J., Arquier, M., Ferradi, M.-K., and Sab, K. (2020a). Dual finite-element analysis using second-order cone programming for structures including contact. *Engineering Structures*, 208:20 p.

El Boustani, C., Bleyer, J., Arquier, M., Ferradi, M.-K., and Sab, K. (2020b). Elastoplastic and limit analysis of 3D steel assemblies using second-order cone programming and dual finite-elements. *Engineering Structures*, 221:111041.

El Boustani, C., Bleyer, J., Arquier, M., and Sab, K. (2020c). Extending interior-point methods to non-linear second-order cone programming: application to finite-strain elastoplasticity. *International Journal for Numerical Methods in Engineering*, 122(1):270–293.

EN1993–1-1 (2005). *Eurocode 3: Design of Steel Structures, Part 1.1: General rules and rules for buildings*. AFNOR.

EN1993–1-8 (2005). *Eurocode 3: Design of Steel Structures, Part 1.8: Design of Joints*. AFNOR.

Ferradi, M.-K., Fliscounakis, A., Arquier, M., and Bleyer, J. (2023). Elastoplastic and limit analysis of reinforced concrete with an equilibrium-based finite element formulation. *Computers & Structures*, 286:107095.

Fin, J., Borges, L., and Fancello, E. (2018). Structural topology optimization under limit analysis. *Structural and Multidisciplinary Optimization*, 59.

Fineberg, J. and Marder, M. (1999). Instability in dynamic fracture. *Physics Reports*, 313(1):1–108.

Fitzpatrick, S. and Simons, S. (2001). The conjugates, compositions and marginals of convex functions. *Journal of Convex Analysis*, 8(2):423–446.

Fortin, M. and Glowinski, R. (1982). *Méthodes de lagrangien augmenté: applications à la résolution numérique de problèmes aux limites*. Dunod.

Fraeijs de Veubeke, B. (1971). The dual principles of elastodynamics: finite element applications. Technical report, LTAS.

Francfort, G. A. and Marigo, J.-J. (1998). Revisiting brittle fracture as an energy minimization problem. *Journal of the Mechanics and Physics of Solids*, 46(8):1319–1342.

Frémond, M. and Nedjar, B. (1996). Damage, gradient of damage and principle of virtual power. *International journal of solids and structures*, 33(8):1083–1103.

Garstka, M., Cannon, M., and Goulart, P. (2021). Cosmo: A conic operator splitting method for convex conic problems. *Journal of Optimization Theory and Applications*, 190(3):779–810.

Ge, D., Huangfu, Q., Wang, Z., Wu, J., and Ye, Y. (2022). Cardinal optimizer (copt) user guide. *arXiv preprint arXiv:2208.14314*.

Georghiou, A., Wiesemann, W., and Kuhn, D. (2015). Generalized decision rule approximations for stochastic programming via liftings. *Mathematical Programming*, 152:301–338.

Germain, P. (1973a). La méthode des puissances virtuelles en mécanique des milieux continus, premiere partie: théorie du second gradient. *Journal de mécanique*, 12(2):235–274.

Germain, P. (1973b). The method of virtual power in continuum mechanics. part 2: Microstructure. *SIAM Journal on Applied Mathematics*, 25(3):556–575.

Ghanem, R. G. and Spanos, P. D. (2003). *Stochastic finite elements: a spectral approach*. Courier Corporation.

Glowinski, R. and Le Tallec, P. (1989). *Augmented Lagrangian and operator-splitting methods in nonlinear mechanics*. SIAM.

Glowinski, R. and Wachs, A. (2011). On the numerical simulation of viscoplastic fluid flow. *Handbook of numerical analysis*, 16(1):483–718.

Gong, S., Wu, S., and Xu, J. (2019). New hybridized mixed methods for linear elasticity and optimal multilevel solvers. *Numerische Mathematik*, 141:569–604.

Goulard, P. and Chen, Y. (2023). Clarabel.jl documentation.

Grant, M. and Boyd, S. (2014). CVX: Matlab software for disciplined convex programming, version 2.1.

Gurobi Optimization, LLC (2023). Gurobi Optimizer Reference Manual.

Halphen, B. and Nguyen, Q. S. (1975). Sur les matériaux standard généralisés. *Journal de mécanique*, 14(1):39–63.

Helfer, T., Bleyer, J., Frondelius, T., Yashchuk, I., Nagel, T., and Naumov, D. (2020). The MFrontGenericInterfaceSupport project. *Journal of Open Source Software*, 5(48):2003.

Helfer, T., Bleyer, J., Russo, R., and Dancheva, T. (2021). mgis.fenics: Coupling MFront and FEniCS for complex solid mechanics simulations. In *FEniCS 2021*, Proceedings of FEniCS 2021, Cambridge, United Kingdom.

Herfelt, M., Poulsen, P., and Hoang, L. (2018). Strength-based topology optimisation of plastic isotropic von mises materials. *Structural and Multidisciplinary Optimization*.

Heuzé, T. and Stainier, L. (2022). A variational formulation of thermomechanical constitutive update for hyperbolic conservation laws. *Computer Methods in Applied Mechanics and Engineering*, 394:114893.

Heyman, J. (1966). The stone skeleton. *International Journal of solids and structures*, 2(2):249–279.

Hill, R. (1948). A variational principle of maximum plastic work in classical plasticity. *The Quarterly Journal of Mechanics and Applied Mathematics*, 1(1):18–28.

Hill, R. (1950). *The mathematical theory of plasticity*. Clarendon Press, Oxford.

Ilyushin, A. (1956). *Plasticité*. Eyrolles, Paris.

Jirásek, M. and Rolshoven, S. (2009). Localization properties of strain-softening gradient plasticity models. part ii: Theories with gradients of internal variables. *International Journal of Solids and Structures*, 46(11-12):2239–2254.

Johansen, K. (1962). *Yield-line theory*. Cement and Concrete Association London.

Juditsky, A. and Nemirovski, A. (2021). On well-structured convex-concave saddle point problems and variational inequalities with monotone operators. *arXiv preprint arXiv:2102.01002*.

Junker, P. and Nagel, J. (2019). A relaxation approach to modeling the stochastic behavior of elastic materials. *European Journal of Mechanics-A/Solids*, 73:192–203.

Kammoun, Z. and Smaoui, H. (2014). A direct approach for continuous topology optimization subject to admissible loading. *Comptes Rendus Mécanique*, 342(9):520–531.

Kanno, Y. (2011). *Nonsmooth mechanics and convex optimization*. Crc Press.

Kanno, Y. (2016). A fast first-order optimization approach to elastoplastic analysis of skeletal structures. *Optimization and Engineering*, 17:861–896.

Karmarkar, N. (1984). A new polynomial-time algorithm for linear programming. *Combinatorica*, 4(4):373–395.

Kilian, M., Pellis, D., Wallner, J., and Pottmann, H. (2017). Material-minimizing forms and structures. *ACM Transactions on Graphics (TOG)*, 36(6):173.

Krabbenhoft, K. and Damkilde, L. (2002). Lower bound limit analysis of slabs with nonlinear yield criteria. *Computers & structures*, 80(27):2043–2057.

Krabbenhøft, K., Lyamin, A., and Sloan, S. (2007). Formulation and solution of some plasticity problems as conic programs. *International Journal of Solids and Structures*, 44(5):1533–1549.

Krabbenhoft, K., Lyamin, A., Sloan, S., and Wriggers, P. (2007). An interior-point algorithm for elastoplasticity. *International Journal for Numerical Methods in Engineering*, 69(3):592–626.

Krabbenhoft, K., Lyamin, A. V., Hjiaj, M., and Sloan, S. W. (2005). A new discontinuous upper bound limit analysis formulation. *International Journal for Numerical Methods in Engineering*, 63(7):1069–1088.

Krabbenhøft, K., Lyamin, A. V., and Sloan, S. W. (2008). Three-dimensional mohr–coulomb limit analysis using semidefinite programming. *Communications in Numerical Methods in Engineering*, 24(11):1107–1119.

Kumar, J. and Rahaman, O. (2020). Lower bound limit analysis using power cone programming for solving stability problems in rock mechanics for generalized hoek–brown criterion. *Rock Mechanics and Rock Engineering*, pages 1–16.

Leguillon, D. (1993). Asymptotic and numerical analysis of a crack branching in nonisotropic materials. *European J. Mech. A Solids*, 12:33–51.

Li, B. and Maurini, C. (2019). Crack kinking in a variational phase-field model of brittle fracture with strongly anisotropic surface energy. *Journal of the Mechanics and Physics of Solids*, 125:502–522.

Lobo, M. S., Vandenberghe, L., Boyd, S., and Lebret, H. (1998). Applications of second-order cone programming. *Linear algebra and its applications*, 284(1-3):193–228.

Logg, A., Mardal, K.-A., and Wells, G. (2012). *Automated solution of differential equations by the finite element method: The FEniCS book*, volume 84. Springer Science & Business Media.

Logg, A. and Wells, G. N. (2010). Dolfin: Automated finite element computing. *ACM Transactions on Mathematical Software*, 37(2).

Lysmer, J. (1970). Limit analysis of plane problems in soil mechanics. *Journal of Soil Mechanics & Foundations Div*, 96:1311–1334.

Mafusalov, A. and Uryasev, S. (2013). Conditional value-at-risk (cvar) norm: Stochastic case. Technical report, Research Report 2013-5, Department of Industrial Systems and Engineering ....

Maier, G. (1968). Quadratic programming and theory of elastic-perfectly plastic structures. *Meccanica*, 3(4):265–273.

Maitenaz, S., Mesnil, R., Onfroy, P., Metge, N., and Caron, J.-F. (2020). Sustainable reinforced concrete beams: Mechanical optimisation and 3d-printed formwork. In *RILEM International Conference on Concrete and Digital Fabrication*, pages 1164–1173. Springer.

Makrodimopoulos, A. (2010). Remarks on some properties of conic yield restrictions in limit analysis. *International Journal for Numerical Methods in Biomedical Engineering*, 26(11):1449–1461.

Makrodimopoulos, A. and Martin, C. (2007). Upper bound limit analysis using simplex strain elements and second-order cone programming. *International journal for numerical and analytical methods in geomechanics*, 31(6):835–865.

Makrodimopoulos, A. and Martin, C. (2008). Upper bound limit analysis using discontinuous quadratic displacement fields. *Communications in Numerical Methods in Engineering*, 24(11):911–927.

Marigo, J.-J. (2023). L'approche variationnelle de la rupture : un exemple de collaboration fructueuse entre mécaniciens et mathématiciens. *Comptes Rendus. Mécanique*. Online first.

Martin, C. M. and Makrodimopoulos, A. (2008). Finite-element limit analysis of Mohr–Coulomb materials in 3d using semidefinite programming. *Journal of Engineering Mechanics*, 134(4):339–347.

Maso, G. D., DeSimone, A., and Mora, M. G. (2006). Quasistatic evolution problems for linearly elastic–perfectly plastic materials. *Archive for rational mechanics and analysis*, 180:237–291.

Maugin, G. A. (1990). *Internal variables and dissipative structures*. Walter de Gruyter, Berlin/New York Berlin, New York.

Mehrotra, S. (1992). On the implementation of a primal-dual interior point method. *SIAM Journal on optimization*, 2(4):575–601.

Michell, A. G. M. (1904). LVIII. The limits of economy of material in frame-structures. *The London, Edinburgh, and Dublin Philosophical Magazine and Journal of Science*, 8(47):589–597.

Miehe, C. (2002). Strain-driven homogenization of inelastic microstructures and composites based on an incremental variational formulation. *International Journal for numerical methods in engineering*, 55(11):1285–1322.

Miehe, C., Apel, N., and Lambrecht, M. (2002). Anisotropic additive plasticity in the logarithmic strain space: modular kinematic formulation and implementation based on incremental minimization principles for standard materials. *Computer Methods in Applied Mechanics and Engineering*, 191(47-48):5383–5425.

Mielke, A. (2005). Evolution of rate-independent systems. *Evolutionary equations*, 2:461–559.

Mielke, A. and Ortiz, M. (2008). A class of minimum principles for characterizing the trajectories and the relaxation of dissipative systems. *ESAIM: Control, Optimisation and Calculus of Variations*, 14(3):494–516.

Moreau, J. J. (1970). Sur les lois de frottement, de plasticitã© et de viscositã©. *Comptes rendus hebdomadaires des sÃ© ances de l'AcadÃ© mie des sciences*, 271:608–611.

MOSEK ApS, . (2019a). MOSEK Modeling Cookbook. https://docs.mosek.com/modeling-cookbook/index.html.

MOSEK ApS, . (2019b). *The MOSEK Optimizer API for Python. Version 9.0.*

Mourad, L., Bleyer, J., Mesnil, R., Nseir, J., Sab, K., and Raphael, W. (2021). Topology optimization of load-bearing capacity. *Structural and Multidisciplinary Optimization*, 64(3):1367–1383.

Mourad, L., Bleyer, J., Mesnil, R., Nseir, J., Sab, K., and Raphael, W. (2022). Multi-material topology optimization of structural load-bearing capacity using limit analysis. working paper or preprint.

Muttoni, A., Fernández Ruiz, M., and Niketić, F. (2015). Design versus assessment of concrete structures using stress fields and strut-and-tie models. *ACI Structural Journal*, 112(5).

Nagtegaal, J. C., Parks, D. M., and Rice, J. (1974). On numerically accurate finite element solutions in the fully plastic range. *Computer methods in applied mechanics and engineering*, 4(2):153–177.

Nesterov, Y. and Nemirovskii, A. (1994). *Interior-Point Polynomial Algorithms in Convex Programming*. Studies in Applied and Numerical Mathematics. Society for Industrial and Applied Mathematics.

Nesterov, Y. and Nemirovsky, A. (1992). Conic formulation of a convex programming problem and duality. *Optimization Methods and Software*, 1(2):95–115.

Nesterov, Y. E. and Todd, M. J. (1997). Self-scaled barriers and interior-point methods for convex programming. *Mathematics of Operations research*, 22(1):1–42.

Nesterov, Y. E. and Todd, M. J. (1998). Primal-dual interior-point methods for self-scaled cones. *SIAM Journal on optimization*, 8(2):324–364.

Nielsen, M. P. and Hoang, L. C. (2016). *Limit analysis and concrete plasticity*. CRC press.

Niu, F., Xu, S., and Cheng, G. (2011). A general formulation of structural topology optimization for maximizing structural stiffness. *Structural and Multidisciplinary Optimization*, 43(4):561–572.

Nocedal, J. and Wright, S. J. (1999). *Numerical optimization*. Springer.

O'Donoghue, B., Chu, E., Parikh, N., and Boyd, S. (2016). Conic optimization via operator splitting and homogeneous self-dual embedding. *Journal of Optimization Theory and Applications*, 169(3):1042–1068.

O'Donoghue, B., Chu, E., Parikh, N., and Boyd, S. (2016). Conic optimization via operator splitting and homogeneous self-dual embedding. *Journal of Optimization Theory and Applications*, 169:1042–1068.

Ortiz, M. and Stainier, L. (1999). The variational formulation of viscoplastic constitutive updates. *Computer methods in applied mechanics and engineering*, 171(3-4):419–444.

Papanastasiou, T. C. (1987). Flows of materials with yield. *Journal of Rheology*, 31:385.

Parikh, N., Boyd, S., et al. (2014). Proximal algorithms. *Foundations and trends® in Optimization*, 1(3):127–239.

Pastor, J. and Turgeman, S. (1976). Mise en œuvre numérique des méthodes de l'analyse limite pour les matériaux de von mises et de coulomb standards en déformation plane. *Mechanics Research Communications*, 3(6):469–474.

Pavlikov, K. and Uryasev, S. P. (2014). Cvar norm and applications in optimization. *Optimization Letters*, 8:1999–2020.

Petersson, J. and Sigmund, O. (1998). Slope constrained topology optimization. *International Journal for Numerical Methods in Engineering*, 41(8):1417–1434.

Pham, K., Amor, H., Marigo, J.-J., and Maurini, C. (2011). Gradient damage models and their use to approximate brittle fracture. *International Journal of Damage Mechanics*, 20(4):618–652.

Pipkin, A. C. (1994). Relaxed energy densities for large deformations of membranes. *IMA Journal of Applied Mathematics*, 52(3):297–308.

Portioli, F., Casapulla, C., Gilbert, M., and Cascini, L. (2014). Limit analysis of 3d masonry block structures with non-associative frictional joints using cone programming. *Computers & Structures*, 143:108–121.

Quintanas-Corominas, A., Turon, A., Reinoso, J., Casoni, E., Paggi, M., and Mayugo, J. (2020). A phase field approach enhanced with a cohesive zone model for modeling delamination induced by matrix cracking. *Computer Methods in Applied Mechanics and Engineering*, 358:112618.

Ravi-Chandar, K. and Knauss, W. (1984a). An experimental investigation into dynamic fracture: II. Microstructural aspects. *International Journal of Fracture*, 26(1):65–80.

Ravi-Chandar, K. and Knauss, W. (1984b). An experimental investigation into dynamic fracture: III. On steady-state crack propagation and crack branching. *International Journal of Fracture*, 26(2):141–154.

Reissner, E. (1938). On tension field theory. *Proc. of the 5th Int. Congr. for Applied Mechanics Harvard Univ. & MIT*, pages 88–92.

Robinson, M. (1971). A comparison of yield surfaces for thin shells. *International Journal of Mechanical Sciences*, 13(4):345–354.

Rockafellar, R. T. (1970). *Convex analysis*, volume 18. Princeton university press.

Rockafellar, R. T. (2007). Coherent approaches to risk in optimization under uncertainty. In *OR Tools and Applications: Glimpses of Future Technologies*, pages 38–61. Informs.

Rockafellar, R. T. and Uryasev, S. (2002). Conditional value-at-risk for general loss distributions. *Journal of banking & finance*, 26(7):1443–1471.

Rockafellar, R. T., Uryasev, S., et al. (2000). Optimization of conditional value-at-risk. *Journal of risk*, 2:21–42.

Rozvany, G. I. and Prager, W. (1979). A new class of structural optimization problems: optimal archgrids. *Computer methods in applied mechanics and engineering*, 19(1):127–150.

Salençon, J. (1983). *Calcul à la rupture et analyse limite*. Presses de l'Ecole Nationale des Ponts et Chaussées.

Salençon, J. (2013). *Yield Design*. London, Hoboken : ISTE Ltd., John Wiley & Sons, Inc.

Sander, O. and Jaap, P. (2020). Solving primal plasticity increment problems in the time of a single predictor–corrector iteration. *Computational Mechanics*, 65(3):663–685.

Saramito, P. and Roquet, N. (2001). An adaptive finite element method for viscoplastic fluid flows in pipes. *Computer methods in applied mechanics and engineering*, 190(40):5391–5412.

Saramito, P. and Wachs, A. (2017). Progress in numerical simulation of yield stress fluid flows. *Rheologica Acta*, pages 1–20.

Save, M. (1995). *Atlas of limit loads of metal plates, shells and disks*. North-Holland Series in Applied Mathematics & Mechanics. Elsevier Science Ltd.

Save, M. A., Massonnet, C. E., and de Saxce, G. (1997). *Plastic limit analysis of plates, shells, and disks*. North Holland.

Scherer, J.-M., Besson, J., Forest, S., Hure, J., and Tanguy, B. (2019). Strain gradient crystal plasticity with evolving length scale: Application to voided irradiated materials. *European Journal of Mechanics-A/Solids*, 77:103768.

Scherer, J.-M., Brach, S., and Bleyer, J. (2022). An assessment of anisotropic phase-field models of brittle fracture. *Computer Methods in Applied Mechanics and Engineering*, 395:115036.

Schlaich, J., Schäfer, K., and Jennewein, M. (1987). Toward a consistent design of structural concrete. *PCI journal*, 32(3):74–150.

Sigmund, O. and Petersson, J. (1998). Numerical instabilities in topology optimization: a survey on procedures dealing with checkerboards, mesh-dependencies and local minima. *Structural optimization*, 16(1):68–75.

Simo, J. C. and Hughes, T. J. (2006). *Computational inelasticity*, volume 7. Springer Science & Business Media.

Simões, J. T., Faria, D. M., Ruiz, M. F., and Muttoni, A. (2016). Strength of reinforced concrete footings without transverse reinforcement according to limit analysis. *Engineering structures*, 112:146–161.

Sloan, S. W. (1988). Lower bound limit analysis using finite elements and linear programming. *International Journal for Numerical and Analytical Methods in Geomechanics*, 12(1):61–77.

Sloan, S. W. and Kleeman, P. W. (1995). Upper bound limit analysis using discontinuous velocity fields. *Computer Methods in Applied Mechanics and Engineering*, 127(1-4):293 – 314.

Smith, M. (2009). *ABAQUS/Standard User's Manual, Version 6.9*. Simulia.

Strang, G. and Kohn, R. V. (1983). Hencky-Prandtl nets and constrained Michell trusses. *Computer Methods in Applied Mechanics and Engineering*, 36(2):207–222.

Stroh, A. N. (1957). A theory of the fracture of metals. *Advances in Physics*, 6(24):418–465.

Syrakos, A., Georgiou, G. C., and Alexandrou, A. N. (2013). Solution of the square lid-driven cavity flow of a Bingham plastic using the finite volume method. *Journal of Non-Newtonian Fluid Mechanics*, 195:19–31.

Tabarrok, B. (1984). Complementary variational principles in elastodynamics. *Computers & Structures*, 19(1-2):239–246.

Tanné, E., Li, T., Bourdin, B., Marigo, J.-J., and Maurini, C. (2018). Crack nucleation in variational phase-field models of brittle fracture. *Journal of the Mechanics and Physics of Solids*, 110:80–99.

Toh, K.-C., Todd, M. J., and Tütüncü, R. H. (1999). Sdpt3—a matlab software package for semidefinite programming, version 1.3. *Optimization methods and software*, 11(1-4):545–581.

Toupin, R. (1952). A variational principle for the mesh-type analysis of a mechanical system. *Journal of Applied Mechanics-Transactions of the ASME*, 19(2):151–152.

Treskatis, T., Moyers-González, M. A., and Price, C. J. (2016). An accelerated dual proximal gradient method for applications in viscoplasticity. *Journal of Non-Newtonian Fluid Mechanics*, 238:115–130.

Upadhyay, M. V. and Bleyer, J. (2022). Dislocation transport using a time-explicit Runge-Kutta discontinuous Galerkin finite element approach. *Modelling and Simulation in Materials Science and Engineering*.

Vincent, H. (2018). *Développement d'un modèle de calcul de la capacité ultime d'éléments de structure (3D) en béton armé, basé sur la théorie du calcul à la rupture*. PhD thesis, Paris Est.

Vincent, H., Arquier, M., Bleyer, J., and de Buhan, P. (2018). Yield design-based numerical analysis of three-dimensional reinforced concrete structures. *International Journal for Numerical and Analytical Methods in Geomechanics*, 42(18):2177–2192.

Vincent, H., Arquier, M., Bleyer, J., and de Buhan, P. (2020). Numerical upper bounds to the ultimate load bearing capacity of three-dimensional reinforced concrete structures. *International Journal for Numerical and Analytical Methods in Geomechanics*, 44(16):2216–2240.

Wagner, H. (1929). Flat sheet metal girders with very thin metal web. *Z. Flugtechn. Motorluftschiffahrt*, 20:200–314.

Wright, M. (2005). The interior-point revolution in optimization: history, recent developments, and lasting consequences. *Bulletin of the American mathematical society*, 42(1):39–56.

Xie, Y. M. and Steven, G. P. (1997). Basic evolutionary structural optimization. In *Evolutionary structural optimization*, pages 12–29. Springer.

Zheng, Y., Fantuzzi, G., Papachristodoulou, A., Goulart, P., and Wynn, A. (2017). Chordal decomposition in operator-splitting methods for sparse semidefinite programs.

Zhou, F. (1996). *Study on the macroscopic behavior and the microscopic process of dynamic crack propagation*. PhD thesis, PhD dissertation. The University of Tokyo, Tokyo.

Ziegler, H. (1963). Some extremum principles in irreversible thermodynamics, with application to continuum mechanics. *Progress in solid mechanics, vol. 4*, pages 93–193.

Zowe, J., Kočvara, M., and Bendsøe, M. P. (1997). Free material optimization via mathematical programming. *Mathematical programming*, 79(1):445–466.